Analysis of Ion Migration and Ageing Characteristics for Triple-cation and CH3NH3PbI3-xClx Perovskite Based Thin-Film Solar Cells

Minjin Kim

INSTITUT POLYTECHNIQUE DE PARIS

NNT : 2021IPPAX092

Thèse de doctorat

Analysis of Ion Migration and Ageing Characteristics for Triple-cation and $CH_3NH_3PbI_{3-x}Cl_x$ Perovskite Based Thin-Film Solar Cells

Thèse de doctorat de l'Institut Polytechnique de Paris
préparée à Ecole Polytechnique

École doctorale n°626 Ecole Doctorale de l'Institut Polytechnique de Paris (ED IP Paris)
Spécialité de doctorat: Physique

Thèse présentée et soutenue à Palaiseau, le 22 Octobre 2021, par

MINJIN KIM

Composition du Jury:

Guillaume, Wantz Prof., Bordeaux INP, IMS / CNRS (UMR 5218), France	Président
Emmanuelle Deleporte Prof., Lumin, ENS Paris-Saclay / CNRS, France	Rapporteur
Johann Bouclé Prof., XLIM, Universite de Limoges / CNRS, France	Rapporteur
Noëlla Lemaitre Dr., LCT, CEA-INES, Le Bourget-du-Lac, France	Examinateur
Yvan Bonnassieux Prof., LPICM, Ecole polytechnique, IP Paris (UMR 7647), France	Directeur de thèse
Bernard Geffroy Dr., LICSEN, NIMBE-CEA&Ecole polytechnique, Paris-Saclay, France	Co-encadrant
Patrick Chapon Dr., Horiba Scientific, France	Invité

Acknowledgement

I would like to express profound gratitude to Prof. Emmanuelle Deleporte, Dr. Johann Bouclé, Prof. Guillaume Wantz, Dr. Noella Lemaitre, who reviewed this thesis manuscript, and Dr. Patrick Chapon for accepting to be part of the jury. This study was possible with the Ecole Doctorale of Ecole Polytechnique for their Ph.D. grants.

Foremost, I would like to express sincere gratitude to my director Prof. Yvan Bonnassieux for the continuous support of my Ph.D. study in LPICM—Ecole Polytechnique. Thanks to his considerate support and encouragement for my studies, I was able to quickly adapt to the perovskite research field and maintained my passion for my Ph.D. research.

Especially, I would like to express my deep gratitude to Dr. Bernard Geffroy, Dr. Jean-Eric and Dr. Denis Tondelier, who are co-directors of my thesis. Their enthusiastic teaching and advice led me to finish my doctoral dissertation. Dr. Bernard Geffroy, he always shared his knowledge and assisted in collaborating research with other laboratories, such as LPS, Geeps, ILV-UVSQ, Synchrotron SOLEIL. Dr. Jean-Eric Bourée, he did not hesitate to discuss theoretical interpretation to improve my research quality. Dr. Denis Tondelier, who taught me how to use and manage machines fabricating perovskite solar cells.

I would like to thank Dr. Heejae Lee as a previous researcher on my subject. He introduced me to the perovskite research field and taught me about experimental methods, how to manage research, and interpretation from various perspectives.

I would like to thank my fellow group members, Dr. Novikova Tatiana, Prof. Pere Roca I Cabarrocas, Dr. Jean-Charles Vanel, Prof. Abderrahim Yassar, and Dr. Gael Zucchi, for academic and emotional support. Conversations with them always brought new perspectives to my study.

I take this opportunity to sincerely thank CHARM pole and all the support teams of the lab (BEER team, Laurence, Gaby, Fred).

It is important to thank Jacqueline Tran that part of the SEM analyses was performed at centre interdisciplinaire de microscopie électronique de l'X (CIMEX), which is gratefully acknowledged for the use of the electron microscopes at Ecole Polytechnique.

I extremely grateful to Dr. Sandrine Tusseau-nenez and her support for the X-ray crystallography facility, DIFFRAX Ecole Polytechnique, Institut Polytechnique de Paris.

I would like to thank Dr. Patrick Chapon (Horiba Scientific), Dr. Sofia Gaiaschi (Horiba Scientific), Dr. Pavel Bulkin (LPICM-Ecole Polytechnique), and Prof. Muriel Bouttemy (Institut Lavoisier de Versailles—Université de Versailles Saint-Quentin-en-Yvelines), Dr. Mathieu Fregnaux (ILV-UVSQ), Dr. Pia Dally (IPVF and ILV—UVSQ) for sharing me unlimited knowledge to measure GD-OES, XPS, and UPS. I felt comfortable during my research because of their warm-hearted care.

I started the fruitful collaboration with Dr. Olivier Plantevin, Dr. Subodh Kumar Gautam (LPS, Université Paris-Saclay), Dr. Douglas Rodrigues Miquita (Centre de Micropia-Universidade Federal de Minas Gerais Belo Horizonte) was the result of an inspiring discussion. I would like to express deep gratitude to them.

As for the collaboration with the GEEPS laboratory, I would like to thank Prof. Denis Mencaraglia and Dr. Guillaume Chau. The low-temperature conductivity study for perovskite carried out with them gave me a lesson, given at below pico ampere unit measurement, allowed me to refine and mature my PhD topic at the end of my first year.

I would like to thank Dr. Vincent Jacques (LPS/CNRS), Dr. Kadda Medjoubi (Synchrotron Soleil), and Mr. Antoine Loncle (Synchrotron Soleil, PHENIX) for the great collaboration to analyze the stoichiometry of triple cation perovskite layers.

I would like to thank Dr. Sufal Swaraj, who taught the X-ray analytics and STXM system working principle. X-ray analytics became the basis for understanding photo excitation-based analysis equipment.

I would also like to thank my past and present co-workers for their assistance and friendship: Dr. Arthur Marronnier, Dr. Heechul Woo, Dr. Seonyoung Park, Dr. Hee Ruyng Lee, Hindia Nahdi, Akiki Ghewa, Junkang Wang, Anatole Desthieux, Corentin Paillassard, Haeyeon Jun, Michel Concalves, Seong Gil Kang, Seongbin Lim, Yun Ho Ahn, Youngro Lee, Jisoo Oh, Hangyeol Kang, Wonseok Lee, Wonjae Kim, Seoungbum Lim.

Finally, I would like to thank my family in South Korea.

Contents

Abstract

Hybrid organic-inorganic perovskite materials (HOIPs) have emerged as an exciting research topic in chemistry and materials science for their attractive photoelectrical properties. The discovery of the potential of this material was considered by the journal Science as one of the ten most significant scientific breakthroughs in 2013. Lead-halide perovskite materials have been extensively studied for photovoltaic applications with power conversion efficiency nowadays over 25%. However, despite their processing advantages (low-cost solution process) and outstanding solar to electrical energy conversion properties, HOIPs materials suffer from several drawbacks such as environmental stability impeding their commercialization. It has been suggested that ionic migration in HOIPs could impact optoelectronic performance and affect device operation and long-term stability. However, despite considerable advancements in this research domain, several questions with respect to the physics of ions in perovskite materials remain unsolved. In this thesis, analyses of $CH_3NH_3PbI_{3-x}Cl_x$ (MAPI) and Triple-cation Lead Halide {3CP: $(MA_{0.17}FA_{0.83})_{0.95}Cs_{0.05}Pb(I_{0.83}Br_{0.17})_3$ (MA: Methylammonium, FA: Formamidinium)} based perovskite thin films and solar cells are presented.

In a first step, the synthesis of the halide perovskite layer (3CP) is optimized by controlling the deposition conditions such as anti-solvent treatment, annealing condition, and dynamic- dispense process. 3CP based Perovskite Solar Cells (PSCs) are then manufactured in the inverted (p-i-n) planar structure and characterized optically and electrically in a second step.

Direct experimental evidence of ion migration in HOIPs (MAPI and 3CP) under an applied constant electric field was found by the Glow Discharge Optical Emission Spectroscopy (GD-OES). In-situ and ex-situ GD-OES results showed that 3CP had faster ion migration recovery compared to MAPI. Through Impedance Spectroscopy (IS), the ion accumulation phenomenon at the interface was observed only with a voltage sweep for 2 min (range: -0.5 V ↔ +1.0 V). From IS measurement, a relative dielectric constant of 17 (MAPI) and 19 (3CP) is calculated for the perovskite materials.

Finally, the ageing mechanism of the PSCs was investigated with solar cell performance ageing, IS, and GD-OES. An increase in ageing-related ion accumulation at the interface was observed for ten days. After long-term ageing, halogen ions were observed in the top silver electrode with GD-OES. The results demonstrate that halide ions in the HOIP layer diffuse into the top silver electrode in the form of silver halide (AgI and AgBr), as already mentioned in the literature.

Researching ion migration and ageing characteristics proposes a perspective to understand why 3CP is more stable than MAPI. When developing a more improved perovskite material and evaluating the material properties, this study can suggest one criterion for material evaluation.

Résumé

Les matériaux pérovskites hybrides organiques-inorganiques (HOIPs) sont devenus un sujet de recherche passionnant en chimie et en science des matériaux pour leurs propriétés photoélectriques attrayantes. La découverte du potentiel de ce matériau a été considérée par la revue Science comme l'une des dix percées scientifiques les plus importantes en 2013. Les pérovskites aux halogénures de plomb ont été largement étudiées pour les applications photovoltaïques avec aujourd'hui un rendement de conversion énergétique de plus de 25 %.

Cependant, malgré leur faible coût de fabrication et leurs propriétés exceptionnelles de conversion de l'énergie solaire en énergie électrique, les matériaux HOIP souffrent de plusieurs inconvénients tels que la stabilité environnementale qui entrave leur commercialisation. Il a été suggéré que la migration ionique dans les HOIP pourrait avoir un impact sur les performances optoélectroniques et affecter le fonctionnement et la stabilité à long terme des dispositifs. Cependant, malgré des avancées considérables dans ce domaine de recherche, plusieurs questions concernant la physique des ions dans les matériaux pérovskites restent en suspens. Dans cette thèse, l'analyse de pérovskites hybrides de type $CH_3NH_3PbI_{3-x}Clx$ (MAPI) et de type {3CP: $(MA_{0.17}FA_{0.83})_{0.95}Cs_{0.05}Pb(I_{0.83}Br_{0.17})_3$ (MA: Methylammonium, FA: Formamidinium)} sont présentées à la fois en films minces et en cellules solaires (PSCs).
Dans une première étape, L'optimisation de la synthèse de la pérovskite hybride halogénée de type 3CP sera présentée. La synthèse de la couche de pérovskite aux halogénures (3CP) est optimisée en contrôlant les conditions de dépôt telles que le traitement anti-solvant, les conditions de recuit et le processus de distribution dynamique. Les cellules solaires à base de pérovskite 3CP seront ensuite fabriquées selon une structure inversée (type p-i-n) et caractérisées optiquement et électroniquement.
Des preuves expérimentales directes de la migration des ions dans les HOIP (MAPI et 3CP) sous un champ électrique constant ont été démontrées par la spectroscopie d'émission optique par décharge plasma (GD-OES). Les résultats GD-OES in-situ et ex-situ ont montré que le 3CP avait une récupération plus rapide de la migration des ions par rapport au MAPI. Grâce à la Spectroscopie d'Impédance (IS), le phénomène d'accumulation d'ions à l'interface n'a été observé qu'avec un balayage de tension pendant 2 minutes. A partir de la mesure IS, une constante diélectrique relative de 17 (MAPI) et 19 (3CP) est calculée pour les matériaux pérovskites.

Enfin, le mécanisme de vieillissement des PSCs a été étudié avec le vieillissement des performances des cellules solaires, les mesures d'IS et GD-OES. Une augmentation des ions accumulés à l'interface, due au vieillissement, est observée au bout de 10 jours. Après un vieillissement à long terme, des ions halogènes ont été observés dans l'électrode d'argent supérieure avec GD-OES. Les résultats démontrent que les ions halogénures de la couche HOIP diffusent dans l'électrode d'argent supérieure sous forme d'halogénures d'argent (AgI et AgBr) comme cela a déjà été proposé dans la littérature.

La recherche des caractéristiques de migration et de vieillissement des ions propose une perspective pour comprendre pourquoi le 3CP est plus stable que le MAPI. Lors du développement d'une pérovskite encore améliorée, cette étude peut suggérer un critère d'évaluation du matériau.

Chapter 1. Introduction

1.1. Global Energy Transition

Global energy consumption has increased manifold over the last thirty years. In addition, the problem of global warming caused by CO_2 from fossil fuel consumption is steadily on the rise. To improve the current worldwide problem, research on alternative non-fossil energy sources is actively taking place [1-4].Currently, most of the global energy demand is still fed either by fossil fuels or nuclear energy. However, these are unsuitable as sustainable energy sources and pose serious environmental and security problems/issues [5]. Therefore, the most crucial challenge for the present generation is to enable a complete transition in energy production and consumption towards cleaner, safer options. In this respect, renewable energy sources are excellent alternatives. Besides being environmentally friendly, they offer several other advantages [6].

Figure 1. 1. Application of solar cell technology to harvest solar energy [7].

Several renewable energy resources are being developed or have already been introduced commercially. Among those, solar energy is one of the most important ones today.

In nature, solar energy facilitates photosynthesis in plants that convert electromagnetic energy from solar radiation into chemical energy. Thus, solar energy is a clean and free energy source promising weapons in our fight against climate change and energy poverty. Researchers are constantly developing solutions to efficiently convert solar radiation into heat energy (solar thermal systems) or electrical energy (photovoltaics) to enable this energy transition. Solar cells are now widely recognized as a promising energy source.

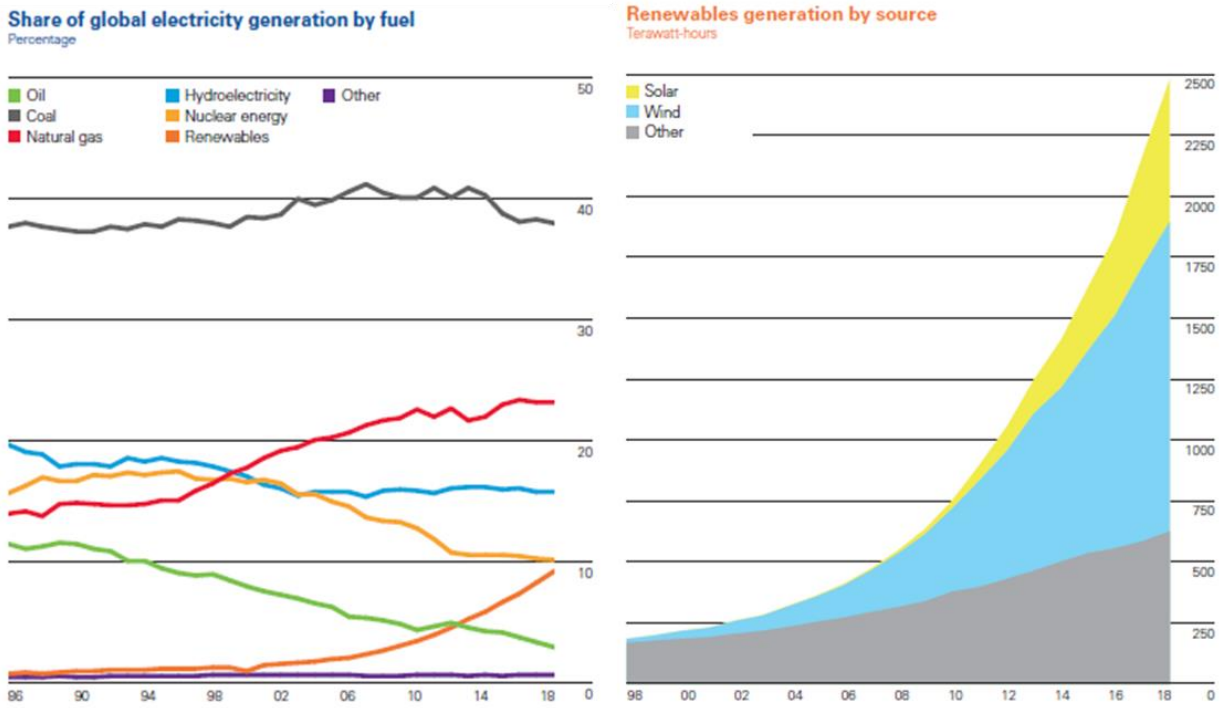

Figure 1. 2. Share of global electricity generation (percentage vs. year) and solar energy generation (terawatt hours vs. year) [3].

1.1.1 Air Mass (AM)

The Air Mass is the path length that light takes through the atmosphere normalized to the shortest possible path length (when the sun is directly overhead). Thus, the Air Mass quantifies the reduction in the power of light as it passes through the atmosphere and is absorbed into air and dust. It is defined as follows:

$$AM = \frac{L}{L_0} \approx \frac{1}{cos\, z} \qquad 2.1 - (1)$$

; where L is the path length through the atmosphere, L_0 is the zenith path length at sea level, and z is the solar radiation zenith angle.

The AM is commonly used to characterize the operating environment of solar cells under standardized conditions. “AM1.5” indicates the spectrum of 100mW/cm^2 irradiance and is useful to represent the overall yearly average for mid-latitudes. It is thus used for standardized testing or rating of terrestrial solar cells or modules. “AM0” is the spectrum outside the atmosphere, and it is used for space power applications. “AM1” is the spectrum after traveling through the atmosphere to sea level with the sun

directly overhead and it is useful to estimate the performance of solar cells in equatorial and tropical regions.

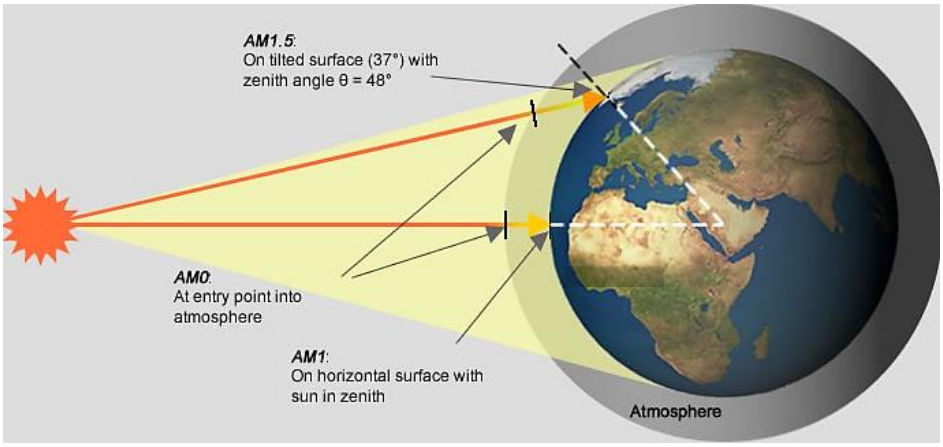

Figure 1. 3. Schematic representation of the concept of Air Mass

1.2. Operating Principles of Solar Cells

When a solar cell is placed under illumination, a difference of potential is generated across the cell, giving rise to the flow of electrical current that is then directed into an external circuit. The current flowing from the anode (positive terminal) to the cathode (negative terminal) produces a current-voltage relationship (I-V curve) that is similar to the behavior of an ordinary semiconductor diode. Under illumination, charge separation and collection in the cell are enhanced rapidly. Thus, the solar cell function switches from a diode to a generator of electrical power. Solar cell operation can be described by the following steps [8-10]:

1.2.1. Light absorption

Photons of energy higher than the bandgap of the solar cell material are absorbed as light energy. This absorbed energy generates electron-hole pairs (EHP) in the photoactive layer of the solar cell. After the absorption of energy, these excited electrons and holes can exist in the material for a length of time called minority carrier lifetime before they recombine each other. A hole is an absence of an electron. Moreover, it is a positive charge moving in the opposite direction from an electron with an electrical field. This process is called the charge carrier generation.

1.2.2. Carrier actions: drift, diffusion, and generation-recombination

Two mechanisms govern the flow of charge carriers in semiconductor devices. The first one, “Diffusion,” is caused by a gradient of carrier concentration in the material that leads to the random motion of carriers from regions of high concentration to regions of low concentration. “Drift” is the second movement mechanism that involves the movement of charge carriers under the influence of an (external, internal, or both) electric field in the material. For example, in the solar cell structure, a built-in electric field causes electrons to move toward the cathode and holes to move toward the anode. Depending on the type of material used in the solar cell, the charge carrier transport mechanism is called “hopping transport” (organic solar cells) and “band transport” (inorganic solar cells).

The electron (charge carrier) has two energy states. One is the excited state, and the other is the ground state. When the photoactive layer absorbs photons with enough energy in the solar cell, electrons get excited. We call this phenomenon “photogeneration”. When the excited electrons relax back to the ground state by losing excited energy, we call this phenomenon “recombination”. Since collecting the

excited electrons and holes outside of the solar cell constitutes electricity generation, recombination negatively affects the solar cell. For a good solar cell, longer diffusion lengths are desirable so that the carriers can be collected as current before they are lost to recombination. Diffusion length is the distance that a carrier (electron or a hole) can travel before the recombination. Furthermore, the carrier lifetime is the time it takes to diffuse before the recombination.

1.3. Solar cell parameters

Electrical characteristics: I-V, FF, PCE, R_s, R_{sh}, EQE

1.3.1. Photo Current (I_L) & Dark Current (I_0)

The current-voltage (IV) curve of a solar cell is the superposition of the IV curve of the solar cell diode in the dark (I_0) with the light-generated current (I_L). The light has the effect of shifting the IV curve down into the fourth quadrant, where power can be extracted from the diode, and the solar cell becomes a generator. Although the actual solar cells do not strictly accompany this shift, solar cells have a dominant tendency of the shift. Illuminating a cell adds the photo-generated current to the normal "dark" current in the diode so that the diode current equation becomes [10-12]:

$$I = I_0 \left[exp\ exp\left(\frac{qV}{nKT}\right) - 1\right] - I_L \qquad 1.3-(1)$$

where $1 \leq n \leq 2$ is the ideality factor, $k = 1.38 \times 10^{-23}$ m^2kg/s^2K is the Boltzmann constant, q is an electronic charge, and T is the absolute temperature

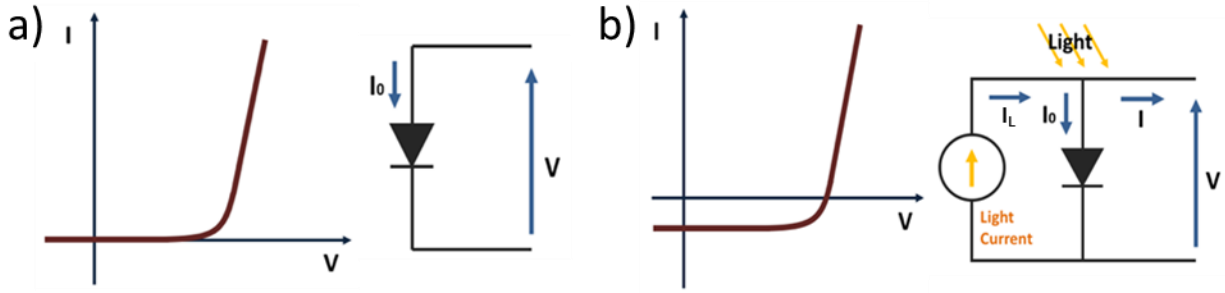

Figure 1. 4. I-V characteristics and equivalent circuits for a solar cell: a) in dark condition, and b) under illumination.

It is a common convention to take I_L as positive and move the curve to the first quadrant, the equation for the IV curve in the first quadrant becomes:

$$I = I_L - I_0 \left[exp\ exp\left(\frac{qV}{nKT}\right) - 1\right] \qquad 1.3-(2)$$

The -1 term in the eq 1.3 - (2) is negligible since the exponential term is dominant (>> 1) except for the voltage (V) term below 100mV. Besides, photo current term (I_L) dominates the I_0 (…) term at low voltage. Thus, the -1 term is not necessary under illumination conditions.

$$I = I_L - I_0 \left[exp\ exp\ \left(\frac{qV}{nKT} \right) \right] \qquad 1.3 - (3)$$

We presented the electrical characteristics of the solar cell with equation 1.3 – (3). In the following, we will introduce some factors, which are commonly in use to characterize a solar cell, like the short circuit current (I_{sc}), the open-circuit voltage (V_{oc}), and the fill factor (FF).

1.3.2. Short circuit current (I_{SC})

The short-circuit current is the current through the solar cell when the bias voltage across the solar cell is zero (i.e., when the solar cell is short-circuited). So, as an operating point, the power from the solar cell is zero. Usually written as I_{SC}, the short-circuit current is shown on the IV curve in Figure 1.5 below.

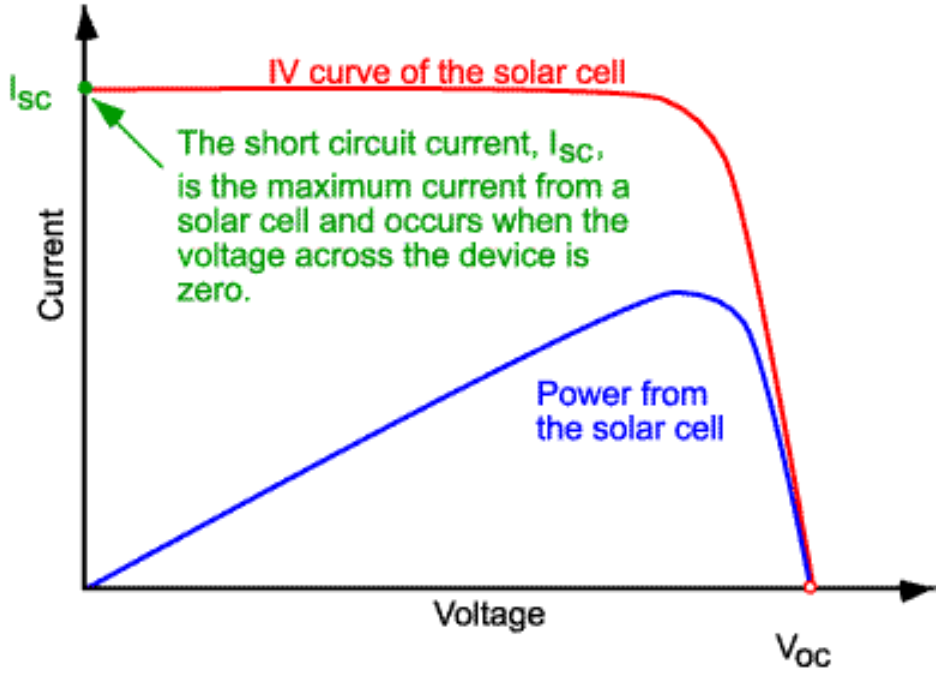

Figure 1. 5. I-V curves of a solar cell showing the short-circuit current. [13]

The short-circuit current is due to the generation and collection of light-generated carriers. For an ideal solar cell at most moderate resistive loss mechanisms, the short-circuit current and the light-generated current are identical, i.e., $I_{SC} = I\ (V=0) = I_L$. Therefore, the short-circuit current is the largest current that may be drawn from the solar cell. To remove the current dependence on the solar cell area, it is more common to write the current density (Jsc or J in mA/cm2) rather than the current by dividing the current Isc by the active area of the current measured solar cell.

1.3.3. Open circuit voltage (V_{OC})

The open-circuit voltage, V_{OC}, is the maximum voltage available from a solar cell, and this occurs at zero current. So, as an operating point, the output power from the solar cell is zero. The open-circuit voltage corresponds to the amount of forward bias on the solar cell due to the bias of the solar cell junction with the light-generated current. The maximum value is limited by the bandgap (E_g) of the material. The open-circuit voltage is shown on the IV curve in Fig. 1.6 below.

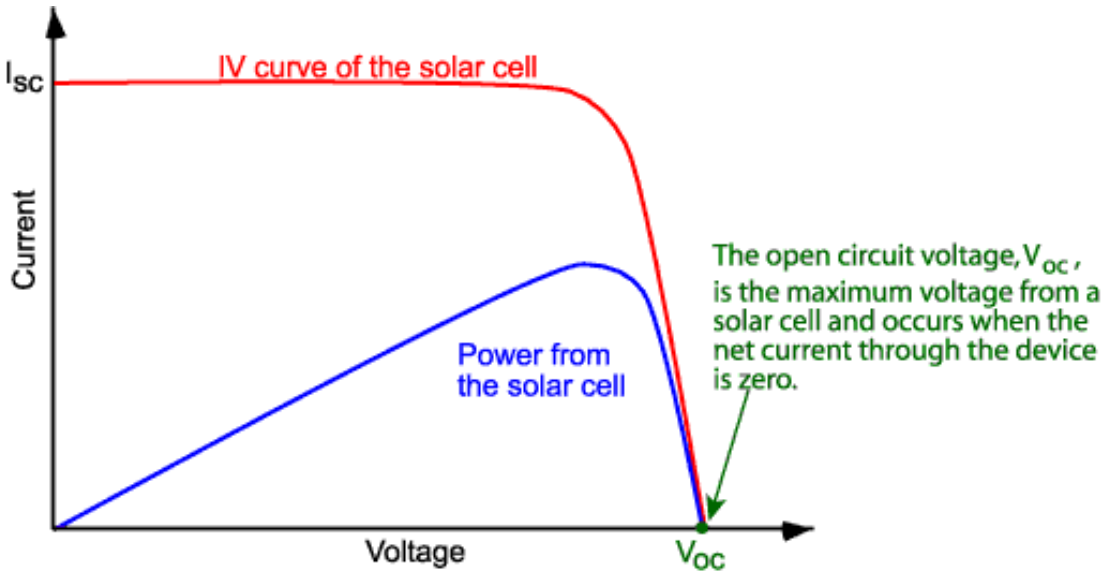

Figure 1. 6. I-V curves of a solar cell showing the open-circuit voltage [13].

An equation for V_{oc} is found by setting the net current equal to zero in the solar cell equation to give:

$$V_{OC} = \frac{nKT}{q}\, ln\left(\frac{I_L}{I_0} + 1\right) \qquad 1.3 - (4)$$

V_{oc}: open-circuit voltage, I_L: illuminated current, I_0: dark current.

Since open circuit voltage is known as the maximum potential difference when there is no current and the circuit is not closed, its values are often quoted under particular conditions (state-of-charge, illumination, temperature) for solar cells [14]. The open-circuit voltage increases by increasing the bandgap. Under the illumination, electrons and holes accumulate in the light-absorbing layer. The accumulation of electrons and holes on the two sides of the junction produces the open-circuit voltage.

1.3.4. Maximum Power Point (MPP), Fill Factor (FF) and Power Conversion Efficiency (PCE)

Power Conversion Efficiency (PCE) is a commonly used parameter to compare the performances of different solar cells. To calculate the PCE, the Maximum Power Point (MPP) and Fill Factor (FF) are required [15-17]. A desirable operating point (I_M, V_M) called the Maximum Power Point should be obtained by maximizing the product of current and voltage.

The product $I_M \cdot V_M$ corresponds to the maximum power that can be extracted from a solar cell under certain fixed conditions, and in an ideal cell, it should be equal to $I_{sc} \cdot V_{oc}$. Fill Factor is the ratio defined by:

$$FF = \frac{I_M V_M}{I_{SC} V_{OC}} \quad ; \text{(ideal = 1, worst = 0)} \qquad 1.3 - (5)$$

Moreover, it gives a quantitative measure of the "squareness" of the I-V curve. For good quality, real, non-ideal cells, its value usually lies within the range of 0.6 to 0.85. Applying the definition of Fill Factor, the Power Conversion Efficiency, which is defined as the ratio between the maximum electrical power that can be delivered to the load, P_{max}, to the power of the radiation incident on the cell, P_{in}, can be expressed as:

$$PCE = \frac{Maximum\ output\ power\ from\ the\ solar\ cells}{Input\ power} = \eta = \frac{P_{max}}{P_{in}} = \frac{I_M V_M}{P_{in}} = \frac{FF \cdot I_{SC} \cdot V_{OC}}{P_{in}} \qquad 1.3 - (6)$$

(Note: 'I' can be replaced by 'J' as current density in all the above equations if incident power is given regarding power per unit area)

The efficiency is affected by several factors, including the intensity of the incident solar radiation and the temperature of the solar cells. In order to achieve maximum efficiency, we need to optimize external conditions carefully. Most terrestrial commercial solar cells are measured at AM1.5 and 25ºC.

1.3.5. Series Resistance (R_S) and Shunt Resistance (R_{Sh})

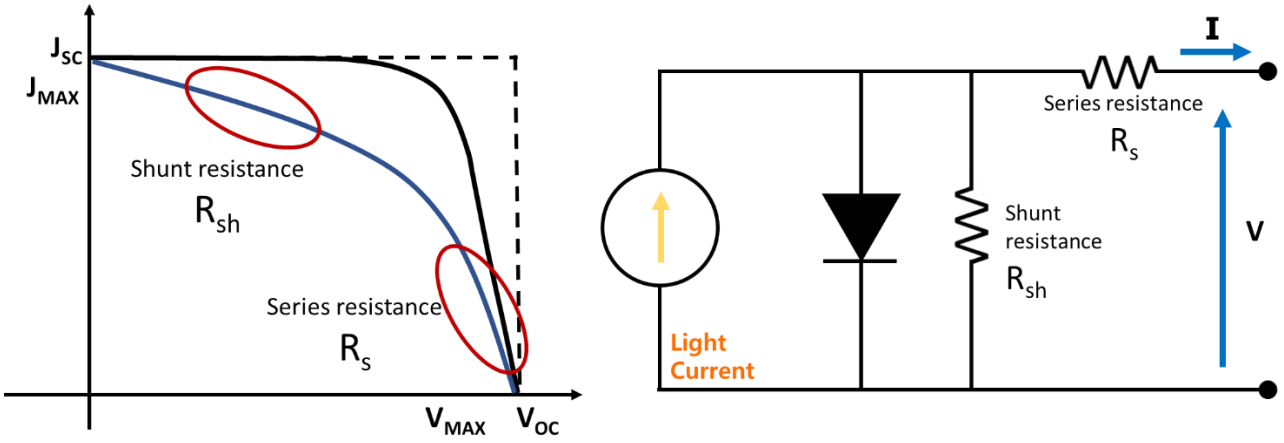

Figure 1. 7. Shunt resistance and series resistance in the J-V characteristics and the equivalent circuits.

From an analysis of the J-V characteristics of actual solar cells, the effect of two types of resistances, series resistance (R_s) and shunt resistance (R_{sh}), can be observed [18,19]. First, R_s represents the contact resistance of two-terminal electrodes. Between two terminal electrodes, the layers constituting the solar cell are connected in series. The thicker photo absorbing layer, therefore, can increase the series resistance. High-series resistance's impact is to reduce the fill factor, although excessively high values may reduce the short-circuit current. Second, the R_{sh} indicates the leakage current through the solar cell. Defects in the solar cell cause the leakage current—higher leakage current results in a lower fill factor and lower V_{oc} through the p-n junction. Finally, the effect of shunt resistance is dominant when the light density is low.

Among these four basic solar cell parameters, FF decreases by high R_s and low R_{sh}. The equation that summarizes these relations is:

$$J = J_{sc} - J_0\left[exp\left\{\frac{q(V+JR_s)}{kT}\right\}\right] - \frac{V+JR_s}{R_{sh}} \qquad 1.3-(7)$$

The zero R_s and infinite R_{sh} is the ideal case. Fig. 1.7 shows equivalent circuits and an example of J-V curve with poor R_s and R_{sh}. Ideal R_s and R_{sh} make the curve close to the ideal diode form (dashed perpendicular line in Fig. 1.7). In addition, R_s has a bigger effect on the whole I-V curve shape than R_{sh}.

1.3.6. Quantum efficiency

The "quantum efficiency" (Q.E.) is the ratio of the number of carriers collected by the solar cell to the number of photons of a given energy incident on the solar cell. The quantum efficiency may be given either as a function of wavelength or as energy. If all photons of a specific wavelength are absorbed, and the resulting electron and hole pairs are collected, then the quantum efficiency at that particular wavelength is unity. The quantum efficiency for photons with energy below the bandgap is zero. The quantum efficiency curve of an ideal solar cell is shown in Fig. 1.8 below.

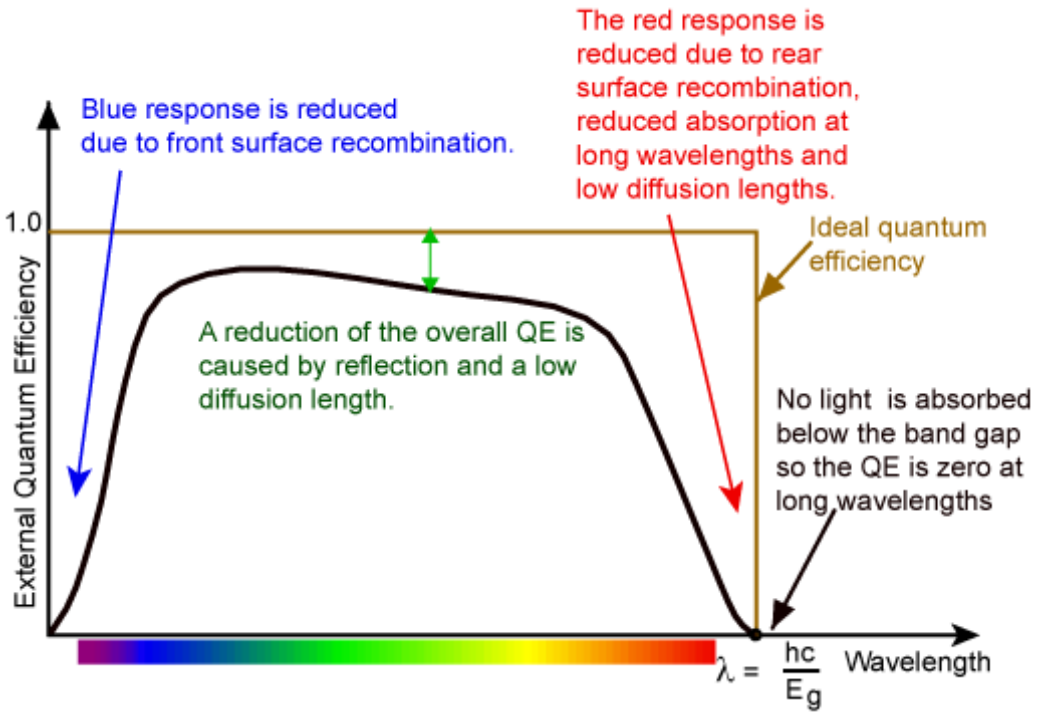

Figure 1. 8. Quantum Efficiency of an ideal solar cell plotted against the wavelength of incident photons [13].

Quantum efficiency is usually not measured much below 350 nm as the power from the AM1.5 contained in such low wavelengths is low. While quantum efficiency ideally has the square shape shown above, the quantum efficiency for most solar cells is reduced due to recombination effects. The same mechanisms which affect the collection probability also affect the quantum efficiency. For example, front surface passivation affects carriers generated near the surface. Since blue light is absorbed very close to the surface, high front surface recombination will affect the "blue" portion of the quantum efficiency. Similarly, green light is absorbed in the bulk of a solar cell. A low diffusion length will affect the collection probability from the solar cell bulk and reduce the quantum efficiency in the green portion of

the spectrum. The quantum efficiency can be viewed as the collection probability due to the generation profile of a single wavelength, integrated over the device thickness and normalized to the incident number of photons.

The "external" quantum efficiency includes the effect of optical losses such as transmission and reflection. However, it is often useful to look at the quantum efficiency of the light left after the reflected, and transmitted light has been lost. "Internal" quantum efficiency refers to the efficiency with which photons that are not reflected or transmitted out of the cell can generate charge carriers. By measuring the reflection and transmission of a device, the external quantum efficiency curve can be corrected to obtain the internal quantum efficiency curve.

Following these definitions, to determine $J_{sc,}$ we combine the photon flow at a wavelength with the EQE at this same wavelength, leading to the flow of electrons crossing the cathode and the flow of holes crossing the anode of the solar cell at this wavelength. J_{SC} is then obtained by integrating across all the relevant wavelengths from λ_1 to λ_2 (λ_1 the shortest wavelength absorbed in the solar cell, λ_2 starting wavelength absorbed in the solar cell):

$$J_{SC} = -q \int_{\lambda_1}^{\lambda_2} EQE(\lambda) \cdot \psi_{Ph,\lambda}^{AM1.5} \, d\lambda \qquad 1.3 - (8)$$

With the spectral photon flux $\psi_{ph,\lambda}$. For formal type solar cells, the important range would be from 300 to 1200 nm.

1.4 Perovskite Solar Cells

1.4.1. Perovskite lattice structure

A perovskite, named after being discovered by the Russian mineralogist L. A. Perovski, is any material with the same type of crystal structure as the naturally occurring calcium titanium oxide ($CaTiO_3$). The general chemical formula of the perovskite structure is 'ABX_3' in the cubic unit cells where the 'A' atom (large atomic or molecular cation) sits at cube-corner positions (0, 0, 0), the 'B' atom (smaller atomic or molecular cation) sits at body-centered position (1/2, 1/2, 1/2) and the 'X' atoms (anions) sit at face-centered positions (1/2, 1/2, 0).

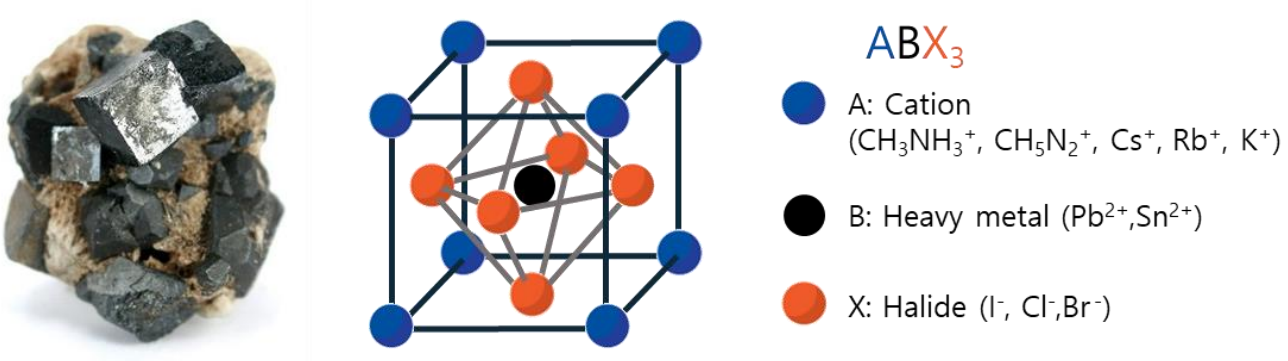

Figure 1. 9. Naturally occurring perovskite and the perovskite structure are commonly used for applications in solar cells. [20]

The crystalline phase and structure of artificial perovskites can be changed by varying the relative ion size or temperature. The most common perovskites contain oxygen molecules. Therefore, these compounds are commonly used in solar cell applications. For example, A = organic cation (ex. methylammonium ($CH_3NH_3^+$), B = inorganic cation (ex. Lead (II), (PbI_2)) and 'X'= halide anion (ex. chloride (Cl^-), iodide (I^-) are perovskite structures of the generic form ABX_3. Since the first perovskite solar cell study (Kojima *et al.*) [21], the basic material's chemical formula is $MAPbI_3$. The material is also called methylammonium lead halide (MAPI for short). In this study, it was used as a reference material to compare with a triple-cation perovskite {3CP: $(MA_{0.17}FA_{0.83})_{0.95}Cs_{0.05}Pb(I_{0.83}Br_{0.17})_3$}.

1.4.2. Advantages of perovskite solar cells

In recent years, the study of perovskites has been focused on various fields, and photovoltaics is one of the most popular ones. The Power Conversion Efficiency of solar cells based on perovskite materials has been increasing rapidly over a relatively short period compared to other conventional solar cells (Fig. 1.10). Although there are some disadvantages (degradation in moisture, safety concerns of using lead) related to perovskite solar cells, this impressive rise in performance in the last few years is still very significant and highly motivating.

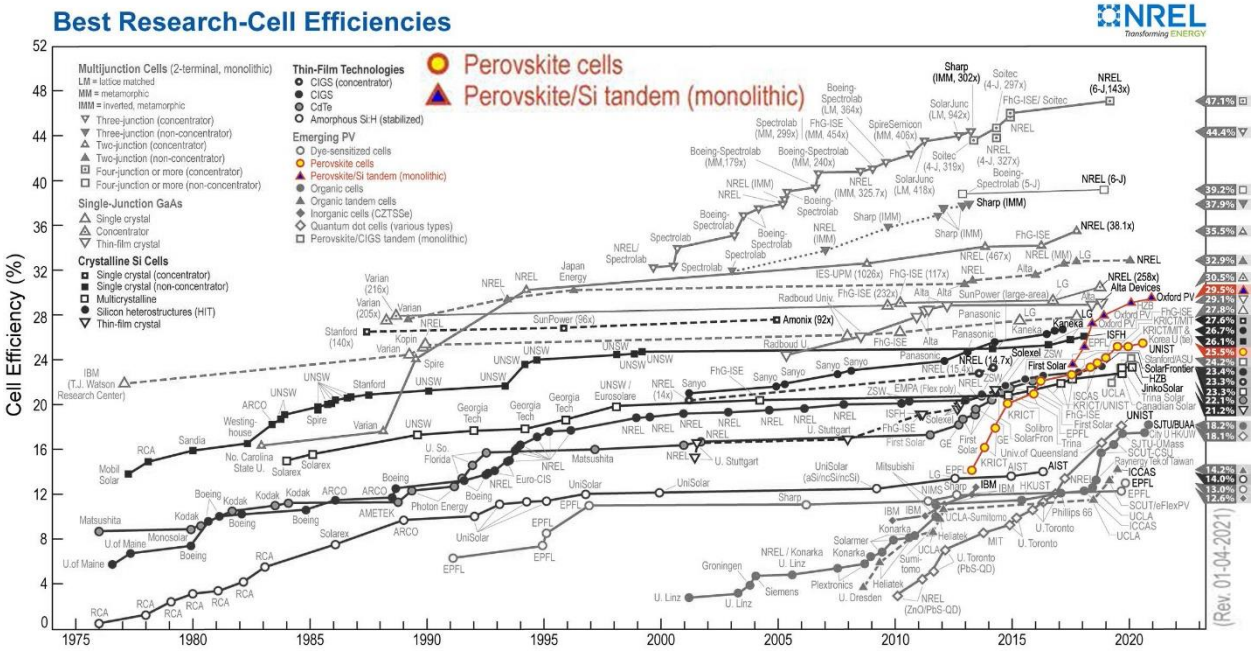

Figure 1. 10. The growth of solar cell efficiencies. [22]

Perovskites have lots of merits which makes them a good candidate for solar cells. The process of converting light into electricity through a solar cell consists of:

a. Absorption

b. Diffusion of excited carriers to the anode (for holes) and cathode (for electrons)

c. Collection of excited carriers at each electrode.

The material should have an appropriate bandgap to absorb and utilize sunlight spectrum and a excellent absorption coefficient for efficient absorption. For example, MAPI and 3CP have a bandgap of 1.6 eV [23]. The 1.6eV bandgap is a suitable property to absorb the solar spectrum in the visible range. For the other property, MAPI has an excellent absorption coefficient of 0.91×10^5 cm^{-1} [24]. Because of

these optical characteristics, perovskite film absorbs most of the sunshine with only several hundred nanometers thick.

A representative feature of diffusion of excited carriers is small exciton binding energy (E_b). Depending on the E_b, excited electrons have different movement mechanisms. If E_b is less than or similar to the energy provided by room temperature (RT), $E_b \leq$ RT ~25.7 meV, the material tends to dissociate electron/hole pair at RT. Thus, a material having a small E_b ($\cong$ 25.7 meV) is a good factor for solar cells. At RT, the MAPI's E_b is 30 meV [25], and 3CP's E_b is 24 meV [26].

MAPI and 3CP based perovskite have advantages including high absorption coefficient, high dielectric constant (~60.9) [27,28], long carrier diffusion lengths (100~1000 nm) [29,30], long lifetimes (~100 μs) [31], appropriate bandgaps for absorption in the visible range (~1.6 eV) [32], low temperature (<100 °C) fabrication processes [33,34] and low cost of fabrication. These advantages are the key reasons behind the rising efficiencies (over 25 %).

For a PV system fully competitive with the conventional energy source, a cost-effective energy-efficient module is required. The competitive energy-efficient solar cell is commonly a tandem cell as III–V semiconductors used on top of the silicon. However, their large area production is costly and difficult [35]. The brilliant advancement of perovskite solar cell fabrication research reached 29.5 % power conversion efficiency with c-Si based tandems [22]. The properties of perovskite lead to the high efficiency possible:

- suitable bandgap of 1.60 eV [23]
- a high absorption coefficient [24]
- a sharp absorption edge with little sub-bandgap absorption [36]

1.4.3. Drawbacks of perovskite solar cells

Despite the improvement in efficiency, perovskite solar cells suffer from thermal and environmental stability (light [37], moisture [38], oxygen [39]). However, there is a solution to this problem by replacing the volatile methylammonium cation with cesium [40]. On the other hand, the "ion migration" causing hysteresis phenomenon reduces electrical reliability in PSC device operation [41-44]. This study aims to understand triple-cation perovskite's environmental stability and ion migration properties containing only 17% of volatile methylammonium cation.

1.5. Ion migration in perovskite solar cell

Although perovskite has excellent performance as a solar cell, a fundamental question remains unanswered. Can it retain its photoactive properties under harsh and long-term operating conditions? A primary concern that can explain this problem is ion migration. The ions' migration and accumulation have been discovered to burst the perovskite crystal and adjacent functional layers resulting in severe degradation of device performance [41-44]. Therefore, an in-depth understanding of this unique physical process is paramount to ensure the long-term stability of perovskite. Ions migrate by hopping through defects such as grain boundaries or vacancies in the lattice. Thus, possible phenomena occurring the ion migration are introduced.

Polycrystalline perovskite films, fabricated by solution process, were deduced to have high defect density. For instance, the Schottky defect formation energy per a defect for $MAPbI_3$ is calculated as 0.14 eV, 0.08 eV, and 0.22 eV (per a defect) for $MAPbI_3$, MAI, and PbI_2, respectively [45]. As a result, the calculated number of vacancies per cube, at 300 K, is 1.6 x 10^{19} cm^{-3} (0.4% per cube). Draguta *et al.* [46] also identified the defect density as 10^{16}-10^{18} cm^{-3} in the polycrystalline perovskite film. This value of the defect density implies the presence of ionic species with high density originated from defects. The defect density is correlated with measured low free carrier density under dark (10^{9}–10^{14} cm^{-3}) in the materials, and thus high defect density can be attributed to the self-regulation process accompanied by charge compensation [45]. The perovskite's defect density is similar to KCl and NaCl, which are considered ionic conductors [47].

Eames *et al.* [48]. calculated the activation energy for vacancy-mediated ion migration in $MAPbI_3$ using the defect density. The activation energy is the lowest free energy barrier required for an ion to move from its original site to an adjacent vacancy site (Fig. 1.11a and b).

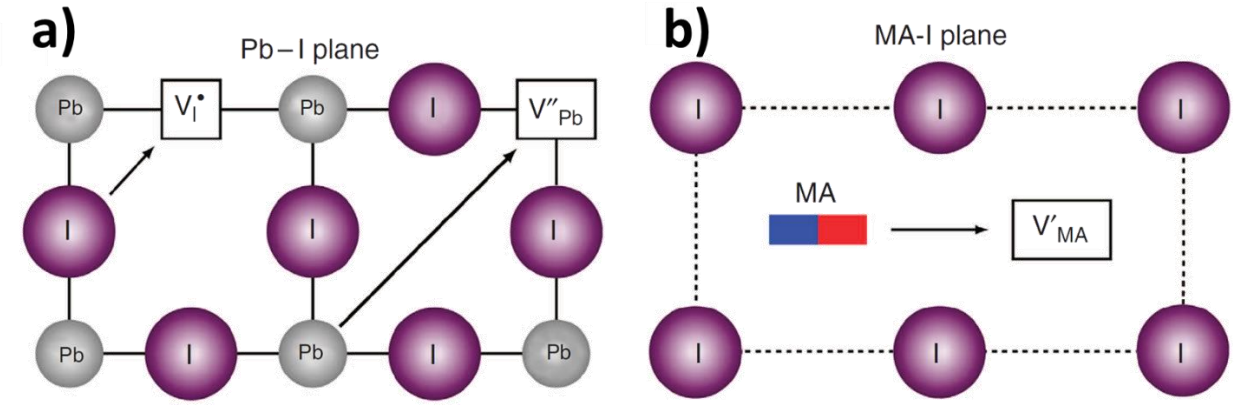

Figure 1. 11. Schematic illustration of the three ionic transport mechanisms involving conventional vacancy (V_I*: iodine vacancy, V"$_{Pb}$: lead vacancy, and V'$_{MA}$: $CH_3NH_3^+$ vacancy) hopping between neighboring positions: a) I^- migration along an octahedron edge; Pb^{2+} migration along the diagonal direction <110>; b) $CH_3NH_3^+$ migration into a neighboring vacant A-site cage involving motion normal to the unit cell face composed of four iodide ions. [45].

The estimated activation energy for MA^{+}($CH_3NH_3^+$), Pb^{2+}, and I^- are 0.58 eV, 2.31 eV and 0.84 eV, respectively [45]. The calculated ion diffusion coefficient for MA^+ is around 10^{-16} cm^2/s and for I- is $10^{-12}cm^2/s$. The lowest activation energy and high ion diffusion coefficient for I^- ion mean the I- vacancies dominantly originate ion migration at 300 K with a short time scale. The research presented the coherence between measured photocurrent relaxation around 0.60 eV and calculated activation energy to support this opinion. The proposed mechanism is shown in Fig. 1.12:

1. Under the built-in electric field, I^- vacancies, having positive polarity, migrate to an interface with a contact.
2. Accumulated vacancies block the internal electric field and generate a band banding.

The localized band banding negatively affects the charge collection property of the device with the redistribution process. Then, the redistribution changes photocurrent density.

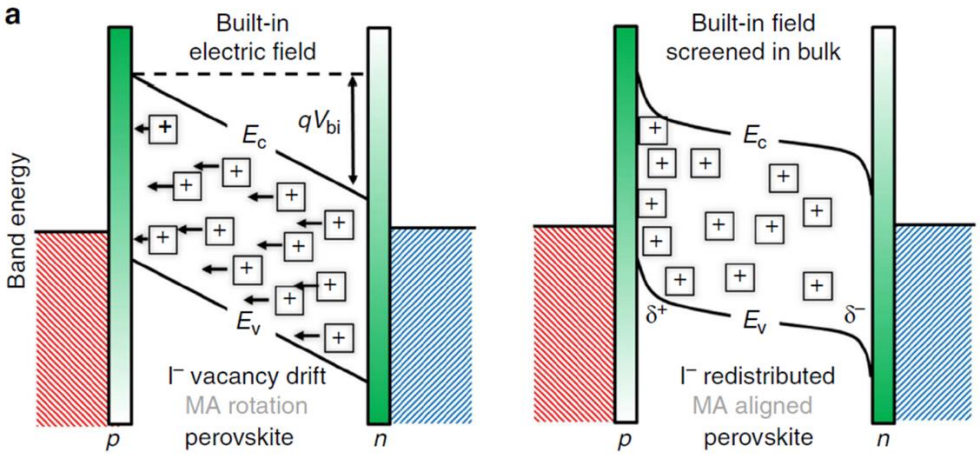

Figure 1. 12. Influence of iodide vacancies on band energies of a perovskite thin film. Schematic diagrams indicate the influence of vacancy drift on the band energies of a p-i-n device at a short circuit. E_C is the conduction band energy, E_V is the valence band energy, and V_{bi} is the built-in potential. The squares represent iodide ion vacancies with 'plus' signs. The diagram implies that the vacancies with effective positive charges are balanced by immobile cation vacancies (not shown) with effective negative charges [45].

Snaith *et al.* [49] proposed that under forward bias, $MAPbI_3$ becomes polarized due to the accumulation of positive and negative space charges near the electron and hole collector interfaces. This charge accumulation is assumed to cause n-type and p-type doping at the interfaces (formation of p-i-n structure), which temporarily enhances photocurrent generation. In addition, the accumulation of migrated ions at the interfaces can change the polarity [50] (Fig. 1.13). The dynamic change in the accumulation of these charges with the scanning voltage (changing internal field) is assumed to generate hysteresis in the photocurrent of the perovskite devices [49,50].

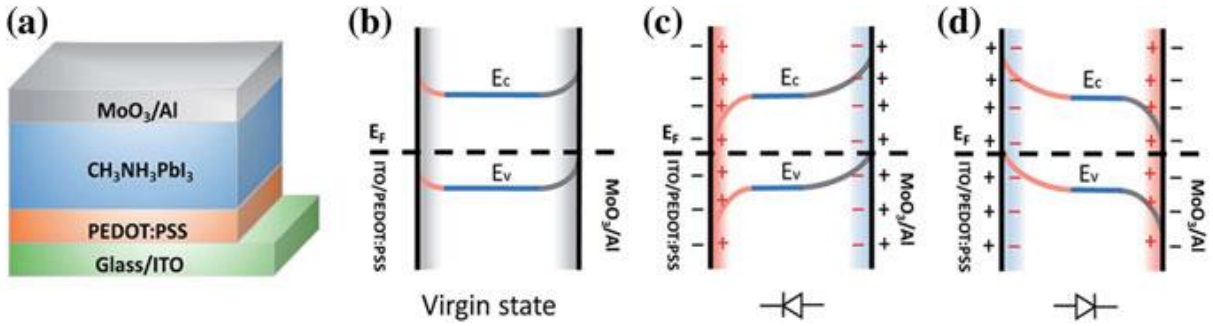

Figure 1. 13. Device structure and mechanism of switchable polarity in perovskite photovoltaic devices leading to hysteresis [50].

Li *et al.* [51] confirmed iodide migration to the positive electrode, leading to iodide vacancies at the negative electrode.

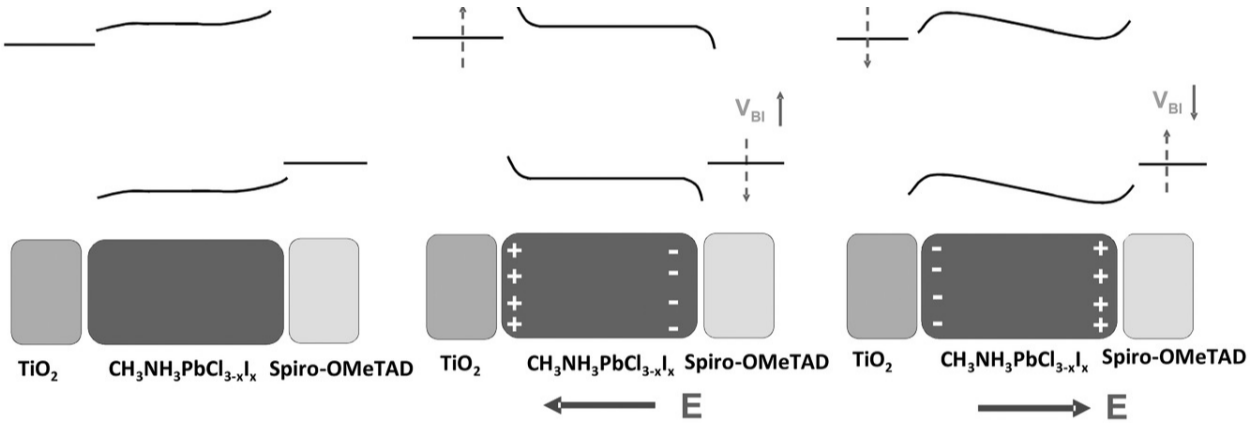

Figure 1. 14. Schematic diagrams of band bending in the perovskite solar cells under electrical fields. The dashed arrows indicate the direction of the effective work function movement. For example, E presents the direction of the external electrical field [51].

According to the authors, the accumulation of iodide ions at one interface and the related vacancies at the other create barriers for carrier extraction (Fig. 1.14). Modulation of such interfacial barriers at $CH_3NH_3PbI_{3-x}Cl_x$/Spiro-OMeTAD and $TiO_2/CH_3NH_3PbI_{3-x}Cl_x$, caused by the migration of iodide

ions/interstitials driven by an external electrical bias, leads to J-V hysteresis in planar (FTO/TiO_2 CL/$CH_3NH_3PbI_{3-x}Cl_x$/Spiro-OMeTAD/Au) perovskite solar cells.

Based on the temperature dependence of hysteretic change in current density, Bryant, *et al.* [52] estimated the activation energy for the diffusion of different ions in $MAPbI_3$. They found that the iodide ions have the highest mobility with the lowest activation energy.

Our previous work attempted to identify the mobile ion species under operating conditions [53]. This study directly demonstrated the halogen (I^- and Cl^-) ions' migration in $MAPbI_{3-x}Cl_x$ films (Fig.1.15 a and b) according to the applied DC voltage polarity using glow discharge optical emission spectrometry (GD-OES). Furthermore, the voltage polarization for a short time, less than 2 minutes, did not cause the lead and nitrogen ions migration (Fig.1.15c and d). The proportion of fixed ions that do not migrate because there are no adjacent defects in the crystal was also inferred by GD-OES profile line analysis. The fixed iodine species ratio saturates at 35 % both in positive and negative applied voltage. Consequently, 65% of iodide ions migrate toward polarization in the perovskite film.

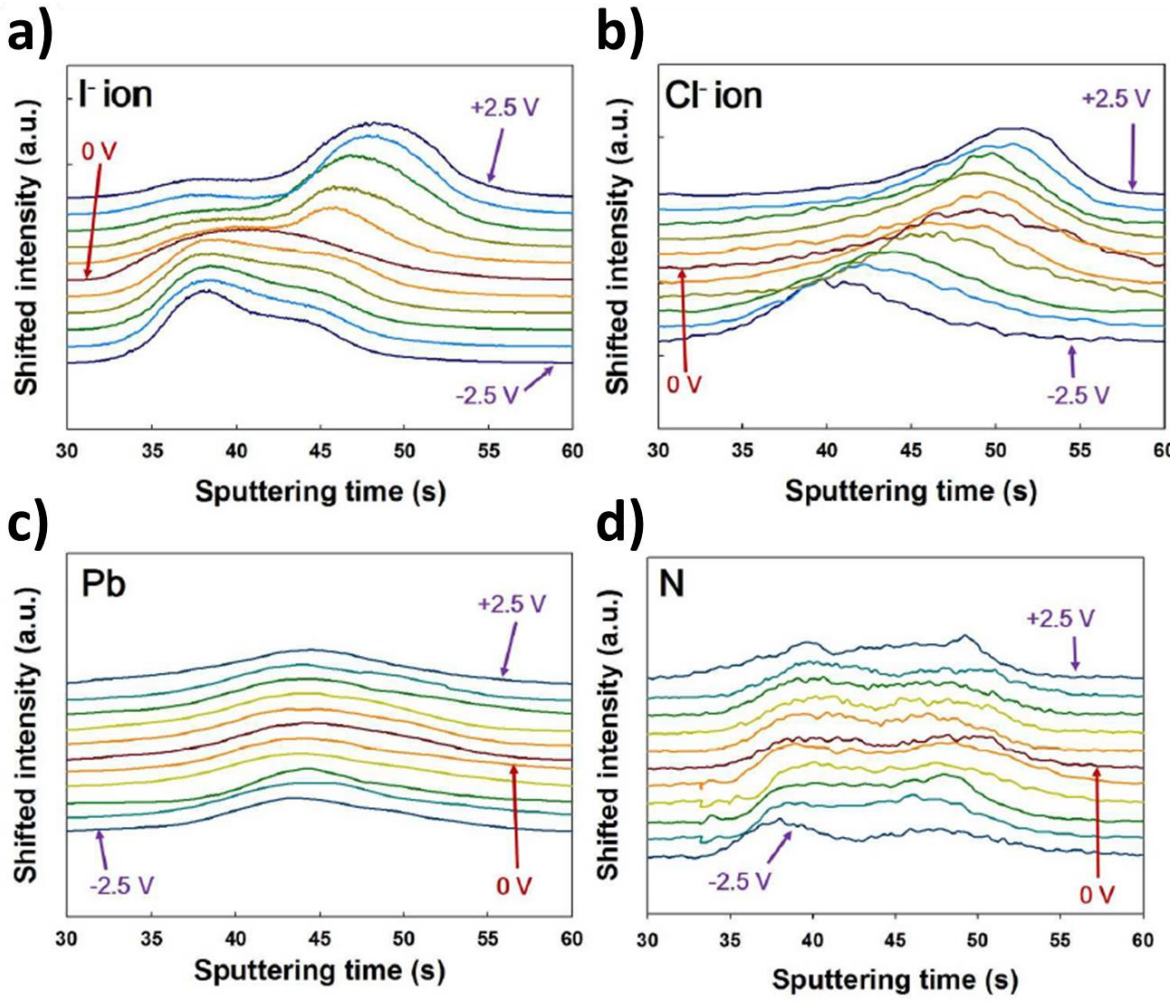

Figure 1. 15. GD-OES profile lines versus sputtering time for a) iodide, b) chloride, c) lead, and d) nitrogen ions as a function of the amplitude of the applied bias. For better clarity, the profile line intensities are shifted [53].

Hence, the halide anions (I^-), not the MA^+ cations, migrate more easily in the perovskite. This ion migration causes polarization and charge accumulation at interfaces under bias and eventually creates hysteresis, which will be discussed in the next section. Thus, investigating ion migration is the purpose of the thesis, and GD-OES served as a powerful tool to evaluate the stability of ion mobility in this thesis.

1.6. Hysteresis

When perovskite solar cells (PSCs) appeared, research was actively conducted to elucidate the unique properties of these materials. Hysteresis is the substantial discrepancy between forward scan (from short circuit to open circuit) and reverse scan (from open circuit to short circuit) of the J-V curves (photocurrent density vs. voltage). This J-V hysteresis is previously observed in dye-sensitized solar cells (DSSCs), Si solar cells, and organic thin-film solar cells (OSCs) when the voltage scan is too fast [54].

The J-V hysteresis is also found in PSCs. Changes in photocurrent characteristics with scan speed and voltage sweep direction have been reported by several groups [55-57]. In general, hysteresis can be mitigated by measurement delay time latency or light soaking pre-conditioning. The presence of hysteresis causes the I-V measurement to underestimate or overestimate the performance of the PSC. To settle this uncertainty, steady-state I-V performance measurement is proposed [55] and is now considered a standard protocol for PSC performance evaluation.

Kim *et al.* [57] found that hysteresis is inversely proportional to the size of perovskite crystals in the film. (Fig. 1.16). This means that the thin-film manufacturing process that contributes to the morphology and composition of the perovskite layer has a close relationship with the hysteresis. They introduced a hysteresis index (HI) to quantify hysteresis. When the perovskite grain size is large and small, the HI values were 0.059 and 0.362, respectively. They also reported that PSCs composed of small grains increase capacitance in the 0.1–1Hz frequency range.

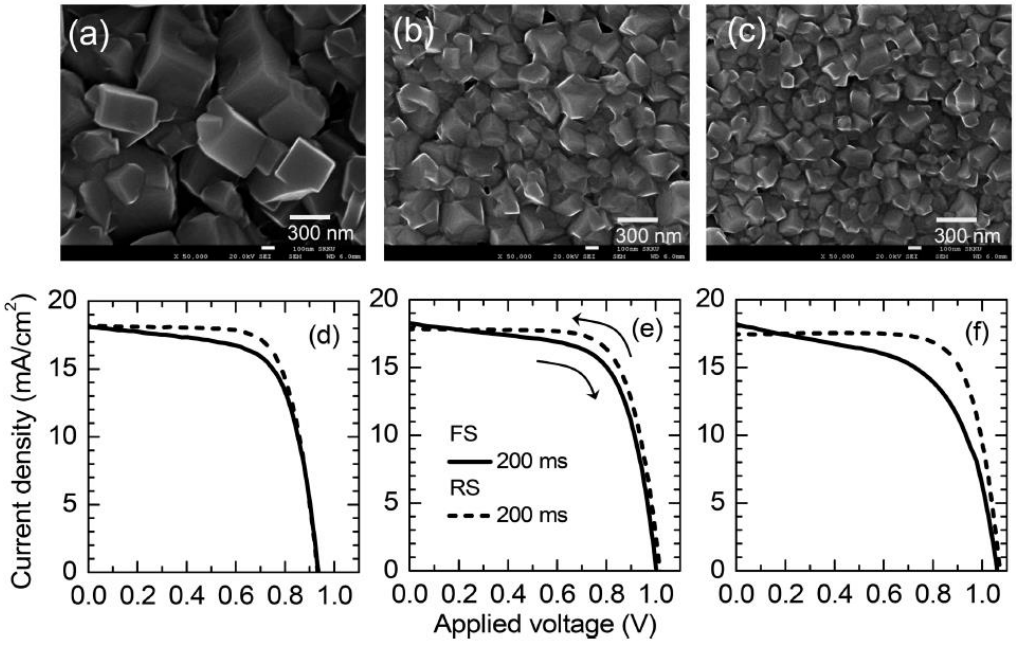

Figure 1. 16. SEM images of $CH_3NH_3PbI_3$ perovskite grown in two-step spin-coating procedure with different CH_3NH_3I concentrations of (a) 41.94, (b) 52.42, and (c) 62.91 mM, leading to the average dimension of 440, 170, and 130 nm, respectively. I−V curves measured at Forward Scan (FS: solid line) and Reverse Scan (RS: dashed line) for the perovskite solar cell employing $CH_3NH_3PbI_3$ with the size of (d) 440, (e) 170, and (f) 130 nm. The voltage settling time was 200 ms, and the light intensity was AM 1.5G (100 mW/cm^2). [57]

1.7. Direction of the research

This chapter introduced the basics and prospects of solar cells as the best hope for the global energy transition. The solar cell operating principle and important parameters (J_{sc}, V_{oc}, FF, R_s, and R_{sh}) were introduced as fundamental notions. Perovskite as a photovoltaic material is introduced for this study. The promising points and weak points of perovskite are then explained. Finally, it was introduced that research on ageing characteristics and ion migration of the weakness is worth research to improve the perovskite solar cell.

The Ph.D. research consists of three steps:

1. The fabrication and optimization of perovskite solar cells,
2. Secure optimum conditions for a technique to observe ion migration (e.g., GD-OES) applied to perovskite solar cells.
3. The presentation of ion migration observation results and scientific explanation.

After optimizing solar cell fabrication, we need to consider and apply a method to analyze ion migration. Our laboratory observed the iodide ion migration along the external electric field in the MAPI layer through GD-OES [53]. Dark J-V also showed ion migration [58]. Based on the works, we plan to analyze the ion migration with two perovskites (MAPI and 3CP). We also intend to use impedance spectroscopy to observe ion migration. The next chapter will therefore explain solar cell fabrication and analysis methods.

1.8 References

[1] International Energy Agency. Renewables in Global Energy Supply. *Renew. Energy* 30 (2020).

[2] Agency for Natural Resources and Energy. Key World Energy statistics. IEA Int. Energy Agency (2018). *IEA Int. Energy Agency* (2018). doi:10.1017/CBO9781107415324.004

[3] J. Goldenberg, T.B. Johansson, *World Energy Assesment Overview 2004*. *Energy* (2018).

[4] A. K. Akella, R. P. Saini, M.P. Sharma, Social, economical and environmental impacts of renewable energy systems. *Renew. Energy*. **2009**, *34*, 390–396.

[5] HLGOR. Future Financing of the EU. Final report and recommendations of the High Level Group on Own Resources. **2016**, 1–104.

[6] D.Harmonies, The, I. N. & Transition, E. World Energy Scenarios **2019** THE FUTURE OF NUCLEAR.

[7] https://www.eletimes.com/top-10-solar-companies-india

[8] K.Vandewal, S. Albrecht, E.T. Hoke, K.R. Graham, J. Widmer, J.D. Douglas, M. Schubert, W.R. Mateker, J.T. Bloking, G.F. Burkhard, A. Sellinger, J. M.J. Fréchet, A. Amassian, M. K. Riede, D.M. Michael, D. Neher, A. Salleo, Efficient charge generation by relaxed charge-transfer states at organic interfaces. *Nat. Mater.* **2014**, 13, 63–68.

[9] D.K. Davies, Charge generation on dielectric surfaces. *J. Phys. D: Appl. Phys.* **1969**, *2*, 1533.

[10] J-L. Bredas, J.E. Norton, J. Cornil, V. Coropceanu, Molecular understanding of organic solar cells: the challenges. *Acc. Chem. Res.* **2009**, *42*, 1691–1699 (2009).

[11] V. D. Mihailetchi, J. Wildeman, P. W. M. Blom, Space-charge limited photocurrent. *Phys. Rev. Lett.* **2005**, *94*, 1–4.

[12] V. D. Mihailetchi, L. J. A. Koster, J. C. Hummelen, P. W. M. Blom, Photocurrent generation in polymer-fullerene bulk heterojunctions. *Phys. Rev. Lett.* **2004**, *93*, 19–22.

[13] https://www.pveducation.org/

[14] M. Liu, M. B. Johnston, H. J. Snaith, Efficient planar heterojunction perovskite solar cells by vapour deposition. *Nature.* **2013**, *501*, 395–398.

[15] E. Edri, S. Kirmayer, D. Cahen, G. Hodes, High open-circuit voltage solar cells based on organic-inorganic lead bromide perovskite. *J. Phys. Chem. Lett.* **2013**, *4*,897–902.

[16] S. Ryu, J. H. Noh, N. J. Jeon, Y. C. Kim, W. S. Yang, J. Seo, J. S. I. Seok, Voltage output of efficient perovskite solar cells with high open-circuit voltage and fill factor. *Energy Environ. Sci.* **2014**, *7*, 2614–2618.

[17] M.M. Lee, J. Teuscher, T. Miyasaka, N, Takurou, H.J.S. Murakami, *References and Notes 1*. **2012**, *338*, 1209–1214.

[18] J. Shi, J. Dong, S. Lu, Y. Xu, L. Zhu, J. Xiao, X. Xu, H. Wu, D. Li, Y. Luo, Q. Meng, Hole-conductor-free perovskite organic lead iodide heterojunction thin-film solar cells: High efficiency and junction property. *Appl. Phys. Lett.* **2014**, *104*, 063901.

[19] S. H. Jeon, B.H. Park, J. Lee, B. Lee, S. Han, First-principles modeling of resistance switching in perovskite oxide material. *Appl. Phys. Lett.* **2006**, *89*, 1–4.

[20] https://en.wikipedia.org/wiki/Perovskite

[21] A. Kojima, K. Teshima, Y. Shirai, T. Miyasaka, Organometal Halide Perovskites as Visible-Light Sensitizers for Photovoltaic Cells. *J Am Chem Soc.* **2009**, *131*, 6050–6051.

[22] National Renewable Energy Laboratory, N.R.E.L. https://www.nrel.gov/pv/assets/pdfs/best-research-cell-efficiencies-rev210726.pdf. Accessed 26 July 2021.

[23] J. Chae, Q. Dong, J. Huang, A. Centrone, Chloride Incorporation Process in $CH_3NH_3PbI_{3-x}Cl_x$ Perovskites via Nanoscale Bandgap Maps. *Nano Lett.* **2015**, *15*, 12, 8114-8121.

[24] B. A. Al-asbahi, S.M. H. Qaid, M. Hezam, I. Bedja, H.M. Ghaithan, A.S. Aldwayyan, Effect of deposition method on the structural and optical properties of $CH_3NH_3PbI_3$ perovskite thin films. *Optical Materials.* **2020**, *103*, 109836.

[25] C.S. Ponseca, T. J. Savenije, M. Abdellah, K. Zheng, A. Yartsev, T. Pascher, T. Harlang, P. Chabera, T. Pullerits, A. Stepanov, J-P. Wolf, V. Sundstrom, *J. Am. Chem. Soc.* **2014**, *136*, 14, 5189–5192

[26] F. Ruf, M.F. Ayguler, N. Giesbrecht, B. Rendenbach, A. Magin, P. Docampo, K. Heinz. M. Hetterich, Temperature-dependent studies of exciton binding energy and phase-transition suppression in $(Cs,FA,MA)Pb(I,Br)_3$ perovskites *APL Materials.* **2019**, *7*, 031113.

[27] Y. Tian, I. G. Scheblykin, Artifacts in absorption measurements of organometal halide perovskite materials: What are the real spectra? *J. Phys. Chem. Lett.* **2015**, *6*, 3466–3470.

[28] N. Onoda-Yamamuro, T. Matsuo, H. Suga, Dielectric study of $CH_3NH_3PbX_3$ (X = Cl, Br, I). *J. Phys. Chem. Solids.* **1992**, *53*, 935–939.

[29] S.D. Stranks, G. E. Eperon, G. Grancini, C. Menelaou, M. J. P. Alcocer, T. Leijtens, L. M. Herz, A. Petrozza, H. J. Snaith, Electron-Hole Diffusion Lengths Exceeding 1 Micrometer in an Organometal Trihalide Perovskite Absorber. *Science (80-.).* **2014**, *342*, 341–344 (2014).

[30] Y. Yamada, T. Nakamura, M. Endo, A. Wakamiya, Y. Kanemitsu, Near-band-edge optical responses of solution-processed organic–inorganic hybrid perovskite $CH_3NH_3PbI_3$ on mesoporous TiO_2 electrodes. *Appl. Phys. Express*. **2014** *7*, 032302.

[31] A. L. Sobolewski, W. Domcke, C. Httig, Photophysics of Organic Photostabilizers . Ab Initio Study of the Excited- State Deactivation Mechanisms of 2- (2 ' -Hydroxyphenyl) benzotriazole Photophysics of Organic Photostabilizers . Ab Initio Study of the Excited-State Deactivation. *J. Phys. Chem. A.* **2006**, *110*, 6301–6306.

[32] E.J. Juarez-Perez, R.S. Sanchez, L. Badia, G. Garcia-Belmonte, Y.S. Kang, I. Mora-Sero, J. Bisquert, Photoinduced giant dielectric constant in lead halide perovskite solar cells. *J. Phys. Chem. Lett.* **2014**, *5*, 2390–239.

[33] J. W. Jung, S. T. Williams, A. K. Y. Jen, Low-temperature processed high-performance flexible perovskite solar cells via rationally optimized solvent washing treatments. *RSC Adv.* **2014**, *4*, 62971–62977.

[34] J. You, Z. Hong, Y. Yang, Q. Chen, M. Cai, T.B. Song, C.C. Chen, S. Lu, Y. Liu, H. Y. Y. Zhou, Low-temperature solution-processed perovskite solar cells with high efficiency and flexibility. *ACS Nano.* **2014**, *8*, 1674–80.

[35] C. D. Bailie, M. D. McGehee, High-efficiency tandem perovskite solar cells. *MRS Bull.* **2015**, *40*, 681–686.

[36] S. De Wolf, J. Holovsky, S. Moon, P. Löper, B. Niesen, M. Ledinsky, F-J. Haug, J. Yum, and C. Ballif. Organometallic halide perovskites: sharp optical absorption edge and its relation to photovoltaic performance. *J. Phys. Chem. Lett.* **2014**, *5*, 1035–1039.

[37] T. A. Berhe, W-N. Su, C-H. Chen, C-J. Pan, J-H. Cheng, H-M. Chen, M-C. Tsai, L-Y. Chen, A. A. Dubaleb and B-J Hwang. Organometal halide perovskite solar cells: degradation and stability. *Energy Environ. Sci*. **2016**, *9*, 323–356.

[38] Y. Han, S. Meyer, Y. Dkhissi, K. Weber, J. M. Pringle, U. Bach, L. Spiccia and Y-B. Cheng. Degradation observations of encapsulated planar $CH_3NH_3PbI_3$ perovskite solar cells at high temperatures and humidity. *J. Mater. Chem. A,* **2015**, *3*, 8139–8147.

[39] M. Kaltenbrunner, G. Adam, E. D. Głowacki, M. Drack, R. Schwödiauer, L. Leonat, D. H. Apaydin, H. Groiss, M. C. Scharber, M. S. White, N. S. Sariciftci and S. Bauer. *Nat. Mater*. **2015**, *14*, 1032–1039.

[40] K. A. Bush, C. D. Bailie, Y. Chen, A. R. Bowring, W. Wang, W. Ma, T. Leijtens, F. Moghadam, and M. D. McGehee. Thermal and Environmental Stability of Semi-Transparent Perovskite Solar Cells for Tandems Enabled by a Solution-Processed Nanoparticle Buffer Layer and Sputtered ITO Electrode. *Adv. Mater.* **2016**, *28*, 20, 3937-3943.

[41] K. Domanski, B. Roose, T. Matsui, M. Saliba, S-H. Turren-Cruz, J-P. Correa-Baena, C.R. Carmona, G. Richardson, J.M. Foster, F. De Angelis, J.M. Vall, A. Petrozza, N. Mine, M.K. Nazeeruddin, W. Tress, M. Gratzel, U. Steiner, A. Hagfeldt, A. Abate, Migration of cations induces reversible performance losses over day/night cycling in perovskite solar cells. *Energy Environ. Sci.*, **2017**, *10*, 604-613.

[42] M. Bag, L.A. Renna, R.Y. Adhikari, S. Karak, F. Liu, P.M. Lahti, T.P. Russell, M.T. Tuominen, D. Venkataraman, Kinetics of Ion Transport in Perovskite Active Layers and Its Implications for Active Layer Stability. *J. Am. Chem. Soc*. **2015**, *137*, 40, 13130–13137.

[43] J. Li, Q. Dong, N. Li, L. Wang, Direct Evidence of Ion Diffusion for the Silver-Electrode-Induced Thermal Degradation of Inverted Perovskite Solar Cells. *Advanced Energy Materials*, **2017**, *7*, 14, 1602922.

[44] J. Carrillo, A. Guerrero, S. Rahimnejad, O. Almora, I. Zarazua, E. Mas-Marza, J. Bisquert, G. Garcia-Belmonte, Ionic Reactivity at Contacts and Aging of Methylammonium Lead Triiodide Perovskite Solar Cells. *Advanced Energy Materials*, **2016**, *6*, 9, 1502246.

[45] A. Walsh, D.O. Scanlon, S. Chen, X.G. Gong, S-H. Wei, Self-Regulation Mechanism for Charged Point Defects in Hybrid Halide Perovskites. *Angewandte Chemie International Edition.* **2014**, *54*, 6, 1791-1794.

[46] S. Draguta, S. Thakur, Y.V. Morozov, Y. Wang, J.S. Manser, P.V. Kamat, M. Kuno, Spatially Non-uniform Trap State Densities in Solution-Processed Hybrid Perovskite Thin Films *J. Phys. Chem. Lett.* **2016**, *7*, 4, 715–721

[47] P.P. Kumar, S. Yashonath, Ionic conduction in the solid state. *Journal of Chemical Sciences*, **2006**, *118*, 135-154.

[48] C. Eames, J. M. Frost, P. R. Barnes, B. C. O'regan, A. Walsh, M. S. Islam, Ionic transport in hybrid lead iodide perovskite solar cells. *Nat. Commun.* **2005**, *6*, 7497.

[49] Y. Zhang, M. Liu, G.E. Eperon, T.C. Leijtens, D. McMeekin, M. Saliba, W. Zhang, M. De Bastiani, A. Petrozza, L.M. Herz, M.B. Johnston, H. Lin, H.J. Snaith, Charge selective contacts, mobile ions and anomalous hysteresis in organic-inorganic perovskite solar cells. *Mater. Horizons.* **2015**, *2*, 315–322.

[50] Y. Zhao, C. Liang, H. Zhang, D. Li, D. Tian, G. Li, X. Jing, W. Zhang, W. Xiao, Q. Liu, F. Zhang, Z. He, Anomalously large interface charge in polarity-switchable photovoltaic devices: An indication of mobile ions in organic-inorganic halide perovskites. *Energy Environ. Sci.* **2015**, *8*, 1256–1260.

[51] C. Li, S. Tscheuschner, F. Paulus, P.E. Hopkinson, J. Kiebling, A. Kohler, Y. Vayzof, S. Huettner, Iodine Migration and its Effect on Hysteresis in Perovskite Solar Cells. *Adv. Mater.* **2016**, *28*, 2446–2454.

[52] D. Bryant, S. Wheeler, B.C. O'regan, T. Watson, P.R.F. Barnes, D. Worsley, J. Durrant, Observable hysteresis at low temperature in 'hysteresis free' lead halide perovskite solar cells. *J. Phys. Chem. Lett.* **2015**, *6*, 3190–3194.

[53] H. Lee, S. Gaiaschi, P. Chapon, A. Marronnier, H. Lee, J-C. Vanel, D. Tondelier, J-E. Bouree, Y. Bonnassieux, B. Geffroy, Direct Experimental Evidence of Halide Ionic Migration under Bias in $CH_3NH_3PbI_{3-x}Cl_x$-Based Perovskite Solar Cells Using GD-OES Analysis. *ACS Energy Lett.* **2017,** *2*, 943–949.

[54] K. Naoki, C. Yasuo, H. Liyuan, Methods of measuring energy conversion efficiency in dye-sensitized solar cells. *Jpn. J. Appl. Phys*. **2005**, *44*, 4176.

[55] H. J. Snaith, A. Abate, J. M. Ball, G. E. Eperon, T. Leijtens, N. K. Noel, S. D. Stranks, J. T.W. Wang, K. Wojciechowski, W. Zhang, Anomalous Hysteresis in Perovskite Solar Cells. *J. Phys. Chem. Lett*. **2014**, *5*, 9, 1511.

[56] E. Unger, E. Hoke, C. Bailie, W. Nguyen, A. Bowring, T. Heumüller, M. Christoforo, M. McGehee, Hysteresis and transient behavior in current–voltage measurements of hybrid-perovskite absorber solar cells. *Energy Environ. Sci.* **2014**, *7*, 11, 3690.

[57] H-S. Kim, N.-G. Park, Parameters Affecting I–V Hysteresis of $CH_3NH_3PbI_3$ Perovskite Solar Cells: Effects of Perovskite Crystal Size and Mesoporous TiO_2 Layer. *J. Phys. Chem. Lett.* **2014**, *5*, 17, 2927.

[58] H. Lee, S. Gaiaschi, P. Chapon, D. Tondelier, J-E. Bouree, Y. Bonnassieux, V. Derycke, B. Geffroy, Effect of Halide Ion Migration on the Electrical Properties of Methylammonium Lead Tri-Iodide Perovskite Solar Cells. *J. Phys. Chem. C.* **2019**, *123*, 17728–17734.

Chapter 2. Experimental methods

This chapter presents descriptions of manufacturing details and analysis methods. The chapter consists of three main parts: device manufacturing, thin-film analysis, and device characterization. In the first part, the device manufacturing explains preparations of substrate and solution, information of the materials used in this study, and various techniques for depositing all layers. The second part describes the analysis methods of perovskite thin film in a physical approach. Each analysis method guides the working principle and result derivation. The last part explains J-V characteristics measurements for perovskite solar cells and device analysis methods.

2.1. Substrate Preparation

Substrate preparation is the first step in any cell fabrication. In this step, we introduce ITO etching (patterning), cleaning, and contact electrode deposition.

A 30x30 cm^2 ITO coated glass substrate (purchased from Xin Yan Tech: 20 ohm/sq) is cut into 25x17 mm^2 by a diamond glass cutter. We pattern the "glass/ITO" substrate in Fig.2.1a through the wet etching process. 3M scotch tape covers 70% of the ITO surface. We etch the uncovered area with zinc powder (<150 µm, 99.995% trace metal basis from Aldrich) and hydrochloric acid (HCl) [1]. We detach the scotch tape after this process.

We then clean the substrates in sequential ultrasonic baths of 1% detergent (Liqui-Nox Phosphate-Free Liquid Detergent, Alconox, Inc.) diluted in deionized water, pure deionized water, acetone, and 2-propanol (IPA) for 15 minutes each. N_2 gas blows to dry the substrates for each ultrasonication. Fig. 2.1b shows the ITO substrate after etching.

To make ohmic contacts to perform J-V measurements, we deposit metallic chromium (Cr 10nm) and gold (Au 80 nm) on the two short edges of the substrate, as seen in Fig. 2.1c. A 10nm thin chromium layer plays a role in increasing the adhesion between glass and gold [2]. To deposit these metals, we use the thermal evaporation technique (chapter 2.2.6).

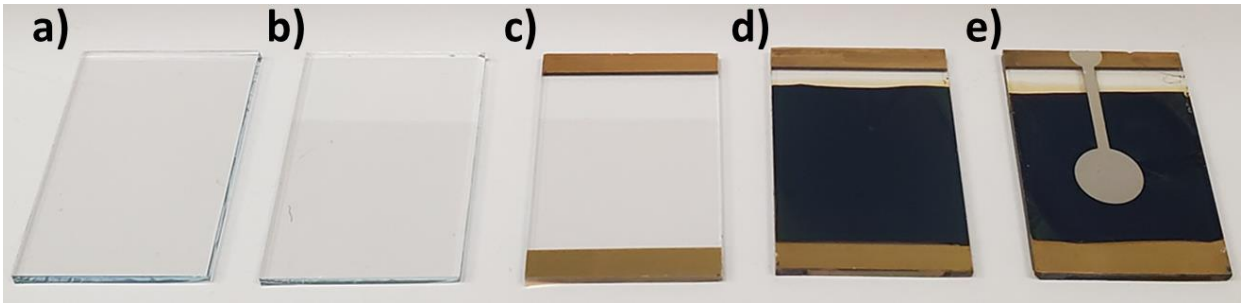

Figure 2. 1. The different steps of device manufacturing: a) ITO coated glass, b) ITO patterning, c) device substrate with gold for Ohmic contact, d) fabricated layers (PEDOT:PSS/Perovskite/$PC_{60}BM$ on the substrate), and e) top (Ag) electrode deposition with the thermal evaporator.

Before making a perovskite solar cell, we cleaned the patterned substrates (Fig.2.1c) in an ultrasonic bath with IPA for 15 minutes. The nitrogen gas gun blows and dries the cleaned substrates. Then the UV-ozone chamber cures the substrates for 15 minutes. This method has proven to be highly effective for non-acidic, dry, non-destructive atomic cleaning and removal of organic contaminants since process researchers used intense ultraviolet light [3].

2.2. Organic-Inorganic Hybrid Perovskite Solar Cells Device Fabrication

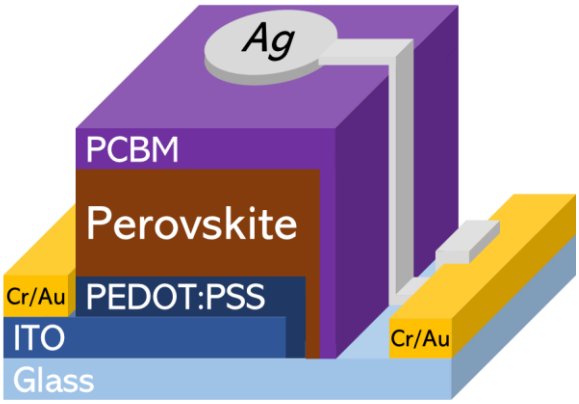

Figure 2. 2. The laboratory selected perovskite solar cell structure. The applied perovskite materials are MAPI ($MAPbI_{3-x}Cl_x$) and Triple cation $\{(MA_{0.17}FA_{0.83})_{0.95}Cs_{0.05}Pb(I_{0.83}Br_{0.17})_3\}$.

2.2.1. Solution Preparation

Solution preparation is the first step to build a perovskite solar cell. In this study, we use a solution to fabricate three layers. They are the hole transport layer (HTL), perovskite layer, and electron transport layer (ETL).

Our HTL is AI 4083 PEDOT:PSS aqueous solution (Ossila), a polymer mixture of two ionomers {poly(3,4-ethylene dioxythiophene) polystyrene sulfonate}.

We prepare two different perovskite solution, MAPI ($MAPbI_{3-x}Cl_x$) and Triple cation $\{(MA_{0.17}FA_{0.83})_{0.95}Cs_{0.05}Pb(I_{0.83}Br_{0.17})_3\}$, in this study. Perovskite precursor solutions should be well agitated overnight to dissolve all the solutes and should be consumed between 6 to 24 hours after dissolving the solvent.

For the MAPI solution, Dimethylformamide (DMF) solvent dissolves solutes {(Methylammonium iodide (MAI), lead iodide (PbI_2), and lead chloride ($PbCl_2$)} for 38 % weight percent.

For the triple-cation perovskite solution, the solutes [Formamidinium iodide (FAI), methylammonium bromide (MABr), lead iodide (PbI_2) and lead bromide ($PbBr_2$)] are prepared in a molar ratio of 1.0M (FAI):0.2M (MABr):1.1M (PbI_2):0.2M ($PbBr_2$). These solutes are dissolved in a solvent for 75 % weight percent. The solute is an 8:2 mixture of DMF and Dimethylsulfoxide (DMSO) in a molar ratio. Then, add 0.05 molar ratio of CsI (dissolved in DMSO) Solution.

We use $PC_{60}BM$ as ETL, chlorobenzene (CB) solvent dissolves the molecule as 3.5 % by weight. Table 2.1 presents the quantity of solute and solvent.

SOLUTION		SOLUTE		SOLVENT	
SOLUTION 1	$(MA_{0.17}FA_{0.83})Pb(I_{0.83}Br_{0.17})_3$	FAI: MABr: PbI_2: $PbBr_2$:	0.1720g 0.0224g 0.5071g 0.0734g	DMF: DMSO:	0.8mL 0.2mL
SOLUTION 2	CsI	CsI:	0.3897g	DMSO:	1.0mL
SOLUTION 3	$(MA_{0.17}FA_{0.83})_{0.95}Cs_{0.05}Pb(I_{0.83}Br_{0.17})_3$	Solution 1 + 42 µL Solution 2			
SOLUTION 4	$PC_{60}BM$	$PC_{60}BM$:	0.0400g	CB:	1.0mL
SOLUTION 5	$MAPbI_{3-x}Cl_x$	MAI: PbI_2: $PbCl_2$:	0.2910g 0.2110g 0.1270g	DMF:	1.0mL

Table 2. 1. Summary of the solution preparation

2.2.2. Study of experimental background

Before making Triple cations solar cells, the study of the material is mandatory. Our material structure $\{(MA_{0.87}FA_{0.13})_{0.95}Cs_{0.05}PbI_{0.87}Br_{0.13}$: Triple cation perovskite(3CP)} was designed to improve stability (Saliba *et. al.*) [4]. Previous experiments in this field have been showing the instability of Methylammonium (MA) based perovskite material. Recent research trend is leading us to exchange the MA organic cation into better performing cations such as Formamidinium (FA). Although highly performing perovskite solar cells still contain MA cation, FA-rich perovskite boasts high efficiency. Thus, we need to understand which properties of FA contribute to high efficiency.

If we refer to our solution preparation, we can notice it contains DMSO solvent and FAI. A few years ago, the presence of DMSO in the PbI_2 skeleton helped to form a column shape (see Fig. 2.3 and 2.4) because the molecular volume of DMSO attains enough space for substitution between DMSO and FA^+I^- during annealing [5].

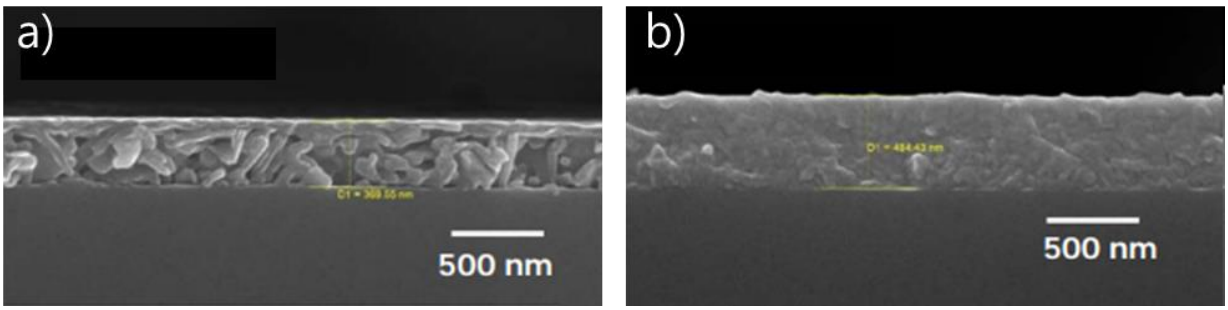

Figure 2. 3. SEM image show difference of PbI_2 skeleton depending on solvent a) PbI_2 in DMF b) PbI_2 in DMSO[5]

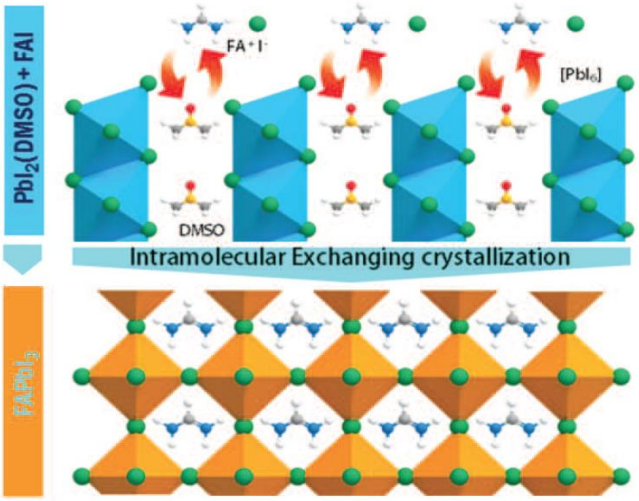

Figure 2. 4. Schematics of $FAPbI_3$ perovskite crystallization involving the direct intramolecular exchange of DMSO molecules intercalated in PbI_2 with formamidinium iodide (FAI) [5].

The subsequent study is the anti-solvent treatment by Chlorobenzene (CB) for the 3CP deposition [6]. The anti-solvent treatment enhances crystallinity, grain size (from 110nm to 270 nm) and reduces grain boundaries of perovskite films (Fig. 2.5). By understanding these backgrounds, I applied 3CP material into an inverted (PEDOT:PSS/Perovskite/PCBM) planar structure (Fig. 2.6a).

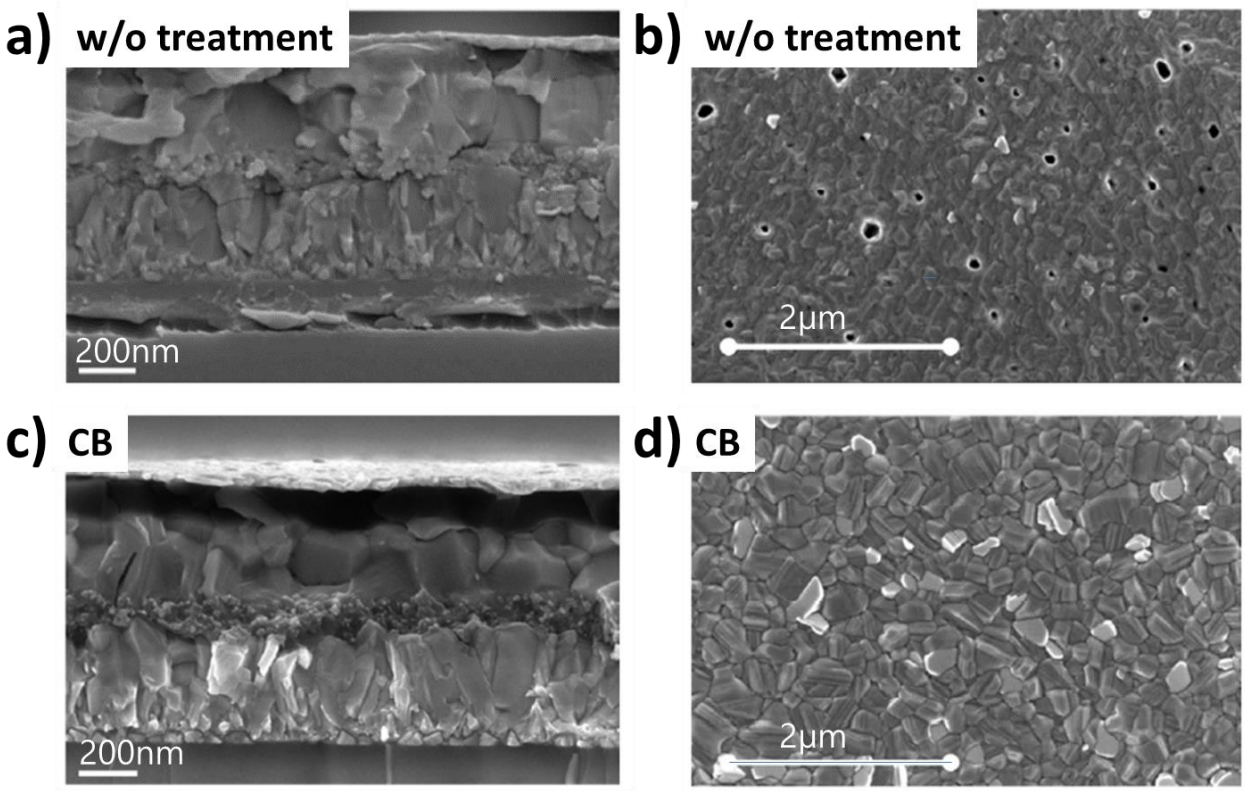

Figure 2. 5. SEM images showing FTO/compact TiO_2/meso-porous TiO_2/perovskite/Spiro-OMeTAD/Au structured perovskite solar cell. The improved crystallinity of the perovskite layer through chlorobenzene anti-solvent treatment is demonstrated comparing without anti-solvent treatment {a) cross-section and b) grain image} and chlorobenzene anti-solvent treatment {c) cross-section and d) grain image} [6].

2.2.3. Solar cell structure decision

In order to understand the material properties in the form of a device, it is first necessary to know the features of the device structure. The conventional structure (Fig. 2.6b) has an n-i-p structure based on an efficient electron collecting layer. This structure achieved the highest power conversion efficiency (25.5%) with a single cell structure [7]. However, it has an electrically unstable property. According to the scanning direction, when the J-V curve is different, we call this phenomenon hysteresis [8].

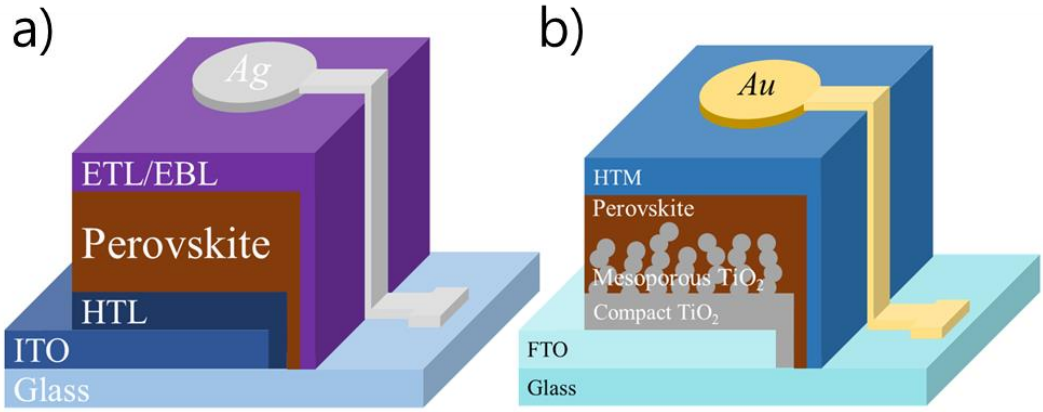

Figure 2. 6. Schematics of Solar cell device structure a) inverted planar structure, b) conventional structure.

Although we can get high performances with the conventional structure because of the mesoporous (generally TiO_2) charge transport layer, the hysteresis-causing structure is unsuitable for approaching ion movement (Thesis subject). It is also expected to show a data overlap problem between titanium and the perovskite material when we analyze it through GD-OES. Since this process uses sputtering, the material detaching rate can be different at the perovskite penetrated layer (Fig. 2.6b, part of perovskite:mp-TiO_2) by material selectivity.

In the case of inverted planar structure (Fig. 2.6a), the fullerene derivatives (ETL) homogeneously distributed to the grain boundary of perovskite fill antisites of defects that cause hysteresis [9,10]. Because of this, we chose the PEDOT:PSS/Perovskite/PCBM structure to reduce hysteresis by structure.

Unbalanced carrier extraction (hole extraction rate ≠ electron extraction rate) caused by imperfect matching of the properties of layers also results in J-V hysteresis (Heo et al. [11]). In the case of PEDOT:PSS/Perovskite/PCBM structure, the carrier extraction rate of PEDOT:PSS and PCBM are well

balanced. Moreover, the planar structure is suitable for GD-OES measurement. This structural feature is more suitable for the perovskite film's characteristics study.

2.2.4. Spin-coating

Spin-coating is one of the most common techniques to make a thin film onto a substrate. Its advantages are the ability to deposit films of uniform thickness easily and quickly, making a permissible thickness error range of a few microns or nanometers depending on the material [12], and a wide range of industry technology applications use it due to its simplicity.

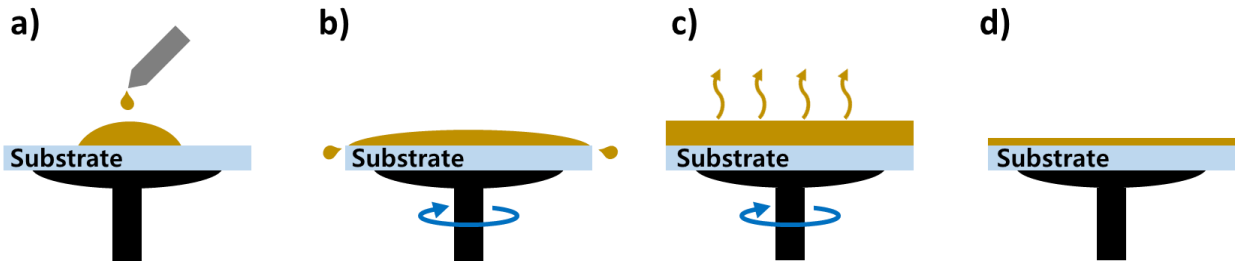

Figure 2. 7. Spin-coating process schematics a) solution dispense on the substrate, b) the solution spreading step due to centrifugal force at high-speed revolution, c) the thin film formation step during the spin, d) The fixing step of the thin film after removal of the excess solvent by annealing.

The coating process occurs evenly across a substrate's surface by controlling a solution of the desired material in a solvent while the substrate is rotating. First, a solution containing the molecules dissolved in a solvent covers the substrate. Then, the stage turns the substrate at high speed. This revolution spreads the solution by centrifugal force [13]. During the spin, the functional molecules form a film on the substrate while an airflow blows away most of the solvent. This step leaves a plasticized film before the film fully dries. To remove the last remaining solvent, we anneal the devices on a hot plate leaving only the desired material on the substrate (Fig. 2.7).

Usually, we set a temperature higher than the boiling point of the solvent, but there are cases when the annealing temperature criterion is different:

- The layer requires thermal curing to form better morphology [14].

- Perovskite layer varies poly-crystallinity depending on endothermic reaction → annealing at best crystallization temperature [15].

This study uses spin-coating to deposit PEDOT:PSS (HTL) and $PC_{60}BM$ (ETL) layers in air and N_2 conditions.

2.2.5. Dynamic dispense (Spin-casting)

There is a technical difference between spin coating and dynamic dispense/spin casting. For the dynamic dispense, the substrate first starts to rotate and reaches the stable spin speed before a user dispenses the solution onto the substrate's center. The solution then rapidly spreads from the center across the entire area by centrifugal force before it dries (Fig. 2.8).

After the solution is dropped on the substrate, the solvent starts to evaporate. Spin-coating has a longer time loss before reaching the target rpm than dynamic dispense. The film's thickness becomes thicker as the solvent evaporates at a lower revolution, and the film uniformity decreases due to the low centrifugal force. Dynamic dispense forms a more uniform thin film because the solution is spread after the target rotation speed is achieved. For this reason, when the thickness variation sample by sample is considerable with spin coating or a more consistent thickness control process is required, users apply dynamic dispense [16]. When a user uses a solution with high concentration spin-coating's thickness difference is notable compared sample by sample [17]. For these reasons, dynamic dispense was applied to make perovskite films with well-controlled film thickness variation.

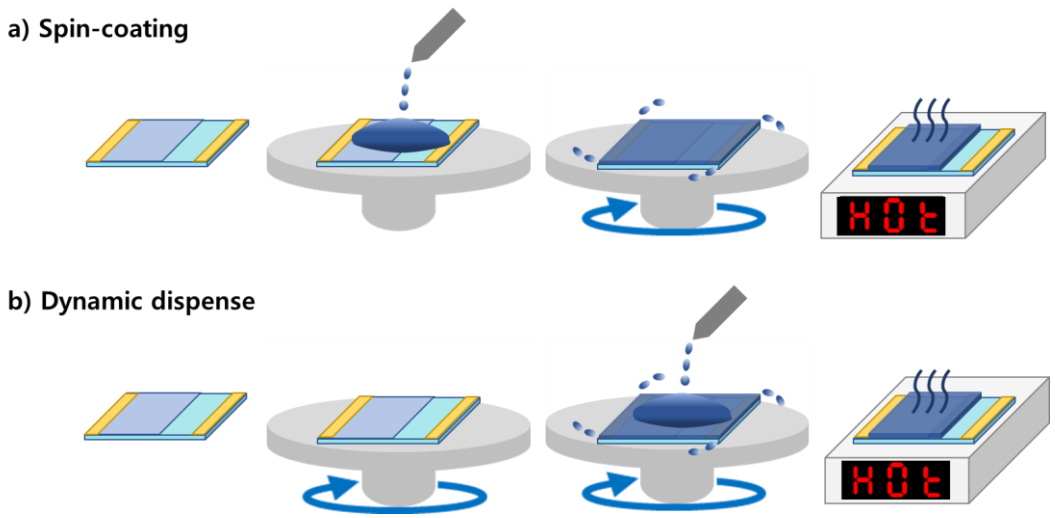

Figure 2. 8. (a) process of spin coating (b) process of dynamic dispense

2.2.6. Thermal evaporation

Thermal evaporation is in Physical Vapor Deposition (PVD) category [18]. An evaporation source heats mounted material (metal in our work) in a vacuum chamber until its atoms have sufficient energy

to evaporate from the surface. At this temperature, the evaporating material traverses the vacuum chamber with acquired thermal energy and collides with a substrate on top (Fig. 2.9a).

The pressure in the chamber must be below the point (typically under $3.0x10^{-4}$ Torr) where the material's mean free path is longer than the distance between the evaporation source and the substrate [19]. The mean free path is the average distance an atom or molecule can travel in a space before it collides with another particle, thereby disturbing its direction to some degree.

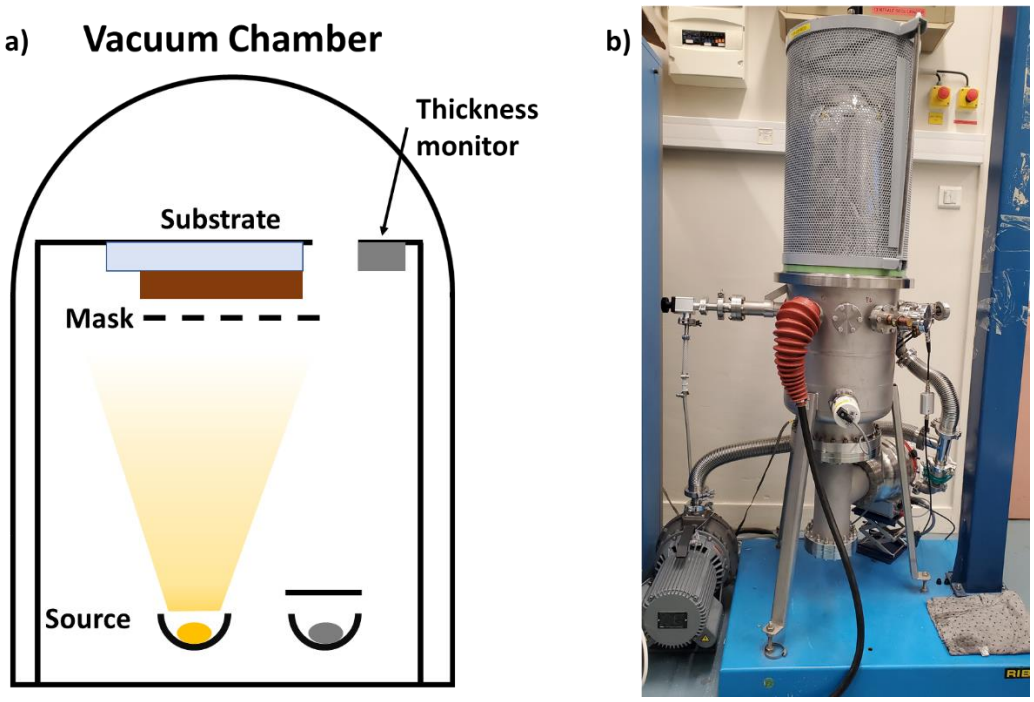

Figure 2. 9. a) Schematic diagram of the thermal evaporation system. b) RIBER thermal evaporator which is used during this work.

Fig. 2.9 shows the thermal evaporator for metal film deposition. We use the thermal evaporation system to deposit contact electrodes (Cr/Au) and silver (Ag) cathode. In this study, we make an Ag cathode on top of the $PC_{60}BM$ (ETL) layer, and the deposition rate is 4.0 Å/s.

Fig. 2.10 a) and b) show the exterior and interior of the thermal evaporator that deposits the metallic contacts on the device. The gold (Au) deposition rate is 4.0 Å/s, and the final thickness is 80 nm. The vacuum during the contact deposition is around 10^{-7} mbar displayed on the gauge (Fig. 2.10c).

This equipment also deposits the top electrode with a silver (Ag). Since we deposit Ag after fabricating the HTL, the perovskite layer (photoactive layer), and ETL, the top electrode works as cathode collecting electrons. Fig. 2.1d) is the entire device after top Ag electrode deposition. The electrode area of each cell is $0.28cm^2$.

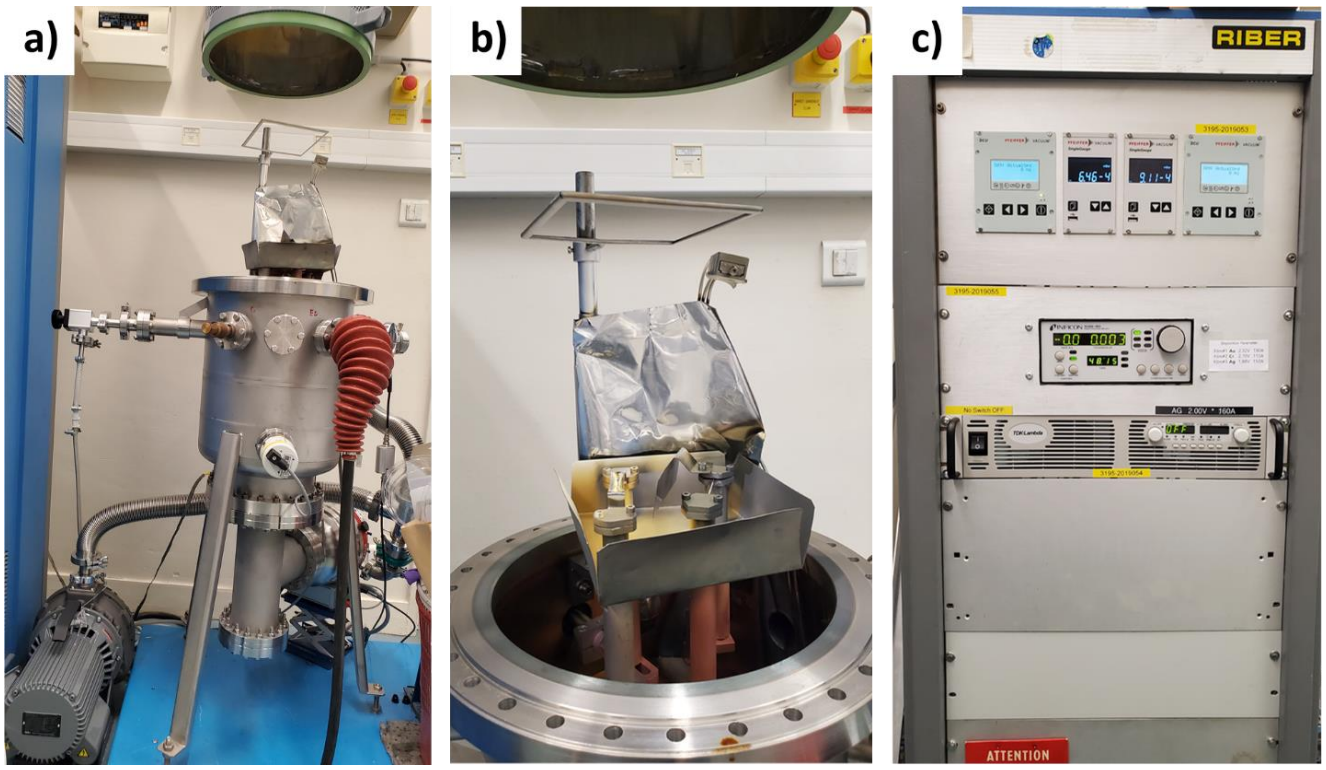

Figure 2. 10. The vacuum thermal evaporator for gold contact and silver electrode: a) Exterior, b) Interior images with tungsten boat for Au, Ag, and Cr bar, c) Evaporator controller.

2.2.7. Two-step spin-coating of PEDOT:PSS layer

Spin-coating for PEDOT:PSS layer is performed in the open air. It takes two steps (step 1: 3000 rpm - 35 s, step 2: 5000 rpm - 35 s). The concentration and speed in the first step determine the film thickness. Since I use Ossila AI4083 commercial PEDOT:PSS product without changing concentration, the thickness is controlled by spin revolution. The first step determines the film thickness, and the second step mainly removes the water solvent and impacts the film uniformity. Filtered PEDOT:PSS through the PVDF (hydrophilic / 45 μm) filter is dispensed on the substrate at room temperature and is spun for two steps. After spin-coating, methanol-drenched cotton swab swipes steadily along the red line to make a clear and straight edge, *cf.* Figure 2.11., then wipe off the shadowed part. As the last step, the PEDOT:PSS deposit samples are annealed at 120°C for 20 minutes in the glove box.

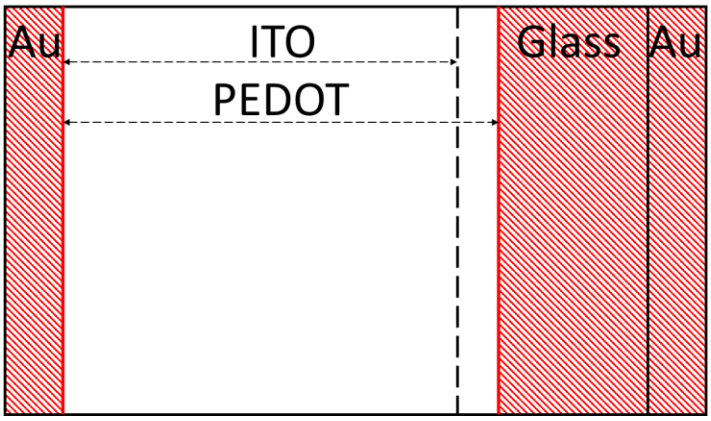

Figure 2. 11. Patterning method for the PEDOT:PSS film. The processor removes the red-shadowed part.

2.2.8. Dynamic dispense applied $MAPbI_{3-x}Cl_x$ layer deposition

Dynamic dispense for $MAPbI_{3-x}Cl_x$ (MAPI) layer is manufactured in N_2 filled glove box. The spin parameters are 6000 rpm - 30 s with 1200 rpm/s acceleration. The samples, after the spin, are annealed at 80°C for 60 minutes in the glove box. (The detailed process is introduced in chapter 3.3.2.) When I make ITO/PEDOT:PSS/MAPI/PCBM/Ag solar cells I remove the red shadowed part as shown in Figure 2.12. Starting from the Au side, for each side, then remove the shadowed part. The perovskite active layer should wrap the PEDOT:PSS hole transporting layer beneath it.

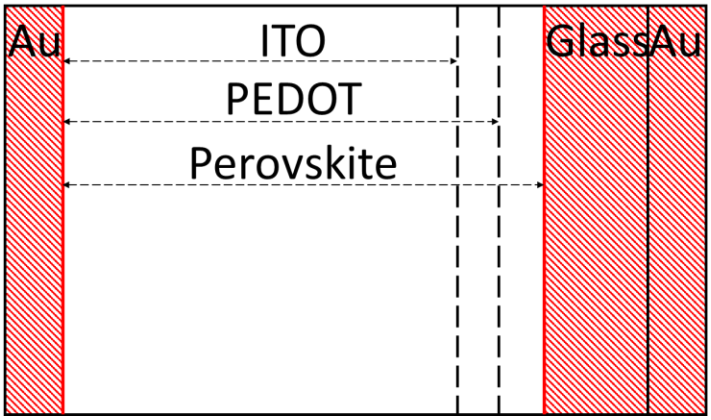

Figure 2. 12. Patterning method for the perovskite film. Processor removes the red-shadowed part.

2.2.9. One-step spin coating of PCBM layer

PCBM layer is fabricated in N_2 filled glove box. PCBM solution is filtered through PTFE (hydrophobic / 45 µm)before the spin-coating. The spin parameters are 2000 rpm - 30 s with 400 rpm/s accerlation. The PCBM film is patterned with chlorobenzene drenched cotton swabs as shown in Figure 2.13 in the same manner as for the PEDOT:PSS layer. The PCBM electron transporting layer (or hole

blocking layer) must completely wrap the perovskite active layer, the PEDOT:PSS, and the ITO anode layer beneath. Not well covered under layers can cause current leakage. In general, PCBM layer is annealed at 100°C for 10 minutes. But, the perovskite layer is possibly degraded by 100°C heat stress. In addition, since ITO/PEDOT:PSS/Perovskite/PCBM samples spend almost 2 hours in a vacuum condition ($\cong 10^{-6}$ mbar) for Ag deposition, the remaining solvent (Chlorobenzene) in the PCBM layer is dried enough. For these two reasons, annealing is not performed in the PCBM layer process.

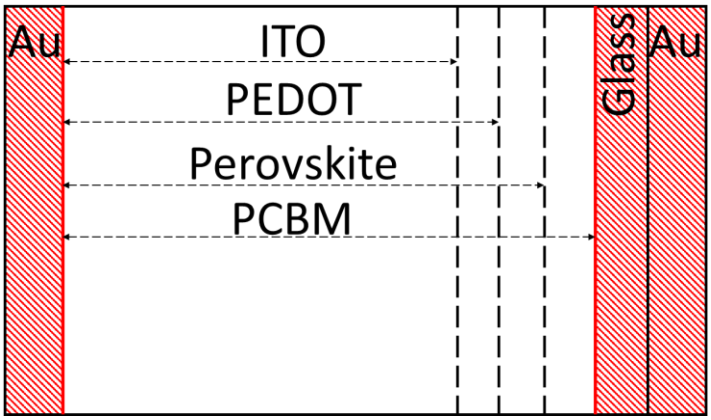

Figure 2. 13. Patterning method for the PCBM layer. The processor removes the red-shadowed part.

2.3. Glow Discharge Optical Emission Spectroscopy (GD-OES)

2.3.1. Introduction of GD-OES history

In 1968, Werner Grimm introduced a light source using a glow discharge tube to analyze the chemical composition of metallic materials [20,21]. A unique arrangement of electrodes is the feature of the tube, which is called a Grimm discharge tube. The two electrodes of DC sources consist of the sample as cathode and a cylindrical hollow anode. In particular, the cathode must tightly seal the cylinder anode (Fig. 2.14).

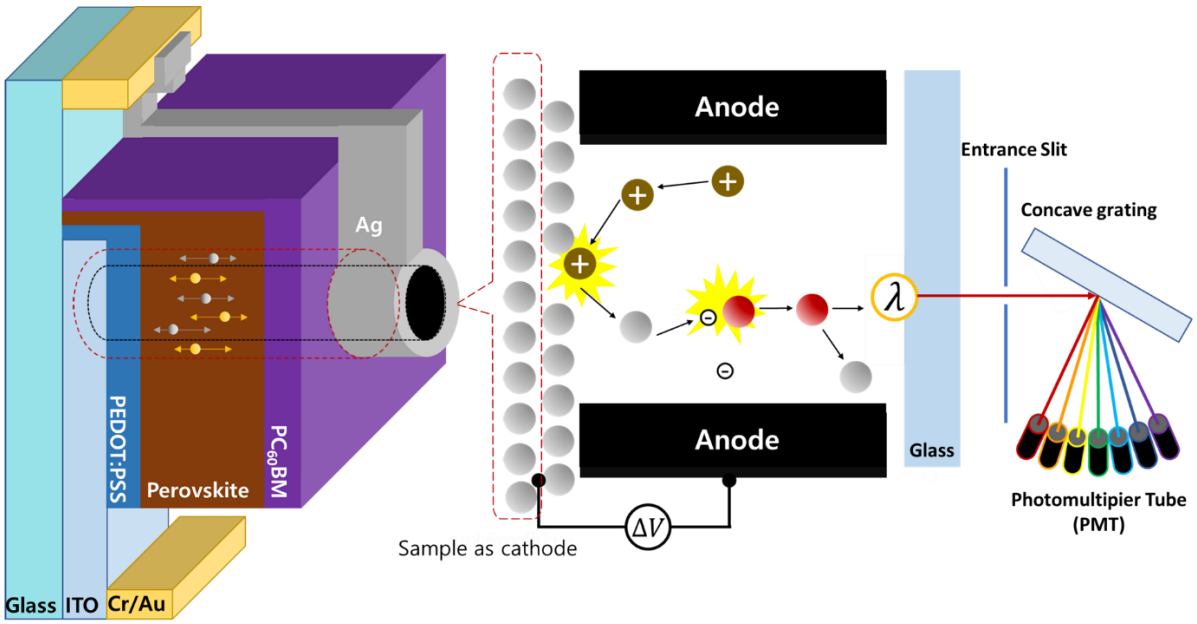

Figure 2. 14. Schematic of GD-OED system working principle from the sputtering to optical analysis.

The glow discharge source is usually filled with low-pressure argon gas (0.5 – 10 hPa). Figure 2.14 describes a simple classical configuration using DC power. When a DC source applies a high voltage between the anode and the sample (cathode), the sample releases electrons from the surface. It accelerates these electrons towards the anode gaining kinetic energy. Inelastic collisions between electrons and argon gas transfer the kinetic energy of the electrons to the argon atoms, which dissociates into argon cations and electrons. This avalanche effect triggers an increase in charge carrier (argon cations and electrons) density, making the insulating argon gas conductive. The conductive argon gas state (mixture of neutral argon atoms and free charge carriers) is plasma.

The sample surface strongly attracts argon cations with high negative potential. At this time, argon cations hit the sample surface and knock out the atoms on the surface. This process is called sputtering. The sample surface is ablated in a planar parallel manner.

The knocked-out sample atoms diffuse into the plasma and collide with high-energy electrons. During these collisions, the sample atoms absorb energy and become an excited energy state. Returning to the ground state, the atoms emit inherent light in a characteristic wavelength spectrum.

The light emitted through the entrance slit reaches the concave grating and is scattered into the spectral components. The detection system registers these components. The intensity of the detected light is proportional to the concentration of the corresponding element in the plasma.

Since then, this technology and its applications have been continuously evolved. A significant advancement related to my work has been introducing a pulsed RF (Radio-Frequency) power source. The pulsed RF allows us to measure fragile and heat-sensitive materials and analyze non-conductive specimens and layers [22].

GD-OES consists of a low-pressure RF glow discharge source (plasma source) and a fast-optical detection. The instrument relies on the steady erosion of the material by the plasma and simultaneous optical detection of the elemental species excited by the plasma. Since each atom emits an inherent wavelength, the equipped optical spectrometer can measure all elemental depth profiles in real-time. The analytical thickness ranges from less than 10 nanometers (nm) to several hundreds of micrometers (μm). Note that the sputtering rate is not constant for different materials (so-called selectivity). If the target is a lamination structure with different materials, organic layers are etched slower than inorganic layers because of carbon. For this reason, GD-OES cannot show the exact thickness information for lamination structures like PSC because of sputtering's selectivity.

2.3.2. GD-OES for perovskite solar cells

In this study, I used GD-OES to investigate the direct experimental evidence of ionic migration in perovskite thin film, one of the key factors of current-voltage hysteresis and poor stability. I used the GD-OES system installed in two different institutions. One is GD Profiler 2 from HORIBA Jobin Yvon Demo Lab (GD-DL). The other is GD Profiler 2 from ILV-UVSQ (GD-ILV). GD-DL and GD-ILV are the same models, but GD-ILV is equipped with an optical configuration to detect bromine (Br).

Because the in-situ method (Chapter 4.3) can damage the equipment, it is recommended that you work with equipment expert Dr. Patrick Chapon. Due to the pandemic, the in-situ method was performed at the HORIBA Jobin Yvon Demo Lab with Patrick Chapon, so Br ion migration could not be observed. Other studies were observed using the GD-ILV system.

This technique has been widely used to analyze inorganic layers. The system works cooperatively with a sputtering cylinder part and an optical configuration part. The sputtering cylinder's internal diameter for this study was 4 mm. The cylinder works as an anode of AC power. In the GD Profiler 2, an RF-AC generator (at 13.56 MHz) and a standard HORIBA Jobin Yvon glow discharge source are equipped to generate the plasma. As the cathode, the solar cell is mounted on an o-ring outside the plasma chamber (Fig. 2.14). When a user loads a sample on the cylinder, the AC cathode covers the sample on the back side of the sample. Plasma is formed by applying RF power to these two electrodes. Plasma is formed by i) removing air using a pump, ii) injecting plasma gas, and then iii) applying RF power to these two electrodes. The plasma gas used in this study is 100 % Ar and Ar : O_2 (96 % : 4 %). Due to the bombardment of ionized plasma gas, the sample is etched from the top layer. Each etched atom is excited by the high energy provided by the plasma and emits a specific wavelength. The optical configuration part detects these specific wavelengths and analyzes the distribution of atoms according to depth from the top layer to the moment the measurement stops.

The user should find the optimal conditions for sample analysis while changing the sputtering conditions. In the case of organic layers (carbon atoms dominating material), the sputtering rate with Ar 100% plasma is too slow. It spends almost five times a slower sputtering rate than the inorganic layer. To increase the sputtering rate, there are two options: increasing AC power or using Ar plasma gas mixed with O_2. Mixing O_2 serves to fast the etching rate without increasing the power (detail information for these two options is introduced in Appendix A.2). This method provides less heat stress to the sample. The balance of low power and O_2 is essential because too much O_2 also obstructs sputtering. As the sample is continuously sputtered, the collected light reflects the temporal evolution of the sputtered species. Therefore, it is possible to obtain depth-resolved elemental analysis with nanometric depth resolution. However, the GD-OES technique is destructive, and a crater is made in the sample after measurement.

The plasma optimization is performed with Horiba technical support. The plasma conditions for GD-DL are plasma gas pressure 420 Pa with Ar : O_2 (96%:4%), AC power 17 W, duty cycle 3000Hz. The plasma conditions for GD-ILV are plasma gas pressure 250 Pa with Ar 100 %, AC power 17W, duty

cycle 3000Hz. Considering the measured test results, GD-ILV showed that the O_2 concentration was higher than 4%. For this reason, GD-ILV used 100% Ar.

2.4. Impedance Spectroscopy (IS)

The impedance spectroscopy (IS) measurements were performed with the SP-200 by Biologic. Equipment setup was carried out in the dark. The AC bias (10^{-2}-10^{6} Hz, 10 mV) was applied first, and DC bias was not applied (0V). EC-Lab software from Bilogics© drives IS equipment and supports IS data fitting from the Nyquist plot.

2.5. Complementary Analysis

2.5.1. Electrical characterization

2.5.1.1 Solar cell performance measurement

After making the solar cell, Keithley 2635 source-measure unit and a homemade acquisition program (by LabVIEW) record J-V curves under illumination or dark condition. The light source is an AM1.5 Solar Cell Test 575 from ATLAS MTT, equipped with a metal halogen lamp of 100 mW/cm^2 in the glove box. The combination of the light source and voltammetry system extracts the key parameters of perovskite solar cells using the methods mentioned in chapter 1.4.

The measurement conditions for illuminated PSC's performance:

- Voltage range: -0.1 V ~ 1.0 V.
- Data point: 1 point / 10 mV.
- Voltage scanning rate: 10 mV/s
- Current limit: 100 mA. (to protect PSC from degradation)

2.5.1.2 External Quantum Efficiency (EQE)

In this study, we use a TSFC-Instrument's EQE. The light source is LEDs.

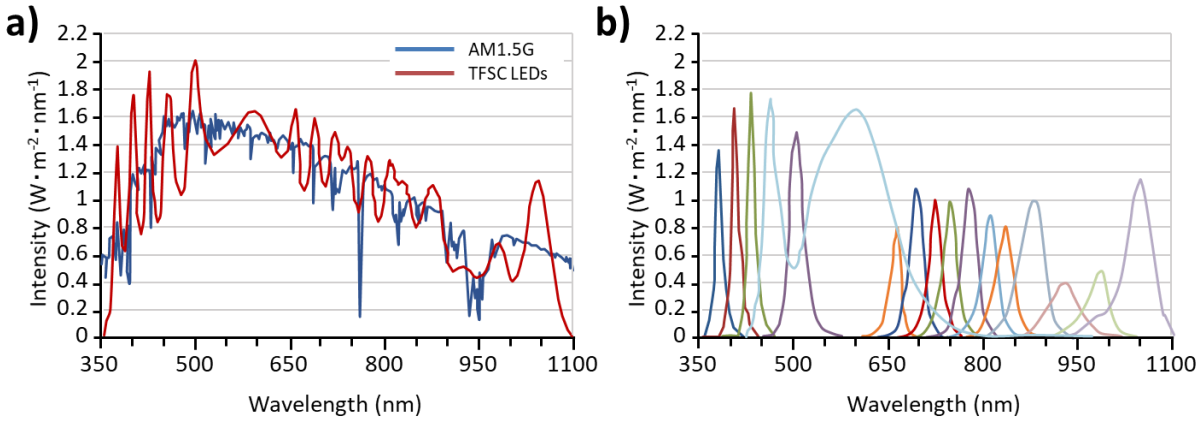

Figure 2. 15. EQE instrument light source specifications. a) Comparison of AM 1.5G condition and combination of LEDs b) detailed LED light source spectra of the instrument.

The system measures input power to LEDs and the output current from a single solar cell. The ratio of them is $S(\lambda)$: spectral response (SR) as the unit of (A/W). Measured SR has a relation with EQE:

$$S(\lambda) = -\frac{q\lambda}{hc} EQE(\lambda) \qquad 2.5 - (1)$$

EQE is deduced with equation 2.5- (1). As far as we can see in Fig. 2.15a, LEDs spectra do not correspond to AM 1.5G condition. So, the instrument registers only the data corresponding to the standard solar spectrum (Fig. 2.16). This approximation can produce errors and will be discussed in the following chapter.

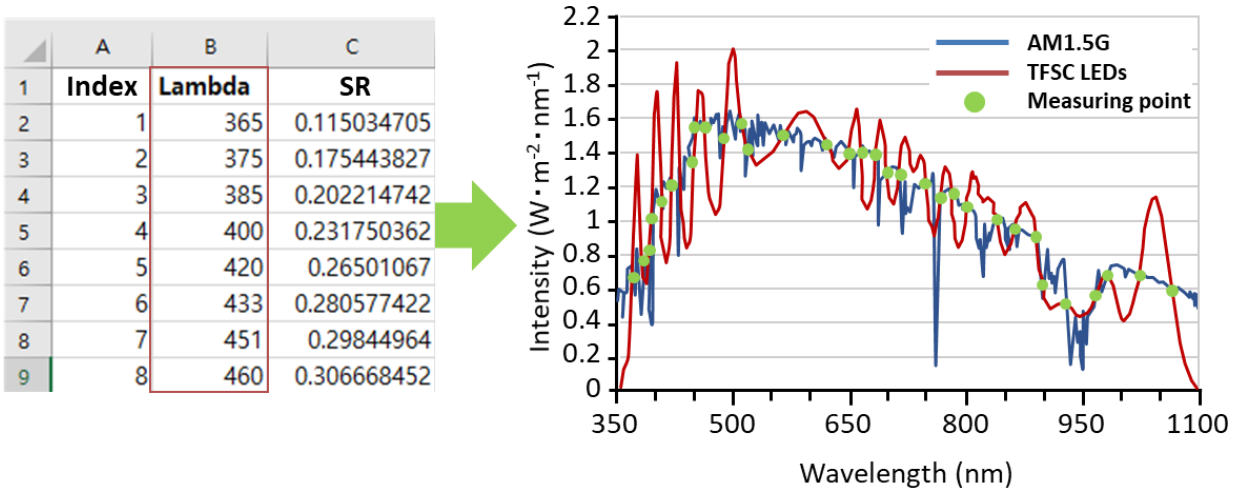

	A	B	C
1	Index	Lambda	SR
2	1	365	0.115034705
3	2	375	0.175443827
4	3	385	0.202214742
5	4	400	0.231750362
6	5	420	0.26501067
7	6	433	0.280577422
8	7	451	0.29844964
9	8	460	0.306668452

Figure 2. 16. The datasheet of EQE instrument (TSFC instrument©) provides sparse row data missing every single nanometer. Green dots are the measured data where the AM 1.5G spectrum and LED spectrum to coincide.

2.5.2. Optical characterization

2.5.2.1UV-Vis Spectroscopy

UV-Vis Spectroscopy (ultraviolet-visible spectroscopy) quotes absorption or transmittance in using light in the visible and adjacent (near-UV and near-infrared/IR) spectral region. In the visible range, absorption or transmittance affects the perceived materials' colour. This technique is based on the principle of electronic transition in atoms or molecules upon absorption of suitable energy from incident light, allowing the electron to transition from a lower energy state to a higher excited energy state. In the light spectrum above specific energy, atoms or molecules undergo electron transitions.

In the direction of the transition, absorption measures transition from the ground state to the excited state with photons absorption [23]. The transition from the lower state to the higher state is called excitation. UV (200 nm to 400 nm) and visible (400 nm to 800 nm) light absorption are based on the suitable energy absorption allowing the excitation. While IR light makes atoms or molecules undergo vibrational transitions.

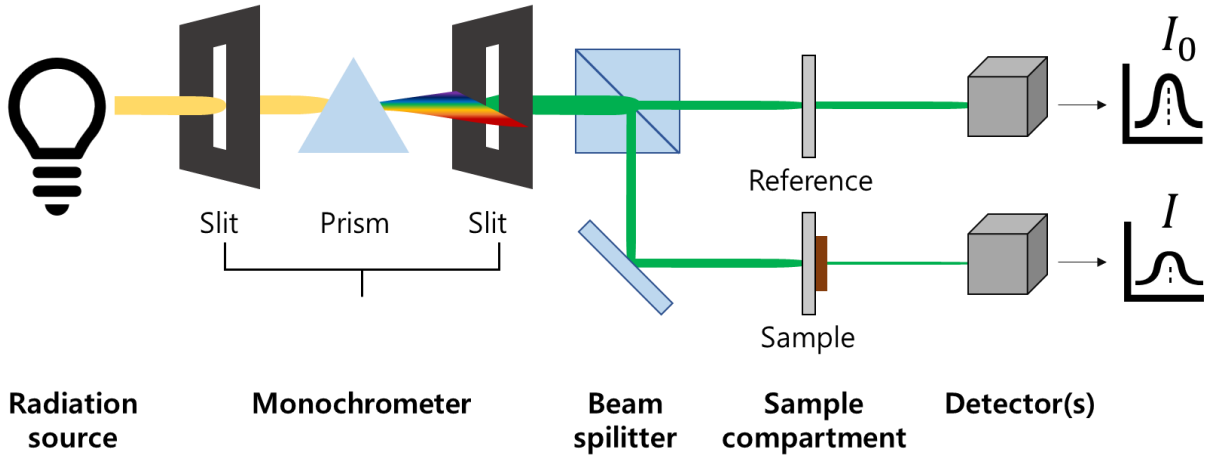

Figure 2. 17. The schematic working mechanism of UV-Vis spectrophotometer.

Fig. 2. 17. presents a scheme of the components of a typical spectrometer. The working principle of this instrument is intuitive. A prism or diffraction grating monochrometer separates a ray of light emitted from light sources (the visible and UV lamp) into its monochromic wavelengths. A beam splitter, a half-mirrored device, in turn, splits the incident beam into two equal intensities. One shaft transmits through a reference substrate. The other beam sends through a target containing the sample film on a reference

substrate. The electronic photodetectors then measure these light intensities that have passed through the reference and sample.

The data analyzer the data according to the Beer-Lambert law.

$$A = log_{10}\left(\frac{I_0}{I}\right) = \varepsilon cL, \qquad 2.5 - (2)$$

where A is the measured absorbance {unit: Absorbance Units (AU)}, I_0 is the incident light intensity before transmitting the sample, I is the light intensity transmitted the sample, ε is a material's absorption coefficient, c is the density/concentration of material, and L the path length through the sample (thickness in the case of a film).

Assuming that the sample film does not absorb light at a given wavelength, then A is zero with I_0=I. Likewise, when the sample absorbs light, then I is less than I_0, the instrument displays this difference in a logarithmic relationship at the given wavelength (A =1, 90 % absorption, and A=2, 99 % absorption). This spectrometer can show the measured results as transmittance {T= $\frac{I}{I_0}$ (%)} or absorbance {A=$log_{10}(I_0/I)$}. T = 0, and A = ∞ mean perfect absorption. Depending on the user's purpose, selecting the absorbance or transmittance on the vertical axis is possible. In general, the effective absorption range is a measurement between 0 (T=100 %) and 2 (T=1 %) as a reliable result that does not affect noise.

Absorbance result analysis can derive an optical bandgap. We can derive the optical bandgap (E_{opt}) in the unit: electronvolts (eV), with the incident photon's wavelength, in the unit: nanometers (nm) by the Planck relation:

$$\mathrm{E}\ (eV) = h\upsilon = h\frac{c}{\lambda} = \frac{1240}{\lambda\ (nm)} \qquad 2.5 - (3)$$

Where h is the Planck constant, υ is the wave frequency, and c is the speed of light in a vacuum.

The pristine result from the measurement is AU vs λ. Experimentally, the optical bandgap (E_{opt}) of the thin film is estimated by linear extrapolation from the absorption edge where A = 0 and subsequent conversion of the wavelength into energy. The E_{opt} can be determined by absorbance spectra.

To derive the exact optical bandgap as the, the Tauc equation is employed:

$$\alpha h\upsilon = A\left(h\upsilon - E_{opt}\right)^{\frac{1}{2}}$$

$$\alpha h\upsilon^2 = (2.303 * AU * E_{(eV)})^2 \qquad 2.5 - (4)$$

When α is the absorption coefficient, h as the Plank's constant, υ corresponding frequency of radiation, while A as a constant and E_{opt} being the optical bandgap. The Tauc plot is made with $(\alpha h\upsilon)^2$

vs $h\upsilon$ {unit: (eV/cm)^2 vs eV} from AU vs λ (nm). The minimum energy (eV) absorbing light by the sample is the optical bandgap (E_{opt}):

$$\text{when } h\upsilon = E_{opt}, \text{ absorption} = 0$$

In conclusion, we can determine the sample's E_{opt} by absorbance spectra analysis [24]. In this study, I use "Jenway 6800 UV/Vis Spectrophotometer" to calculate the E_{opt} value of the perovskite film. It covers the UV scan region from 190 nm to 400 nm, the visible portion between 400 and 800 nm, and IR range from 800 nm to 1100 nm. When I measure absorption spectra, the glass side is the incident surface against the light because the reflectance of the first incident surface must be constant to compare with the reference substrate.

2.5.2.2 X-Ray Diffraction (XRD)

When monochromatic X-rays hit a crystal, some of them cause diffraction, and their diffraction angle and intensity are unique in the lattice structure of the material. The constructive interference of diffracted X-rays provides information about the type and amount of crystalline substances in the crystal [25]. Likewise, X-ray diffraction (XRD) is the method to obtain information on the crystalline structure:

- Identification of crystalline material
- Quantify the percentage crystallinity of a material
- Identification of various polymorphisms
- Identification of amorphous and crystalline material: The diffraction also occurs in amorphous materials, but since the distance and angle between atoms are not constant, the XRD result is observed as an irregular broad peak.

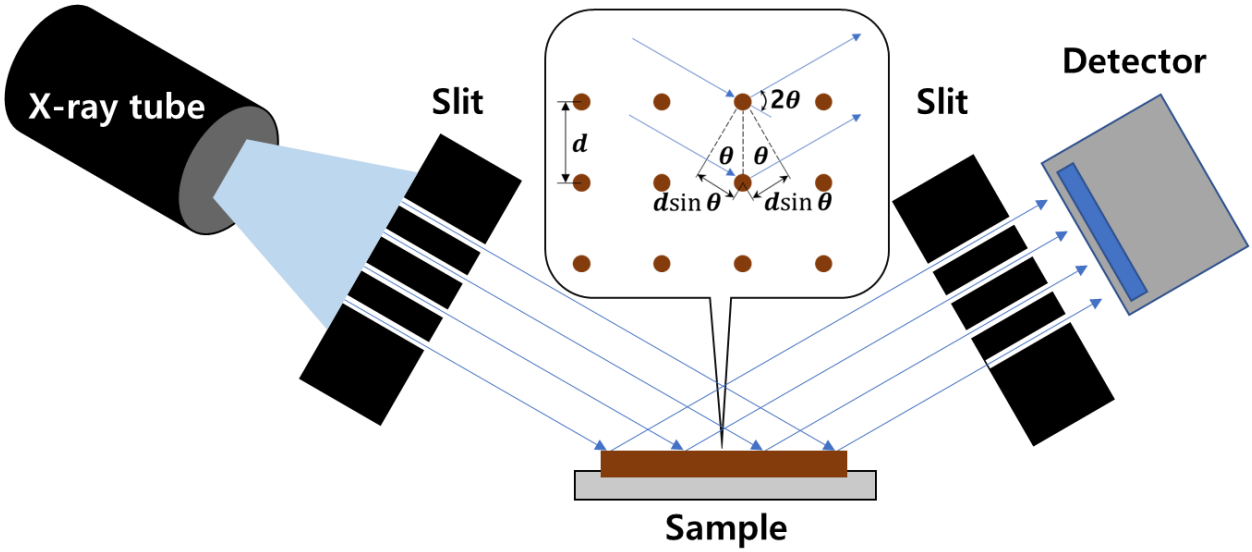

Figure 2. 18. XRD working mechanism schematic showing a measurement system.

Fig 2.18 is a simple schematic of the XRD system. From the left, the X-ray tube generates the X-rays. The monochromator-set (e.g., slit) filters, collimate, and sends X-rays to the sample. Angle controller changes the glancing angle of the monochrome X-ray and diffraction angle of the detector. The diffraction of the incident rays by the sample produces constructive interference when the diffracted beams meet the Bragg's law:

$$n\lambda = 2d\ sin\theta \qquad 2.5\text{-}(4)$$

Where n is a positive integer, λ is the incident ray's wavelength, d is an inter-planar distance separating the planes of a crystalline solid, and θ is the glancing angle. When XRD measures the intensity of the

scattered wave as a function of the scattering angle, it obtains the diffraction pattern. When the scattering angle meets the Bragg condition, the diffraction pattern gets significant intensity known as the Bragg peak.

In this study, I applied XRD, in the solar cell development stage, to confirm that the crystallinity of perovskite grown on a PEDOT:PSS thin film corresponds to the relevant articles. I also used XRD to observe that perovskite loses crystallinity as it ages.

For diffraction, the surface of the aiming material must be exposed. The reference substrate thus exposes PEDOT:PSS side to the X-ray beamline while, for the control sample, the perovskite side irradiates the X-ray. The result of the reference sample helps to identify the noise data when analysing the perovskite sample (glass/PEDOT:PSS/perovskite). For this experiment, we used the Bruker D8 advance model (accuracy in peak position 2θ <0.007°, $2\theta_{max}$ = 160°).

2.5.2.3 Scanning Electron Microscopy (SEM)

In this study, the SEM equipment is Hitachi S-4800 FE (Field Emission)-SEM:

- Magnification: x20 ~ x 800 000.
- Resolution: 1 nm at 15 kV / 1.4 nm at 1 kV

SEM is used to identify the crystallinity, grain size, and thickness of the perovskite film.

Scanning electron microscopy (SEM) is one of the most widely used equipment due to high magnification, ease of observation, deep depth of focus, and high resolution. SEM uses a beam that high-energy electrons are focused. The beam generates various signals at the surface of a solid target. The signals, the result of electron-sample interactions, reveal an external texture (morphology), a crystalline structure, an orientation of the materials that make up the sample, and chemical composition (elements and compounds that make up an object and their relative amounts) [26]. Fig 2.19 shows the illustration of the SEM operating mechanism.

When an electron beam strike excites another electron and loses some of its energy in the sample, this electronic impact with the most intense emission produces Secondary Electrons (SE) [27]. In detail, excited electrons travel along the sample's surface, and if there is still enough energy, the surface emits electrons (SE). If the sample is a non-conductive material, the user can coat a thin layer as a conductive material. The thin conductive layer increases the number of SEs released with less than 50 eV of energy.

An electron beam striking the sample also makes scattering of the electron when there is an elastic collision between electrons and atoms. These elastically scattered electrons that rebound from the sample surface do not lose energy (high energy electrons). Backscattered electrons (BSEs) are the definition for these electrons.

For most materials, the mean free path of SE is about 10 Å (1 nm). Excited electrons are generated at the entire depth of the sample hit by the electron beam, but only electrons emitted at shallow depths (less than 10 Å) can be detected. The number of SEs is, therefore, significantly less than BSE or X-rays. This SE's feature is ideal for examining surface morphology. And microscopic images using SE have better resolution than BSE or X-rays. The yield of secondary electrons proportional to the following factors [28]:

- high atomic number of atoms constituting the specimen
- high incident angle

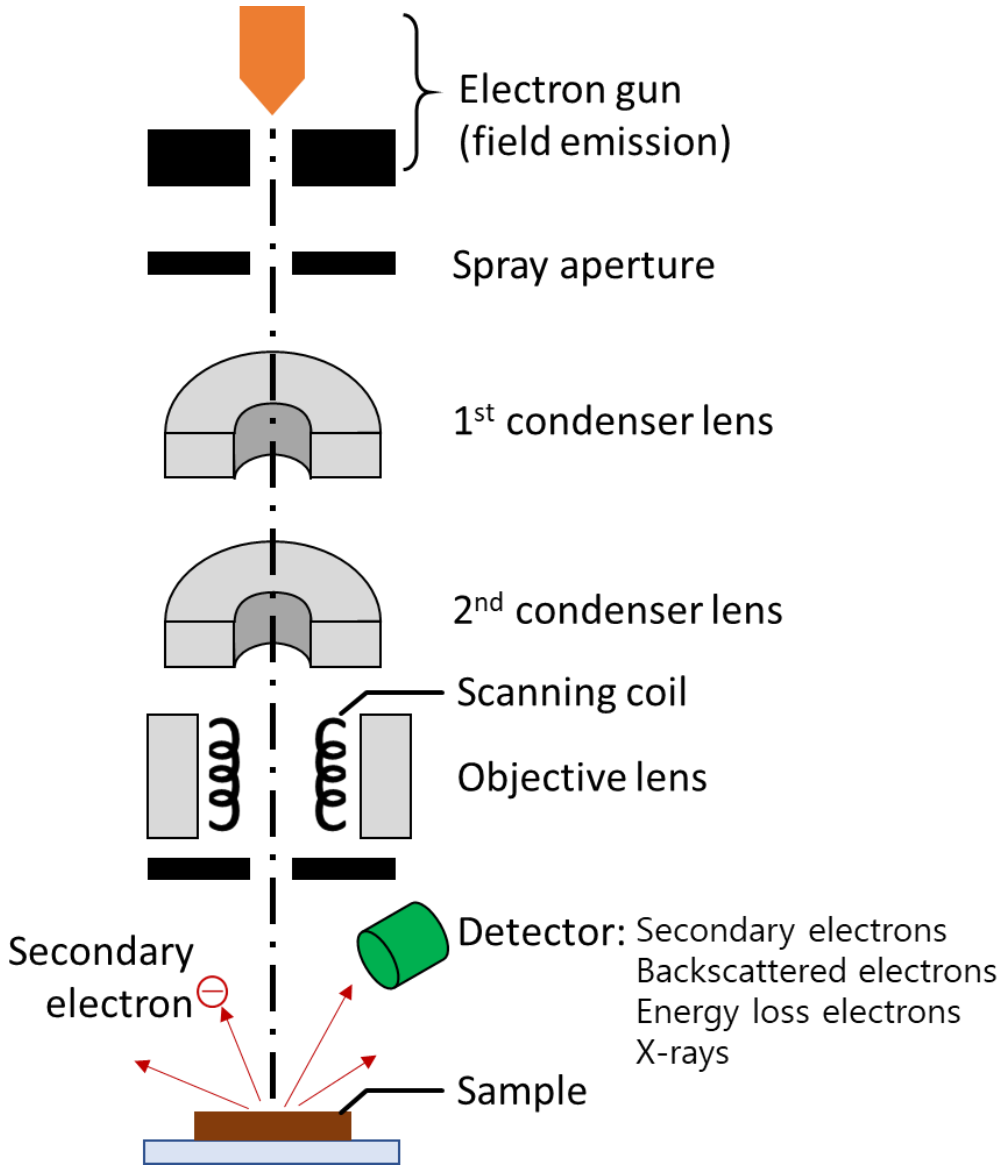

Figure 2. 19. Scheme of the operating mechanism of the Scanning Electron Microscope.

SEM utilises BSE to generate a microscopic image that displays the different elements existing in the sample [29]. Every element has a different atomic and nucleus size. As the nucleus size increases, the number of BSEs is proportional. The emission of many BSEs from an atom appears brighter point on the image (more BSEs are detected). For instance, in a mineral image, the ^{26}Fe component appears brighter than ^{12}Mg. The BSE micrograph, thus, contains the information of composition and topography of a sample.

The depth of BSE emission is tens of nanometers, which is a deeper scale compared to SE. This characteristic of BSEs gives sparse resolution (more insufficient than SEs). Instead, since they have higher energy than SEs, they are less influenced by specimen contamination and charge-up. (charge-up:

when analyzing the specimen of organic, non-conductive matter, some are too bright, and some are too dark in the image, which is a phenomenon that interferes with precise imaging. This phenomenon is because the specimen is partially charged).

In conjunction with the SEM, energy dispersive x-ray spectroscopy (EDS or EDX) is an analytical method to quantify and identify elemental compositions in a few cubic micrometers scale. EDX systems are generally equipped with SEM. When atoms on the surface are excited by the electron beam, they emit specific wavelengths of X-rays. Analysis of X-ray wavelength reveals characteristics of the atomic structure of the elements. EDX analysis displays the result as a spectrum that contains the peaks correlated to the elemental composition of the investigated specimen.

2.6. Conclusion

In this chapter, the perovskite solar cell fabrication process techniques are introduced:

- Substrate preparation
- Solution preparation
- Film deposition techniques (Spin-coating, Dynamic dispense, and Thermal evaporation)

And the working principle and measurement conditions of characterization tools are informed. The GD-OES gives physical approach to observe ions migrating in the perovskite solar cell. The IS is used to analyze phenomena at an interface. And the complemrntary analysis supports development of solae cells performance and studying material characteristics (ion migration and ageing).

2.7. References

[1] C. J. Huang, Y. K. Su, S. L. Wu, The effect of solvent on the etching of ITO electrode. *Mater. Chem. Phys.* **2004**, *84*, 146–150.

[2] AMP. Technical Report Golden Rules: Guidelines For The Use Of Gold On Connector Contacts. Physics (College. Park. Md). **2004**, 1–11.

[3] J. R. Vig, J. W. L. Bus, UV/Ozone Cleaning of Surfaces. IEEE Trans. Parts, Hybrids, Packag. **1976**, *12*, 365–370.

[4] M. Saliba, T. Matsui, J-Y. Seo, K. Domanski, J-P. Correa-Baena, M. K. Nazzeruddin, S. M. Zakeeruddin, W. Tress, A. Abate, A. Hagfeldt, M. Gratzel, Cesium-containing triple cation perovskite solar cells: Improved stability, reproducibility, and high efficiency. *Energy Environ. Sci*. **2016**, *9*, 1989–1997.

[5] W. S. Yang, J. H. Noh, N. J. Jeon, Y. C. Kim, S. Ryu. K. Seo, S.I. Seok, High-performance photovoltaic perovskite layers fabricated through intramolecular exchange. *Science.* **2015**, 348, 1234–1237.

[6] S. Paek, P. Schouwink, E. Nefeli Athanasopoulou, K. T. Cho, G. Grancini, Y. Lee, Y. Zhang, F. Stellacci, M. K. Nazeeruddin, and P. Gao. From Nano- to Micrometer Scale: The Role of Antisolvent Treatment on High Performance Perovskite Solar Cells. *Chem. Mater*. **2017**, *29*, *8*, 3490–3498

[7] National Renewable Energy Laboratory, N.R.E.L. https://www.nrel.gov/pv/assets/pdfs/best-research-cell-efficiencies-rev210726.pdf. Accessed 26 July 2021.

[8] H. J. Snaith, A. Abate, J. M. Ball, G. E. Eperon, T. Leijtens, N. K. Noel, S. D. Stranks, J. T-W. Wang, K. Wojciechowski, and W. Zhang, Anomalous Hysteresis in Perovskite Solar Cells. *J. Phys. Chem. Lett.* **2014**, *5*, 9, 1511–1515.

[9] J. Xu, A. Buin, A. H. Ip, W. Li, O. Voznyy, R. Comin, M. Yuan, S. Jeon, Z. Ning, J. J. McDowell, P. Kanjanaboos, J-P Sun, X. Lan, L. N. Quan, D. H. Kim, I. G. Hill, P. Maksymovych, E. H. Sargent, Perovskite–fullerene hybrid materials suppress hysteresis in planar diodes. *Nat. Commun.* **2015**, *6*, 1–8.

[10] C. Bi, Q. Wang, Y. Shao, Y. Yuan, Z. Xiao, J. Huang, Non-wetting surface-driven high-aspect-ratio crystalline grain growth for efficient hybrid perovskite solar cells. *Nat. Commun*, **2015**, *6*, 1–7.

[11] J. H. Heo, H. J. Han, D. Kim, T. K. Ahn, S. H. Im, Hysteresis-less inverted $CH_3NH_3PbI_3$ planar perovskite hybrid solar cells with 18.1% power conversion efficien. *Energy Environ. Sci*. **2015**, *8*, 1602–1608.

[12] N. Sahu, B. Parija, S. Panigrahi, Fundamental understanding and modeling of spin coating process: A review. *Indian J. Phys.* **2009**, *83*, 493–502.

[13] D. B. Hall, P. Underhill, J. M. Torkelson, Spin coating of thin and ultrathin polymer films. *Polym. Eng. Sci*. **1998**, *38*, 2039–2045.

[14] S. Sanjeev, D. Kekuda. Effect of Annealing Temperature on the Structural and Optical Properties of Zinc Oxide (ZnO) Thin Films Prepared by Spin Coating Process. *Mater. Sci. Eng.* **2021**, *73*, 012149.

[15] A. Dualeh, N. Tétreault, T. Moehl, P. Gao, M. K. Nazeeruddin, M. Grätzel. Effect of Annealing Temperature on Film Morphology of Organic–Inorganic Hybrid Pervoskite Solid-State Solar Cells. *Adv. Func. Mat.* **2014**, *24*, 21, 3250-3258.

[16] Applications, S. C. Spin Coating: A Guide to Theory and Techniques Introduction to Spin Coating. **2016**, 1–27.

[17] C. J. Lawrence, The mechanics of spin coating of polymer films. *Phys. Fluids.* **1988**, *31*, 2786–2795.

[18] G.S. May, S. M. Sze. Fundamentals of Semiconductor Fabrication. *Wiley*, **2004**.

[19] R. C. Jaeger, Introduction to Microelectronic Second Edition. *Pearson*, **2002**.

[20] W. Grimm, A new glow discharge lamp for optical emission spectral analysis-English version, Spectrochimica Acta Part B: Atomic Spectroscopy, **1968**, *23*, 7, 443-454.

[21] Grimm W. Glow discharge tube for spectral analysis, *United States Patent US3543077*, **1970.**

[22] P. Belenguer, M. Ganciu, P. Guillot, T. Nelis, Pulsed glow discharges for analytical applications, Spectrochimica Acta Part B, **2009**, *64*, 623-641.

[23] D. A. Skoog, F. J. Holler, S. R. Crouch, Principles of Instrumental Analysis. *Cengage learning*, **2017**, *7th Ed*, 1-992.

[24] N. Ghobadi, Band gap determination using absorption spectrum fitting procedure. *Int. Nano Lett*. **2013**, *3*, 2.

[25] H. P. Klug, L. E. Alexander, X-Ray Diffraction Procedures: For Polycrystalline and Amorphous Materials. *Wiley*, **1974**, *2nd Ed*, 1-992.

[26] C.W. Oatley, W.C. Nixon, R.F.W. Pease, Scanning electron microscopy, *Adv. Electronics Electron Phys.* **1965**, *21*, 181-247.

[27] J. Goldstein, D.E. Newbury, P. Echlin, D.C. Joy, C. Fiori, E. Lifshin, Scanning electron microscopy and x-ray microanalysis, *Springer*, **1981**, *1st Ed*, 1-673.

[28] L. Reimer, Scanning electron microscopy: Physics of image formation and microanalysis, *Springer*, **1998**, *2nd Ed*, 1-529.

[29] K. Kalantar-zadeh, B.Fry, Nanotechnology-Enabled Sensor, *Springer*, **2007**, *1st Ed*, 1-492.

Chapter 3. Development of cells performance and studying material characteristics

3.1. Introduction

A natural perovskite mineral was discovered in the Ural Mountains of Russia by Gustav Rose in 1839. The general chemical formula of the perovskite structure is 'ABX_3' in the cubic unit cells where the 'A' atom (large atomic or molecular cation) sits at cube-corner positions (0, 0, 0), the 'B' atom (smaller atomic or molecular cation) sits at body-centered position (1/2, 1/2, 1/2) and the 'X' atoms (anions) sit at face-centered positions (1/2, 1/2, 0). The most studied Hybrid Organic−Inorganic Perovskites (HOIPs) for PSCs are $MAPbI_3$ (MA = methylammonium; $CH_3NH_3^+$) and $FAPbI_3$ (FA = formamidinium; $HC(NH_2)_2^+$), where "mixed cations" in the A site and/or "mixed anions" in the X site are also available. In this study, triple cation lead double anion perovskite is analyzed comparing to $MAPbI_3$ as reference material.

The application of HOIP as a light absorber in dye-sensitized solar cell (DSSC) structures was first attempted in 2009 with 3.8 % of efficiency [1]. Moreover, improved efficiency to 6.5 % was reported in 2011 [2]. However, the dissolution of the perovskite nano-dots on the TiO_2 surface in a liquid electrolyte remained as an obstacle. Since 2012, high efficiency has been achieved by an effective coating method and composition engineering [3]. Starting with PCE of 9.7 %, Park *et al*. improved device stability using

the organic hole transport layer (Spiro-OMeTAD). Then, a certified 25.5% efficiency was developed and was reported NREL efficiency chart in 2021 [3-18].

Most world best efficient PSCs are using mesoporous electron-harvesting structure underlying DSSC. This structure is therefore named a conventional structure. However, the mesoporous layer requires high-temperature sintering above 400 °C, increasing processing time and cost of cell production. It has been shown that HOIP materials can have long carrier diffusion lengths (~ 100 nm for MAPbI3 and ~ 1000 nm for $MAPbI_{3-x}Cl_x$ [19-20]. Xing *et al*. demonstrated that perovskites could transport both holes and electrons between the cell terminals, which means perovskites have ambipolar characteristics [19]. This transporting feature indicated that a planar structure (without the mesoporous layer) was feasible. Planar structures fall into two categories, depending on which selective contact is used for the bottom: regular (n-i-p) and inverted (p-i-n) structures. The first planar structure was successfully demonstrated as perovskite/fullerene architecture reported by Jeng *et al*. showing a 3.9 % efficiency [21]. In 2013, Snaith *et al*. [22] obtained a 15.4 % efficiency with the planar structure using a dual-source vapor deposition. Recently, the 23.3 % efficiency of the planar structure was through interface passivation and morphology-controlled perovskite film in n-i-p architecture [23]. These results prove that those planar structures can achieve similar device performance to mesoporous structures.

The inverted (p-i-n) planar structure is derived from the organic solar cell. Several charge transport layers used in organic solar cells were practically suitable for perovskite solar cells [24]. The p-i-n perovskite solar cells have the advantages of lower temperature processing, faster fabricating, low cost, and negligible J-V hysteresis. Furthermore, in order to compare the new material {3CP: $(MA_{0.17}FA_{0.83})_{0.95}Cs_{0.05}Pb(I_{0.83}Br_{0.17})_3$} with the previously studied material {MAPI: $MAPbI_3$} in our laboratory, it is preferable to keep the same device structure i.e. p-i-n structure (ITO/PEDOT:PSS/Perovskite/$PC_{60}BM$/Ag).

3.2. Reference $MAPbI_{3-x}Cl_x$ solar cell

This study is to observe the stability of triple cation lead double halide {3CP: $(MA_{0.17}FA_{0.83})_{0.95}Cs_{0.05}Pb(I_{0.83}Br_{0.17})_3$} material against ageing and ion migration. For an accurate study, the fabrication method is based on the previous work of Dr. Heejae Lee's thesis [25]. The process development for using the $MAPbI_{3-x}Cl_x$ p-i-n solar cell is described below.

3.2.1. $MAPbI_{3-x}Cl_x$ solution preparation

To make ITO/PEDOT:PSS/$MAPbI_{3-x}Cl_x$/$PC_{60}BM$/Ag structure, we need to prepare three solutions (PEDOT:PSS, $MAPbI_{3-x}Cl_x$, and $PC_{60}BM$). For the PEDOT:PSS and $PC_{60}BM$ preparation, the process is already introduced in chapter 2.2.1. The $MAPbI_{3-x}Cl_x$ solution is made as a mixture of methylammonium iodide (MAI, Ossila), lead iodide (PbI_2, Ossila), and lead chloride ($PbCl_2$, Aldrich) at the 4:1:1 molar ratio (MAI: PbI_2: $PbCl_2$). Then, these solutes are dissolved in a solvent for 40 % weight percent in anhydrous N,N-Dimethylformamide (DMF, Aldrich). The solution was stirred at 70 °C in the glove box for more than 16 hours (overnight).

3.2.2. $MAPbI_{3-x}Cl_x$ Device fabrication

The inverted planar structure is composed of anode/HTL/light-absorbing layer/ETL/cathode. The $MAPbI_{3-x}Cl_x$ solar cell uses ITO, PEDOT:PSS, $MAPbI_{3-x}Cl_x$, $PC_{60}BM$, and silver (Ag) as an anode, HTL, light-absorbing layer, ETL, and cathode, respectively.

3.2.2.1 PEDOT:PSS layer deposition

Before using the solution, it is passed through a hydrophilic filter (40 μm). When the substrate is ready to deposit a layer on it (chapter 2.1), 400 μL of PEDOT:PSS solution covers the substrate surface. The substrate is spun with the revolution condition (3000 rpm – 30 s + 5000 rpm – 30 s). After patterning with a cotton swab moistened with methanol, it is annealed at 120 °C for 20 minutes.

3.2.2.2 $MAPbI_{3-x}Cl_x$ layer deposition

The 38 wt% concentration of $MAPbI_{3-x}Cl_x$ solution is so viscous, and the solvent (DMF) evaporates fast. The spin-coating technique spends a few seconds from the solution is dropped on the stationary substrate to the set rotation is started. This short time causes an error of tens or 100 nanometers in the

thickness of the $MAPbI_{3-x}Cl_x$ film due to the nature of the $MAPbI_{3-x}Cl_x$ solution. The way to remove this time is the dynamic dispense introduced in chapter 2.2.5. Fig. 3.1 is the summary of Power Conversion Efficiency (PCE) to demonstrate the effect of dynamic dispense for $MAPbI_{3-x}Cl_x$.

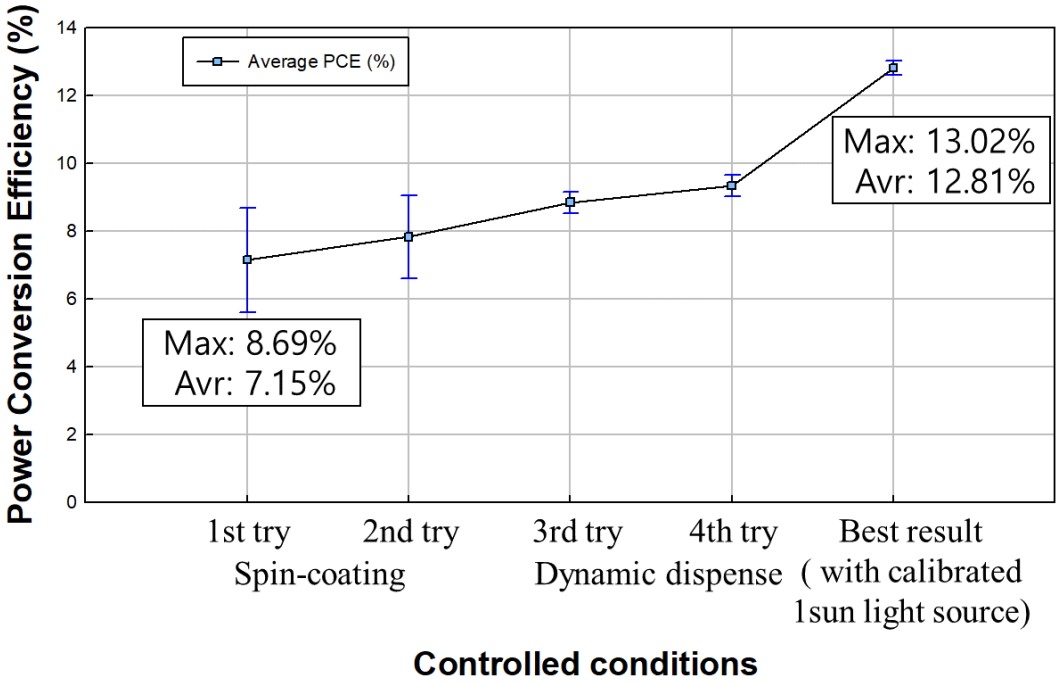

Figure 3.1. Summary of Power Conversion Efficiency (PCE) to demonstrate the effect of dynamic dispense for $MAPbI_{3-x}Cl_x$. The blue square is the average PCE, and the blue vertical line is the PCE variety of the batch. 1st and 2nd try: with spin-coating technique, 3rd, 4th try, and Best result: with dynamic dispense.

When the 60 µL solution is ready in the micropipette in advance, the substrate (Glass/ITO/PEDOT:PSS) is rotated under the condition of 6000 rpm-30 s. The solution is dispensed onto the substrate when the spin is sufficiently saturated at 6000 rpm. The thin film is brown after this process because the solution evaporates during rotation. This substrate (Glass/ITO/PEDOT:PSS/$MAPbI_{3-x}Cl_x$) is placed onto the hot plate at 80°C because patterning the perovskite layer is different from other layers. DMF adversely affects the perovskite film quality, so do not pattern immediately after dynamic dispense. To minimize the damage by DMF, the substrate is firstly annealed at 80 °C to evaporate the remaining DMF in the perovskite film as fast. This annealing process lasts for 120 minutes, and patterning is performed on the hot plate when 30 minutes remain. With the heat of 80 °C, it is possible to prevent damage to the thin film by a cotton swab moistened with DMF used for patterning.

3.2.2.3 $PC_{60}BM$ layer deposition

Before using the solution, it is passed through a hydrophobic filter (40 µm). 60 µL solution covers onto the substrate (Glass/ITO/PEDOT:PSS/$MAPbI_{3-x}Cl_x$) and is spun with 2000 rpm-30 s condition. With cotton swap soaked in chlorobenzene (CB), the $PC_{60}BM$ layer is patterned. This substrate (Glass/ITO/PEDOT:PSS/$MAPbI_{3-x}Cl_x$) is delivered in the thermal evaporator without annealing.

The 120 nm of silver (Ag) cathode is manufactured, as explained in chapter 2.2.6. While reproducing Dr. Lee's $MAPbI_{3-x}Cl_x$ solar cell, the reference device for this study, the manufactured devices showed different Jsc values from performance and EQE measurements. We found a problem in the calibration of the performance meter's light source. The best result in Fig. 3.1. is obtained through an improved calibration method.

3.3. Triple cation perovskite solar cell

This study is to observe the stability of triple cation lead double halide {3CP: $(MA_{0.17}FA_{0.83})_{0.95}Cs_{0.05}Pb(I_{0.83}Br_{0.17})_3$} material against ageing and ion migration. As mentioned previously, all processes (PEDOT:PSS, $PC_{60}BM$, Ag) were kept the same except for the synthesis of 3CP material.

3.3.1. 3CP solution preparation

The composition ratio of the precursor solution is introduced in Chapter 2. After composing the precursor, the important condition is the temperature of the solution. Although it is not mentioned in the original paper [26], 3CP solution improves crystallinity by depositing in a warm (60 °C) condition. Because the solution has a problem of ageing, it is recommended to use between 6 and 24 hours after the solution is made [27]. Therefore, the solution is stirred at room temperature overnight and heated to 60 °C one hour before use.

3.3.2. 3CP layer deposition

Apply the prepared solution on the substrate (Glass/ITO/PEDOT:PSS) and run the spin-coater under the conditions of 1000 rpm-10 s + 6000 rpm-20 s as shown in Fig. 3.2. Then, when 5 seconds remain, 100 µL chlorobenzene (CB) is dropped onto the center of the rotating substrate.

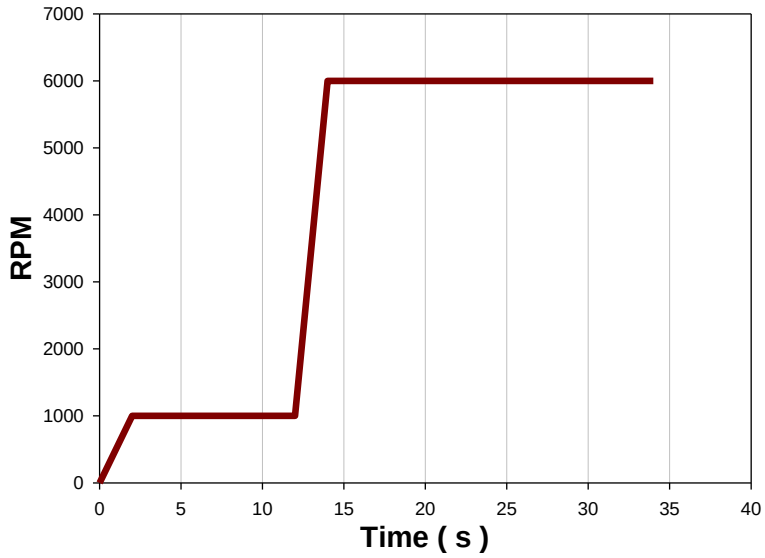

Figure 3.2. Revolution condition for 3CP layer spin-coating

The film is placed onto the hot plate at 100 °C for 10 minutes.

3.3.3. Development of solution deposition engineering suit to lab environment

The first purpose of this project was attaining reproducibility above 8 % of power conversion efficiency (PCE) for 3CP based perovskite solar cells. Using the fabrication process described by Saliba *et al*. [26], I got 4.0 % of PCE in the first experiment (Fig. 3.3).

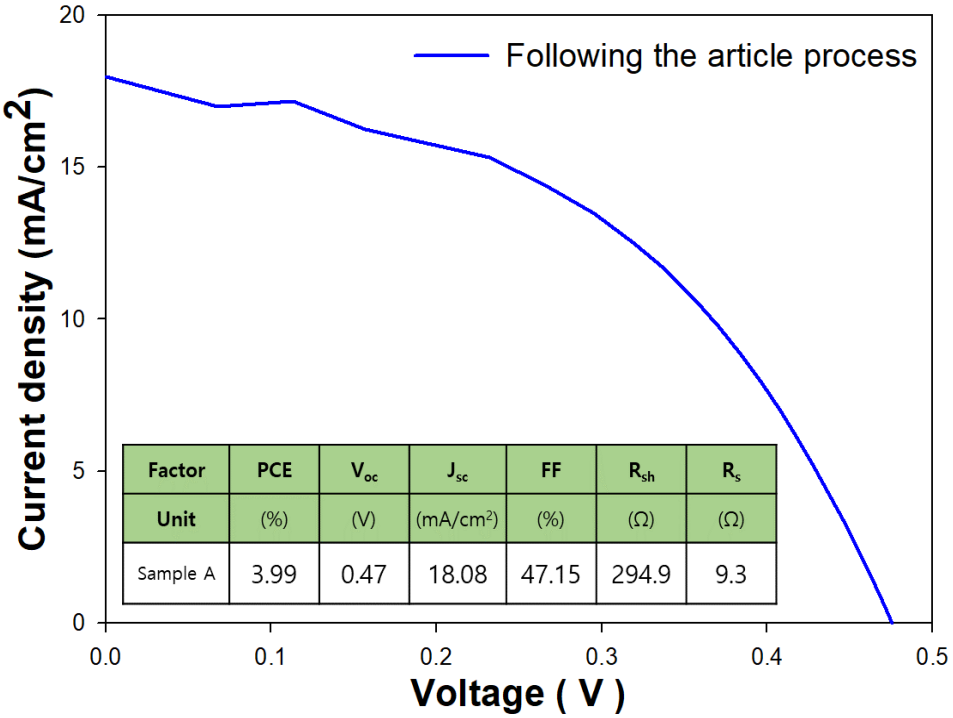

Figure 3.3. First J-V performance of 3CP solar cells

In the case of the solution process, we have to consider various conditions because the deposition mechanism can be affected by the underlayer (PEDOT:PSS), humidity, temperature. This is because the sparsely formed perovskite layer creates parasitic circuits such as direct contact between the PEDOT:PSS layer and the $PC_{60}BM$ layer. Because of the parasitic circuits, leakage current increased significantly (while also decreasing shunt resistance), and V_{oc} is reduced. In general, a well-made light absorbing layer of the solar cell should show higher open-circuit voltage in accordance with the material's inherent bandgap. Therefore, obtaining a reading where V_{oc} is too low is one of the clues to deducing the layer has a problem. For this reason, our performance had lower V_{oc}, R_{sh} than other planar structured perovskite solar cells and various J_{sc} (from 11.74 mA/cm^2 to 18.08 mA/cm^2) results in the same batch. Fig. 3.3. shows the performance of 3CP-based perovskite solar cells after applying Saliba's process [26].

3.3.3.1 Anti-solvent treatment

The significant key factor was anti-solvent {chlorobenzene (CB)} treatment because CB affects the crystallinity of perovskite. At the final step of spin coating, the control of the film thickness is achieved, and most of the remaining solvent is blown off. The anti-solvent treatment timing depends on many factors (spin rate, type of anti-solvent, dispensing volume per second [28]). If the CB is dropped

prematurely or too late, the crystallization occurs too early or is not affected by treatment respectively (Fig. 3.4). By changing the CB drop timing from 24s to 34s, we were finally able to get a densely crystallized perovskite layer at the 29s in the same conditions as the referenced article [26]. Fig. 3.5. b) shows improved film crystallinity by SEM (scanning electron microscopy).

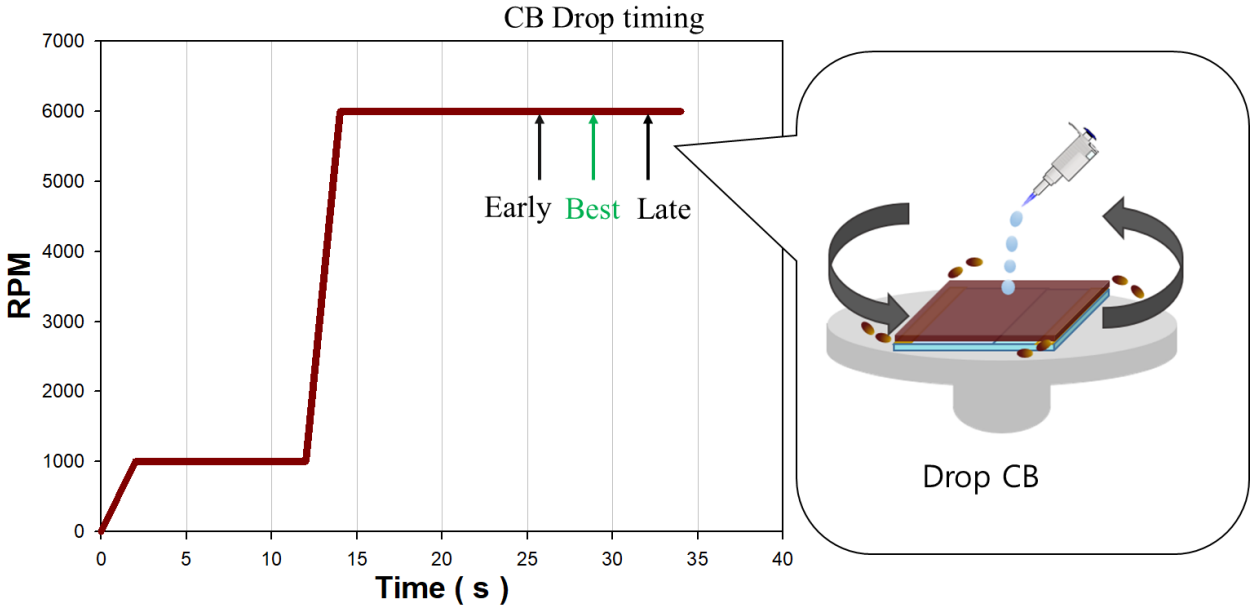

Figure 3.4. Schematic of Chlorobenzene drop timing.

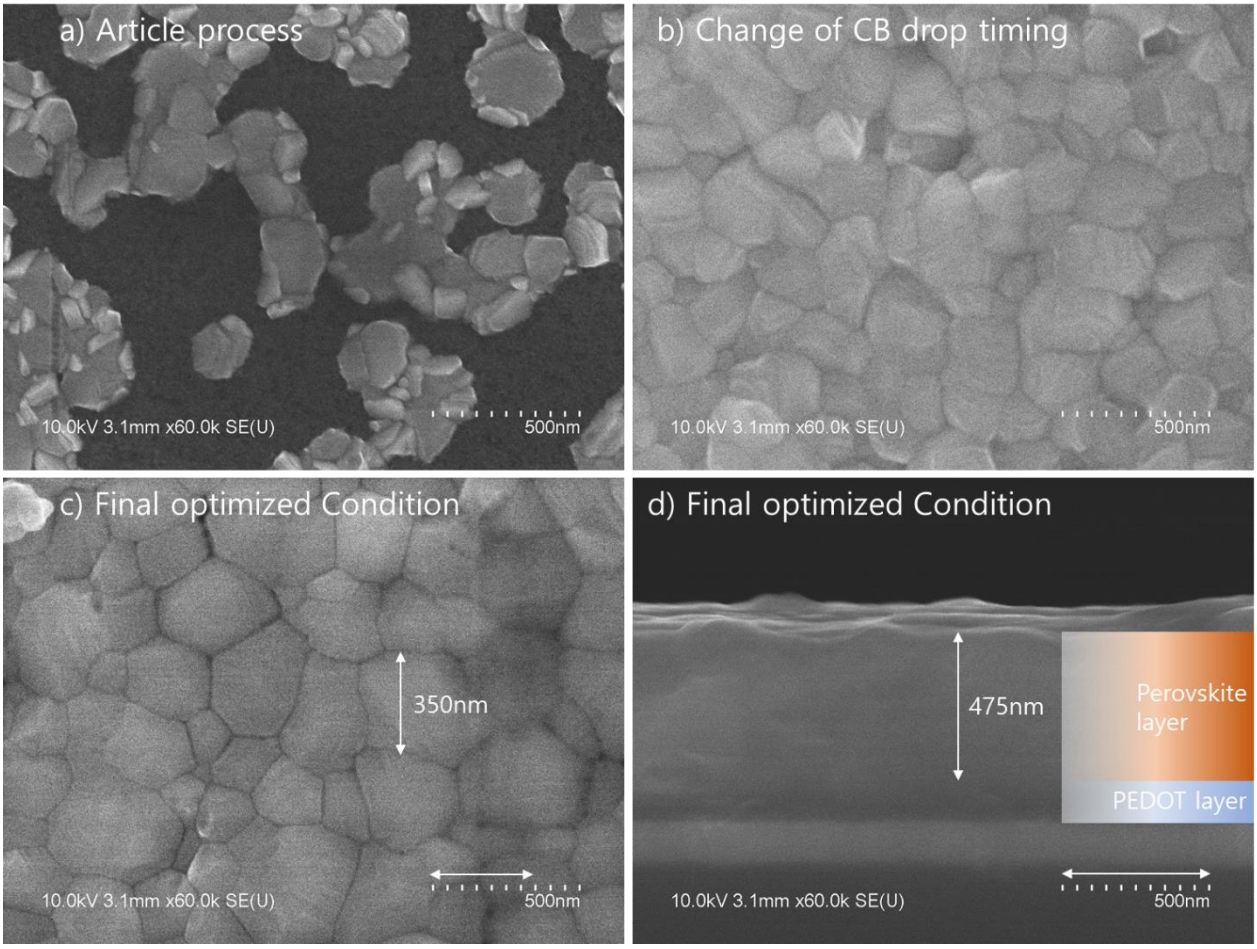

Figure 3.5. Top view of scanning electron microscopy (SEM) image a) Saliba's article process b) change of CB drop timing c), d) final optimized conditions.

3.3.3.2 Thickness control

After learning the importance of CB dispense timing, we focused on thickness control. The first step of spin coating controls the film thickness. In summary, higher rpm gets a thinner layer. In the case of planar structures, they should have a thinner layer because of the absence of efficient charge collecting structures. The study of planar perovskite film addresses the excited carrier diffusion length being 330nm [29]. After obtaining the dense crystal layer, our sample layers thickness varied from 493 nm to 548 nm. We, however, needed to test a thinner layer for the solar cell. By changing the first step conditions (Fig.3.6) of the spin coating, we finally achieved a 475 nm (Fig. 3.5 d) thickness layer with 6000 rpm.

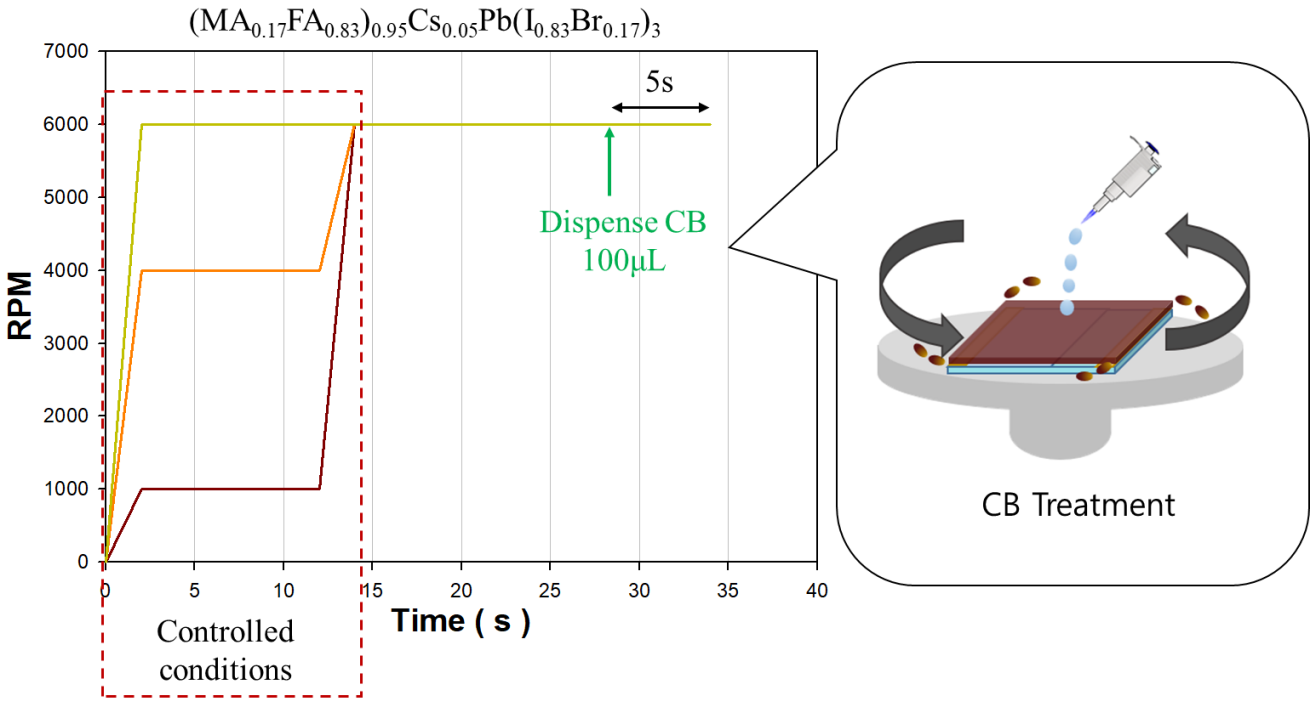

Figure 3.6. change of detail spin coating process

3.3.3.3 Dynamic dispense for uniformity

Since the spin-coating process has high thickness variations sample by sample and the ability to reproduce the film thickness is a key parameter to get a good reproducibility, dynamic dispense technique (spin casting) is instead applied to get lower thickness variations. In addition, when we anneal the samples in the dark, the solar cell performances are dramatically improved following the advice of Saliba. This is also due to the light sensitivity of perovskite. As a result, the maximum performance achieved was PCE: 13.03 %, with an average of 12.72 % and an error margin of 0.31. Fig. 3.7, 3.8, and Table 3.1 show the details of the development.

	Method	1st step	2nd step	CB treatment	CB volume	Annealing
Saliba process	Spin-coating	1000rpm	6000rpm	29s	100µL at once	100°C for 1h
Optimization	Dynamic dispense	6000rpm	6000rpm	29s	100µL at once	80°C for 1h in the dark

Table 3.1. Summary of optimized condition comparing to reference (Saliba) process.

Table 3.1 is the summary of the optimization process. The green-colored cases show which parameters are differently applied. As addressed before, dynamic dispense with high revolution is used to obtain constant thickness. As the CB treatment relies on a user/person/operator, timing and dispensing

duration vary. This thus critically determines performance variations sample by sample of the 3CP solar cells. To consider the sensitive character of perovskite, we chose a lower temperature of annealing in dark conditions.

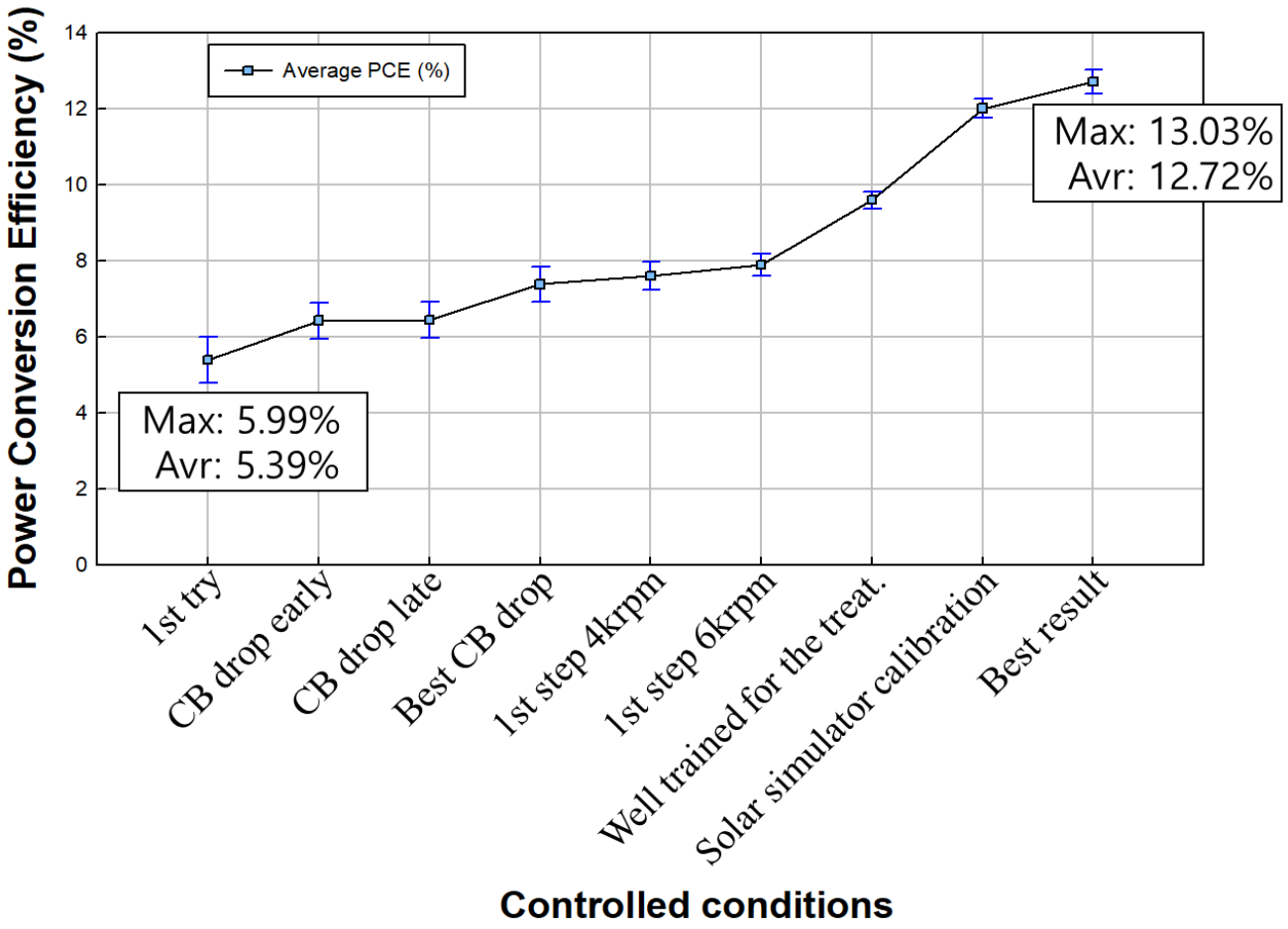

Figure 3.7. Summary of 3CP solar cell performance development history.

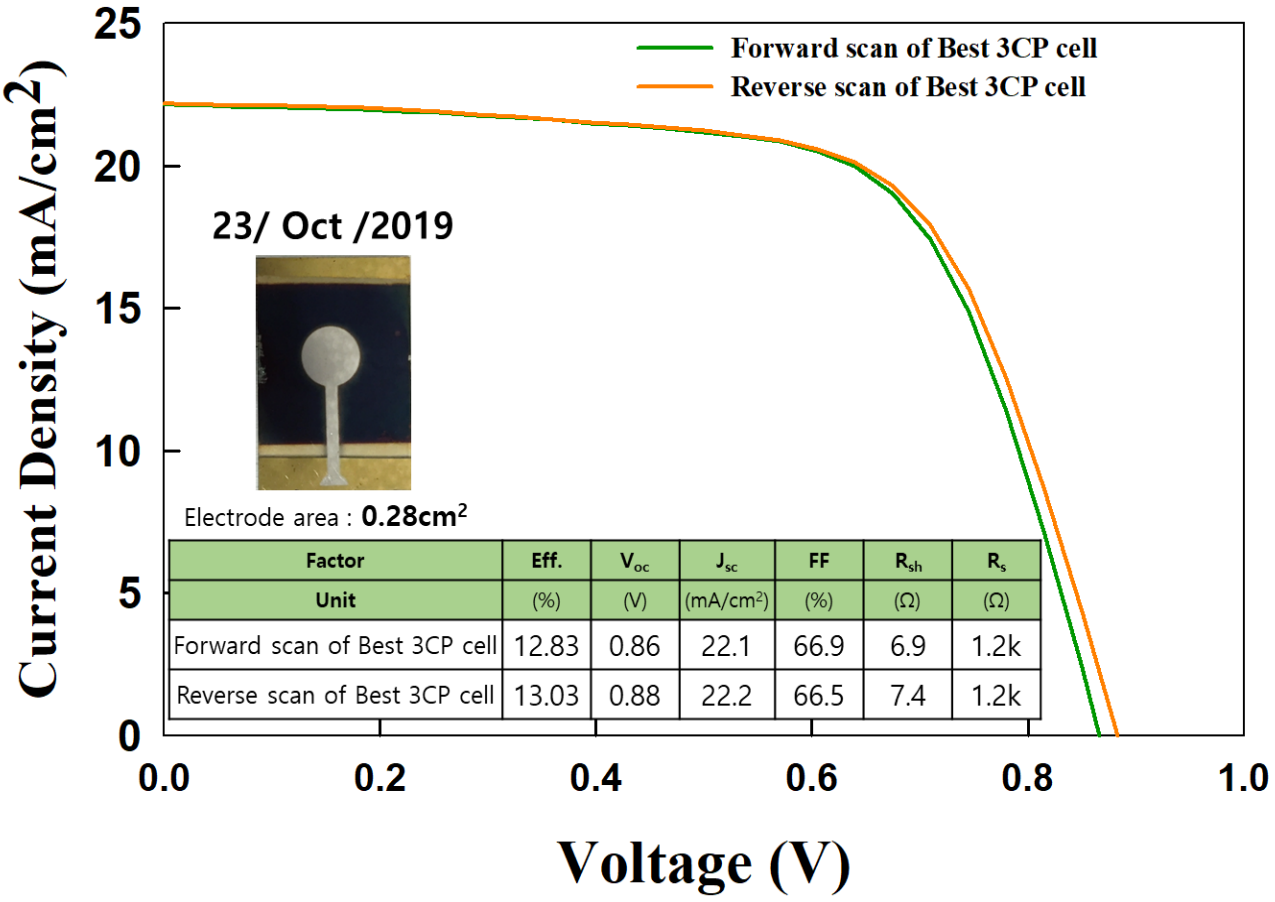

Factor	Eff.	V_{oc}	J_{sc}	FF	R_{sh}	R_s
Unit	(%)	(V)	(mA/cm^2)	(%)	(Ω)	(Ω)
Forward scan of Best 3CP cell	12.83	0.86	22.1	66.9	6.9	1.2k
Reverse scan of Best 3CP cell	13.03	0.88	22.2	66.5	7.4	1.2k

Figure 3.8. Detail performance of the best performance.

3.4. Analysis of EQE, the crucial question concerning our performance measurement system.

The way to understand the characteristics of solar cells is EQE analysis, as explained in chapter 2.5.1.2. If we keep all factors and change only the thickness, EQE data curves and the thickness of perovskite layers show a clear correlation. A film of appropriate thickness loses longer wavelength light that requires more extended absorption depth; it can collect more excited carriers. Therefore, Fig. 3.9 shows higher EQE at a medium wavelength and a bit less EQE at a longer wavelength.

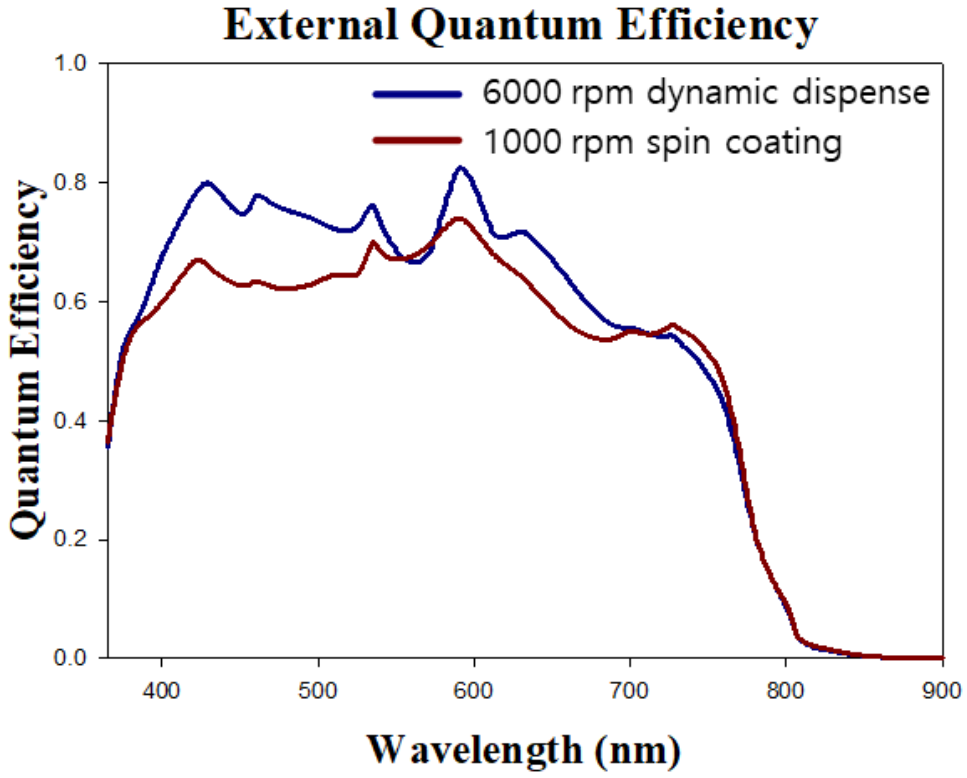

Figure 3.9. External Quantum Efficiency Result

Another parameter that can be analyzed with EQE is J_{sc}. Fundamentally, the machine measures the spectral response (SR), which calculates the ratio of the power input to the light source and the output current from the solar cell. Therefore, the relation between J_{sc} and EQE is:

$$J_{sc} = -q\int EQE(\lambda)\cdot \Phi_{AM1.5G} d\lambda \quad \text{- 3.4 – (1)} \quad \text{* Spectral response (SR): } S(\lambda) = \frac{-q\lambda}{hc} EQE(\lambda)$$

$$Jsc = \int S(\lambda) E_0(\lambda) d\lambda \quad \text{- 3.4 – (2)} \quad \text{* Irradiance } E_0(\lambda) = \frac{hc}{\lambda}\Phi_{AM1.5G}(\lambda)$$

According to this equation, J_{sc} derived by EQE (J_{sc}^{EQE}) must correspond to J_{sc} obtained experimental J_{sc}^{Exp} by the solar performance simulator.

The J_{sc}^{EQE} is 16.38mA/cm^2 (TFSC instrument). The value is very different from J_{SC}^{Exp} = 20.2mA from the same sample. This theoretically does not make sense as the experimental J_{sc}^{Exp} we got was ±20% different from J_{sc}^{EQE}. The findings of Zimmermann et al. [30] show that it is a possible error because the actual irradiance of 100μW/cm^2 used by the EQE machine is three orders lower than AM1.5G. These differences can contribute to the calculation of J_{sc}^{EQE} as error (Fig. 3.10).

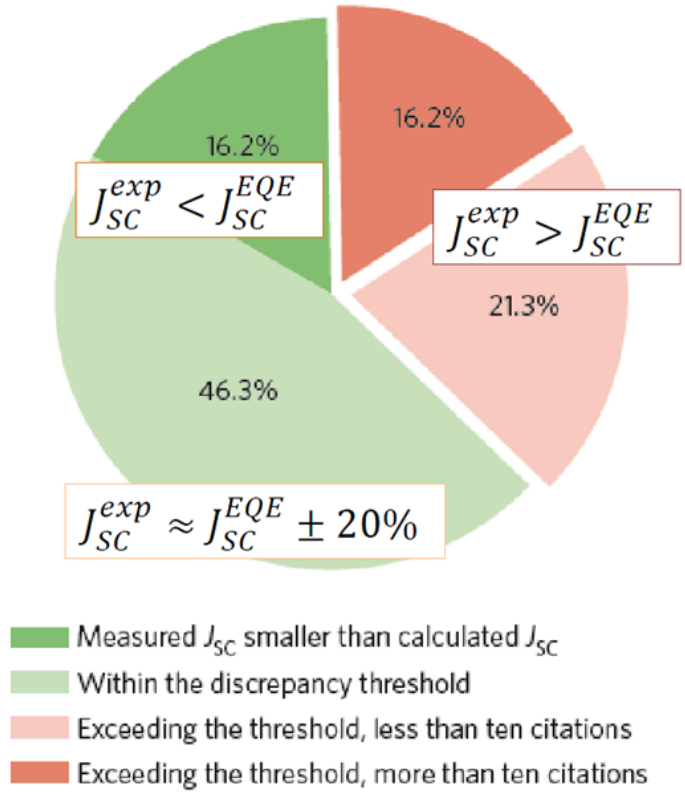

Figure 3.10. Survey of current mismatch between experimental J_{sc} and calculated J_{sc} by EQE [30].

The following question arose: "what would be the ideal method to calibrate the light source?". According to the theory, with Eq 3.4 - (2), we can note that c-Si calibration and J_{sc}^{EQE} matching calibration has an error on irradiance ($E(\lambda)$). The theoretical Solution would hence be as follows [31]:

$$M = \frac{\int E_R(\lambda)S_R(\lambda)\partial\lambda}{\int E_S(\lambda)S_R(\lambda)\partial\lambda} \times \frac{\int E_S(\lambda)S_T(\lambda)\partial\lambda}{\int E_R(\lambda)S_T(\lambda)\partial\lambda} = \frac{J_{Ref}^{AM1.5}}{J_{Ref}^{lamp}} \times \frac{J_{perovskite}^{lamp}}{J_{perovskite}^{AM1.5}} \qquad 3.4 - (3)$$

The first condition is that the reference cell must achieve: $J_{Ref}^{AM1.5} = J_{Ref}^{lamp}$. This relation means the solar simulator must be calibrated according to the reference cell. This calibrated intensity will be referred to as "A".

Then, eq 3.4 - (3) is equal to:

$$M = \frac{J_{perovskite}^{lamp}}{J_{perovskite}^{AM1.5}} \qquad 3.4 - (4)$$

To calculate the current mismatch factor (*M*), we need these four factors.

a. $E_{AM1.5}(\lambda)$ [32]

b. $E_{Lamp}(\lambda)$

c. $S_{Pero}(\lambda)$

d. J_{sc}^{Ref} of reference cell under intensity A

1. $E_{AM1.5}(\lambda)$ data is taken from IEC 60904-3 standard.
2. $E_{Lamp}(\lambda)$ is measured by Black-comet-SR (StellarNet Inc form Xlim). (Fig.3.11)
3. $S_{Pero}(\lambda)$ is measured by TFSC EQE analyzer.
4. J_{sc}^{Ref} = 12.6 mA of the c-Si solar cell (3 single cells in series).

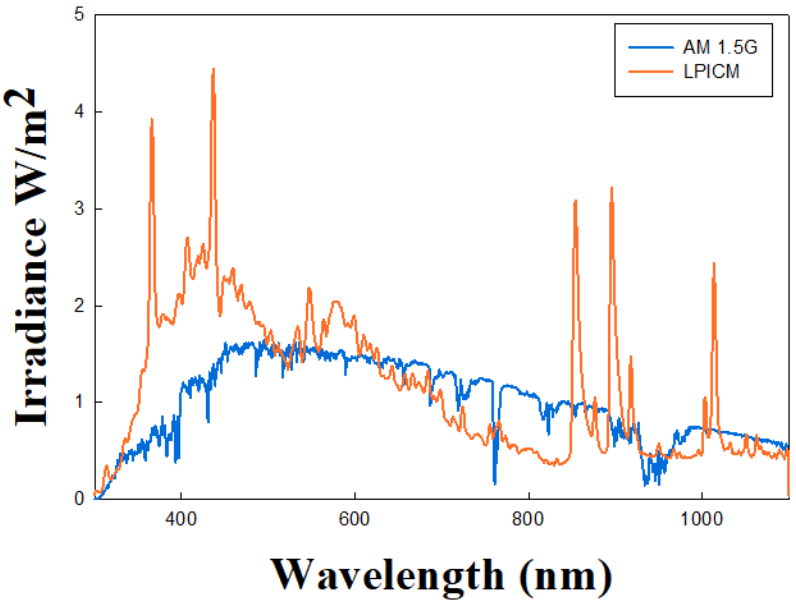

Figure 3.11. The irradiance of AM1.5G IEC standard and LPICM lamp.

Obtained data lets us know the LPICM lamp is grade D, which means it is unlike solar light even though it contains a lot of UV light. In any case, we can approach a similar result by applying that data to eq 3.4 - (4) as a spectral response can cover irradiance error. Through those calculations, the result mismatch becomes M = 1.13 (Fig. 38). If it is applied to $\frac{E_{Lamp}(\lambda)}{M}$ the corrected J_{sc} corresponds to the calculated $J_{sc}^{AM1.5G}$.

The final step is applying M to the reference cell with an estimated value of:

→ 12.60 mA/cm^2 / 1.13 = 11.15 mA/cm^2 3.4 - (5)

However, this value is obtained only when a filter that can eliminate UV and 770-1100 nm range is applied. Following Snaith et al. findings [33], a KG5 filter can be used. With the filter calibrating J_{sc} of c-Si as 11.15 mA, ideal conditions will be achieved. Our next step is to measure the spectral response more accurately (per each nanometer wavelength) for the c-Si and perovskite solar cells.

3.5. Thin film characteristics

After developing the manufacturing process for $MAPbI_{3-x}Cl_x$ (shortly MAPI) and 3CP solar cells, the film characterization was essential to evaluate whether my thin films ($MAPbI_{3-x}Cl_x$ and 3CP) are relevant to the well-known research. Since the SEM results have already mentioned in section 3.3.3.1, in this section UV-visible absorbance spectra and XRD is the tool to evaluate the film quality.

3.5.1. Analysis of UV-Visible spectra

To investigate the bandgap, a UV-Vis spectrophotometer was used. Bromine doping in a $MAPbI_3$ perovskite affects the widening bandgap (higher bandgap value than 1.60 eV) [26,34]. Our solution contains 17 % of bromine. This concentration theoretically results in 1.646 eV [34]. The bromine molar ratio for the solution, however, does not correlate to the same portion in the solid-state (lattice).

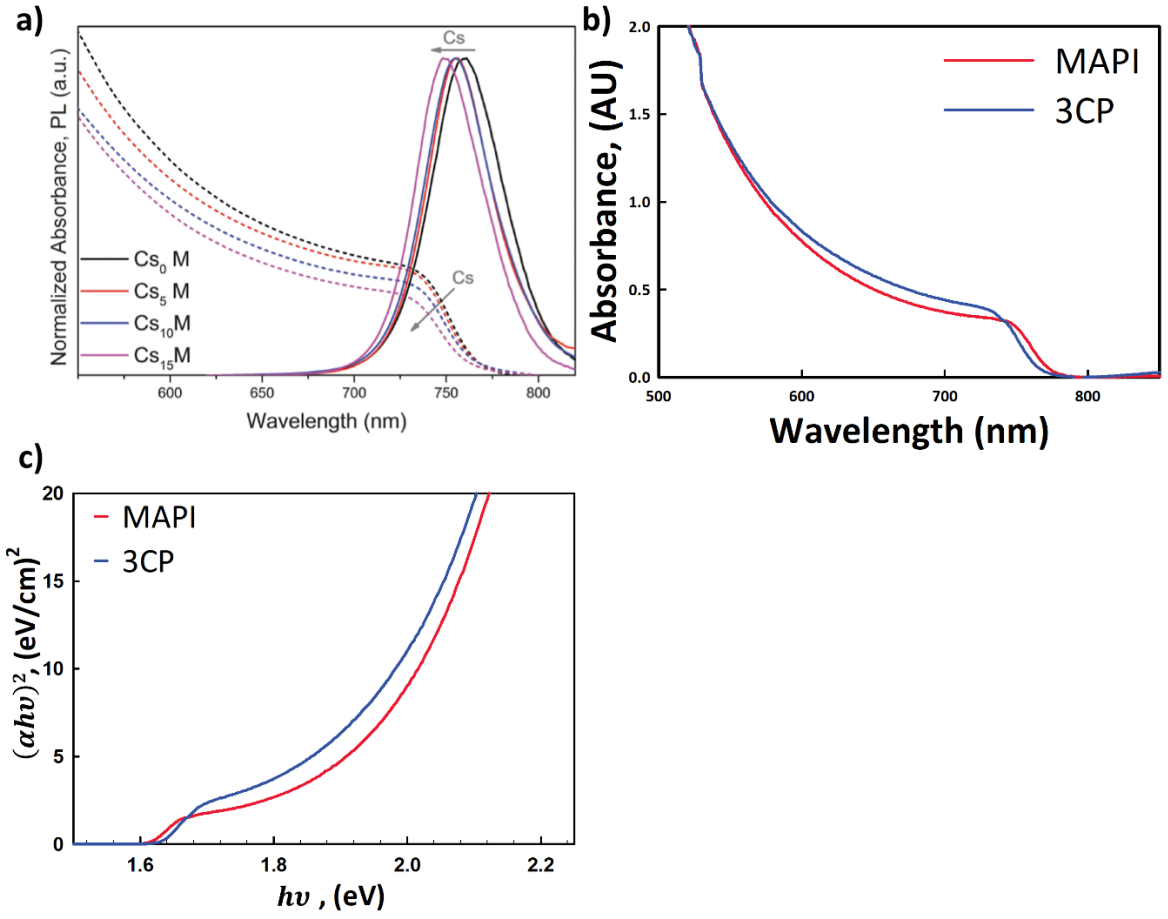

Figure 3.12. UV-Vis spectrophotometer absorbance: a) result of article [26] b) result of MAPI and 3CP with the same plot form (Abs vs. wavelength) to the article. c) Tauc plot derived from b).

The measured 3CP's bandgap energy is 1.62 eV (Fig. 3.12c). This is because of the molecular portion in the 3CP's solid-state changes during the fabrication process. To check optimization progress, it is good to compare it with the reference Saliba's article. The 3CP's bandgap is 1.62 eV which is like our result (Fig. 3.12).

3.5.2. Analysis of XRD

We used XRD to confirm the lattice structure. The bromine ratio in the lattice that the UV-Vis spectra cannot show is approximately visible in XRD. In the XRD fingerprint of the referred article (Fig. 3.13 b), the major peaks (2θ) are 14.2 °, 28.6 ° and 32.2 ° respectively. Our 3CP film shares the same major peaks. These also correspond to the $MAPbI_3$ lattice structure.

Through the derivation from 2θ to the (hkl), the three major peaks 14.2 °, 28.6 °, and 32.2 ° correspond to phases: (110) tetragonal phased $MAPbI_3$, (220) tetragonal phased $MAPbI_3$ and (310) tetragonal phased $MAPbI_3$ respectively [34]. Compared with the article, these results mean our 3CP process is well-optimized.

In the case of other peaks, the presence of one at 20.2° is interesting. This peak corresponds to a phase (110) cubic of $MAPbBr_3$ and is prominent in the result (Fig. 3.13 d), where excessive CB treatment (dispensed more volume of CB) was applied. This analysis implies that the 3CP lattice structure changes depending on the process.

The XRD analysis helped evaluate our optimization progress and suggested a necessity to improve the process. It was, as such, a useful tool in the early stages of optimization. Besides, it made it possible to analyze the lattice mixed within the 3CP layer.

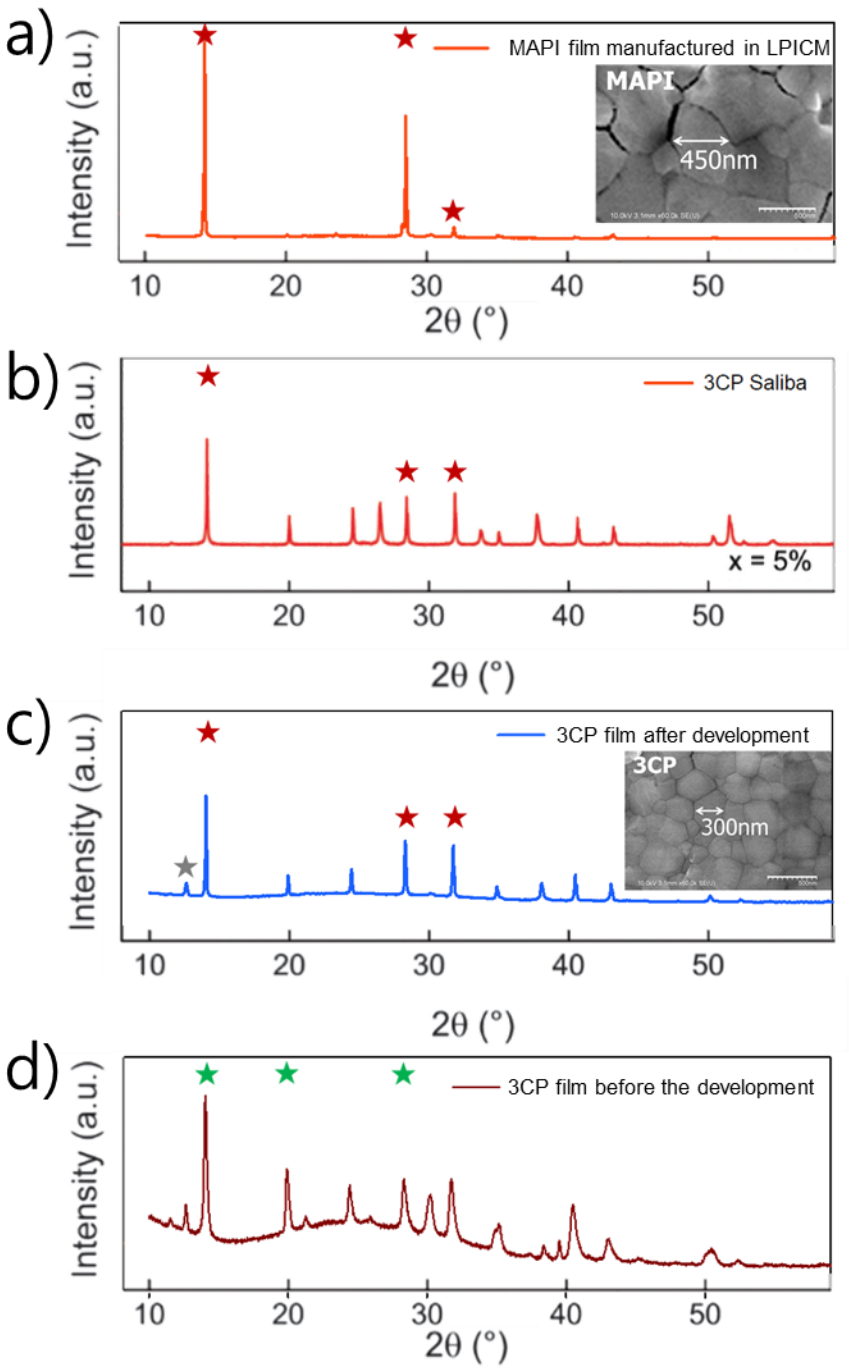

Figure 3.13. XRD pattern of a) MAPI ($MAPbI_{3-x}Cl_x$), b) 3CP from the referenced article, c) 3CP after development, and d) before the development.

3.6. References

[1] A. Kojima, K. Teshima, Y. Shirai, T. Miyasaka, Organometal Halide Perovskites as Visible- Light Sensitizers for Photovoltaic Cells. *J Am Chem Soc.* **2009**, *131*, 6050–6051.

[2] J. Im, C. Lee, J. Lee, S. Park, N.G. Park, 6.5% efficient perovskite quantum-dot-sensitized solar cell. *Nanoscale*, **2011**, *3*, 4088-4093.

[3] H. Kim, C. Lee, J. Im, K. Lee, T. Moehl, A. Marchioro, S. Moon, R. Humphry-Baker, J. Yum, J. E. Moser, M. Gratzel, N.G. Park, Lead Iodide Perovskite Sensitized All-Solid-State Submicron Thin Film Mesoscopic Solar Cell with Efficiency Exceeding 9%. *Scientific Reports.* **2012**, *2*, 591.

[4] M. M. Lee, J. Teuscher, T. Miyasaka, T. N. Murakami, H. J. Snaith, Efficient Hybrid Solar Cells Based on Meso-Superstructured Organometal Halide Perovskites. *Science.* **2012**, *338*, 6107, 643-647.

[5] J. H. Heo, S. H. Im, J. H. Noh, T. N. Mandal, C-S. Lim, J. A. Chang, Y. H. Lee, H-J. Kim, A. Sarkar, M. K. Nazeeruddin, Efficient Inorganic−Organic Hybrid Heterojunction Solar Cells Containing Perovskite Compound and Polymeric Hole Conductors. *Nat. Photonics.* **2013**, *7*, 486−491.

[6] M. A. Green, K. Emery, Y. Hishikawa, W. Warta, E. D. Dunlop, Solar Cell Efficiency Tables (Version 42). *Prog. Photovoltaics*. **2013**, *21*, 827−837.

[7] J. W. Lee, D. J. Seol, A. N. Cho, N. G. Park, High-Efficiency Perovskite Solar Cells Based on the Black Polymorph of HC- $(NH_2)_2PbI_3$. *Adv. Mater.* **2014**, *26*, 4991−4998.

[8] J-H. Im, I-H. Jang, N. Pellet, M. Grätzel, N.G. Park, Growth of $CH_3NH_3PbI_3$ Cuboids with Controlled Size for High-Efficiency Perovskite Solar Cells. *Nat. Nanotechnol.* **2014**, *9*, 927−932.

[9] M. A. Green, K. Emery, Y. Hishikawa, W. Warta, E. D. Dunlop, Solar Cell Efficiency Tables (Version 44). *Prog. Photovoltaics.* **2014**, *22*, 701−710.

[10] H. Zhou, Q. Chen, G. Li, S. Luo, T.-B. Song, H-S. Duan, Z. Hong, J. You, Y. Liu, Y. Yang, Interface Engineering of Highly Efficient Perovskite Solar Cells. *Science.* **2014**, *345*, 542−546.

[11] M. A. Green, K. Emery, Y. Hishikawa, W. Warta, E. D. Dunlop, Solar Cell Efficiency Tables (Version 45). *Prog. Photovoltaics*. **2015**, *23*, 1−9.

[12] D-Y. Son, J-W. Lee, Y. J. Choi, I.-H. Jang, S. Lee, P. J. Yoo, H. Shin, N. Ahn, M. Choi, D. Kim, Self-Formed Grain Boundary Healing Layer for Highly Efficient $CH_3NH_3PbI_3$ Perovskite Solar Cells. *Nat. Energy.* **2016**, *1*, 16081.

[13] M. A. Green, K. Emery, Y. Hishikawa, W. Warta, E.D. Dunlop, Solar Cell Efficiency Tables (Version 48). *Prog. Photovoltaics*. **2016**, *24*, 905−913.

[14] M. A. Green, Y. Hishikawa, E. D. Dunlop, D. H. Levi, J. Hohl-Ebinger, A. W. Y. Ho-Baillie, Solar Cell Efficiency Tables (Version51). *Prog. Photovoltaics*. **2018**, *26*, 3−12.

[15] M. A. Green, Y. Hishikawa, E. D. Dunlop, D. H. Levi, J. Hohl-Ebinger M. Yoshita, A. W. Y. Ho-Baillie, Solar Cell Efficiency Tables (Version 53). *Prog. Photovoltaics*. **2019**, *27*, 3−12.

[16] M. A. Green, E. D. Dunlop, D. H. Levi, J. Hohl-Ebinger, M. Yoshita, A. W. Ho-Baillie, Solar Cell Efficiency Tables (Version 54). *Prog. Photovoltaics*. **2019**, *27*, 565−575.

[17] M. A. Green, E. D. Dunlop, J. Hohl-Ebinger, M. Yoshita, N. Kopidakis, A. W. Y. Ho-Baillie, Solar Cell Efficiency Tables (Version 55). *Prog. Photovoltaics*. **2020**, *28*, 3−15.

[18] National Renewable Energy Laboratory, N.R.E.L. https://www.nrel.gov/pv/assets/pdfs/best-research-cell-efficiencies-rev210726.pdf. Accessed 26 July 2021.

[19] G.C. Xing, N. Mathews, S.Y. Sun, S.S. Lim, Y.M. Lam, M. Gratzel, S. Mhaisalkar, T.C. Sum, Long-range balanced electron- and hole- transport lengths in organicinorganic $CH_3NH_3PbI_3$, *Science.* **2013**, *342*, 6156, 344-347.

[20] S.D. Stranks, G.E. Eperon, G. Grancini, C. Menelaou, M.J.P. Alcocer, T. Leijtens, L.M. Herz, A. Petrozza, H.J. Snaith, Electron-hole diffusion lengths exceeding 1 micrometer in an organometal trihalide perovskite absorber. *Science.* **2013**, *342*, 6156, 341-344.

[21] J.Y. Jeng, Y.F. Chiang, M.H. Lee, S.R. Peng, T.F. Guo, P. Chen, T.C. Wen, $CH_3NH_3PbI_3$ Perovskite/Fullerene Planar-Heterojunction hybrid solar cells, *Adv. Mater*. **2013**, *25*, 3727.

[22] M. Liu, M.B. Johnston, H.J. Snaith, Efficient planar heterojunction perovskite solar cells by vapour deposition, *Nature.* **2013**, *501*, 395.

[23] Q. Jiang, Y. Zhao, X. Zhang, X. Yang, Y. Chen, Z. Chu, Q. Ye, X. Li, Z. Yin, J. You, Surface passivation of perovskite film for efficient solar cells. *Nature Photonics.* **2019**, *13*, 460–466.

[24] J. You, Y. Yang, Z. Hong, T.B. Song, L. Meng, Y. Liu, C. Jiang, H. Zhou, W. H. Chang, G. Li, Y. Yang, Moisture assisted perovskite film growth for high performance solar cell, *Appl. Phys. Lett*. **2014**, *105*, 183902.

[25] H. Lee, Under the direction of Yvan Bonnassieux, Thesis: Analysis of Current-Voltage Hysteresis and Ageing Characteristics for $CH_3NH_3PbI_{3-x}Cl_x$ Based Perovskite Thin Film Solar Cells: http://theses.fr/2018SACLX009.

[26] M. Saliba, T. Matsui, J-Y. Seo, K. Domanski, J-P. Correa-Baena, M. K. Nazzeruddin, S. M. Zakeeruddin, W. Tress, A. Abate, A. Hagfeldt, M. Gratzel, Cesium-containing triple cation

perovskite solar cells: Improved stability, reproducibility, and high efficiency. *Energy Environ. Sci*. **2016**, *9*, 1989–1997.

[27] P. Boonmongkolras, D. Kim, E.M. Alhabshi, I. Gereige, B. Shin, Understanding effects of precursor solution aging in triple cation lead perovskite. *RSC Adv.*, **2018**, *8*, 21551-21557.

[28] A.D. Tatlor, Q. Sun, K.P. Goetz, Q. An, T. Schramm, Y. Hofstetter, M. Litterst, F. Paulus, Y. Vaynzof, A general approach to high-efficiency perovskite solar cells by any antisolvent. *Nature Communications*. **2021**, 12, 1878.

[29] E.J. Juarez-Perez, R.S. Sanchez, L. Badia, G. Garcia-Belmonte, Y.S. Kang, I. Mora-Sero, J. Bisquert, Photoinduced giant dielectric constant in lead halide perovskite solar cells. *J. Phys. Chem. Lett.* **2014**, *5*, 2390–2394.

[30] E. Zimmermann, P. Ehrenreich, T. Pfadler, J.A. Dorman, J. Weickert, L. Schmidt-Mende, Erroneous efficiency reports harm organic solar cell research. *Nat. Publ. Gr.* **2014**, *8*, 669–672.

[31] V. Shrotriya, G. Li, Y. Yao, T. Moriarty, K. Emery, Y. Yang, Accurate Measurement and Characterization of Organic Solar Cells. *Advanced Functional Materials.*, **2006**, *16*, 15 2016-2023.

[32] NREL. Reference Air Mass 1.5 Spectra. Available at: https://www.nrel.gov/grid/solar-resource/spectra-am1.5.html.

[33] H. J. Snaith, How should you measure your excitonic solar cells? *Energy & Environ. Sci.*, **2012**, *5*, 6513–6520.

[34] J. H. Noh, S. H. Im, J. H. Heo, T. N. Mandal, S. I. Seok, Chemical management for colorful, efficient, and stable inorganic-organic hybrid nanostructured solar cells. *Nano Lett.* **2013**, *13*, 1764–1769.

Chapter 4. Ion migration in triple cation perovskite solar cells

4.1. Introduction

Charged ions and charge carriers move under the applied electric field in perovskite solar cells (PSCs). The phenomenon of ion migration in halide-based perovskite materials was first reported in 1983 [1], but it did not attract considerable attention. In the 2010s, when the current-voltage (J-V) hysteresis problem was widely observed in PSC, ion migration drew attention as an intensive theory to explain this phenomenon. Examples of ion migration were observed from mesoporous structures in 2013 (Unger *et al.* [2]) and planar structures in 2014 (Xiao *et al.* [3]).

For instance, in the $MAPbI_3$ perovskite, MA^+ ions, Pb^{2+} ions, I^- ions [4-6], and hydrogen impurities (H^+ and H^-) [7] are known as mobile ions. Considering the two critical factors for ion migration (activation energy of ion migration and the distance with its nearest neighbor), it is a reasonable expectation that MA^+ ions and I^- ions are mobile and Pb^{2+} ions are difficult to move in the $MAPbI_3$ thin film [4,8-10]. In literature, iodide ions were electrically identified as only mobile ions in $MAPbI_3$ material [11]. Indeed, related perovskites such as $CsPbCl_3$, $CsPbBr_3$, $MAGeCl_3$, or $MASnCl_3$ are known as halide ion conductors [1,12,13]. Furthermore, organic cations' (MA^+) migration is not experimentally observed under the bias [14,15]. The dynamics of MA^+ cations were observed as they disappeared from the perovskite film through ageing [16,17]. The halide ions are, therefore, the major mobile ions in the perovskite film.

This chapter deals with the migration of halide ions and the consideration of the main migration pathways. This chapter discovers the phenomenon of ion accumulation caused by ion migration through Impedance Spectroscopy (IS). In addition, Glow Discharge Optical Emission Spectrometry (GD-OES) directly shows the ion migration of halogen components (I^- and Br^-) of triple cation perovskite depending on material condition.

4.2. Triple cation PSC device reproducibility

In Chapter 3, the inverted planar device architecture of the triple cation (3CP) PSC (ITO = anode, Ag = cathode) was introduced (Fig.3.3). A series of eight samples' photovoltaic performance is summarised in table 4.1. The photovoltaic (J-V) performances are measured from negative bias (-0.1 V) to positive bias (+1.0 V) with scanning the voltage at 0.1 V/s rate without post-treatment processes such as bias pre-applying or light soaking.

Reproducibility is a prerequisite to have credibility with comparative assays that require one sample per one condition. Table 4.1 shows the excellent reproducibility of the device, so it can be considered that all samples used in this study have the same characteristics. As shown in Table 4.1, the power conversion efficiency (PCE) under 1 sun calibrated illumination is 11.7 % for the best device (average: 11.45 % in the same batch) with an electrode area of 0.28 cm^2. Calado *et al*. [18] and Heo *et al*. [19] demonstrated that the PEDOT:PSS/$MAPbI_3$/PCBM based p-i-n structure has negligible hysteresis while the mesoporous TiO_2 based n-i-p architecture has significant hysteresis. The 3CP implanted in the p-i-n devices (Table 4.1) is consistent with the literature results, although the perovskite material is different. For the 3CP-PSC used in all experiments, reproducible batches of devices within 0.4% of efficiency fluctuation were used.

Sample (#)	J_{sc} (mA/cm^2)	V_{oc} (V)	FF (%)	PCE (%)
1	22.3	0.85	59.3	11.24
2	23.1	0.84	60.3	11.69
3	22.8	0.85	58.9	11.42
4	21.9	0.86	60.9	11.47
5	22.4	0.84	60.3	11.35
6	22.3	0.85	60.3	11.43
7	21.9	0.86	60.8	11.45
8	22.5	0.85	60.3	11.53
Average	22.4	0.85	60.1	11.45

Table 4. 1. The photovoltaic performance parameters of the 3CP-PSCs fabricated from one batch.

4.3. Ion migration study under applied bias

Although we made a dense crystalline layer, there are mobile ions in the film [20]. Generally, this material allows movement along with a series of vacancies or grain boundaries in the perovskite film when inherent activation energy is applied. Common mobile ions in $MAPbI_3$ are MA^+, I^-, and Pb_2^+. Activation energy for each ion is respectively 0.84 eV, 0.55 eV and 2.31 eV at room temperature (300 K) [4]. C, H, and N atoms of the MA^+ cation are difficult to trace because they overlap with other organic layers (PEDOT:PSS, PCBM).

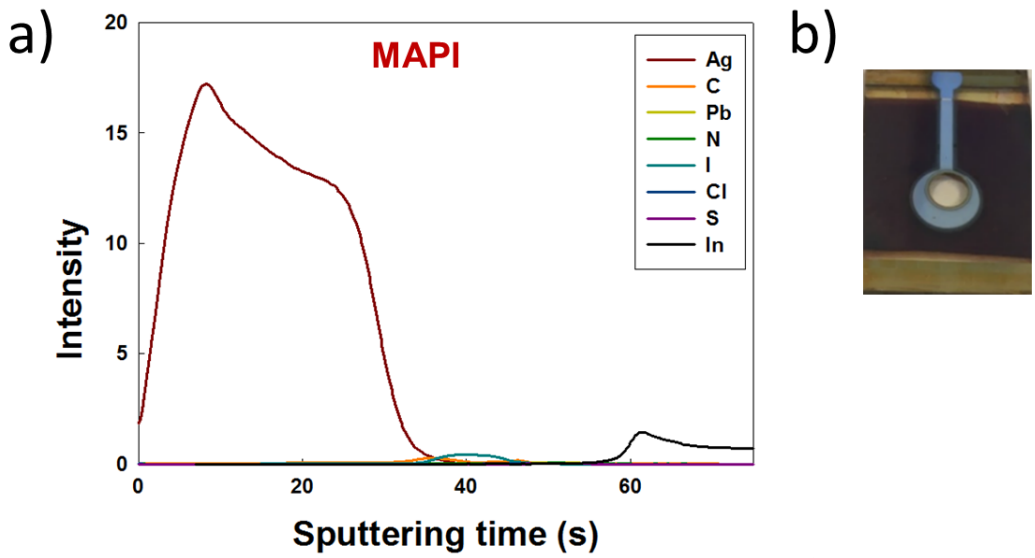

Figure 4.1. GD-OES raw profile lines intensity versus sputtering time before intensity modification. a) profile of $MAPbI_3$ (MAPI) material, b) appearance of a sample after GD-OES analysis.

According to a previous study [14], iodide ion was demonstrated as suitable for tracing ion migration. GD-OES presented in Chapter 2.3 is used to trace ion migration. Since this tool uses dry-etching with plasma, GD-OES detects the top electrode at first. Figure 4.1 is the raw GD-OES result. The silver top electrode is detected earliest in ITO/PEDOT:PSS/MAPI/PCBM/Ag architecture. When positive bias (+ DC voltage) is applied to the device, the polarization of the negative charge occurs at the silver electrode because the cathode of the device is silver. The negative iodine ions are attracted towards ITO. Then they are detected at a later sputtering time than in non-biased case (iodine profile move to the right) in the GD-OES profile. “30 s” on the sputtering time axis is when the silver (120 nm) is etched, and C, H, atoms of the PCBM are detected. Furthermore, “60 s” is the moment when the indium (In) of ITO is detected. The details of equipment setup for using GD-OES are introduced in Appendix.

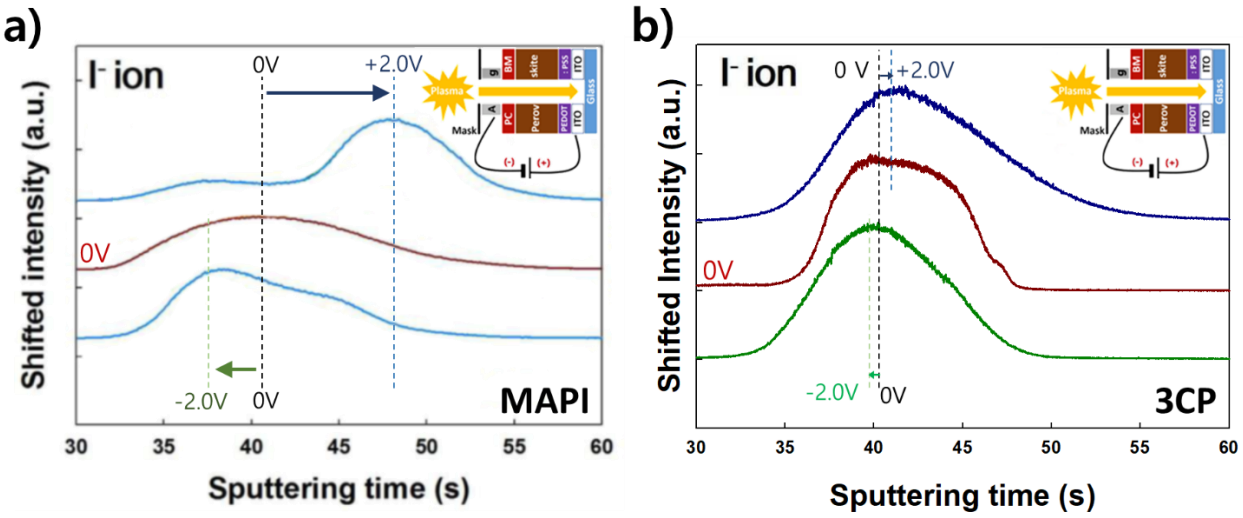

Figure 4.2. GD-OES profile lines versus sputtering time for iodide ions. a) profile of $MAPbI_3$ (MAPI) material [14], b) profile of 3CP{$(MA_{0.17}FA_{0.83})_{0.95}Cs_{0.05}Pb(I_{0.83}Br_{0.17})_3$}.

Figure 4.2a. [14], when ±2.0 V is applied, a bump (remarked with dashed line) in which the profile line moves along the electric field and another bump in a fixed position is observed.

For the ion migration of 3CP, the PSCs introduced in Table 4.1 are used for GD-OES measurements. 3CP-PSC shows no significant ion migration under bias in neither +2.0 V nor -2.0 V. After applying +2 V and -2 V, and the result of the 3CP device differed from the referenced result (Fig. 4.2b). The fact that ion migration occurs negligibly under the same conditions means that 3CP's ion migrating characteristics are not observable compared to MAPI. Also, from the perspective that mobile ions contribute to electrical conductivity at room temperature [15], the idea that 3CP is electrically stable compared to MAPI can be obtained. Since we are studying the 3CP polycrystalline film (~280 nm grain size), we cannot conclude that "3CP has no ion migration". This interpretation negates studies that found ion migration through lattice vacancies and grain boundaries in perovskite thin films. 3CP layer, of course, has grain boundaries and vacancies. The grain size of 3CP observed through SEM (Fig. 4.3) is smaller than that of MAPI. It is thus 3CP film has more grain boundaries than MAPI in the same area.

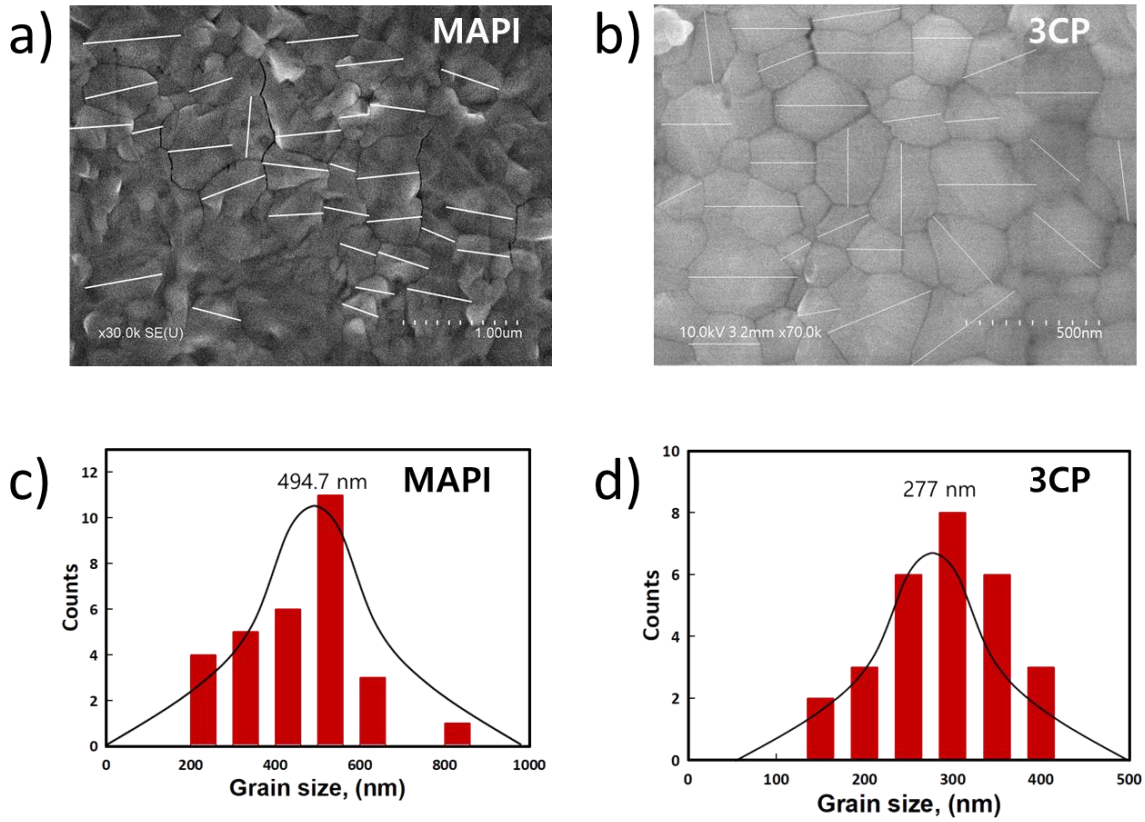

Figure 4.3. SEM images of a) MAPI, b) 3CP. d) and e) are the histograms corresponding to a) and b).

4.3.1. Ion Migration Recovery Delay (IMRD)

A previous study observed that the ions return to their original positions after 4 minutes when the bias migrating ions toward one side is stopped in the ITO/PEDOT:PSS/MAPI/PCBM/Ag structured device [15]. Although 3CP has many possible ion migration pathways, ion migration is not observed due to specific characteristics of the 3CP. The particular characteristic seems to be related to the recovery of ion migration. According to the article [15], if the time required for an ion to return to its original position is defined as IMRD (Ion Migration Recovery Delay), the IMRD of MAPI is 4 minutes.

To obtain the GD-OES profiles in Figure 4.2b, the process arranged in chronological order is presented in Figure 4.4. Since the delay time from DC polarization stop to iodine detection (during the GD-OES measurement) exists, the “wasted time” without the polarization is 90 s at this experiment. The IMRD of 3CP is, therefore, estimated to be less than 90 s. To demonstrate the correct IMRD of 3CP, an experiment with reduced “wasted time” was necessary.

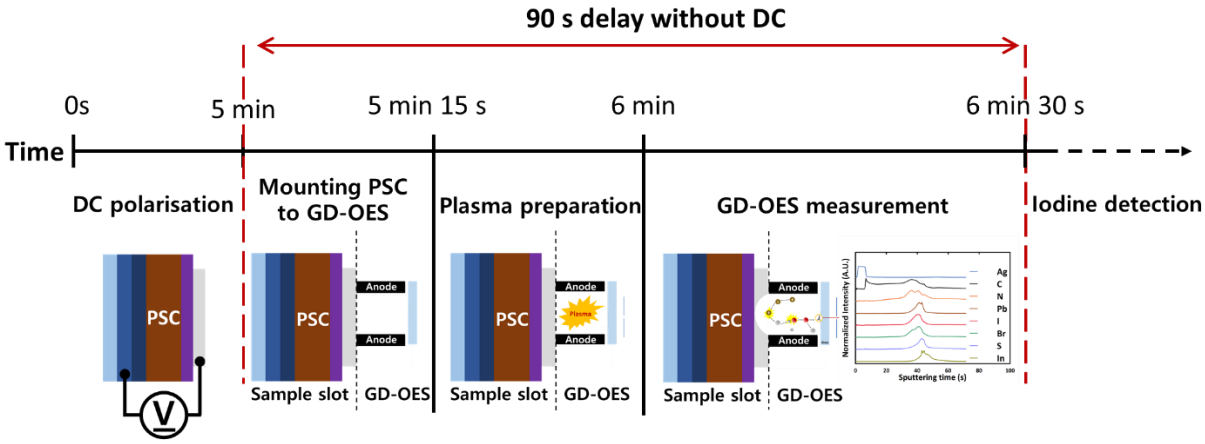

Figure 4.4. Schematic diagram of experimental conditions describing the time delay from stopping DC polarization to iodine detection with GD-OES.

4.3.2. "Wasted time" reduction and mobile ions of 3CP

Plasma preparation of GD-OES has three steps: flushing, vacuum pumping, and plasma forming. Flushing is the step of removing the remnants of previous measurements inside the anode cylinder. This step can be omitted if sufficient flushing is performed before each measurement. By skipping the flushing step, the "wasted time" can be shortened to 60 seconds. The results with and without flushing were the same.

From the 3CP layer $\{(MA_{0.17}FA_{0.83})_{0.95}Cs_{0.05}Pb(I_{0.83}Br_{0.17})_3\}$, the C, H, N (of MA^+ and FA^+ organic cation), Cs, Pb, I, and Br atomic profiles are obtained with GD-OES. The enlisted atoms for study are halide ions (I and Br) and atoms (Pb and N) existing only in the 3CP layer. C and H are also existing in the organic charge transporting layers. Since Cs detection is possible using neon plasma gas, it was excluded from the observation list. The results with the enlisted atoms (I, Br, Pb, and N) are observed with and without DC bias polarization. Figure 4.5 shows GD-OES results through the reduced "wasted time". The red profile lines are obtained from the sample without applying bias. The blue profile lines are measured by applying -2 V dc for 4 minutes before the sample mounting to the anode cylinder.

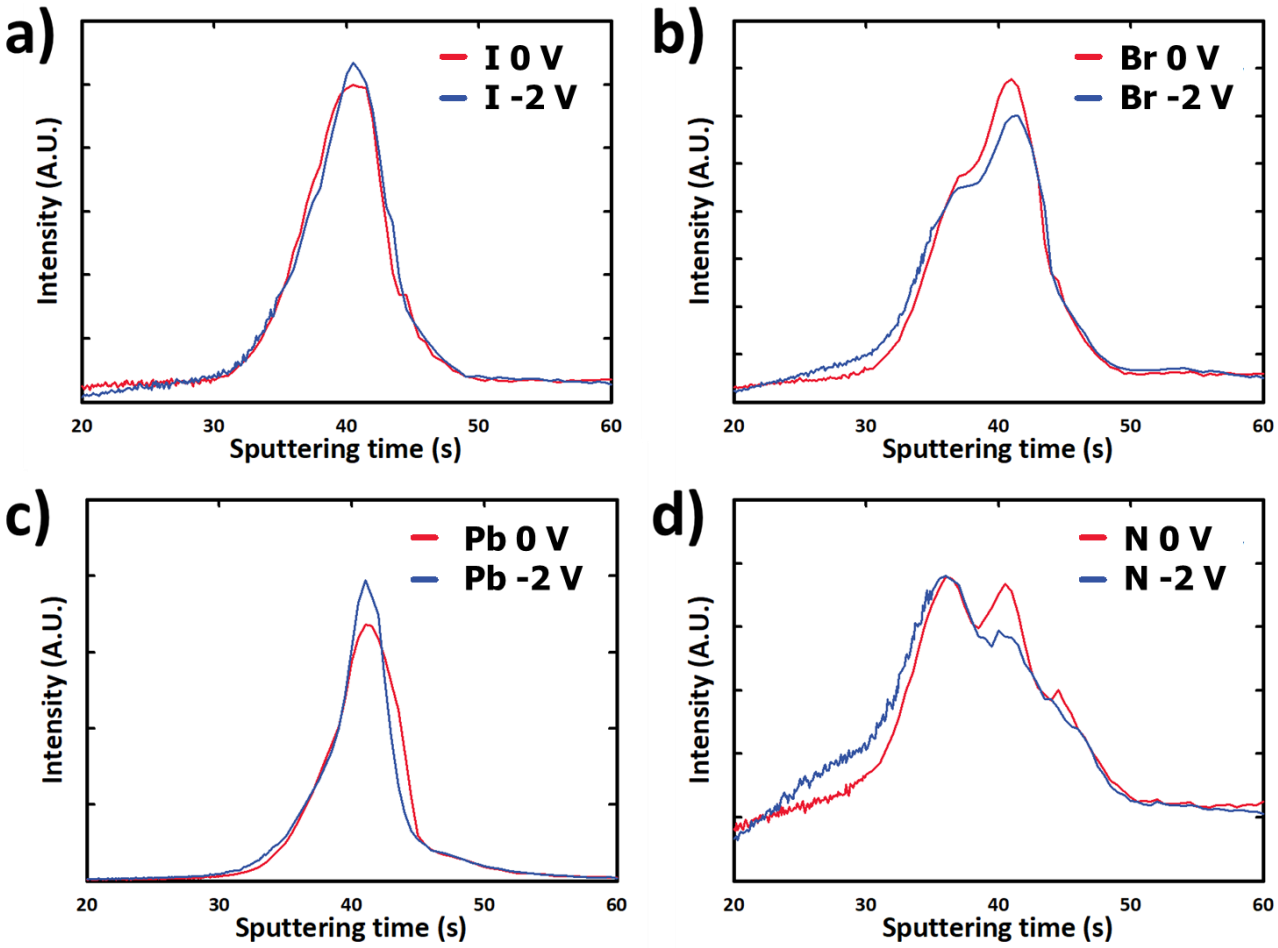

Figure 4.5. GD-OES profile lines versus sputtering time for 3CP-PSC. a) iodine, b) bromine, c) lead, and d) nitrogen.

The ion profiles for the four atoms (I, Br, Pb, and N) are comparable with and without applied bias showing any ion migration. This result is different from what was obtained with MAPI-PSC (Fig. 4.2a). The results suggest that the IMRD is shorter than 60 s and not sufficient to infer ion recovery. In order to further reduce Wasted Time, we designed an "in-situ" polarization method, as shown in Fig. 4.6. Inside the sample slot, a circuit connecting a small battery and 3CP-PSC applies dc bias until the start of the measurement. The voltage application time was prepared so that the bias was applied for 4 minutes until the moment when the iodine was detected ($\pm$2.0 V for 4 minutes). The in-situ method spends Wasted Time almost zero second.

Applying dc to the PSC located between the cathode and anode cylinders of GD-OES can affect the acceleration of Ar^+ ions (sputtering gas) toward the sample. Also, due to the possibility of damaging the GD-OES system, the demo equipment from Horiba Scientific was used for the in-situ measurement with

equipment experts. Although this instrument cannot detect Br atoms, the iodine profile only was measured.

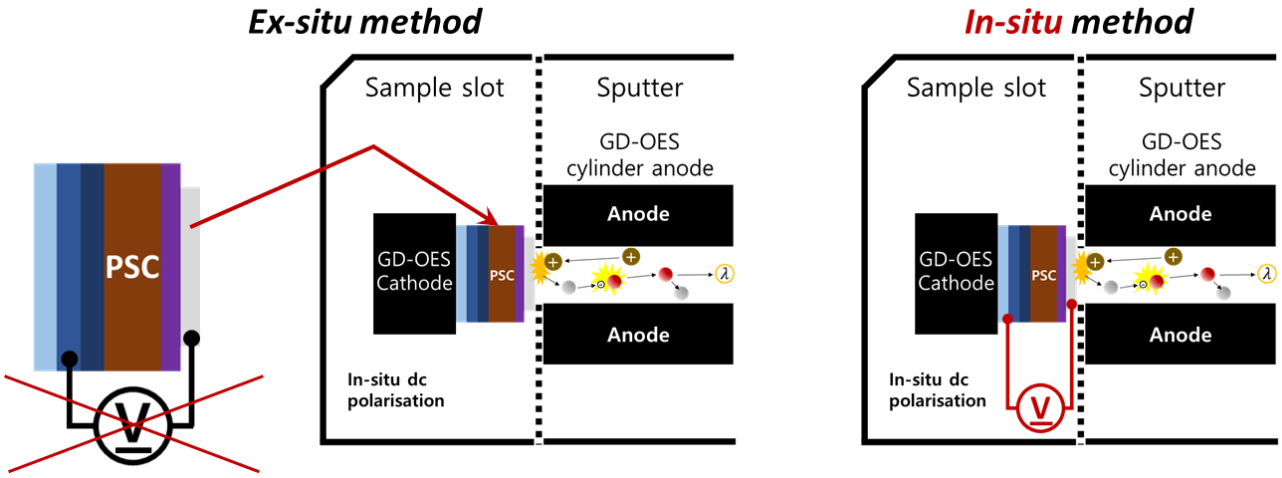

Figure 4.6. Schematics presenting the difference of ex-situ and in-situ DC polarization method for GD-OES.

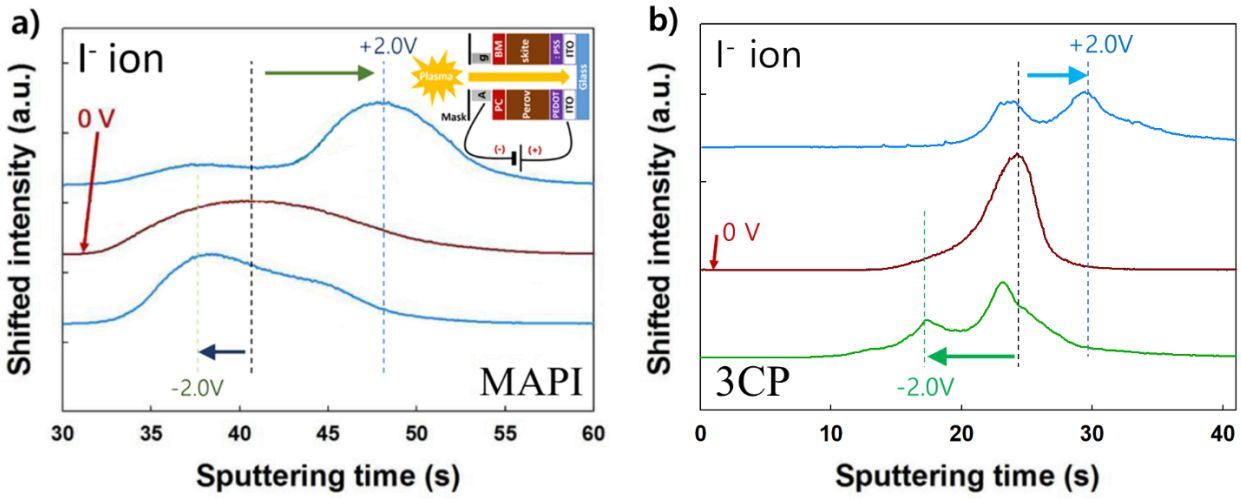

Figure 4.7. GD-OES profile lines versus sputtering time for iodide ions. a) profile of MAPI material [14], b) profile of 3CP with in-situ polarization method.

The in-situ result showed iodide ion migration with fixed ions and migrated ions. This experiment can be the basis for the fact that 3CP has mobile ions and that the recovery rate of ion migration is faster than that of MAPI. In the GD-OES profile, the percentage of ions migrated along the dc polarization is inferred by calculating the ratio of the peak area showing ion migration from the peak without applying bias (Fig. 4.7b. "0 V"). The mobile iodide ion ratio is derived 60% at +2.0 V and 30% at -2.0 V from the 3CP result (Fig. 4.7b). However, this mobile ion ratio is debatable because the sputtering speed is not constant under the same plasma conditions while applying the in-situ method. In the in-situ method, sputtering occurs

faster than the condition in which no voltage (including ex-situ biasing) is applied in the sample slot. It occurs regardless of the dc polarization direction. If the GD-OES measurement time is defined from measurement start (0 s) to the end where the detection of sulfur (S), a component of PEDOT:PSS, is finished, the measurement time is 27 s, 38 s, and 24 s, for in-situ +2.0 V, 0 V, and in-situ -2.0 V, respectively (Fig.4.8).

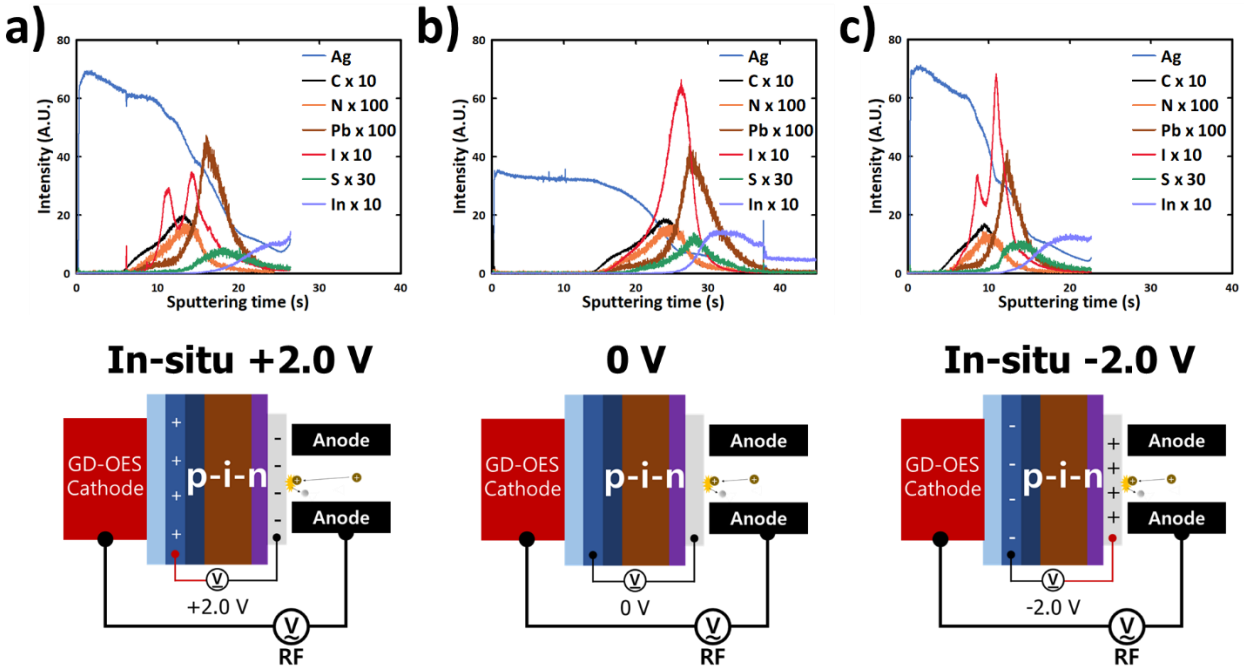

Figure 4.8. GD-OES profile lines versus sputtering time for atoms contained in 3CP layer for different polarization conditions. a) profile lines of in-situ +2.0 V, b) profile lines of 0V, and c) profile lines of in-situ -2.0 V.

As shown in the schematic diagram of Figure 4.8, the device that is applied dc in the in-situ method setting is situated between the RF electrodes of the GD-OES. In this situation, the dc bias can affect the phase of RF-AC for plasma formation. As a result, plasma conditions different from ex-situ were formed, and sputtering occurred rapidly. As far as we can see in Fig. 4.8a, and b profile lines (e.g., the carbon (C) and lead (Pb)) were acquired similarly even though the sputtering rates were different, but in the case of Fig. 4.8c, the profile lines are obtained as different form comparing to Fig. 4.8a and b.

In the in-situ method, deriving the ratio of mobile ions to fixed ions, therefore, is not a meaningful result. The in-situ method is an experiment that supports the ion migration possibility and the rapid recovery of ion migration of 3CP-PSC. In addition, if the in-situ method is attempted with equipment capable of detecting bromine, the possibility of the bromide ion migration can be confirmed.

4.3.3. Conclusion

We used SEM to confirm that the 3CP thin film has grain boundaries, which are pathways where ions migrate. The in-situ experiment was the experiment that supports the ion migration possible. Moreover, the comparison between in-situ and ex-situ dc polarised GD-OES proved that 3CP has the rapid recovery of ion migration in 3CP-PSC. Therefore, 3CP observed using GD-OES demonstrated iodide migration under the dc bias, but migration recovery is faster (recovery time is less than 1 min) than MAPI. In addition, it was not able to confirm the same effect in bromide because in-situ GD-OES cannot detect the Br atoms (with the system provided by Horiba Scientific Demo Lab: GD-DL).

4.4. Halide ion migration and its role at the interfaces in perovskite solar cells

The purpose of the study is to contribute to the understanding of the origin of the current density-voltage hysteresis observed since the early days of the perovskite solar cell [21-23]. The hysteresis, which can be described as short-term instability and which has a significant impact on the measurement of stabilized power conversion efficiencies in PSCs [24-26], consists in the discrepancy of the solar cell performance (or difference in the shape of the current-voltage curve) between backward scan (from open-circuit voltage to short circuit) and forward scan (from short circuit to open-circuit voltage). This discrepancy depends on the bias sweep rate: typically, the hysteresis effect has been observed during the time range of some seconds [21,22,27-30]. One type of reversible hysteresis has also been shown over day/night cycling [31]. Two main mechanisms have been suggested to explain this phenomenon: (a) a slow ferroelectric polarization of the material [32-34]; (b) migration of ions inside the material [29,30]. The ferroelectric hypothesis has been abandoned because a timescale of a ferroelectric domain relaxation within a typical device has been estimated below 1 ms [35], so much faster than the time scale for the hysteresis effect.

At this point, it should be mentioned that ionic conduction in the perovskite-type halides $CsPbCl_3$ and $CsPbBr_3$ was considered since the eighties [36] to be caused by the migration of halide-ion vacancies with activation energy in the range 0.25 – 0.39 eV. Since the activation energy range has been extended to 0.1 – 0.58 eV by many groups working on various lead halide perovskites [11,33,37-41] and has been validated by first-principles molecular dynamics simulations [4,28, 42,43]. This led to the consensus that

hybrid perovskites are mixed conductors (electronic + ionic) with possible interplays between both types of carriers.

To understand the origin of the hysteresis effects, we have taken profit from the different time scales associated with electrons (few ps) and ions (few s) to measure specifically the slow dynamic processes attached to the ion migration. Thus, we have chosen three independent experiments: conductivity versus temperature under dark conditions in the range 250 K to 363 K corresponding essentially to the tetragonal phase of the perovskite; glow-discharge optical emission spectroscopy (GD-OES) under electrical bias and dark conditions at room temperature and finally impedance spectroscopy. With the first two experiments presented in previous papers [14,15], we have confirmed that hybrid perovskites are mixed conductors. In the present work, with the help of complex impedance spectroscopy (IS), which is a time transient measurement based on measuring the impedance as a function of frequency for solar cells with different interface layers, we can address not only the nature of charge distribution in the device but also the kinetics of the charging processes, and how they alter the solar cell photocurrent. The groups of Park and Bisquert have been the first to understand the origin of hysteresis through IS studies [30, 44-48]. These studies allow the evaluation of relaxation time of charge carriers in the frequency domain, which is thus helpful in quantifying the mobile ions within the perovskite at a given temperature and so to lead to an in-depth understanding of the working mechanisms of the PSCs.

Moreover, we chose to work not exclusively with the $MAPbI_3$ (MAPI) perovskite but also with cationic mixing composition like Cs/MA/FA (so-called triple cation perovskite, 3CP, where MA stands for methylammonium and FA for formamidinium), for which a significant reduction of the degradation rate has been observed [49-51]. So, in the present work, we show that the hysteresis is a consequence of the ion migration at the interfaces with the extraction layers: once the iodide ions have reached the interfaces, their accumulation at these interfaces creates very high built-in fields. There is the formation of Debye double layers.

4.4.1. Device structure for the experiment

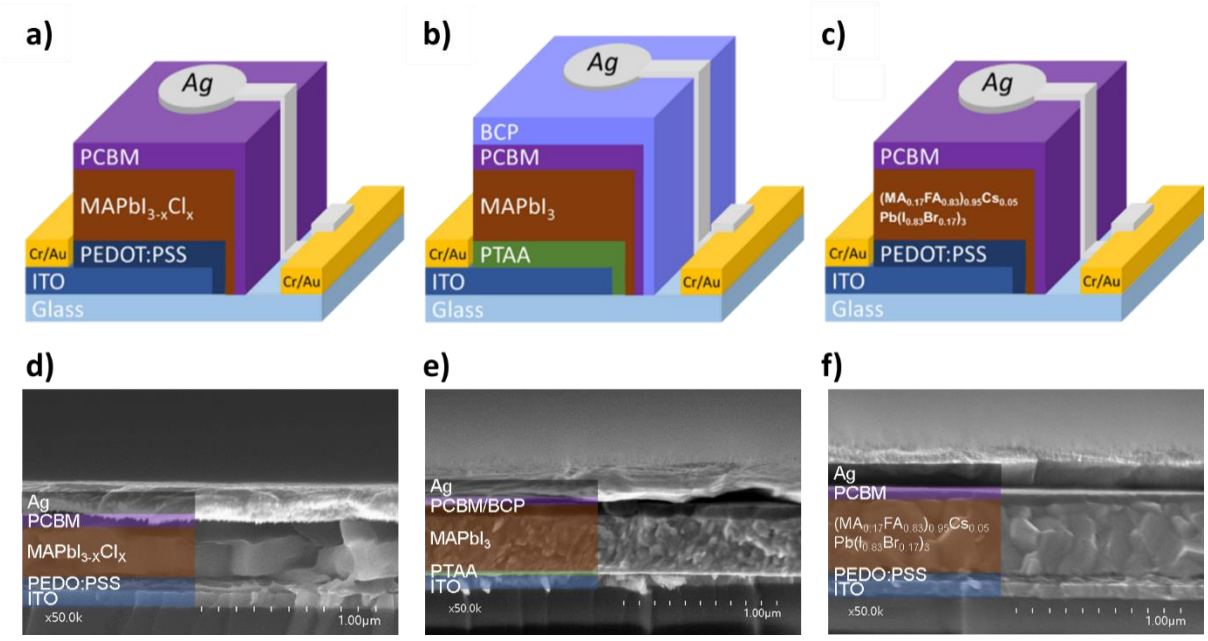

Figure 4.9. Schematics of solar cell p-i-n structures: a) MAPIw (w means wet) b) MAPId (d means dry) c) 3CPw, d), e), and c) correspond to cross-section SEM images of the structures a), b), and c), respectively.

Sample name	Perovskite absorber	Perovskite deposition process	HTL	ETL
MAPIw	$MAPbI_{3-x}Cl_x$	Spin-coating	PEDOT:PSS	PCBM
MAPId	$MAPbI_3$	Vacuum evaporation	PTAA	PCBM/BCP
3CPw	$(MA_{0.17}FA_{0.83})_{0.95}Cs_{0.05}$ $Pb(I_{0.83}Br_{0.17})_3$	Spin-coating	PEDOT:PSS	PCBM

Table 4.2: Different types of PSCs used in this study.

The solar cells used in this study are shown in Figure 4.9 a, b, and c, and each Figure 4.9 d, e, and f present the cross-section scanning electron microscopy (SEM) images of Figure 4.9 a, b, and c. They consist of an inverted p-i-n device planar structure where the halide perovskite material is placed between a hole transport layer (HTL) and an electron transport layer (ETL). The thicknesses of $MAPbI_{3-X}Cl_X$, $MAPbI_3$, and $(MA_{0.17}FA_{0.83})_{0.95}Cs_{0.05}Pb(I_{0.83}Br_{0.17})_3$ are 280 nm, 400nm, and 450 nm, respectively.

4.4.2. J-V characteristics

Current density – voltage (J-V) curves are recorded following chapter 2, section 2.5.1.1. Figure 4.10 a, b, and c show J-V curves under the illumination of MAPIw, MAPId, and 3CP, respectively. Each power conversion efficiency (PCE) of MAPIw, MAPId, and 3CP is 11.9 %, 13.4 %, and 12.8 %. In MAPIw and 3CP, hysteresis is negligible. However, PCE of MAPId in the forward scan direction is higher than those in the reverse scan direction, indicating that hysteresis phenomena appear. (Figure 4.10).

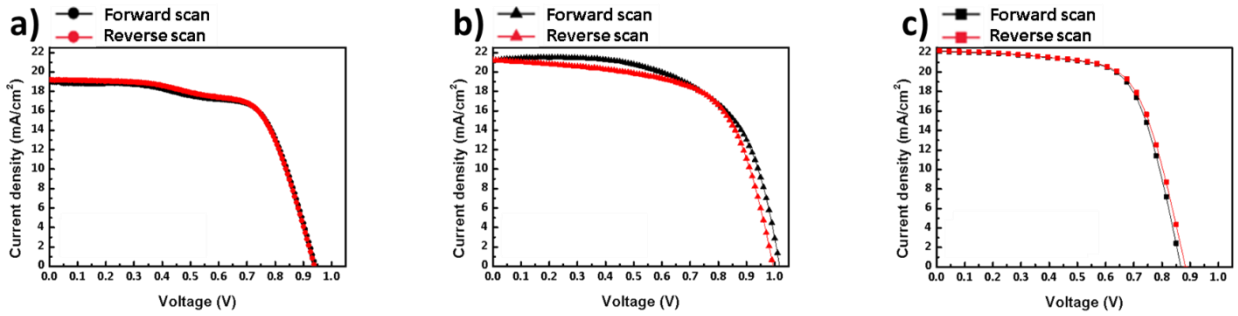

Figure 4.10. J-V curves of perovskite solar cells with p-i-n structures: (a) MAPIw, (b) MAPId and (c) 3CP measured under AM 1.5 illumination (100 mW/cm^2). Each color of black and red indicates J-V curves under forward and reverse scan.

4.4.3. Influence of electric field

From our previous papers [14,15], we have observed using J-V measurements under dark conditions versus temperature (in the range 213 – 363 K), a hysteresis of current (reverse scan versus forward scan) in $MAPbI_3$. This hysteresis increases with temperature. The observation at long time scales under dark conditions of time-dependent current responses under a fixed applied bias is common to both hybrid and all-inorganic lead halide perovskite compounds, these transient responses increasing with temperature [11,40, 45-48, 52, 53]. Without any bias, whatever the temperature, the current is constant, which means compelling evidence that these strong polarization phenomena are connected to ion conduction. More precisely, from GD-OES profiles under bias and conductivity measurements, we could show that ionic conductivity is due to iodine anion migration, whereas no MA^+ neither Pb^{2+} migration could be observed [14,15]. Concerning this last assertion, mobile MA^+ and Pb^{2+} vacancies have been ruled out because of high activation energies (0.84 eV and 2.31 eV, respectively), leading to inefficient diffusion coefficients [4]. These results confirm the existence of a high concentration of charged point defects (vacancies), as mentioned in several experimental and theoretical papers [11,36,39-40]. Observing migration of iodide ions in a range of 120 nm after some seconds, the iodide mobility at 300 K could be estimated at 8 x 10^{-}

^{11} $cm^2/V{\cdot}s$ and iodide diffusion coefficient at 2 $x10^{-12}$ cm^2/s [15]. We should note that a compelling proof of iodine vacancies and not iodine interstitials to be at the origin of ionic conductivity has been given by Senocrate et al. [40]: ionic conductivity decreases when iodine's partial pressure increases. This proof contradicts the theoretical results based on first-principal calculations [54,55]. From the temperature-dependent electrical conductivity, we found 0.25 eV as the activation energy for migration of iodine vacancies [15], the value comparable with those deduced from DFT molecular dynamics simulations of 0.1 - 0.58 eV [4,28, 42,43]. A simple argument about the migration paths of the I^-, $Pb^{2+,}$ and MA^+ ions are to say that a very small distortion of the PbI_6 octahedra in the crystal structure accompanies halide ion (vacancy [40]) migration along with their equatorial and apical sites in octahedron [55], while migration of MA^+ and Pb^{2+} requires a significant distortion of the structure. So, the time scale for migration of the MA^+ and Pb^{2+} ions is considerably larger than I^- ions [28]. The value of ionic conductivity 10^{-7} $ohm^{-1}{\cdot}cm^{-1}$ reported for $MAPbI_3$ at room temperature [15] confirms that such a hybrid perovskite may be classified as a good ionic conductor comparable to alkali halide crystals [36]. At this point, it should be noted that if in a mixed conductor the migration of halides is a necessary condition for the observation of hysteresis, it is not a sufficient condition. Under the influence of an external biasing field or solar illumination, the migration of ionic vacancies in the PSCs may result in a charge accumulation at the contacts. Because perovskites cannot be easily doped, unlike conventional semiconductors, the interfaces between the absorber (perovskite) and the contacting transport layers (HTL and ETL), which are effective heterojunctions, must play the central role in the solar cell operation: they are at the origin of built-in effective fields breaking symmetry for free electrons and holes. Thus, many groups have made major contributions to understanding contact interfaces based on various transient electrical measurements like IS [45-48, 52-61]. In that context, the characteristic time scale for ion migration, whatever the halide (about ten seconds), is always higher than the voltage settling time (waiting period to measure without distortion current after applying a given voltage). The voltage settling time is typically about 0.5 s [48].

The IS results are reported in Figure 4.11 for the different devices before and after applying a bias by using J-V measurement (MAPIw and MAPId) or by shorting the device (3CPw) under the dark. 2 min for J-V measurements was used as stimulation for MAPI based solar cells (MAPIw and MAPId) and 1day for device shorting is applied as stimulation for 3CP solar cell.

Connecting the device contacts creates an internal electric field (built-in field) due to the difference in the Fermi levels of HTL and ETL [62,63]. It appears clearly that the impedance follows the same trends

independently of the device structure (different HTL/ETL), absorber material (MAPI or 3CPw), or deposition process. Before the applied electric field, the complex impedance (|Z|) follows a straight line at high frequency (above ~ 10^3 Hz) with a slope -1 (in log/log scale) characteristic of a pure capacitive behavior. However, at lower frequencies, |Z| becomes independent of the frequency and reaches a plateau corresponding to a pure resistance. Accordingly, the phase Bode plots show logically a phase angle closed to -90 degrees at high frequency and then drop to zero at a lower frequency. If the devices have been previously polarized, the impedance versus frequency behavior is dramatically changed with the reduction of the resistive plateau and the birth of a second capacitive behavior at low frequency. The dominant capacitive behavior is observed by extension to the lower frequency of the phase at -90 degrees. The different parameters of the equivalent circuit are reported in Table 4.4 by fitting the experimental data (see Appendix 4.1 for fitting procedure).

The capacitance C_2 deduced at high frequency is always present in the devices and corresponds to the geometrical capacitance (C_g) of the planar solar cells. From this value, it is possible to deduce the relative dielectric constant (ε_r) of the material. By considering the thicknesses of the fully depleted perovskite layers (Figure 4.9 d, e, and f), ε_r is 17, 17, and 19 for MAPIw, MAPId, and 3CPw, respectively. This value is comparable with those reported by other groups [32, 40, 57, 59, 64] and fits quite well with the recommended value proposed by J. N. Wilson et al. [65]. After having biased, we observe a second capacitance C_3 at low frequency (0.1 - 10 Hz), which we interpret after relaxation of ions as charge accumulation layers at both interfaces. This charge accumulation can be promoted by the presence of the grain boundaries (Fig.4.13). The capacitance in low frequency can be considered as electrode polarization caused by interfacial phenomena, i.e., by ionic charge accumulation at the interfaces of $MAPbI_3$ [23,29,57, 66]. As reported earlier, it takes some seconds for the halide ions or halide ion vacancies to migrate toward the interfaces and then to accumulate, whatever the bias (forward or reverse). The stored charge density can be very high, inducing a large capacitance [23,45]. However, these charges are immediately screened by mobile charges (ions, electrons, holes), so the charge accumulation layers transform into double layers with the Debye screening length, such as seen in electrolytes [23,59, 62]. This means that we can treat the perovskite layer as an ionic solution filling the space between PEDOT:PSS or PTAA and PCBM of a parallel plate capacitor having a potential difference V like in electrolytes. Due to the small value of Debye length (about 1 nm) at each interface, we then consider uniformly charge planes of high surface density that create high built-in fields and control entirely the current densities of electrons and holes (Fig.4.12). In other words, the electric field inside the perovskite

layer itself is very small compared with the before mentioned built-in fields and plays no role in the transport properties of perovskite structures [62].

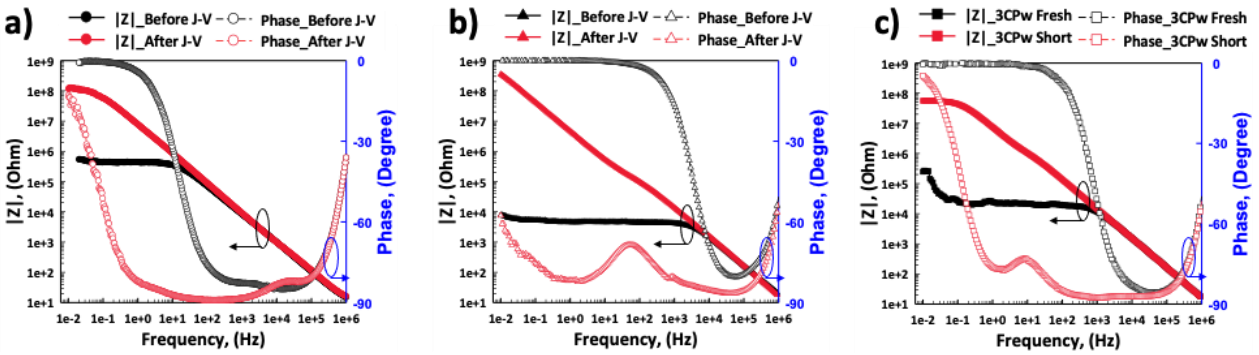

Figure 4.11. Bode plot of the different devices before and after applied electric field under dark conditions; a) MAPIw, b) MAPId, c) 3CPw (Short means shorting conditions.).

Sample name	R_1 (Ohm)	R_2 (Ohm)	C_2 (nF)	R_3 (Ohm)	C_3 (nF)
MAPIw	12.5	4.4×10^5	15.0	-	-
	13.5	$\sim 10^5$	15.0	1.2×10^8	5.0
MAPId	10.1	4.3×10^3	10.4	-	-
	10.1	2.0×10^4	10.4	3.4×10^8	23.8
3CPw	10.9	1.9×10^4	10.3	-	-
	10.3	$\sim 10^6$	10.4	$\sim 10^6$	9.1

Table 4.4. Characteristic parameters extracted by fitting equivalent circuits. For each device, the first line is before polarization and the second line is after polarization.

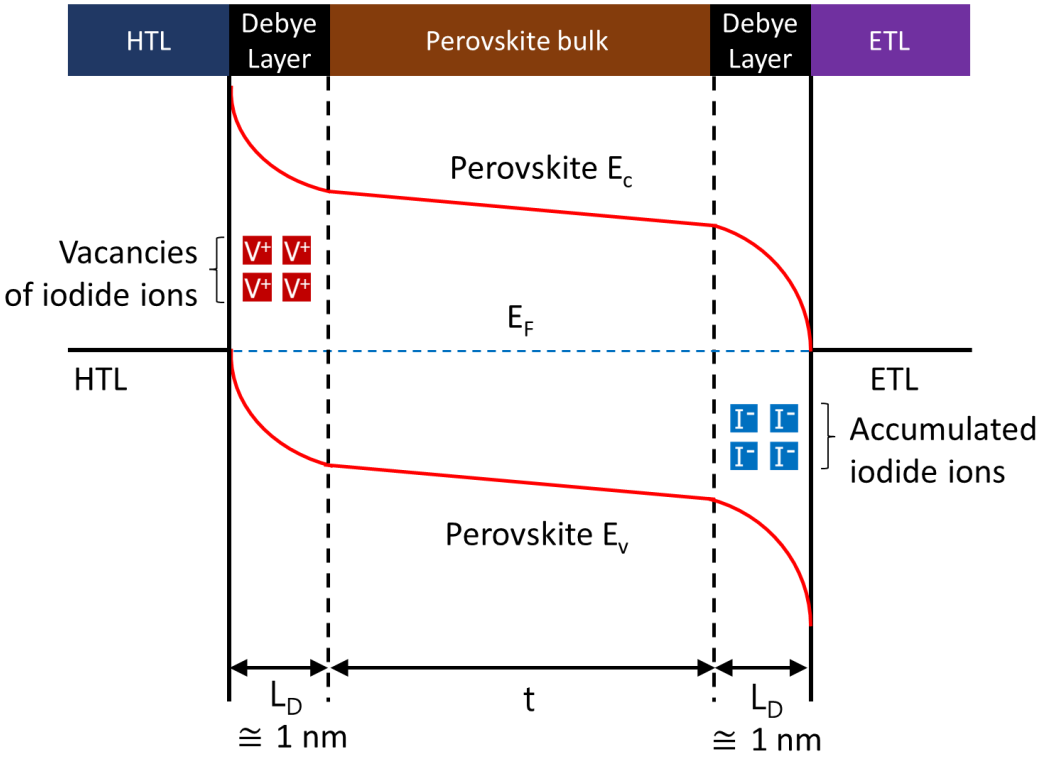

Figure 4.12. Schematic of band energy diagram in the perovskite after ion accumulation at the interfaces [29,62,67] where t is the thickness for the three perovskite materials (MAPIw: 280 nm, MAPId: 400 nm, and 3CPw: 450 nm), and LD is Debye layer thickness.

In previous work, we observed a voltage shift during the measurement of the J-V characteristics under dark conditions at room temperature only for backward scan and when the initial positive voltage exceeds 1.5 V [15]. This result never occurs for conventional semiconductors (Si, GaAs, CdTe). It indicates that carriers in the perovskite are not limited to electrons and holes for which, when the thermal equilibrium is reached, the drift current of carriers is exactly compensated by the diffusion current so that the net carrier flow is zero as in a conventional crystalline semiconductor. As we will confirm later, ions contribute to this voltage shift. Moreover, as the scanning rate is 125 mV/s, which is considered fast [26,27], it only takes a few seconds for the ions to pass through the perovskite layer. As previously noted, the fact that MA^+ cations are not mobile is coherent with a tracer exchange experiment showing the absence of significant MA^+ diffusion [39]. The hybrid perovskites are considered as soft materials [40], which includes from thermodynamically reasons the occurrence of a large concentration of point defects, generally Schottky defects [36].

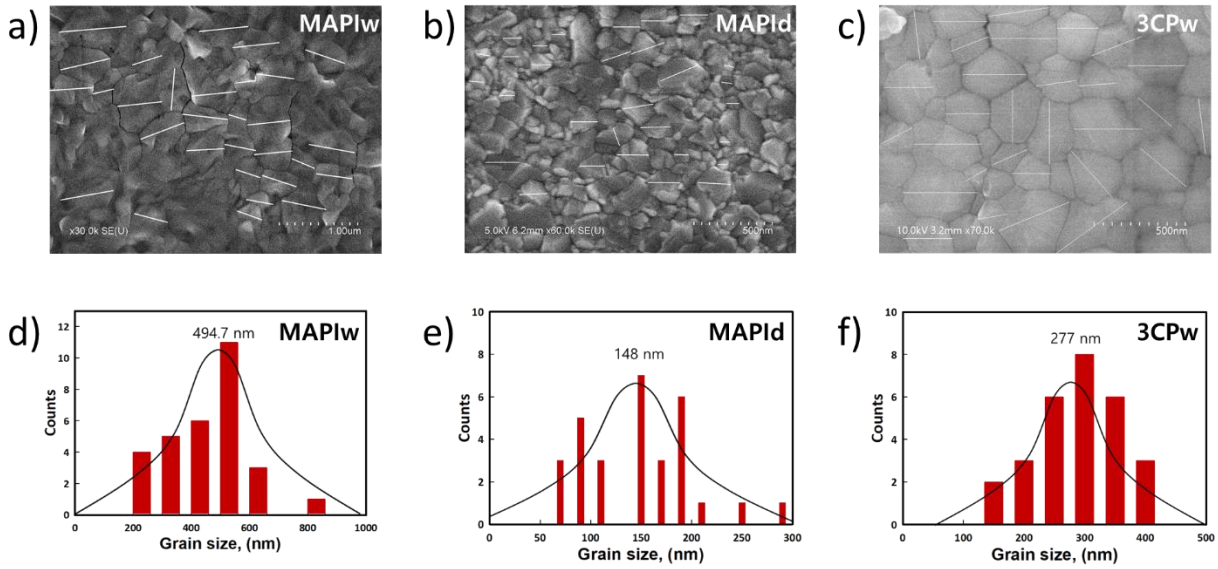

Figure 4.13. SEM images of a) MAPIw, b) MAPId, and c) 3CPw. d), e), and f) are the histograms corresponding to a), b), and c), respectively.

As shown in Fig. 4.13, the films are well crystalized with a distribution of grain size increasing for MAPId, 3CPw, and MAPIw, respectively. Grain sizes, as observed in Fig. 4.13 are known to be preferential ion migration pathways. The smaller is the grain size, and the higher is the density of grain boundaries, and higher is the possibility to ion to move and to accumulate at the interface with the transport layers. This is coherent with the values of C_3 measured by IS. Since the device electrode area is 0.28 cm^2, C_3 must be measured on the scale of µF, if ions are completely accumulated in the 0.28 cm2. Considering that the accumulated area of ions moving along the grain boundary is narrow compared to the electrode area, it is interpreted that C_3 is measured on the scale of nF. Consequently, the C_3 of the three different perovskite solar cells with different grain sizes correlated with the area occupied by grain boundary per unit surface. Table 4.4 shows that MAPId-PSC with the most grain boundaries in the same area has the largest C_3 value.

4.4.3.1 MAPId layer deposition

PTAA layer deposition. Before deposition of HTL, the surface of patterned ITO was treated by UV-ozone chamber for 10 mins. As hole transport layer, PTAA (30 nm) is deposited on UV-Ozone activated ITO layer through spin-coating at 5000 rpm in the air with thermal treatment at 100 °C in N2 for 10 minutes. The PTAA solution is prepared with a concentration of 0.002 g/ml in toluene and filtered through a 0.45 µm PTFE filter. PTAA was purchased from Ossila (M513, CAS: 1333317-99-9) and used as received.

MAPId layer deposition: MAPI was deposited on the PTAA layer by co-evaporation of PbI_2 and MAI with deposition rates of 1.0 Å/s and 2.5 Å/s, respectively. During the evaporation, the vacuum level was 1.6×10^{-6} mbar. The film was annealed at 70 °C for 10 minutes after deposition. PbI_2 was purchased from Sigma Aldrich; MAI from Greatcell Solar Materials.

BCP layer deposition. BCP was used as a hole blocking layer (HBL) in MAPId devices. After drying PCBM for 20 mins in N_2, the BCP layer (5 to 8 nm tick) was deposited onto PCBM by spin-coating at 4000 rpm. The 0.0005 g/ml of BCP was dissolved in chlorobenzene and 2-propanol and filtered through a 0.45 μm PTFE filter. BCP was purchased from Lumtec (> 99%, CAS: 4733-39-5) and used as received. All the chemicals were used as received without further purifications.

4.4.4. Conclusion

We have confirmed using GD-OES and conductivity experiments that MAPI is a mixed electronic/ionic conductor, with ion conductivity being essentially due to iodide migration mediated by vacancy defects. The observed activation energy of 0.25 eV agrees with the value deduced from density functional theory calculations [4]. The diffusion coefficient of iodide ions at room temperature is assessed as $2x10^{-12}$ cm^2/s. The relative dielectric constant of 21 found for the perovskite materials and deduced from geometrical capacitance at high frequency agrees with the literature.

.

4.5. Conclusion

In this chapter, the influence of the electric field on ion migration is studied. When a continuous electric field is applied to the PSCs, the GD-OES results directly showed halide ion migration. Under dc bias, we observed the shift of iodine ion migration in the 3CP $\{(MA_{0.17}FA_{0.83})_{0.95}Cs_{0.05}Pb(I_{0.83}Br_{0.17})_3\}$ layer. Comparison of in-situ and ex-situ dc-polarized GD-OES demonstrated that 3CP has a faster recovery of ion migration. The recovery time of 3CP is confirmed to be less than 1 minute. Furthermore, we cannot confirm the same effect in bromide because in-situ GD-OES cannot detect the Br atoms (with the GD-OES system provided by Horiba Scientific).

When dark-JV sweep (range: -0.5 V ↔ +1.0 V) for 2 minutes is applied to the PSC, interfacial ion accumulation was discovered. IS measured an additional capacitor that is coming from ion accumulation, forming a double layer at the interface. As a result of IS measurement, the relative dielectric constant of

21 found for the perovskite materials was deduced from geometrical capacitance at high frequency and in agreement with the literature [4]. The ion migration characteristic was revealed that ions migrate to the interface and accumulate only with a short-time dark-JV sweep.

The ion migration experimental results demonstrate that 3CP has faster ion migration recovery than MAPI. This is supported by two experimental conditions:

1) GD-OES: restoring ion migration as soon as the dc electric field is stopped
2) IS: 3CP's ion accumulation is observed by stimulating the ions for a more extended period to accumulate than MAPI. Only 3CP required a short circuit condition for one day.

4.6. References

[1] J. Mizusaki, K. Arai, K. Fueki. Ionic conduction of the perovskite-type halides. *Solid State Ion.* **1983**, *11*, 203–211.

[2] E. Unger, E. Hoke, C. Bailie, W. Nguyen, A. Bowring, T. Heumüller, M. Christoforo, M. McGehee, Hysteresis and transient behavior in current–voltage measurements of hybrid-perovskite absorber solar cells. *Energy Environ. Sci.* **2014**, *7*, 3690–3698.

[3] Z. Xiao, Y. Yuan, Y. Shao, Q. Wang, Q. Dong, C. Bi, P. Sharma, A. Gruverman, J. Huang, Giant switchable photovoltaic effect in organometal trihalide perovskite devices. *Nat. Mater.* **2015**, *14*, 193–198.

[4] C. Eames, J.M. Frost, P.R. Barnes, B.C. O'regan, A. Walsh, M.S. Islam, Ionic transport in hybrid lead iodide perovskite solar cells. *Nat. Commun.* **2015**, *6*, 7497.

[5] J. Haruyama, K. Sodeyama, L. Han, Y. Tateyama, First-principles study of ion diffusion in perovskite solar cell sensitizers. *J. Am. Chem. Soc*. **2015**, 137, 10048–10051.

[6] J. M. Azpiroz, E. Mosconi, J. Bisquert, F. De Angelis, Defects migration in methylammonium lead iodide and their role in perovskite solar cells operation. *Energy Environ. Sci.* **2015**, *8*, 2118–2127.

[7] D.A. Egger, L. Kronik, A.M. Rappe, Theory of hydrogen migration in organic–inorganic halide perovskites. *Angew. Chem. Int*. **2015**, Ed. *54*, 12437–12441.

[8] W.-J. Yin, T. Shi, Y. Yan, Unusual defect physics in $CH_3NH_3PbI_3$ perovskite solar cell absorber. *Appl. Phys. Lett.* **2014**, *104*, 063903.

[9] Y. Yuan, Q. Wang, Y. Shao, H. Lu, T. Li, A. Gruverman, J. Huang, Electric field driven reversible conversion between methylammonium lead triiodide perovskites and lead iodide at elevated temperature. *Adv. Energy Mater*. **2015**, *6*, 1501803.

[10] C. Li, S. Tscheuschner, F. Paulus, P.E. Hopkinson, J. Kießling, A. Köhler, Y. Vaynzof, S. Huettner, Iodine migration and its effect on hysteresis in perovskite solar cells. *Adv. Mater*. **2016**, *28*, 2446-2454.

[11] T. Y. Yang, G. Gregori, N. Pellet, M. Grätzel, J. Maier, The Significance of Ion Conduction in a Hybrid Organic-Inorganic Lead-Iodide-Based Perovskite Photosensitizer. *Angew. Chem. Int*. Ed. **2015**, *54*, 7905-7910.

[12] K. Yamada, K. Isobe, E. Tsuyama, T. Okuda, Y. Furukawa, Chloride ion conductor $CH_3NH_3GeCl_3$

studied by Rietveld analysis of X-ray diffraction and 35Cl NMR. *Solid State Ionics.* **1995**, *79*, 152 – 157.

[13] K. Yamada, Y. Kuranaga, K. Ueda, S. Goto, T. Okuda, Y. Furukawa, Phase Transition and Electric Conductivity of $ASnCl_3$ (A = Cs and CH_3NH_3). *Bull. Chem. Soc. Jpn*. **1998**, *71*, 127 – 127.

[14] H. Lee, S. Gaiaschi, P. Chapon, A. Marronnier, H. Lee, J-C. Vanel, D. Tondelier, J-E. Bouree, Y. Bonnassieux, B. Geffroy, Direct Experimental Evidence of Halide Ionic Migration under Bias in $CH_3NH_3PbI_{3-x}Cl_x$-Based Perovskite Solar Cells Using GD-OES Analysis. *ACS Energy Lett.* **2017**, *2*, 943–949.

[15] H. Lee, S. Gaiaschi, P. Chapon, D. Tondelier, J-E. Bouree, Y. Bonnassieux, V. Derycke, B. Geffroy, Effect of Halide Ion Migration on the Electrical Properties of Methylammonium Lead Tri-Iodide Perovskite Solar Cells. *J. Phys. Chem. C.* **2019**, *123*, 17728–17734.

[16] B. Conings, J. Drijkoningen, N. Gauquelin, A. Babayigit, J. D'Haen, L. D'Olieslaeger, A. Ethirajan, J. Verbeeck, J. Manca, E. Mosconi, F. De Angelis, H.-G. Boyen, Intrinsic Thermal Instability of Methylammonium Lead Trihalide Perovskite. *Adv. Energy Mater*. **2015**, *5*, 1500477.

[17] K. A. Bush, C. D. Bailie, Y. Chen, A. R. Bowring, W. Wang, W. Ma, T. Leijtens, F. Moghadam, and M. D. McGehee. Thermal and Environmental Stability of Semi-Transparent Perovskite Solar Cells for Tandems Enabled by a Solution-Processed Nanoparticle Buffer Layer and Sputtered ITO Electrode. **2016**, *Adv. Mater.*, **28**, 20, 3937-3943.

[18] P. Calado, A.M. Telford, D. Bryant, X. Li, J. Nelson, B.C. O'Regan, P.R.F. Barnes, Evidence for ion migration in hybrid perovskite solar cells with minimal hysteresis. *Nat. Commun*. **2016**, *7*, 13831.

[19] J. H. Heo, H. J. Han, D. Kim, T.K. Ahn, S. H. Im, Hysteresisless inverted $CH_3NH_3PbI_3$ planar perovskite hybrid solar cells with 18.1% conversion efficiency. *Energy Environ. Sci*. **2015**, *8*, 1602−1608.

[20] Y. Zhao, C. Liang, H. Zhang, D. Li, D. Tian, G. Li, X. Jing, W. Zhang, W. Xiao, Q. Liu, F. Zhang, Z. He, Anomalously large interface charge in polarity-switchable photovoltaic devices: An indication of mobile ions in organic-inorganic halide perovskites. *Energy Environ. Sci.* **2015**, *8*, 1256–1260.

[21] A. Dualeh, T. Moehl, N. Tétreault, J. Teuscher, P. Gao, M. K. Nazeeruddin, M. Grätzel, Impedance Spectroscopic Analysis of Lead Iodide Perovskite-Sensitized Solid-State Solar Cells. *ACS Nano*. **2014**, *8*, 362 -373.

[22] H. J. Snaith, A. Abate, J. M. Ball, G. E. Eperon, T. Leijtens, N. K. Noel, S. D. Stranks, J. T.-W. Wang, K. Wojciechowski, W. Zhang, Anomalous Hysteresis in Perovskite Solar Cells. *J. Phys. Chem. Lett*. **2014**, *5*, 1511-1515.

[23] E. L. Unger, E. T. Hoke, C. D. Bailie, W. H. Nguyen, A. R. Bowring, T. Heumüller, M. G. Christoforo, M. D. McGehee, Hysteresis and Transient Behavior in Current-Voltage Measurements of Hybrid-Perovskite Absorber Solar Cells. *Energy Environ. Sci*. **2014**, *7*, 3690-3698.

[24] Y. Yang, J. You, Make Perovskite Solar Cells Stable. *Nature*. **2017**, *544*, 155-156.

[25] M. Saliba, Perovskite Solar Cells must Come of Age. *Science*. **2018**, *359*, 388-389.

[26] M. Saliba, M. Stolterfoht, C.M. Wolff, D. Neher, A. Abate, Measuring Aging Stability of Perovskite Solar Cells. *Joule*, **2018**, *2*, 1019-1024.

[27] R. Gottesman, E. Haltzi, L. Gouda, S. Tirosh, Y. Bouhadana, A. Zaban, E. Mosconi, F. De Angelis, Extremely Slow Photoconductivity Response of $CH_3NH_3PbI_3$ Perovskites Suggesting Structural Changes under Working Conditions. *J. Phys. Chem. Lett*. **2014**, *5*, 2662-2669.

[28] S. Meloni, T. Moehl, W. Tress, M. Franckevicius, M. Saliba, Y.H. Lee, P. Gao, M.K. Nazeeruddin, S.M. Zakeeruddin, U. Rothlisberger, M. Graetzel, Ionic Polarization-Induced Current-Voltage Hysteresis in $CH_3NH_3PbX_3$ Perovskite Solar Cells. *Nat. Commun*. **2016**, *7*, 10334.

[29] W. Tress, N. Marinova, T. Moehl, S. M. Zakeeruddin, M. K. Nazeeruddin, M. Grätzel, Understanding the Rate-Dependent J–V Hysteresis, Slow Time Component, and Aging in $CH_3NH_3PbI_3$ Perovskite Solar Cells: the Role of a Compensated Electric Field. *Energy Environ. Sci*. **2015**, *8*, 995-1004.

[30] H.-S. Kim, I.-H. Jang, N. Ahn, M. Choi, A. Guerrero, J. Bisquert, N.-G. Park, Control of I-V Hysteresis in CH3NH3PbI3 Perovskite Solar Cell. *J. Phys. Chem. Lett*. **2015**, *6*, 4633-4639.

[31] K. Domanski, B. Roose, T. Matsui, M. Saliba, S.-H. Turren-Cruz, J.-P. Correa-Baena, C. Roldan Carmona, G. Richardson, J. M. Foster, F. De Angelis, J.M. Ball, A. Petrozza, N. Mine, M.K. Nazeeruddin, W. Tress, M Grätzel, U. Steiner, A. Hagfeldt, A. Abate, Migration of Cations Induces Reversible Performance Losses over Day/Night Cycling in Perovskite Solar Cells. *Energy Environ. Sci*. **2017**, *10*, 604-613.

[32] J. M. Frost, K. T. Butler, A. Walsh, Molecular Ferroelectric Contributions to Anomalous Hysteresis in Hybrid Perovskite Solar Cells. *APL Mater*. **2014**, *2*, 081506.

[33] J. M. Frost, K. T. Butler, F. Brivio, C. H. Hendon, M. van Schilfgaarde, A. Walsh, Atomistic Origins of High-Performance in Hybrid Halide Perovskite Solar Cells. *Nano Lett*. **2014**, *14*, 2584–2590.

[34] J. Wei, Y. Zhao, H. Li, G. Li, J. Pan, D. Xu, Q. Zhao, D. Yu, Hysteresis Analysis Based on Ferroelectric Effect in Hybrid Perovskite Solar Cells. *J. Phys. Chem. Lett*. **2014**, *5*, 3937-3945.

[35] A. M. A. Leguy, J. M. Frost, A. P. McMahon, V. G. Sakai, W. Kockelmann, C. Law, X. Li, F. Foglia, A. Walsh, B. C. O'Regan, J. Nelson, J. T. Cabral, P. R. F. Barnes, The Dynamics of Methylammonium Ions in Hybrid Organic-Inorganic Perovskite Solar Cells. *Nat. Commun*. **2015**, *6*, 7124.

[36] J. Mizusaki, K. Arai, K. Fueki, Ionic Conduction of the Perovskite-type Halides. *Solid State Ionics* **1983**, *11*, 203-211.

[37] T. M. Brenner, D. A. Egger, L. Kronik, G. Hodes, D. Cahen, Hybrid Organic-Inorganic Perovskites: Low-Cost Semiconductors with Intriguing Charge-Transport Properties. *Nat. Rev. Mater*. **2016**, *1*, 15007.

[38] J. M. Frost, A. Walsh, What is moving in Hybrid Halide Perovskite Solar Cells? *Acc. Chem. Res*. **2016**, *49*, 528-535.

[39] A. Walsh, D.O. Scanlon, S. Chen, X.G. Gong, S.-H. Wei, Self-Regulation Mechanism for Charged Point Defects in Hybrid Halide Perovskites. *Angew. Chem. Int*. Ed. **2015**, *54*, 1791-1794.

[40] A. Senocrate, I. Moudrakovski, G. Y. Kim, T.-Y. Yang, G. Gregori, M. Grätzel, J. Maier, The Nature of Ion Conduction in Methylammonium Lead Iodide: A Multimethod Approach. *Angew. Chem. Int.* Ed. **2017**, *56*, 7755-7759.

[41] G. Y. Kim, A. Senocrate, T.-Y. Yang, G. Gregori, M. Grätzel, J. Maier, Large Tunable Photoeffect on Ion Conduction in Halide Perovskites and Implications for Photodecomposition. *Nat. Mater*. **2018**, *17*, 445-449.

[42] J. M. Azpiroz, E. Mosconi, J. Bisquert, F. De Angelis, Defect Migration in Methylammonium lead Iodide and its Role in Perovskite Solar Cell Operation. *Energy Environ. Sci*. **2015**, *8*, 2118-2127.

[43] J. Haruyama, K. Sodeyama, L. Han, Y. Tateyama, First-Principles Study of Ion Diffusion in Perovskite Solar Cell Sensitizers. *J. Am. Chem. Soc*. **2015**, *137*, 10048-10051.

[44] H.-S. Kim, I. Mora-Sero, V. Gonzalez-Pedro, F. Fabregat-Santiago, E. J. Juarez-Perez, N.G. Park, J. Bisquert, Mechanism of Carrier Accumulation in Perovskite Thin-Absorber Solar Cells. *Nat. Commun.* **2013**, *4*, 2242.

[45] R. S. Sanchez, V. Gonzalez-Pedro, J-W. Lee, N-G. Park, Y. S. Kang, I. Mora-Sero, J. Bisquert, Slow Dynamic Processes in Lead Halide Perovskite Solar Cells. Characteristic Times and Hysteresis. *J. Phys. Chem. Lett.* **2014**, *5*, 2357-2363.

[46] E. J. Juarez-Perez, R. S. Sanchez, L. Badia, G. Garcia-Belmonte, Y. S. Kang, I. Mora-Sero, J. Bisquert, Photoinduced Giant Dielectric Constant in Lead Halide Perovskite Solar Cells. *J. Phys. Chem. Lett*. **2014**, *5*, 2390-2394.

[47] Z. Xiao, Y. Yuan, Y. Shao, Q. Wang, Q. Dong, C. Bi, P. Sharma, A. Gruverman, J. Huang, Giant Switchable Photovoltaic Effect in Organometal Trihalide Perovskite Devices. *Nat. Mater*. **2015**, *14*, 193-198.

[48] H-S. Kim, N-G. Park, Parameters Affecting I-V Hysteresis of $CH_3NH_3PbI_3$ Perovskite Solar Cells: Effects of Perovskite Crystal Size and Mesoporous TiO_2 Layer. *J. Phys. Chem. Lett.* **2014**, *5*, 2927-2934.

[49] M. Saliba, T. Matsui, J-Y. Seo, K. Domanski, J-P. Correa-Baena, M.K. Nazeeruddin, S.M. Zakeeruddin, W. Tress, A. Abate, A. Hagfeldt, M. Grätzel, Cesium- Containing Triple Cation Perovskite Solar Cells: Improved Stability, Reproducibility and High Efficiency. *Energy Environ. Sci*. **2016**, *9*, 1989-1997.

[50] M. Saliba, T. Matsui, K. Domanski, J.-Y. Seo, A. Ummadisingu, S.M. Zakeeruddin, J.-P. Correa-Baena, W.R. Tress, A. Abate, A. Hagfeldt, M. Grätzel, Incorporation of Rubidium Cations into Perovskite Solar Cells Improves Photovoltaic Performance. *Science*. **2016**, *354*, 206-209.

[51] B. Charles, J. Dillon, O. J. Weber, M. S. Islam, M. T. Weller, Understanding the Stability of Mixed A-Cation Lead Iodide Perovskites. *J. Mater. Chem. A.* **2017**, *5*, 22495-22499.

[52] D. Li, H. Wu, H.-C. Cheng, G. Wang, Y. Huang, X. Duan, Electronic and Ion Transport Dynamics in Organolead Halide Perovskites. *ACS Nano*. **2016**, *10*, 6933-6941.

[53] C. Chen, Q. Fu, P. Guo, H. Chen, M. Wang, W. Luo, Z. Zheng, Ionic Transport Characteristics of Large-Size $CsPbBr_3$ Single Crystals. *Mater. Res. Express.* **2019**, *6*, 115808.

[54] W.-J. Yin, T. Shi, Y. Yan, Unusual Defect Physics in $CH_3NH_3PbI_3$ Perovskite Solar Cell absorber. *Appl. Phys. Lett*. **2014**, *104*, 063903.

[55] M. H. Du, Efficient Carrier Transport in Halide Perovskites: Theoretical Perspectives. *J. Mater. Chem. A*. **2014**, *2*, 9091-9098.

[56] E. J. Juarez-Perez, M. Wussler, F. Fabregat-Santiago, K. Lakus-Wollny, E. Mankel, T. Mayer, W. Jaegermann, I. Mora-Sero, Role of the Selective Contacts in the Performance of Lead Halide

Perovskite Solar Cells. *J. Phys. Chem. Lett.* **2014**, *5*, 680-685.

[57] O. Almora, I. Zarazua, E. Mas-Marza, I. Mora-Sero, J. Bisquert, G. Garcia-Belmonte, Capacitive Dark Currents, Hysteresis, and Electrode Polarization in Lead Halide Perovskite Solar Cells. *J. Phys. Chem. Lett*. **2015**, *6*, 1645-1652.

[58] I. Zarazua, J. Bisquert, G. Garcia-Belmonte, Light-Induced Space-Charge Accumulation Zone as Photovoltaic Mechanism in Perovskite Solar Cells. *J. Phys. Chem. Lett*. **2016**, *7*, 525-528.

[59] O. Almora, A. Guerrero, G. Garcia-Belmonte, Ionic Charging by local Imbalance at Interfaces in Hybrid Lead Halide Perovskites. *Appl. Phys. Lett*. **2016**, *108*, 043903.

[60] A. Guerrero, G. Garcia-Belmonte, I. Mora-Sero, J. Bisquet, Y. S. Kang, T. J. Jacobsson, J.-P. Correa-Baena, A. Hagfeldt, Properties of Contact and Bulk Impedances in Hybrid Lead Halide Perovskite Solar Cells Including Inductive Loop Elements. *J. Phys. Chem. C*. **2016**, *120*, 8023-8032.

[61] R. Gottesman, P. Lopez-Varo, L. Gouda, J.A. Jimenez-Tejada, J. Hu, S. Tirosh, A. Zaban, J. Bisquert, Dynamic Phenomena at Perovskite/Electron Selective Contact Interface as Interpreted from Photovoltage Decays. *Chem*. **2016**, *1*, 776-789.

[62] G. Richardson, S. E. J. O'Kane, R.G. Niemann, T. A. Peltola, J. M. Foster, P. J. Cameron, A. B. Walker, Can Slow-Moving Ions Explain Hysteresis in the Current-Voltage Curves of Perovskite Solar Cells? *Energy Environ. Sci.* **2016**, *9*, 1476-1485.

[63] J. S. Yun, J. Seidel, J. Kim, A. M. Soufiani, S. Huang, J. Lau, N. J. Jeon, S. I. Seok, M. A. Green, A. Ho-Baillie, Critical Role of Grain Boundaries for Ion Migration in Formamidinium and Methylammonium Lead Halide Perovskite Solar Cells. *Adv. Energy Mater.* **2016**, *6*, 1600330.

[64] J. M. Frost, A. Walsh, What is moving in Hybrid Halide Perovskite Solar Cells? *Acc. Chem. Res*. **2016**, *49*, 528-535.

[65] J. N. Wilson, J. M. Frost, S. K. Wallace, A. Walsh, Dielectric and Ferroic Properties of Metal Halide Perovskites. *APL Mater.* **2019**, *7*, 010901.

[66] Y. Zhang, M. Liu, G. E. Eperon, T. Leijtens, D. McMeekin, M. Saliba, W. Zhang, M. de Bastiani, A. M. Petrozza, L. M. Herz, M. B. Jonhnston, H. Lin, H. J. Snaith, Charge Selective Contacts, Mobile Ions and Anomalous Hysteresis in Organic-Inorganic Perovskite Solar Cells. *Mater. Horiz.* **2015**, *2*, 315-322.

[67] S. E. J. O'Kane, G. Richardson, A. Pockett, R. G. Niemann, J. M. Cave, N. Sakai, G. E. Eperon, H. J. Snaith, J. M. Foster, P. J. Cameron, and A. B. Walker, Measurement and Modelling of Dark

Current Decay Transients in Perovskite Solar Cells. *J. Mater. Chem. C.* **2017**, *5*, 452-462.

Chapter 5. Ageing in triple cation perovskite

5.1. Introduction

Hybrid organic-lead-halide (HOIP) perovskite solar cells (PSCs) are stimulating the photovoltaic research field with power conversion efficiencies (PCE) beyond 25% [1]. Despite the stunning breakthrough, the unacceptably poor device lifespan under operating conditions still represents an unbearable barrier for their commercialization [2-5]. A marketable product requires a 20-to-25-year warranty and should have less than 10% degradation in performance. This is a condition in which the device retains over 90% of its original performance for at least 1,000 hours in standard accelerated ageing tests. Perovskites, although recognized as soft materials [6, 7], behave as if the fast-nuclear motions (ps timescale) had only a disorderly impact at very short ranges for the electronic states affecting little their optoelectronic properties, contrary to what is observed for conventional semiconductors [8, 9]. However, the pervasive issue of these hybrid perovskite solar cells (PSCs) concerns their long-term operational stability versus heat, oxygen, moisture, or UV light, which constitutes a major impediment to their market uptake [5, 10-26]. Many groups have explicitly studied the instability of mixed halide perovskites due to exposure to oxygen [13-18]. For the archetypal methylammonium lead iodide ($MAPbI_3$) absorber, the oxygen incorporation inside the lattice was shown to be strongly enhanced under illumination. This leads to a rapid degradation observed through a severe modification of the electronic and ionic conductivities [13-17, 21, 22]. From this respect, and as noted in many reviews about the stability of perovskites [5, 26-32], it is guessed that complete encapsulation or an utterly oxygen-free environment is required for the stable performance of PSCs.

Suggested solutions to control the material ageing stability are:

- adapting to an extent using crosslinking additives [33]
- compositional engineering [34] (e.g. adding $Pb(CH_3CO_2)_2 \cdot 3H_2O$ and $PbCl_2$ to the precursor [35])
- using cation subordination, including Cs and Rb cations, as demonstrated [2, 3] to reduce the material photo-instability and/or optimize the film morphology.

For this reason, we chose to work not exclusively with the MAPI perovskite but also with cationic mixing composition like Cs/MA/FA (so-called triple cation perovskite, 3CP, where MA stands for methylammonium and FA for formamidinium), for which a significant reduction of the degradation rate has been observed [2, 3, 36]. Our study observes thin films and devices of two different perovskites (MAPI and 3CP) under given ageing conditions. The 3CP thin film, the primary research material, shows stable ageing characteristics under the same conditions. We further found that in p-i-n PSCs, iodide ions pass through the electron transport layer and chemically react with the top metal electrode at an ageing time.

5.2. Ageing of the perovskite film

Studying the ageing characteristics of Perovskite Film (PF) is a cornerstone for studying the ageing characteristics of PSC devices under the same conditions. The ageing tendency of PF exposed to air under the dark can be evaluated for the stability of the PF itself in air. If a difference is discovered when observing the ageing of the PSC device, it is considered an essential factor in identifying the cause. A known ageing mechanism of perovskite is that organic cations (mainly MA^+) dissociate, leaving PbI_2 in the perovskite layer [10, 37]. The PF's ageing characteristics aim to understand the aging characteristics and ageing speed of the film by observing the increase of PbI_2 characteristics and the decrease of the perovskite characteristics over time through XRD and UV-Visible absorption.

5.2.1. Ageing observation with X-ray diffraction

The perovskite stacks were prepared as Glass/ITO/PEDOT:PSS/perovskite structure. Since the substrate influences perovskite formation (thickness and crystallinity), the same condition as the underlayer of the device was selected. The samples were stored in air or a nitrogen-filled glove box without light exposure. The "under dark in the nitrogen" is the storage condition that removed the known ageing factors such as light [7], moisture [38], and oxygen [39]. "The air" is the storage condition at 25°C with air-conditioning.

5.2.1.1. MAPI ageing observation with XRD

Figure 5.1 shows the XRD results of the MAPI film over time. In nitrogen ambient, growth of the PbI_2 phase is not observed even after five weeks (Fig. 5.1a). Any deformation such as color change of the film is not observed in the appearance. In air ambient, the XRD results show the progression of ageing from 1 week to 5 weeks. Ageing is assessed by comparing the intensities of the PbI_2 phases and MAPI phases. Fig. 5.1b shows the notable phase growth of PbI_2 ($2\theta = 12.6°$) and contractions of MAPI phases (the three major peaks 14.2°, 28.6°, and 32.2° correspond to the three tetragonal phased $MAPbI_3$ of (110), (220) and (310) respectively). Trace of ageing is also observed in the appearance of the film. After five weeks, the yellow spots can be easily found on the film. The yellow part is where all MAPI has been dissociated, and only PbI_2 remains [40].

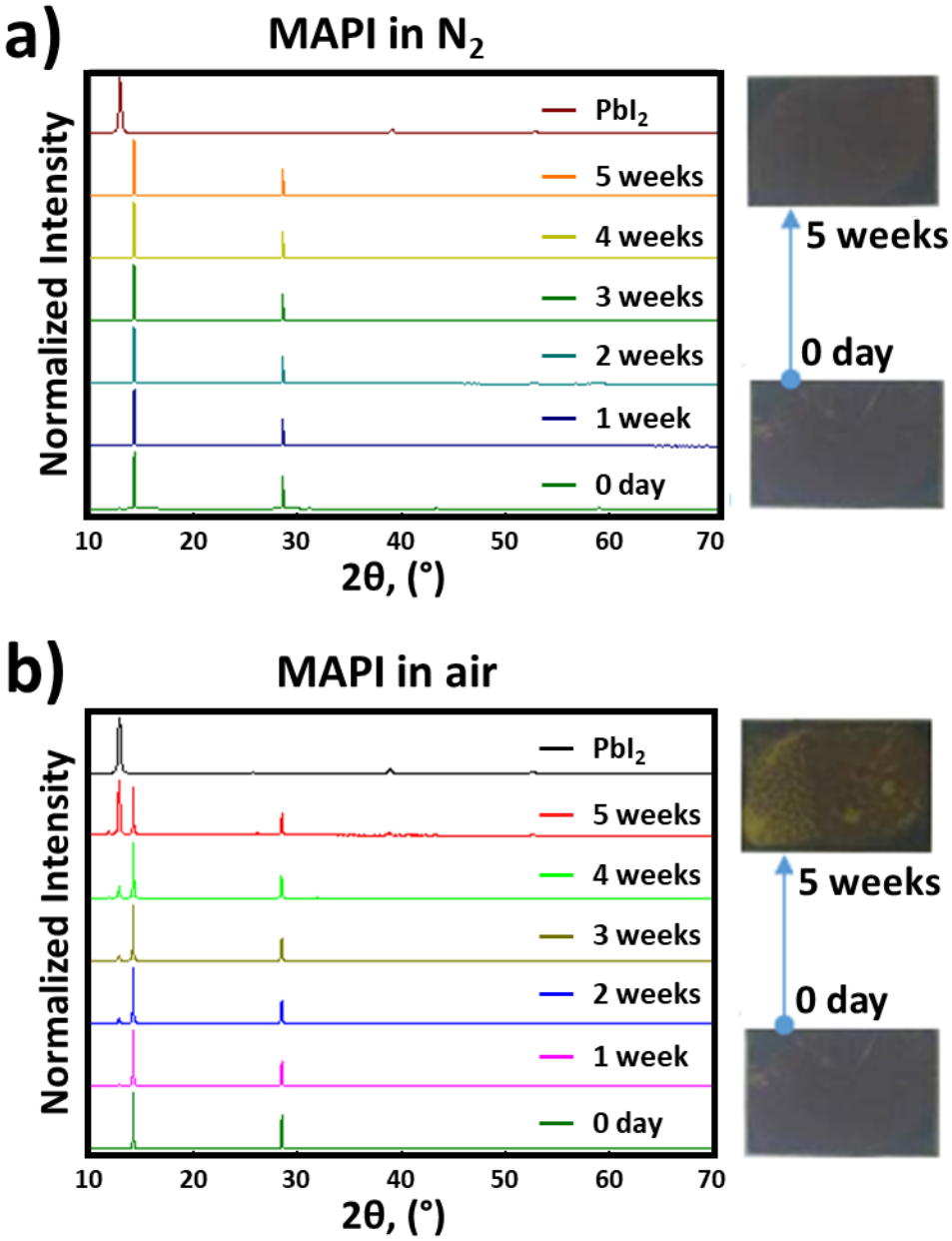

Figure 5.1. X-ray diffraction spectrum of MAPI stacks (Glass/ITO/PEDOT:PSS/MAPI) kept under dark a) in air and b) nitrogen atmosphere.

5.2.1.2. 3CP ageing observation with XRD

Figure 5.2 present the XRD results of 3CP film over time. The PbI_2 phase is observed even in the fresh sample. However, in nitrogen ambient, the evolution of the PbI_2 phase is not observed even after six weeks (Fig.5.2a). In the 3CP film formation reaction, three cations (MA^+, FA^+, Cs^+) and two halide

anions (I^-, Br^-) participates in ABX_3 chemical bonding. The PbI_2 patterns, which did not participate in bonding, are observed after this complex reaction. The low PbI_2 peak was also reported in the 3CP article we referenced to make the sample [3].

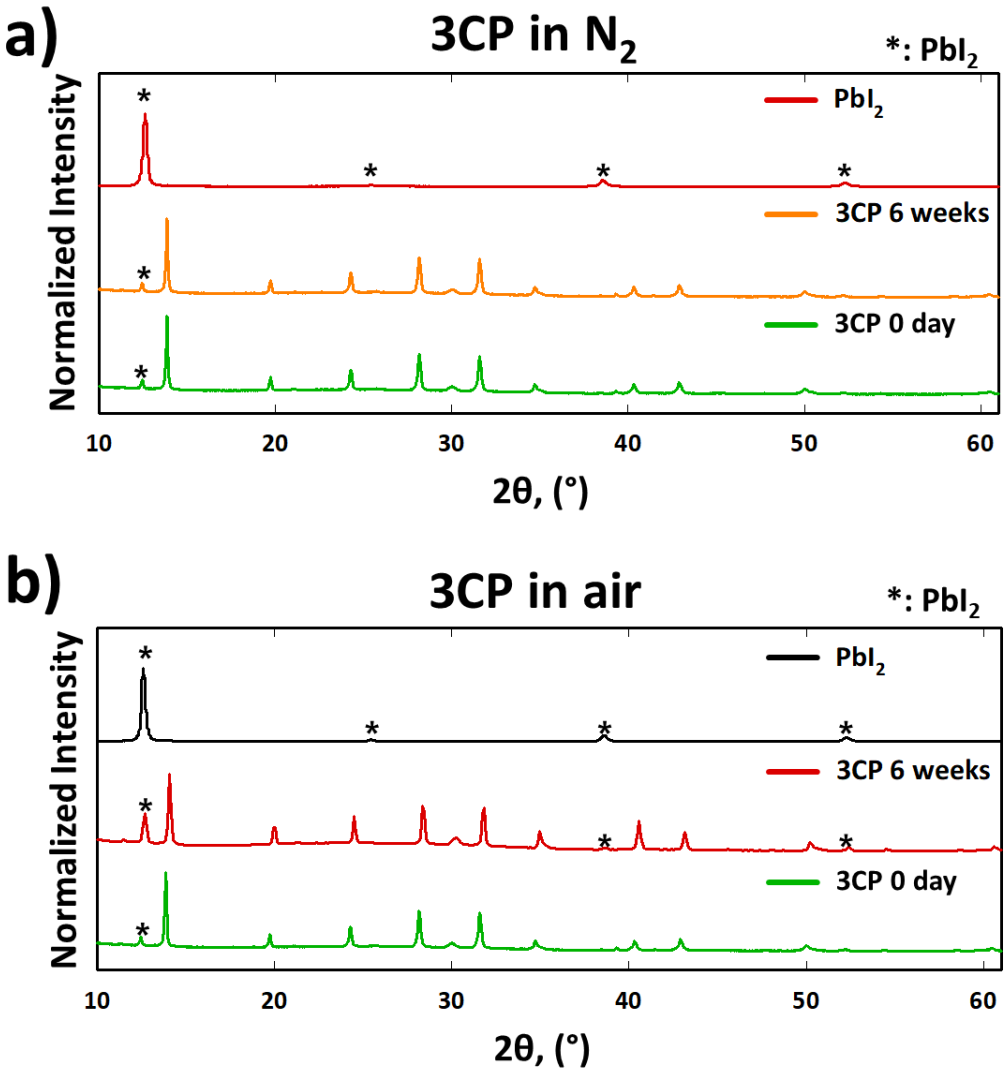

Figure 5.2. X-ray diffraction spectrum of 3CP stacks (Glass/ITO/PEDOT:PSS/3CP) kept under dark a) in air and b) nitrogen atmosphere.

In air ambient, the XRD results show the progression of ageing. It is assessed by comparing the intensities of the PbI_2 phases and 3CP phases. Fig. 5.2b shows the little phase growth of PbI_2 ($2\theta = 12.6°$) and global contractions of 3CP phases as a global decrease in the intensity of the diffraction peak except for the PbI_2

diffraction pattern (with mark "*") shown in Figure 5.2b red line. However, comparing this result with MAPI (Fig. 5.1b), the progress of 3CP ageing is quite slow.

5.2.2.3 Discussion of XRD results

From the viewpoint of ageing, MAPI and 3CP show a stable lifespan, excluding elements (light, moisture, oxygen) exposed in daily life. However, MAPI exposed to only oxygen showed that the ratio of PbI_2 reversed MAPI after five weeks with XRD. This period played a significant role in selecting the period for observing the ageing of PSC devices. On the other hand, 3CP exposed to oxygen showed more extended stability. Even after six weeks, the XRD phases of 3CP still dominate PbI_2.

5.2.2. Ageing observation with UV-visible absorbance

The perovskite stacks were prepared as Glass/ITO/PEDOT:PSS/perovskite structure. Since perovskite formation (thickness and crystallinity) is influenced by the substrate, the same condition as the underlayer of the device were selected. The samples were kept dark in the air at 25°C with air-conditioning.

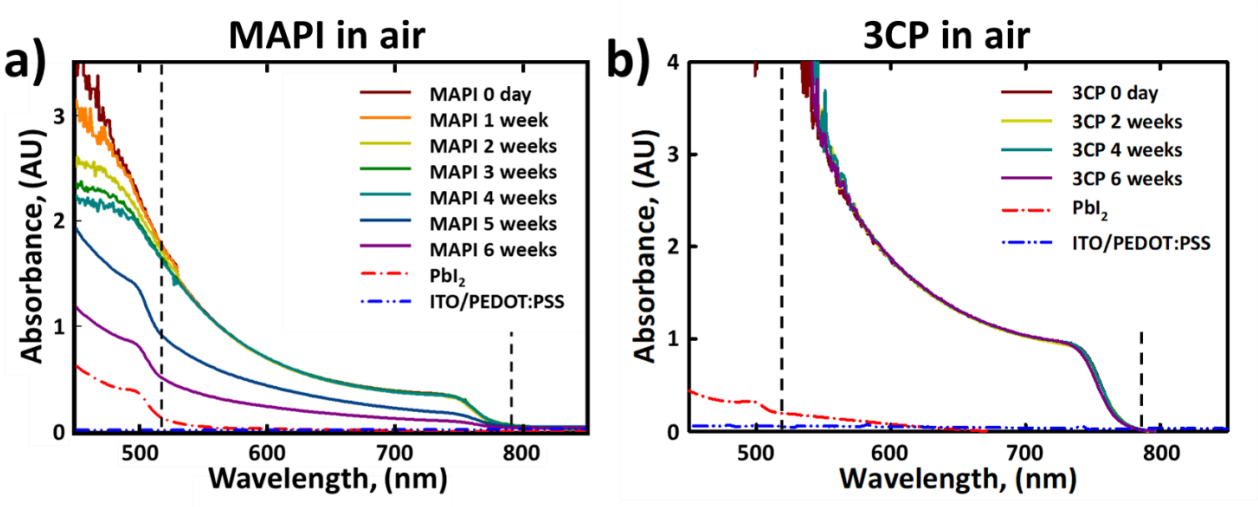

Figure 5.3. UV-Visible absorption spectrum of a) MAPI stacks (Glass/ITO/PEDOT:PSS/MAPI) and b) 3CP stacks (Glass/ITO/PEDOT:PSS/3CP).

5.2.2.1 Definition of the Absorbance Unit (AU)

Figures 5.3a and b are the UV-Visible absorption spectra of MAPI and 3CP stacks over time. Following Beer-Lambert law (eq 2.5-(2)), the Absorbance Unit (AU) = 2 means 99% of light is absorbed in the wavelength. It is not easy to evaluate information with an AU greater than 2. In order to perform

the same experiment as MAPI, 3CP film also needs to reduce the absorbance to less than 2. A possible option is to experiment with reduced thickness. The following paragraphs describe the relationship between thickness and absorbance. Then, the device performance of 3CP-PSC observed after reducing the thickness is shown. In the spin-coating process, the method to reduce the thickness is to fabricate a film by lowering the concentration of the precursor solution. The reason why the thin 3CP absorbance experiment did not proceed further is introduced next because the 3CP layer is formed differently by the change in precursor solution concentration.

5.2.2.2 Relation between absorption coefficient and wavelength of light

The absorption coefficient has the relation:

$$\alpha = \frac{4\pi f \kappa}{c} \qquad 5.1 - (1)$$

where α is absorption coefficient, f is the frequency of monochromatic photon from the incident light spectrum ($f = v\lambda$, where is the velocity of the light wave), κ is extinction coefficient, and c is the speed of light, and π is a constant (≅3.14).

As the velocity of light in a vacuum:

$$c = f\lambda \qquad 5.1 - (2)$$

$$\text{Then, } \alpha = \frac{4\pi\kappa}{\lambda} \qquad 5.1 - (3)$$

The absorption coefficient of a material is inversely related to the wavelength of light. It describes how deeply light penetrates a material before being absorbed. Higher energy light is of a shorter wavelength and is absorbed in a short absorption depth. Since the light with a wavelength shorter than 510 nm (vertical black dash line at 510 nm on Fig. 5.3) has a short absorption depth, the AU of the fresh samples (for MAPI and 3CP) exceed 2.

5.2.2.3 Discussion of UV-Visible absorption

Why is absorption measurement reasonable by reducing the thickness of 3CP?

Considering Sections 5.2.2.1 and 5.2.2.2, the ageing of MAPI stacks in the air shows a rapid progression after four weeks. To discuss the result of 3CP stacks, however, we face the question, "Should we reduce the perovskite thickness to derive the correct absorbance?". Reducing the thickness requires changing the concentration of the perovskite precursor solution, which can result in a change in material properties because perovskite crystalizes during the solution process. Since the optimized 3CP precursor

solution concentration is 75 wt%, the solution for the experiment used a less viscous solution. 40 wt% concentration is selected to compare with MAPI because the optimized concentration for MAPI is 40 wt% [34].

The new film with a thinner 3CP layer shows an abnormality in the grain shape (Fig 5.4a), and the fresh 3CP solar cell's efficiency decreased (Fig 5.4b). It seems that the material "3CP" was formed, as V_{OC} was not significantly different from the optimized efficiency (Fig.3.8). Except for the quality of the 3CP layer, all conditions are the same to make the 3CP PSC device. The measured 3CP device performances are poor even though it is a newly made device (low $J_{sc,}$ low R_{sh}, and high R_s). The poor performance is due to the many voids between the 3CP grains, presented in Fig.5.4a. Even considering the possibility that J_{sc} is lowered due to the thinner 3CP layer, this interpretation reasonably explains the increase in R_s and the decrease in R_{sh}. Small grain size and many voids have more surface area when the sample is exposed to air. Since we test ageing characteristics of the optimized 3CP stacks in air, this condition is not appropriate.

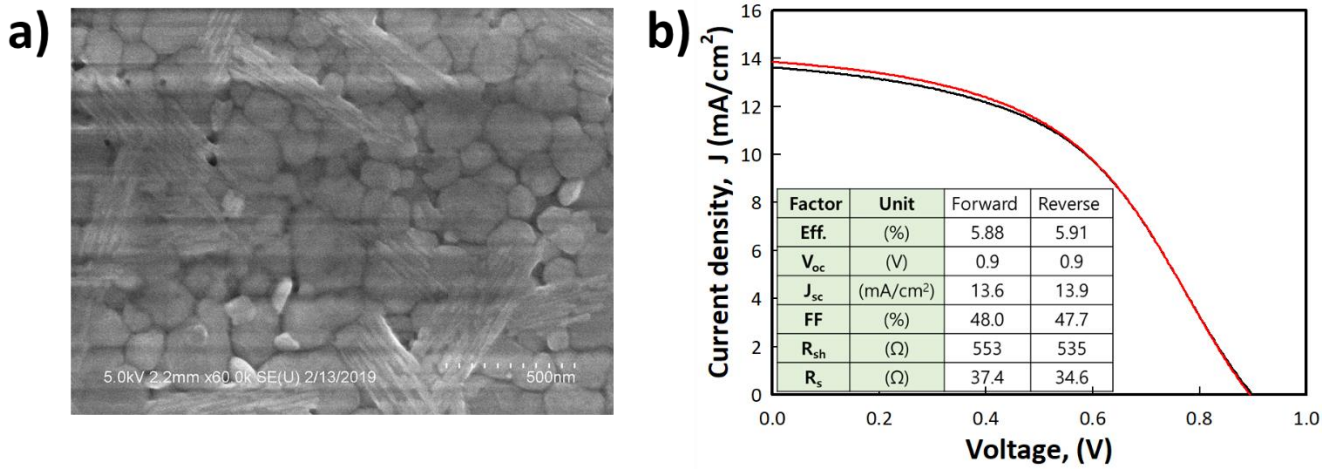

Figure 5.4. a) SEM image of Glass/ITO/PEDOT:PSS/3CP stacks and b) 3CP-PSC performance made by 40wt% 3CP precursor solution. The 40wt% concentration is followed by the MAPI precursor solution to make a similar thickness.

5.2.3. conclusion

XRD studies showed that MAPI and 3CP films have a stable lifespan without elements (light, moisture, oxygen) exposed in daily life. When these materials are surrounded by air, XRD results show that the proportion of PbI_2 reversed MAPI after five weeks. On the other hand, 3CP exposed to air showed more extended stability. Even after six weeks, the XRD phases of 3CP still dominate PbI_2. The duration (5 weeks) played an essential role in planning the time to observe PSC devices ageing.

The absorbance experiment was expected to observe the mixture of PbI_2 absorption characteristics with 3CP's absorbance as with the XRD results (Fig. 5.3b). The results exceed the value 4 of AU in the PbI_2 absorption range (< 510nm). Nevertheless, the overall decrease in the MAPI's absorption characteristics (wavelength range: 510nm - 780nm) after five weeks (Fig. 5.3a) shows that 3CP is relatively stable against ageing under air exposure conditions.

5.3. Ageing of perovskite solar cell

The perovskite solar cells were prepared as Glass/ITO/PEDOT:PSS/perovskite/$PC_{60}BM$/Ag structure. The devices were stored under dark in the nitrogen-filled glovebox at 25°C. Except for the performance measurement, any electrical stimulation was not applied. The performance measurement method is informed in 2.5.1.1.

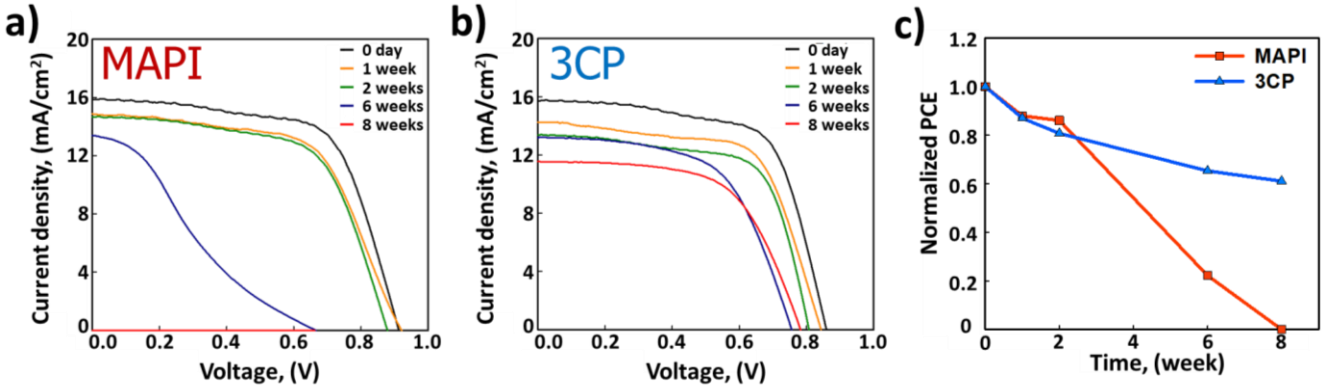

Figure 5.5. Degraded J-V performance of a) MAPI solar cell and b) 3CP solar cell. c) summary of power conversion efficiency decreases for eight weeks in N_2.

The perovskite film aging analysis confirmed that MAPI and 3CP stacks are stable in N_2 ambient. In the MAPI solar cell case, dramatic ageing is observed after the 6th week, even when the device is stored in a nitrogen ambient. The 70% of power conversion efficiency dropped from the initial efficiency (Fig.5.5 a and c). The change in the J-V performance curve is the emergence of the S-shape. This S-shape curve is the representation of the formation of an interfacial barrier between layers. This result means that ageing occurs due to factors other than light, moisture, and oxygen acting on the device in the ITO/PEDOT:PSS/perovskite/$PC_{60}BM$/Ag junction state. The research was divided into short-term ageing (5.3.2) when the global efficiency decreases, and long-term aging, an S shape occurs (5.3.3).

5.3.1 Short-term ageing analysis with Impedance Spectroscopy

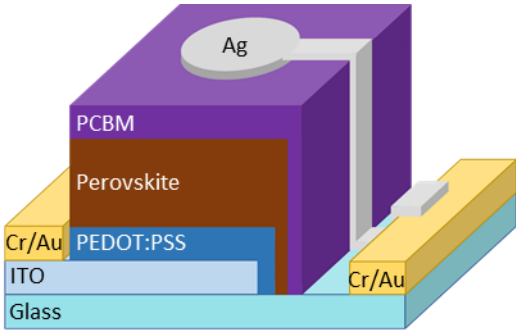

Figure 5.6. 3CP-PSC device structure.

The ageing phenomenon of PSC devices is different from short-term aging and long-term ageing. For the short-term ageing study, 3CP-PSCs are exposed in the air because of the Impedance Spectroscopy measurement environment. The IS system was installed in the air (with air conditioning) and measured for 5 hours per measurement to scan the low-frequency range (10 mHz- 1 Hz).

Figure 5.7 shows impedance data collected from fresh and aged 3CP samples. In the complex impedance plot in the log-log scale (Fig. 5.7a), the complex impedance shows a progressive change of the resistive behavior at the lower frequency range upon ageing while no modification is observed at high frequency. In the Bode phase plot (Fig. 5.7b), there is a phase closed to -90 degrees at 100 kHz in the fresh sample. When time runs out up to 10 days, a second capacitive behavior emerges by the phase close to -90 degrees at a lower frequency range (100 Hz - 1 kHz). This feature at 100 Hz - 1 kHz is attributed to a charge accumulation layer occurring at the interface between 3CP and selective contact materials. In Figure 5.7c, there is a single semicircle in the Nyquist plot, which indicates the single conduction mechanism.

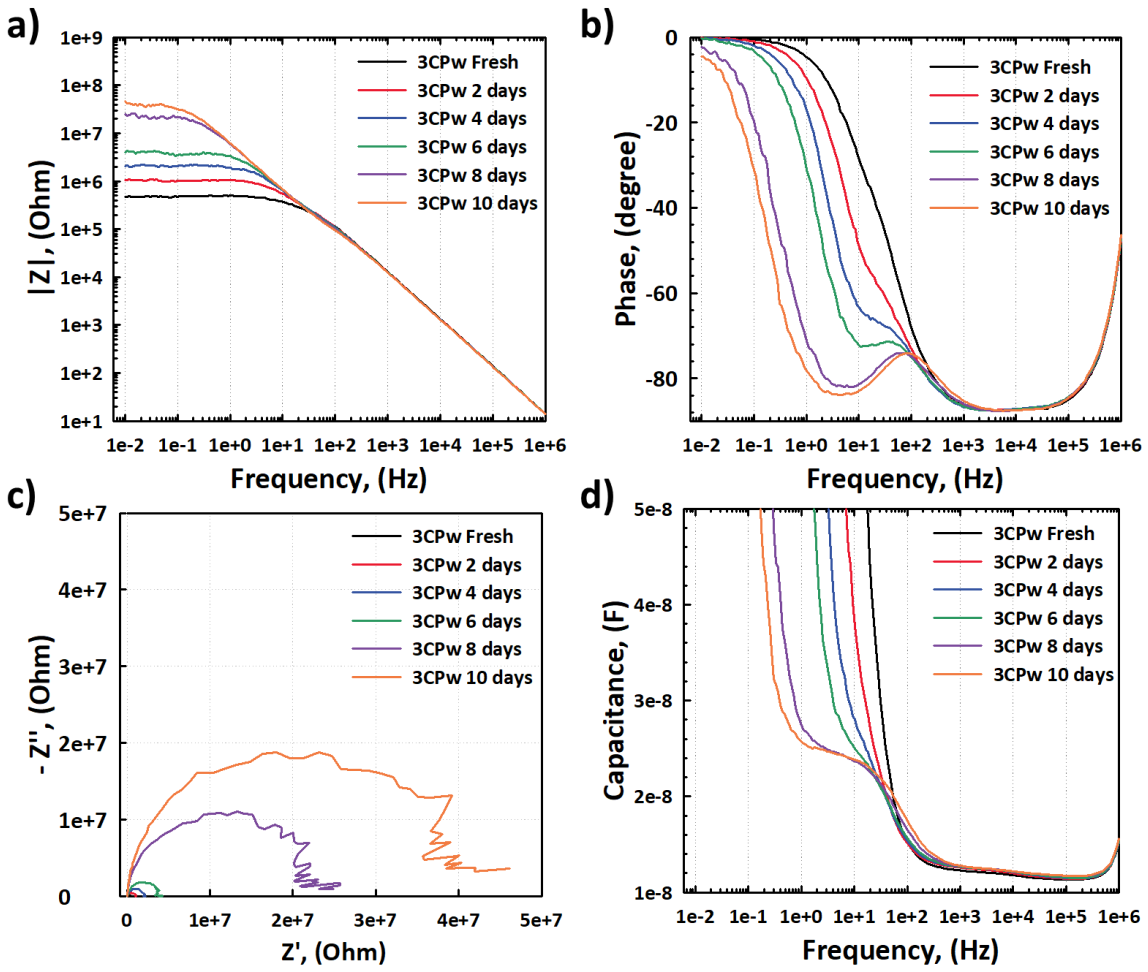

Figure 5.7. IS characteristics evolution as a function of ageing time for 3CP solar cell; a) Complex impedance versus frequency; b) Phase versus frequency; c) Nyquist plot; d) Capacitance versus frequency.

As ageing time increases, the radius of this semicircle increases, suggesting a degradation of the solar cell corresponding to a decrease in the conductivity. In Figure 5.7d, we have plotted the theoretical capacitance deduced from IS measurement as a function of the frequency. Only a single capacitance (Cg ~ 11 nF) is obtained for the pristine device at a high frequency corresponding to the geometrical capacitance mentioned previously. However, after ageing time, a second capacitance (C_3) appears with a value around 14 nF clearly seen after ten days of ageing time (the measured value at lower frequency in Fig. 5.7d is the sum of C_g+C_3).

We investigated the evolution of 3CP solar cells with ageing time using impedance spectroscopy. Interfacial accumulation and non-radiative recombination, as confirmed by impedance spectroscopy measurements, are responsible for the general observation of J-V hysteresis in hybrid perovskites. The double layers at each interface where high built-in fields are created control completely the current

densities of electrons and holes. This assertion is confirmed by the fact that hysteresis depends upon the interface HTL/perovskite when HTL is changed, all the other parameters of the device are fixed. This is a perfect illustration that a good band alignment is necessary for improving both photovoltaic response and stability.

After ten days, a constant C_3 (14 nF) and a persistent increase in R_3 are observed. With high R_3, reliable Nyquist data could not be obtained due to excessive noise in the low-frequency region. Ageing studies using IS had the difficulty of long-term observation when the R_3 excesses $5x10^7$. Since the IS measurement conditions in the air were not optimized for the MAPI device within the study period, it is proposed as a prospective study.

5.3.2. Long-term ageing analysis with GD-OES

To investigate long-term ageing, another tool is introduced as a GD-OES. GD-OES analysis is used to check the atomic composition of aged MAPI and 3CP solar cells. Considering the plasma etching direction and the p-i-n solar cell structure, the silver position corresponds to the shortest sputtering time, and the ITO corresponds to the longest sputtering time [41].

5.3.2.1 MAPI ageing observation

The MAPI samples were stored under dark conditions and N_2 atmosphere without applied bias. Figure 5.8 shows the GD-OES profile lines of nitrogen, chlorine, lead, and iodine atoms in the MAPI thin film. All the prominent peaks of these four atoms (nitrogen, chlorine, lead, and iodine) are observed at the same range between 45 s and 75 s, indicating the perovskite layer. We observe a significant motion of iodide ions upon an ageing time, while the other MAPI components (N, Pb, Cl) are stable (Fig. 5.8 a, b, and c). Nitrogen atoms are located at the whole range of perovskite thin film, and the chlorine atoms are situated toward PEDOT:PSS layer in the perovskite thin film. We may assume there is the formation of CH_3NH_3Cl gas during the annealing process. This gas is escaping from the top of the perovskite layer [42]. Both nitrogen and chlorine are perfectly fixed during the four weeks of progressed ageing, as shown in Fig. 5.8a and Fig. 5.8b. Since Pb has high activation energy than halide and organic cations to migrate, Pb ions cannot migrate following electric field [43-45]. In our results with ageing, a slight shift is observed in the GD-OES profile lines of lead (Pb) toward PCBM, as shown in Figure 5.8c.

On the contrary, the intensity of the iodine peak reduces significantly, and a shoulder increases progressively towards the Ag electrode during ageing process (Fig. 5.8d). After four weeks, the iodine

signal starts at 20 s of sputtering time (50 s for the unaged device), corresponding to the silver position [41]. This means that the iodine atoms diffuse through the PCBM layer towards the silver electrode without applying any external voltage. Figure 5.8e represents the photos of fresh and old PCSs samples. We observed the color variation of the top electrode from silver to yellow after two weeks of ageing (Fig.5.9). We speculate that the color change of the silver metallic cathode is due to a chemical reaction of iodide ions with silver ($Ag^+ + I^- \rightarrow AgI$) [46]. After four weeks, the perovskite film is completely degraded only around the silver electrode showing yellow PbI_2 compound. These GD-OES iodine profiles after ageing are equivalent to ToF-SIMS iodine profiles after thermal treatment for the same inverted structure [47] and confirm the deterioration of $MAPbI_3$ thin films in both cases. The formation of AgI supports the importance of ionic reactivity at contacts in the working principles of PSCs [48].

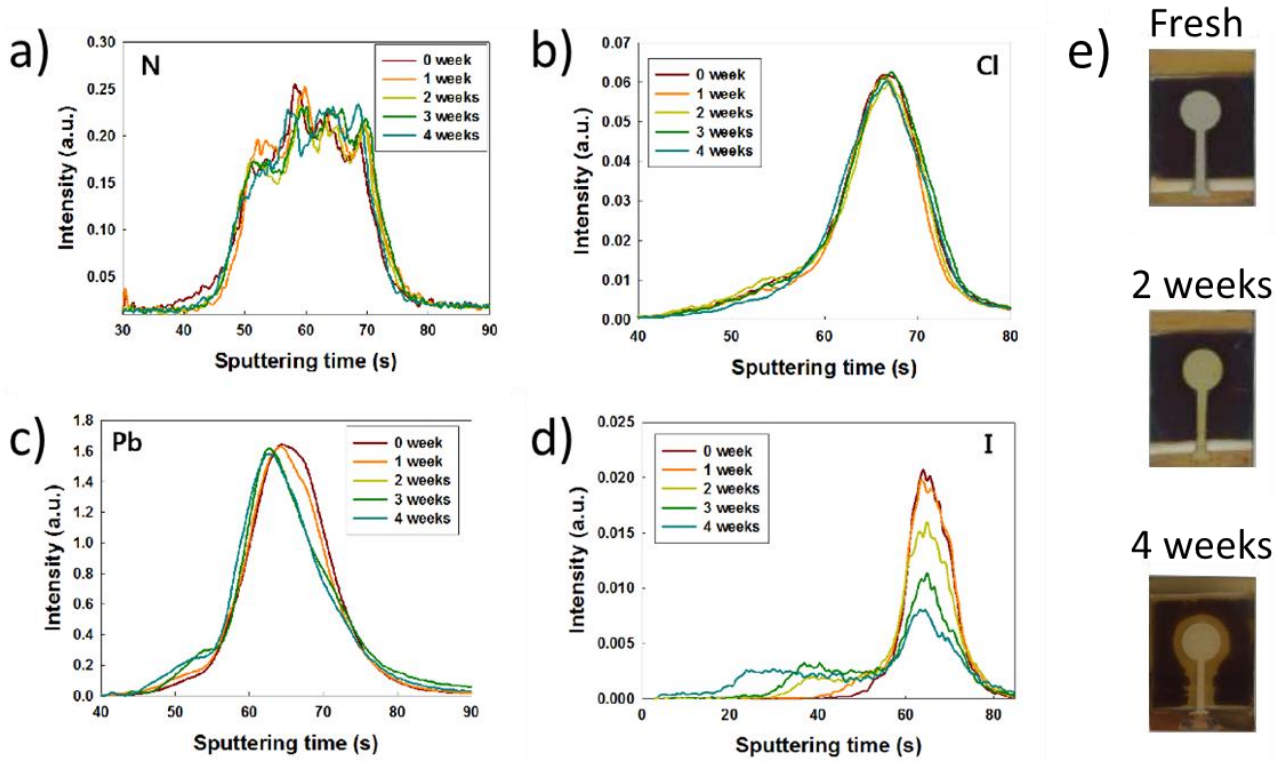

Figure 5.8. MAPI solar cell aged under dark conditions in N_2 atmosphere; the GD-OES profile lines of atoms in the perovskite thin-films upon ageing time. a) nitrogen, b) chlorine, c) lead, and d) iodine. And e) photographs of fresh, 2 weeks and 4 weeks aged PSCs devices.

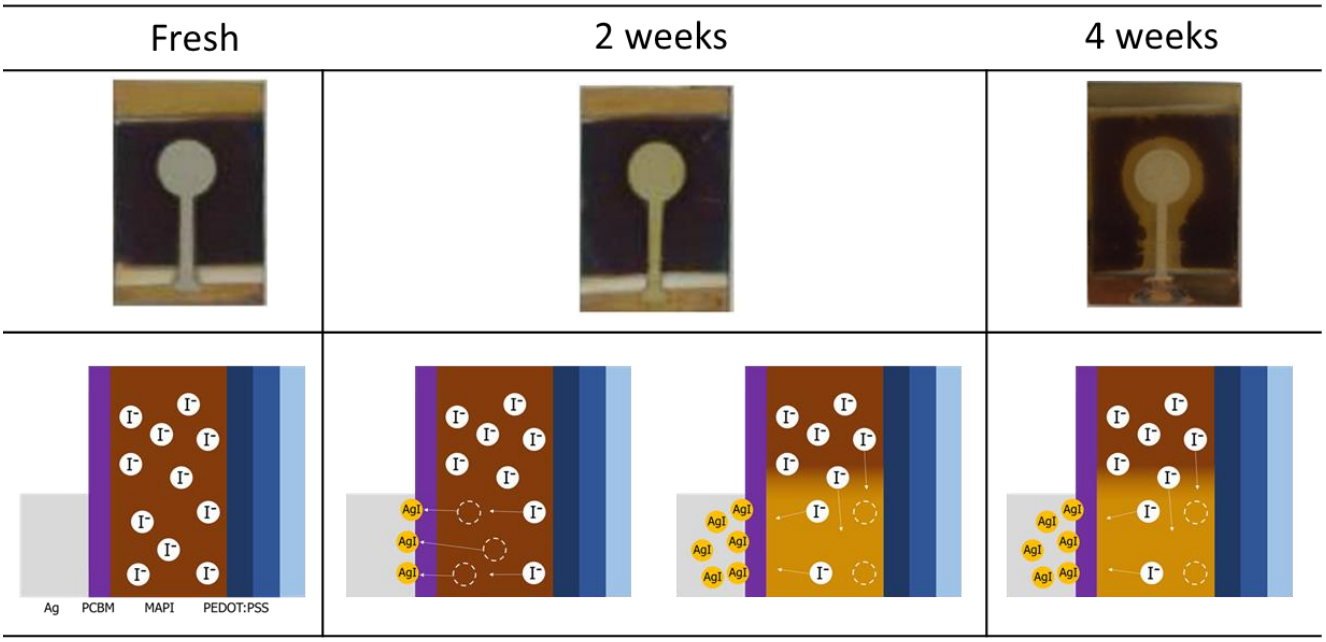

Figure 5.9. Schematic diagram explaining the ageing mechanism of MAPI solar cells; a) unaged iodine distribution in the MAPI layer, b) Generation of voids due to initial chemical reaction ($Ag^+ + I^- \rightarrow AgI$), c) Ion diffusion toward voids (low concentration of iodine), and d) After reaching the reaction equilibrium ($Ag^+ + I^- \rightleftharpoons AgI$).

5.3.2.2. 3CP ageing observation

The 3CP devices were kept under dark conditions and air atmosphere without applied bias. The atmosphere was controlled with a constant temperature (25°C) by an air conditioner. In the N_2 ambient, any GD-OES profile changes were not observed even with a 2-month-old 3CP device. For this reason, the 3CP devices were stored in the air is to accelerate ageing. In addition, the plasma conditions used for the experiment changed because a new GD-OES system was used (provided by Institut Lavoisier de Versailles – ILV and Institut Photovoltaïque d'Île-de-France – IPVF: GD-ILV) – the condition as 250 Pa and 15 W applied power to get the proper etching rate. For sputtering, pure Ar gas is used as plasma gas. The optimization for the new plasma condition is elucidated in Appendix (Chapter A.2.).

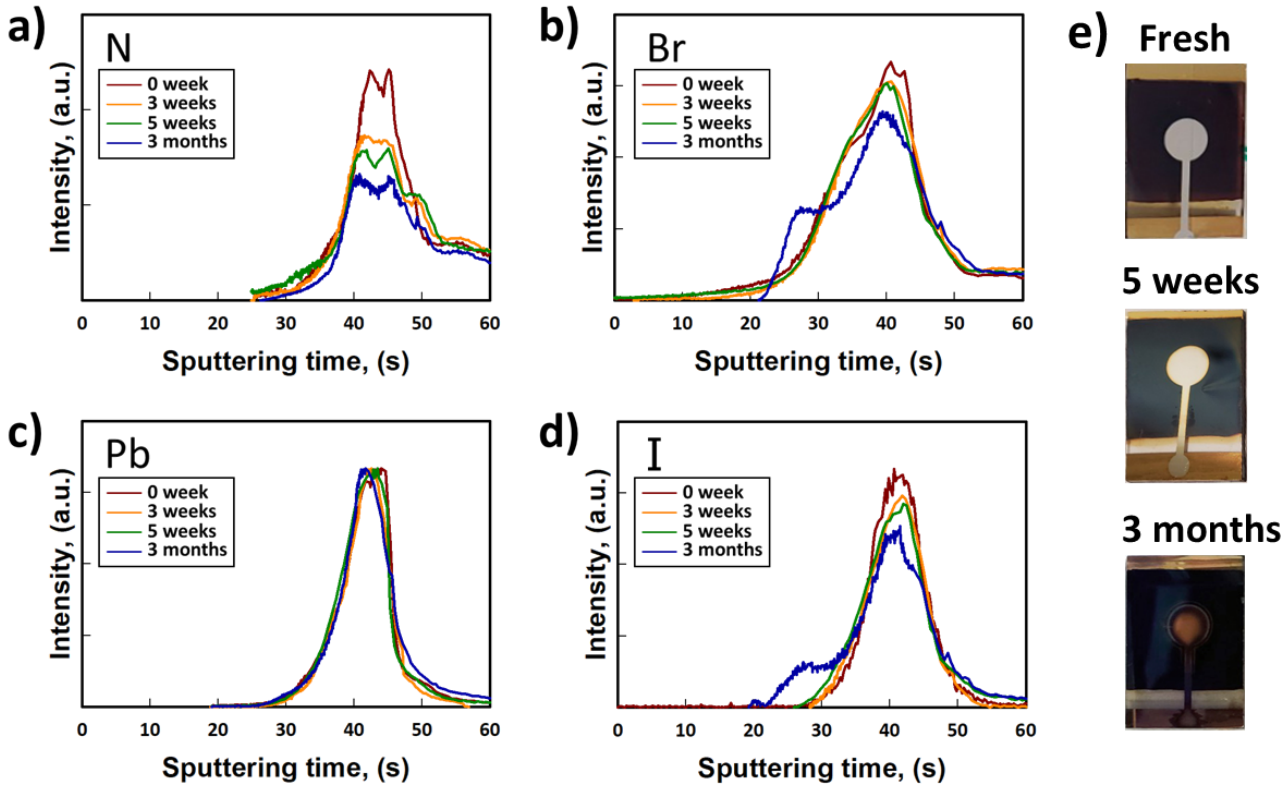

Figure 5.10. 3CP solar cell aged under dark conditions in the air; the GD-OES profile lines of atoms in the perovskite thin-films upon ageing time. a) nitrogen, b) chlorine, c) lead, and d) iodine. And e) photographs of fresh, 5 weeks and 3 months aged 3CP devices.

Figure 5.10 shows the GD-OES profile lines of nitrogen, bromine, lead, and iodine atoms in the 3CP layer. All the main peaks of these four atoms (nitrogen, bromine, lead, and iodine) are observed at the same range between 30 s and 50 s, indicating the perovskite layer. The global intensity of nitrogen profile lines is reduced with ageing (Fig. 5.10a). The reducing N intensity over time is presumed due to the ageing mechanism. The mechanism is speculated that 3CP film loses $CH_3NH_3^+$ (MA^+) cations [10,37] and $CH(NH_2)_2^+$ (FA^+) cations as the gaseous state. Lead atoms are situated at the whole range of 3CP film (Fig. 5.10c). On the contrary, a remarkable motion of bromine and iodide ions upon an ageing time is observed. For bromine and iodine, the intensity of the initial peak reduces notably, and a shoulder increases progressively towards the Ag electrode (Fig. 5.10b and d). After three months, calculating the shoulder area in the range of 30 s to 36 s (Fig. 5.10b), it is deduced that 18 % of the bromine and 14% of the iodine are migrated. The bromine and iodine signals start at 20 s of sputtering time (30 s for the unaged sample), corresponding to the silver layer similar to MAPI (section 5.3.2.1).

The ageing result difference between the MAPI and 3CP devices is the ions species and ion diffusion distance. The 20 s position of sputtering time is the surface of the silver electrode in contact with the PCBM because the Ag signal ends around 21 s (Fig. 5.10 b and d). The halogen ions (Br and I) of 3CP were not diffused inside of the silver layer. Since the thickness of PCBM is 50 nm, the migration distance of halogen ions is estimated to be about 50 to 60 nm. Figure 5.10e represents the photos of fresh and old 3CP devices. The five weeks aged sample shows the top electrode with a yellow edge. Changes in the appearance of the electrode can also be a factor to scale the progress of ageing. After five weeks of ageing, the color variation on the edge of the metal electrode was observed from silver to yellow. The yellow material is speculated as AgBr and AgI due to a chemical reaction of halogen ions with silver [49]. After three months of ageing, the color of the electrode is black (edge) and brown (center of the circle). The black substance is speculated as silver oxide (Ag_2O) because the sample ageing was performed in air. The ageing mechanism is described step by step with schematic diagrams in Fig. 5.11.

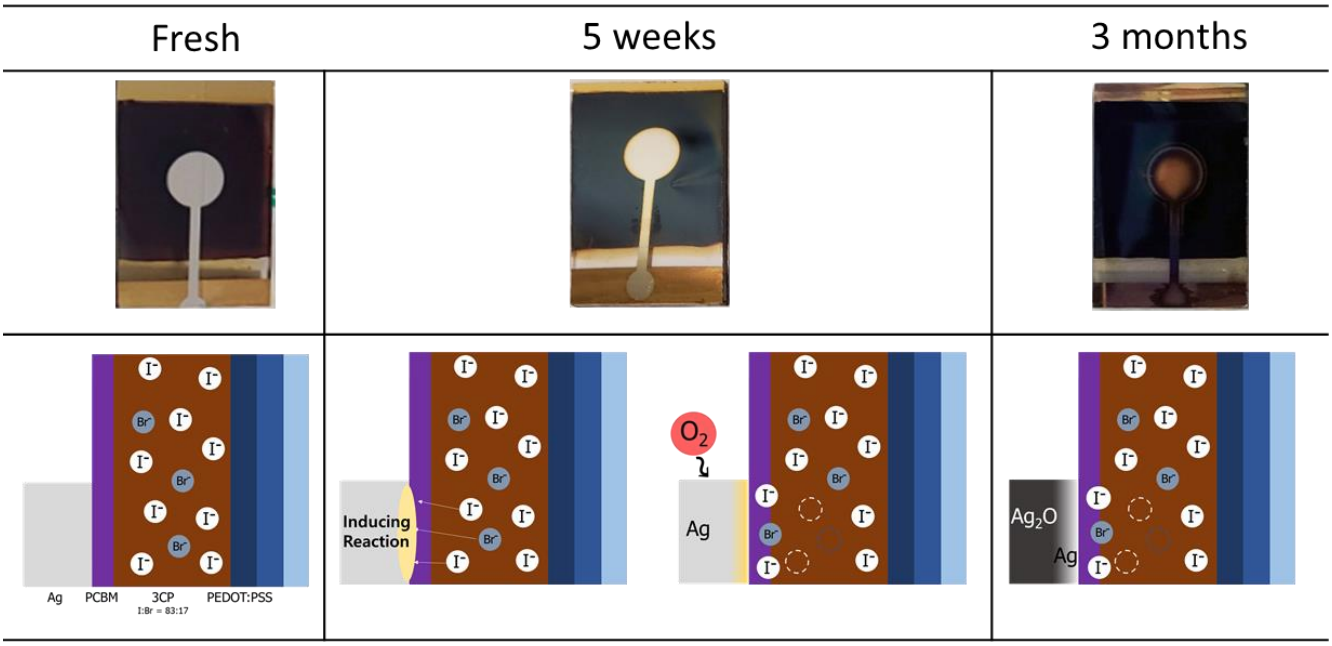

Figure 5.11. Schematic diagram explaining the ageing mechanism of 3CP solar cells; a) unaged halogen ion distribution in the 3CP layer, b) Generation of increased halide vacancies due to initial chemical reaction ($Ag^+ + Br^- \rightarrow AgBr$ *and* $Ag^+ + I^- \rightarrow AgI$), c) Ag_2O reaction in the air ($4Ag + O_2 \rightarrow 2Ag_2O$), and d) After reaching the reaction equilibrium.

The ageing characteristics are summarized in Table 5.1. The ageing of MAPI and 3CP devices discussed in Section 5.3.2 is mainly due to the chemical reaction between the silver electrode and the halide cation—the constituents of the perovskite. Because of the superior stability of the 3CP device over

MAPI in nitrogen, air storage conditions were applied to accelerate the ageing. Even when 3CP cells were exposed to oxygen, stronger ageing resistance was observed. The GD-OES results demonstrate that the diffusion distance of halide ions is related to ageing resistance.

Sample	MAPI	3CP
Storage condition	N_2	O_2
Ageing period	4 weeks	3 months
Diffused ion	I	Br, I
Diffusing direction	Ag electrode	Ag electrode
Principle of diffusion	Concentration difference of halogen ions due to chemical reaction	
Chemical product	AgI	AgBr, AgI, Ag_2O
Ion diffusion distance	>120nm (speculated)	50-60nm
Area of ion diffusion	Electrode area & around (Fig 5.8e)	Electrode area (Fig 5.9e)

Table 5.1. Summary of GD-OES result interpretation.

5.3.3. conclusion

Solar cell aging studies using J-V measurements were conducted under N_2 ambient storage conditions. Over time, the MAPI device showed that the J-V performance curve formed an S-shape as ageing progressed. Then, the cell stopped working after 8 weeks. The aspect inferring that a barrier is formed inside the device was motivated by the S-shaped curve.

The short-term ageing study used an IS installed in the air. The results showing that ions accumulate on one side over time were obtained through the 3CP study. The increase in resistance due to device degradation made it impossible to measure IS due to noise when the resistance exceeds $5x10^7$.

The long-term ageing studies were observed using GD-OES. The main cause of aging is the silver electrode and halide cation, the constituents of perovskite, and the chemical reaction. Compared to MAPI, 3CP showed overwhelming ageing stability results, as mentioned in 3CP studies [3, 32].

5.4. Conclusion

A prerequisite for the commercialization of Perovskite Solar Cells (PSCs) is ageing stability. In this chapter, the ageing process of MAPI and 3CP was discussed with optical (XRD, UV-Vis absorption), electrical (IS), and physical (GD-OES) approaches. Film stack (ITO/PEDOT:PSS/perovskite) ageing and

solar cell device degradation were carried out to distinguish the cause of adjacent layers and the cause of the perovskite itself.

The film ageing observation demonstrated that perovskite (MAPI and 3CP) film is stable in N_2 under dark. When the perovskite stacks were surrounded by air (without light) for five weeks, MAPI stack (ITO/PEDOT:PSS/MAPI) was degraded, and 3CP stack (ITO/PEDOT:PSS/3CP) showed no degradation comparing to MAPI.

The PSCs ageing research was performed with three approaches: Solar Cell Performance Ageing (SCPA), IS, and GD-OES. The SCPA showed that the perovskite solar cells stored in N_2 exhibited faster degradation than the perovskite films stored in N_2. During SCPA, the discovered sigmoid shaped curve allowed us to deduce that a barrier was formed inside the device.

Short-term ageing observed with IS informed that accumulation of ions is observed at the interface after degradation. Accumulated ions create the additional circuit elements increasing over time at an interface. Then, additional capacitance and resistance are measured with IS. However, IS measurement is limited due to harsh noise when the resistance of the degraded device exceeds $5x10^7$.

The long-term ageing studies with GD-OES found the primary cause of ageing in the air. After short-term ageing forming a double-layer at an interface, the transition to long-term ageing results in chemical reaction-dominant. The halide anions react with a silver electrode. The increased halide vacancies are filled with diffusion from neighbors. The total quantity of halide in the perovskite layer reduces by the amount of iodide adsorbed to the Ag layer. 3CP solar cells showed superior degradation stability to MAPI devices, as mentioned in 3CP studies [3,32].

5.5. References

[1] National Renewable Energy Laboratory, N.R.E.L. https://www.nrel.gov/pv/assets/pdfs/best-research-cell-efficiencies-rev210726.pdf. Accessed 26 July 2021.

[2] M. Saliba, T. Matsui, K. Domanski, J.-Y. Seo, A. Ummadisingu, S.M. Zakeeruddin, J.-P. Correa-Baena, W.R. Tress, A. Abate, A. Hagfeldt, M. Grätzel, Incorporation of Rubidium Cations into Perovskite Solar Cells Improves Photovoltaic Performance. Science 2016, 354, 206-209.

[3] M. Saliba, T. Matsui, J-Y. Seo, K. Domanski, J-P. Correa-Baena, M. K. Nazzeruddin, S. M. Zakeeruddin, W. Tress, A. Abate, A. Hagfeldt, M. Gratzel, Cesium-containing triple cation perovskite solar cells: Improved stability, reproducibility, and high efficiency. *Energy Environ. Sci*. **2016**, *9*, 1989–1997.

[4] D. Wang, M. Wright, N. K. Elumalai, A. Uddin, Stability of perovskite solar cells. *Sol. Energy Mater. Sol. Cells*. **2016**, *147*, 255-275.

[5] T.A. Berhe, W.N. Su, C.H. Chen, C.J. Pan, J.H. Cheng, H.M. Chen, M.C. Tsai, L.Y. Chen, A.A. Dubale, B.J. Hwang, Organometal Halide Perovskite Solar Cells: Degradation and Stability. *Energy Environ. Sci*. **2016**, *9*, 323-356.

[6] J. M. Frost, A. Walsh, What is moving in Hybrid Halide Perovskite Solar Cells? *Acc. Chem. Res*. **2016**, *49*, 528-535.

[7] M. Saliba, J.-P. Correa-Baena, M. Grätzel, A. Hagfeldt, A. Abate, Perovskite Solar Cells: From the Atomic Level to Film Quality and Device Performance. *Angew. Chem. Int.* Ed. **2018**, *57*, 2554-2569.

[8] S. Kumar, G. Hodes, D. Cahen, Defects in Halide Perovskites: The Lattice as a Boojum? *MRS Bulletin* **2020**, *45*, 478-484.

[9] C. Gehrmann, D.A. Egger, Dynamic Shortening of Disorder Potentials in Anharmonic Halide Perovskites. *Nat. Commun*. **2019**, *10*, 3141.

[10] B. Conings, J. Drijkoningen, N. Gauquelin, A. Babayigit, J. D'Haen, L. D'Olieslaeger, A. Ethirajan, J. Verbeeck, J. Manca, E. Mosconi, F. De Angelis, H.-G. Boyen, Intrinsic Thermal Instability of Methylammonium Lead Trihalide Perovskite. *Adv. Energy Mater*. **2015**, *5*, 1500477.

[11] R.K. Misra, S. Aharon, B. Li, D. Mogilyansky, I. Visoly-Fisher, L. Etgar, E. A. Katz, Temperature- and Component-Dependent Degradation of Perovskite Photovoltaic Materials under Concentrated Sunlight. *J. Phys. Chem. Lett*. **2015**, *6*, 326-330.

[12] S. Wang, Y. Jiang, E. J. Juarez-Perez, L.K. Ono, Y. Qi, Accelerated Degradation of Methylammonium Lead Iodide Perovskites Induced by Exposure to Iodine Vapour. *Nature Energy*, **2017**, *2*, 16195

[13] N. Aristidou, I. Sanchez-Molina, T. Chotchuangchutchaval, M. Brown, L. Martinez, T. Rath, S.A. Haque, The Role of Oxygen in the Degradation of Methylammonium Lead Trihalide Perovskite Photoactive Layers. *Angew. Chem. Int.* Ed. **2015**, *54*, 8208-8212.

[14] D. Bryant, N. Aristidou, S. Pont, I. Sanchez-Molina, T. Chotchuangchutchaval, S. Wheeler, J.R. Durrant, S.A. Haque, Light and Oxygen Induced Degradation limits the Operational Stability of Methylammonium Lead Triiodide Perovskite Solar Cells. *Energy Environ. Sci.* **2016**, *9*, 1655-1660.

[15] N. Aristidou, C. Eames, I. Sanchez-Molina, X. Bu, J. Kosco, M.S. Islam, S.A. Haque, Fast Oxygen Diffusion and Iodide Defects mediate Oxygen-Induced Degradation of Perovskite Solar Cells. *Nat. Commun.* **2017**, *8*, 15218.

[16] Q. Sun, P. Fassl, D. Becker-Koch, A. Bausch, B. Rivkin, S. Bai, P.E. Hopkinson, H.J. Snaith, Y. Vaynzof, Role of Microstructure in Oxygen Induced Photodegradation of Methylammonium Lead Triiodide Perovskite Films. *Adv. Energy Mater*. **2017**, *7*, 1700977.

[17] A. Senocrate, T. Acartürk, G.Y. Kim, R. Merkle, U. Starke, M. Grätzel, J. Maier, Interaction of Oxygen with Halide Perovskites. *J. Mater. Chem. A*, **2018**, *6*, 10847-10855.

[18] G. Grancini, S. Marras, M. Prato, C. Giannini, C. Quarti, F. De Angelis, M. De Bastiani, G.E. Eperon, H.J. Snaith, L. Manna, A. Petrozza, The Impact of the Crystallization Processes on the Structural and Optical Properties of Hybrid Perovskite Films for Photovoltaics. *J. Phys. Chem. Lett*. **2014**, *5*, 3836-3842.

[19] J. Holovsky, S. De Wolf, J. Werner, Z. Remes, M. Müller, N. Neykova, M. Ledinsky, L. Cerna, P. Hrzina, P. Löper, B. Niesen, C. Ballif, Photocurrent Spectroscopy of Perovskite Layers and Solar Cells: A Sensitive Probe of Material Degradation. *J. Phys. Chem. Lett.* **2017**, *8*, 838-843.

[20] E. T. Hoke, D. J. Slotcavage, E. R. Dohner, A. R. Bowring, H. I. Karudanasa, M. D. McGehee, Reversible, Photo-Induced Trap Formation in Mixed-Halide Hybrid Perovskites for Photovoltaics. *Chem. Sci*. **2015**, *6*, 613-617.

[21] G. Grancini, V. D'Innocenzo, E. R. Dohner, N. Martino, A. R. Srimath Kandada, E. Mosconi, F. De Angelis, H.I. Karunadasa, E.T. Hoke, A. Petrozza, $CH_3NH_3PbI_3$ Perovskite Single Crystals: Surface Photophysics and their Interaction with the Environment. *Chem. Sci.*, **2015**, *6*, 7305-7310.

[22] A. M. A. Leguy, Y. Hu, M. Campoy-Quiles, M. I. Alonso, O. J. Weber, P. Azarhoosh, M. van Schilfgaarde, M. T. Weller, T. Bein, J. Nelson, P. Docampo, P. R. F. Barnes, Reversible Hydration of $CH_3NH_3PbI_3$ in Films, Single Crystals and Solar Cells. *Chem. Mater*. **2015**, *27*, 3397-3407.

[23] J. Huang, S. Tan, P. D. Lund, H.Zhou, Impact of H_2O on Organic-Inorganic Hybrid Perovskite Solar Cells, *Energy Environ. Sci*. **2017**, *10*, 2284-2311.

[24] M.J. Hong, R.Y. Johnson, J.G. Labram, Impact of Moisture on Mobility in Methylammonium Lead Iodide, *J. Phys. Chem. Lett.* **2020**, *11*, 4976-4983.

[25] H. Yuan, E. Debroye, K. Janssen, H. Naiki, C. Steuwe, G. Lu, M. Moris, E. Orgiu, H. Uji-i, F. De Schryver, P. Samori, J. Hofkens, M. Roeffaers, Degradation of Methylammonium Lead Iodide Perovskite Structures through Light and Electron Beam Driven Ion Migration. *J. Phys. Chem. Lett*. **2016**, *7*, 561-566.

[26] Q. Wang, N. Phung, D. Di Girolamo, P. Vivo, A. Abate, Enhancement in Lifespan of Halide Perovskite Solar Cells. *Energy Environ. Sci*. **2019**, *12*, 865-886.

[27] T. Leijtens, G. E. Eperon, N. K. Noel, S. N. Habisreutinger, A. Petrozza, H. J. Snaith, Stability of Metal Halide Perovskite Solar Cells. *Adv. Energy Mater*. **2015**, *5*, 1500963.

[28] G. Niu, X. Guo, L. Wang, Review of Recent Progress in Chemical Stability of Perovskite Solar Cells. *J. Mater. Chem. A*, **2015**, *3*, 8970-8980.

[29] T. Leijtens, K. Bush, R. Cheacharoen, R. Beal, A. Bowring, M.D. McGehee, Towards Enabling Stable Lead Halide Perovskite Solar Cells; Interplay between Structural, Environmental and Thermal Stability. Intrinsic Thermal Instability*J. Mater. Chem. A*, **2017**, *5*, 11483-11500.

[30] Y. Yang, J. You, Make Perovskite Solar Cells Stable. *Nature*, **2017**, *544*, 155-156.

[31] M. Saliba, Perovskite Solar Cells must Come of Age. *Science*, **2018**, *359*, 388-389.

[32] M. Saliba, M. Stolterfoht, C.M. Wolff, D. Neher, A. Abate, Measuring Aging Stability of Perovskite Solar Cells. *Joule*, **2018**, *2*, 1019-1024.

[33] X. Li, M. I. Dar, C. Yi, J. Luo, M. Tschumi, S. M. Zakeeruddin, M. K. Nazeeruddin, H. Han, M. Grätzel, Improved performance and stability of perovskite solar cells by crystal crosslinking with alkylphosphonic acid o-ammonium chlorides. *Nat. Chem*. **2015**, *7*, 703–711.

[34] Z. Yang, A. Rajagopal, S.B. Jo, C-C. Chueh, S. Williams, C-C. Huang, J.K. Katahara, H. W. Hillhouse, A.K-Y. Jen, Stabilized Wide Bandgap Perovskite Solar Cells by Tin Substitution. *Nano Lett*. **2016**, *16*, 7739–7747.

[35] W. Qiu, T. Merckx, M. Jaysankar, C. Masse de la Huerta, L. Rakocevic, W. Zhang, U.W. Paetzold,

R. Gehlhaar, L. Froyen, J. Poortmans, D. Cheyns, H.J. Snaith, P. Heremans, Pinhole-free perovskite films for efficient solar modules. *Energy Environ. Sci*. **2016**, *9*, 484–489.

[36] B. Charles, J. Dillon, O. J. Weber, M. S. Islam, M. T. Weller, Understanding the Stability of Mixed A-Cation Lead Iodide Perovskites. J. Mater. Chem. A 2017, 5, 22495-22499.

[37] K. A. Bush, C. D. Bailie, Y. Chen, A. R. Bowring, W. Wang, W. Ma, T. Leijtens, F. Moghadam, and M. D. McGehee. Thermal and Environmental Stability of Semi-Transparent Perovskite Solar Cells for Tandems Enabled by a Solution-Processed Nanoparticle Buffer Layer and Sputtered ITO Electrode. **2016**, *Adv. Mater*., **28**, 20, 3937-3943.

[38] Y. Han, S. Meyer, Y. Dkhissi, K. Weber, J. M. Pringle, U. Bach, L. Spiccia and Y-B. Cheng. Degradation observations of encapsulated planar $CH_3NH_3PbI_3$ perovskite solar cells at high temperatures and humidity. **2015**, *J. Mater. Chem. A*, **3**, 8139–8147.

[39] M. Kaltenbrunner, G. Adam, E. D. Głowacki, M. Drack, R. Schwödiauer, L. Leonat, D. H. Apaydin, H. Groiss, M. C. Scharber, M. S. White, N. S. Sariciftci and S. Bauer. Flexible high power-per-weight perovskite solar cells with chromium oxide–metal contacts for improved stability in air. **2015**, *Nat. Mater*. **14**, 1032–1039.

[40] A. Marronniera, H. Lee, H. Lee, M. Kim, C. Eypert, J-P. Gaston, G. Roma, D. Tondelier, B. Geffroy, Y. Bonnassieux. Electrical and optical degradation study of methylammonium-based perovskite materials under ambient conditions. **2018**, *Sol. Energy Mater. Sol. Cells*, **178**, 179-185.

[41] H. Lee, S. Gaiaschi, P. Chapon, A. Marronnier, H. Lee, J.-C. Vanel, D. Tondelier, J.E. Bourée, Y. Bonnassieux, B. Geffroy, Direct Experimental Evidence of Halide Ionic Migration under Bias in $CH_3NH_3Pb_{3-x}Cl_x$-Based Perovskite Solar Cells using GD-OES Analysis. ACS Energy Lett. 2017, 2, 943-949.

[42] H. Yu, F. Wang, F. Xie, W. Li, J. Chen, N. Zhao, The Role of Chlorine in the Formation Process of $CH_3NH_3PbI_{3-x}Cl_x$ Perovskite. *Adv. Funct. Mater*. **2014**, *24*, 7102-7108.

[43] J. M. Azpiroz, E. Mosconi, J. Bisquert, F. De Angelis, Defect Migration in Methylammonium lead Iodide and its Role in Perovskite Solar Cell Operation. *Energy Environ. Sci*. **2015**, *8*, 2118-2127.

[44] J. Haruyama, K. Sodeyama, L. Han, Y. Tateyama, First-Principles Study of Ion Diffusion in Perovskite Solar Cell Sensitizers. *J. Am. Chem. Soc*. **2015**, *137*, 10048-10051.

[45] C. Eames, J. M. Frost, P. R. F. Barnes, B. C. O'Regan, A. Walsh, M. S. Islam, Ionic Transport in Hybrid Lead Iodide Solar Cells. *Nat. Commun*. **2015**, *6*, 7497.

[46] Y. Kato, L. K. Ono, M. V. Lee, S. Wang, S. R. Raga, Y. Qi, Silver Iodide Formation in

Methylammonium Lead Iodide Perovskite Solar Cells with Silver Top Electrodes. Adv. Mater. Interfaces 2015, 2, 1500195.

[47] J. Li, Q. Dong, N. Li, L. Wang, Direct Evidence of Ion Diffusion for the Silver-Electrode-Induced Thermal Degradation of Inverted Perovskite Solar Cells. Adv. Energy Mater. 2017, 7, 1602922.

[48] J. Carrillo, A. Guerrero, S. Rahimnejad, O. Almora, I. Zarazua, E. Mas-Marza, J. Bisquert, G. Garcia-Belmonte, IonicReactivity at Contacts and Aging of Methylammonium Lead Triiodide Perovskite Solar Cells. Adv. Energy Mater. 2016,6, 1502246.

[49] S. Fujita. Organic Chemistry of Photography. *Springer*, **2004**, ISBN-13: 978-3540209881.

Chapter 6. Conclusion and Outlook

6.1. Conclusion

In this thesis, investigation of MAPI ($MAPbI_{3-x}Cl_x$) and 3CP ($(MA_{0.17}FA_{0.83})_{0.95}Cs_{0.05}Pb(I_{0.83}Br_{0.17})_3$ perovskite materials has been presented. Ion migration and ageing mechanism have been studied with various approaches. Here, the key findings and related conclusions are summarized, and prospective works are suggested.

First, perovskite solar cell fabrication process was introduced. The optimization process was iterative through thickness control and perovskite crystallinity. Thin film formation is a delicate process that can be tuned in nanometer scale and is an important technique that determines the performance of a device. PEDOT:PSS and $PC_{60}BM$ were fabricated by spin-coating as Hole Transport Layer (HTL) and Electron Transport Layer (ETL). Their thicknesses, confirmed by SEM cross-section image, were determined as a condition leading to the maximum device performance. For destructive analysis, planned to observe ion migration with GD-OES, it was essential to secure the reproducibility with little performance variation between devices. In the spin-coating technique, the perovskite, too viscous solution, had a thickness deviation of more than 100 nm. Dynamic-dispense reduced the thickness variation between perovskite layers to less than 20 nanometers. As a result, the efficiency deviation obtained in 1 batch achieved 0.21%. For MAPI, the process of the previous researcher (Dr. Heejae Lee) was adopted. 3CP, which has significantly improved electrical and ageing stability, was optimized by referring to various literature. The crystallinity of these two perovskite films was optimized while monitoring by SEM and XRD. The power conversion efficiency in p-i-n planar configuration devices was reached at 13.0%, indicating the competitive performance considering electrode area (0.28 cm^2).

Second, the GD-OES was attempted to obtain direct experimental evidence of ion (I and Br) migration in 3CP [$\{(CH_3NH_3)_{0.17}(CH(NH_2)_2)_{0.83}\}_{0.95}Cs_{0.05}Pb(I_{0.83}Br_{0.17})_3$] {$MA^+$: CH_3NH_3, FA^+: $CH(NH_2)_2{}^+$} based perovskite solar cells under electric field. The migration of organic cations (MA^+ and FA^+) and

Pb^{2+} was not observed under an electric field. The ratio of fixed to mobile iodide in MAPI was 35% and the migrating average length was 120 nm determined with ex-situ measurement [1]. However, with 3CP, the observed recovery of ion migration was faster (less than 1 min). So, halide ion migration was observed through the in-situ electric field method. Since the sputtering speed is changed according to the magnitude of applied voltage (for the in-situ method), we cannot calculate the ratio of fixed ions and the migration distance. In addition, the interfacial ion accumulation was also observed with Impedance Spectroscopy (IS), when 2 minutes J-V sweep was applied. IS results demonstrated newly formed capacitance which is due to the double layer at the interface formed by ion accumulation (halide ion as proved by GD-OES). An interpretation complemented by SEM is that the accumulation of ions occurs through grain boundaries, which is the fastest path for ion movement.

Third, the film ageing observation demonstrated that perovskite (MAPI and 3CP) film is stable in N_2 under dark. When the perovskite stacks were surrounded by air (without light) for five weeks, the MAPI stack (ITO/PEDOT:PSS/MAPI) was degraded, and the 3CP stack (ITO/PEDOT:PSS/3CP) was stable. The PSC ageing research was performed with three approaches: Solar Cell Performance Ageing (SCPA), IS, and GD-OES. The SCPA analysis showed that the perovskite solar cells stored in N_2 exhibited faster degradation than the perovskite films stored in N_2. During the SCPA, the discovered sigmoid shape allowed us to deduce that a barrier was formed inside the device. The IS result informed that additional capacitance and resistance are formed in the solar cell over time. Accumulated ions create the additional circuit elements increasing over time.

Long-term ageing found the primary cause of ageing in the air with GD-OES. The long-term ageing results in chemical reaction-dominant degradation. The halide anions, the components of perovskite, react with a silver electrode after diffusion through the perovskite and $PC_{60}BM$ layers (the hopping process through vacancies).

Of course, there are other various processes and causes for the ageing phenomena of the PSCs. The halide ionic diffusion, which we discovered, must be one of them. Our results suggest a favorable guideline to understanding PSCs' device degradation and design future stable PSCs devices.

6.2. Outlook

6.2.1 Prospective work: Suggestion to improve device ageing stability

In the aging study, a cause of promoting the lifespan of the perovskite device was the condition in which mobile ions and silver (Ag) top could react. The experimental observation that PCBM is the mediator of iodine ion migration supports our interpretation [2,3]. J. Li et al. [3] observed AgI formation through thermal degradation. In addition, there is a study in which iodine ions migrated via Spiro-OMeTAD (HTL) from the perovskite layer in the conventional n-i-p structure (FTO/cp-TiO_2/mp-TiO_2/$MAPbI_3$/Spiro-OMeTAD/Mo/Ag) [4].

We introduce and suggest a method to increase the lifespan of the p-i-n structured PSCs. Bathocuproine (BCP) is hydrophobic organic material. BCP performs sufficient hydrophobic effect even it is used a little in the PSC device. Two studies demonstrated hydrophobicity:

- When a small amount of BCP was doped into the PCBM layer [5].
- When an ultra-thin (less than 10 nm) BCP was deposed on the perovskite thin film [6].

In both methods, the effect of increasing device efficiency (especially improving FF) is observed. Y. The effect of improving the device lifespan is also reported from Wang et al. [6], and the ageing stability was also observed in the device manufactured by depositing about 5-10 nm of BCP between PCBM and Ag (Fig.6.1.). The device fabrication and ageing analysis are performed by Ph.D. Haeyeon Jun of Ecole Polytechnique.

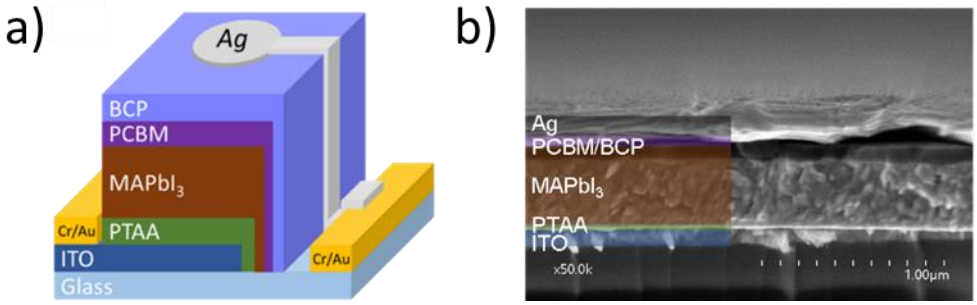

Figure 6.1. a) Schematic of thermally evaporated MAPI based PSC and b) SEM cross-section image of the solar cell made by PhD. Haeyeon Jun @LPICM/Ecole Polytechnique (hae-yeon.jun@polytechnique.edu).

The ageing stability is discovered in IS ageing observation (Fig. 6.2) and J-V performance (Fig. 6.3). Figure 6.2 shows impedance data collected from a single ITO/PTAA/MAPI-evap/PCBM/BCP/Ag device when fresh and 40 days aged in air. In the complex impedance plot in the log-log scale (Figure 6.2a), the

complex impedance shows a progressive change of the resistive behavior at the lower frequency range upon ageing while no modification is observed at high frequency. In the Bode phase plot (Figure 6.2b), there is a phase closed to -90 degrees at 100 kHz in the fresh sample. When time runs out up to 40 days, a second capacitive behavior emerges by the phase close to -90 degrees at a lower frequency range (100 Hz - 1 kHz). This feature at 100 Hz - 1 kHz is attributed to a charge accumulation layer occurring at the interface between MAPId and selective contact materials. In Figure 6.2c, a single semicircle in the Nyquist plot indicates the single conduction mechanism. As ageing time increases, the radius of this semicircle increases, suggesting a degradation of the solar cell corresponding to a decrease in the conductivity. In figure 4d, we have plotted the theoretical capacitance deduced from IS measurement as a function of the frequency. For the fresh device, only a single capacitance (C_g ~ 10 nF) is obtained at a high frequency corresponding to the geometrical capacitance mentioned previously. However, after ageing time, a second capacitance (C_3) appears with a value around 6 nF clearly seen after 40 days of ageing time (the measured value at lower frequency in Figure 6.2d is the sum of C_g+C_3).

The BCP inserted MAPI solar cell's degradation seems to be much slower than the 3CP solar cell (Chapter 5.3.1, Fig.5.7) since the evolution second capacitance (C_3) is observed after 40 days of ageing. If we name the solar cell for IS ageing as "MAPI-a", another solar cell (name as "MAPI-b") is manufactured in the same batch (and same structure) is employed to compare J-V performance degradation and IS ageing. J-V performance is measured only when 0 day and 40 days for MAPI-b. During 40 days, the MAPI-a and MAPI-b were stored under the same condition (under dark in the air). MAPI-b is not used to measure J-V performance while it is stored for 40 days.

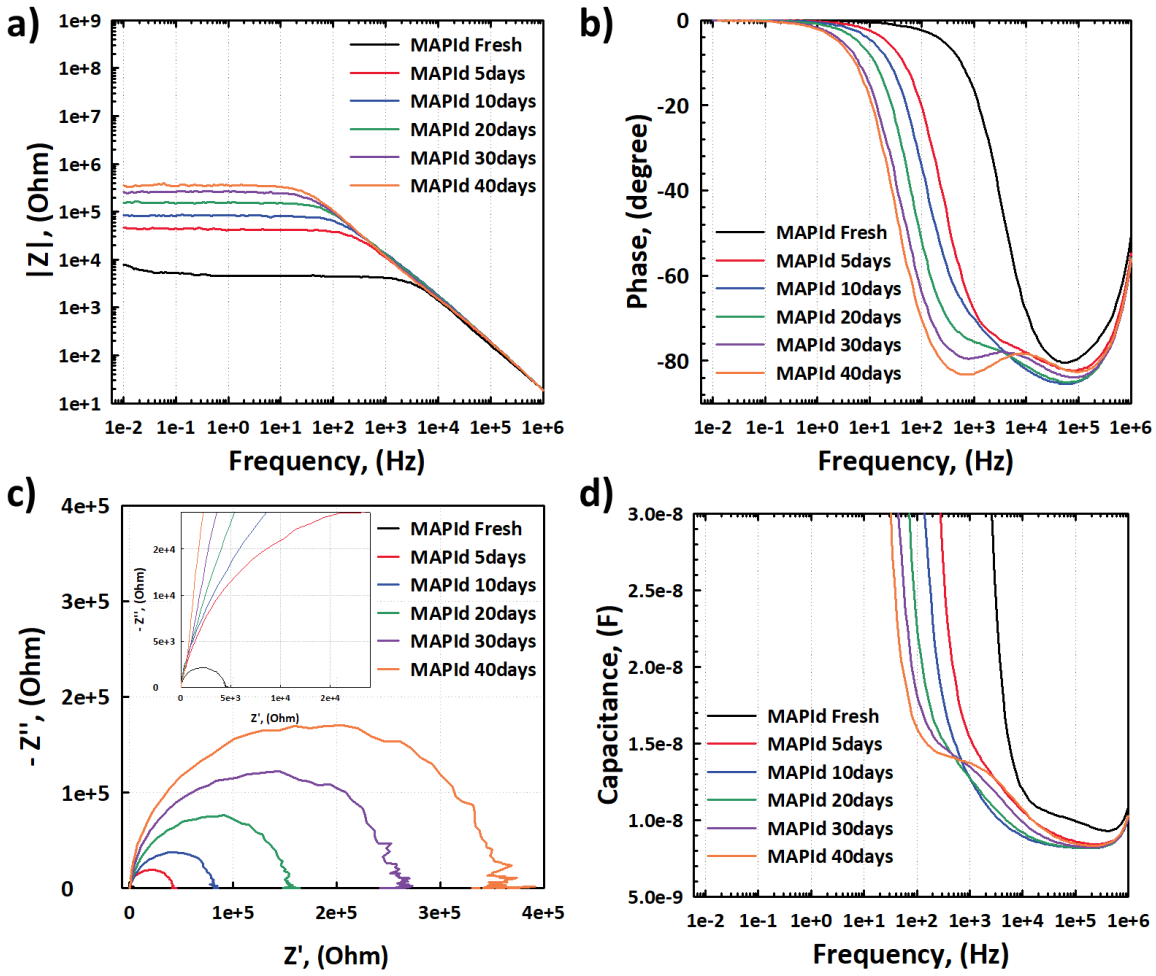

Figure 6.2. IS characteristics evolution as a function of ageing time for MAPId solar cell; a) Complex impedance versus frequency; b) Phase versus frequency; c) Nyquist plot; d) Capacitance versus frequency.

As a result, the same trend is obtained for the MAPI-b solar cell (Figure 6.3) upon ageing. According to Fig. 6.3 and Table 6.1, the fill factor increases due to an increase of shunt resistance after 40 days. This result is quite impressive compared to the general short lifespan of MAPI and 3CP without BCP (Chap 5.3, Fig.5.5). Such a difference could be explained by the presence of solvent traces in solution-processed solar cells, which facilitate the ion displacement within the perovskite layer. The use of BCP as a buffer layer prevents the diffusion of polar solvents due to the hydrophobicity, thereby blocking the reaction of Ag with the halides from the perovskite layer.

Ph.D. Haeyeon Jun's excellent devices (ITO/PTAA/MAPI/PCBM/BCP/Ag) were fabricated with thermally evaporated MAPI and BCP. It can be suggested that solvent-free deposition is the key role of

anti-ageing. However, C. Besleaga et al. [4] observed AgI even when the molybdenum (Mo) layer was evaporated (FTO/cp-TiO_2/mp-TiO_2/MAPI/Spiro-OMeTAD/Mo/Ag). Considering the works of literature [2-6], the ion diffusion prevention effect of BCP is reasonable.

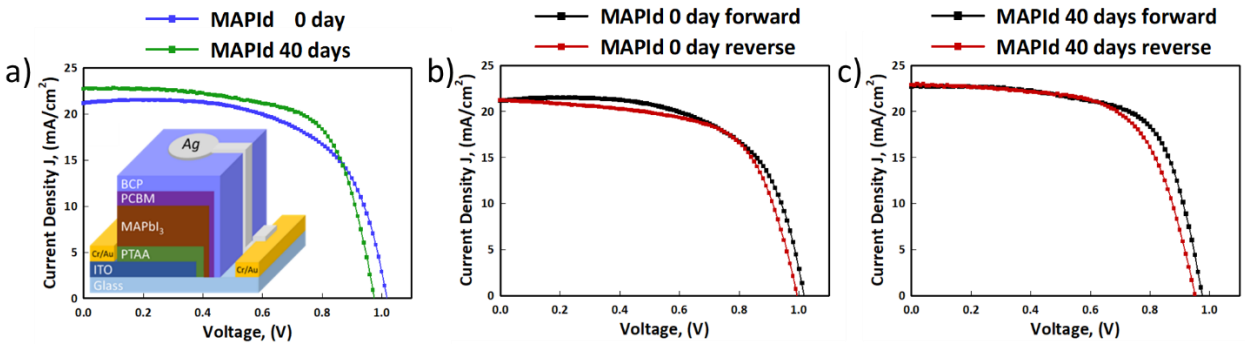

Figure 6.3. Ageing observation with J-V performances. a) device performance comparison between 0 day and after 40 days in the air (the curve is recorded with forward bias), b) fresh, and c) 40-day-old BCP inserted MAPI device performance under 1 sun illumination (100 mW/cm^2).

Factor **(Unit)**	Eff. (%)	V_{oc} (V)	J_{sc} (mA/cm^2)	F.F. (%)	R_{sh} (Ω)	R_s (Ω)
MAPId 0 day Forward Bias	13.4	1.00	21.2	62.3	233	5.6
MAPId 0 day Reverse Bias	13.4	0.99	21.2	63.5	524	6.7
MAPId 40 days Forward Bias	14.8	0.98	22.7	66.9	1.8k	5.3
MAPId 40 days Reverse Bias	13.9	0.95	22.9	63.9	1.0k	6.2

Table 6.1. Summary of BCP inserted MAPI device performance before and after ageing.

For the perspective work, I propose to conduct a study to confirm the anti-aging effect of BCP:

- Confirming optimal BCP thickness for device efficiency.
- Most extended lifespan of BCP device.
- Confirming AgI formation at the top silver electrode through XPS.

Although perovskite solar cells have price competitiveness compared to commercial solar cells [7], their short lifespan is still an obstacle. Studying how to overcome the ageing problem will be an exciting and promising study.

6.3. Conference

During the first doctoral period, I attended the following conferences about device lifetime and the observation of ion migration using GD-OES:

- JNPV 2021 (Journées Nationales du PhotoVoltaïque) - organising assistant
- JNPV 2019 (Journées Nationales du PhotoVoltaïque)
- JPH 2019 (Journées Pérovskites Halogénées)
- JNPV 2018

6.4. Publications

With the help of my lab LPICM and Horiba scientific, I published an article with Arthur Marronnier, Heeryung Lee, Heejae Lee, Céline Eypert, Jean-Paul Gaston, Guido Roma, Denis Tondelier, Bernard Geffroy, Yvan Bonnassieux called:

1. "Electrical and optical degradation study of methylammonium-based perovskite materials under ambient conditions". *Sol. Energy Mater. Sol. Cells* 178, 179–185 (2018). doi.org/10.1016/j.solmat.2018.01.020.

Collaborating with LPS (Laboratoire de Physique des Solides) of Université Paris Saclay, we (Subodh K. Gautam, Minjin Kim, Douglas R. Miquita, Jean-Eric Bourée, Bernard Geffroy, and Olivier Plantevin published (Appendix A.4):

2. "Reversible Photo-Induced Phase Segregation and Origin of Long Carrier Lifetime in Mixed-Halide Perovskite Films." *Adv. Funct. Mater*. **2020**, 2002622. DOI: 10.1002/adfm.202002622

Minjin Kim, Haeyeon Jun, Heejae Lee, Hindia Nahdi, Denis Tondelier, Yvan Bonnassieux, Jean-Éric Bourée, and Bernard Geffroy of LPICM submitted the first revision to EUR-JIC in September 9th as:

3. "Halide ion migration and its role at the interfaces in perovskite solar cells" *Eur. Jic*. **2021**, submission: ejic.202100654R1.

6.5. References

[1] H, Lee, Under the direction of Yvan Bonnassieux, Thesis: Analysis of Current-Voltage Hysteresis and Ageing Characteristics for $CH_3NH_3PbI_{3-x}Cl_x$ Based Perovskite Thin Film Solar Cells: http://theses.fr/2018SACLX009.

[2] M. De Bastiani, G. Dell'Erba, M. Gandini, V. D'Innocenzo, S. Neutzner, A. R. S. Kandada, G. Grancini, M. Binda, M. Prato, J. M. Ball, M. Caironi, and A. Petrozza., *Adv. Energy Mater*. **2016**, 6, 1501453.

[3] J. Li, Q. Dong, N. Li, L. Wang, Direct Evidence of Ion Diffusion for the Silver-Electrode-Induced Thermal Degradation of Inverted Perovskite Solar Cells, *Adv. Energy Mater*. **2017**, 1602922.

[4] C. Besleaga, L. E. Abramiuc, V. Stancu, A. G. Tomulescu, M. Sima, L. Trinca, N. Plugaru, L. Pintilie, G. A. Nemnes, M. Iliescu, H. G. Svavarsson, A. Manolescu, and I. Pintilie., *J. Phys. Chem. Lett*. **2016**, 7, 5168–5175.

[5] R. Chen, B. Long, S. Wang, Y. Liu, J. Bai, S. Huang, H. Li, X. Chen, Efficient and Stable Perovskite Solar Cells Using Bathocuproine Bilateral-Modified Perovskite Layers. *ACS Appl. Mater. Interfaces*. **2021**, *13*, 24747−24755

[6] Y. Wang, S. Dong, Y. Miao, D. Li, W. Qin, H. Cao, L. Yang, L. Li, S. Yin, BCP as Additive for Solution-Processed PCBM Electron Transport Layer in Efficient Planar Heterojunction Perovskite Solar Cells. *IEEE J. Photovolt*. **2017**, *7*, 550-557.

[7] M. Cai, Y. Wu, H. Chen, X. Yang, Y. Qiang, L. Han, Cost-Performance Analysis of Perovskite Solar Modules. *Adv. Sci.* **2017**, *4*, 1, 1600269.

Appendix

A.1. Fundamentals of Impedance Spectroscopy (IS)

Impedance (Z) is the ratio of voltage and current over time:

$$Z = \frac{V(t)}{i(t)} \qquad \text{A.1 - (1)}$$

Unlike resistance, impedance changes in time and frequency. The impedance measurement is the method of measuring the current response $i(t) = i_0 cos(\omega t - \varphi)$ when applying a sinusoidal voltage perturbation or AC voltage $V(t) = V_0 cos(\omega t)$ to the system under evaluation, where V_0 and i_0 are the amplitudes of the voltage and current. ω is the radiation frequency (ω=2πf). Therefore, the current response of the system is out of phase of φ relative to the AC voltage (Fig. A.1.1).

$$Z = \frac{V_0 cos(\omega t)}{i_0 cos(\omega t - \varphi)} = Z_0 \frac{cos(\omega t)}{cos(\omega t - \varphi)} \qquad \text{A.1 - (2)}$$

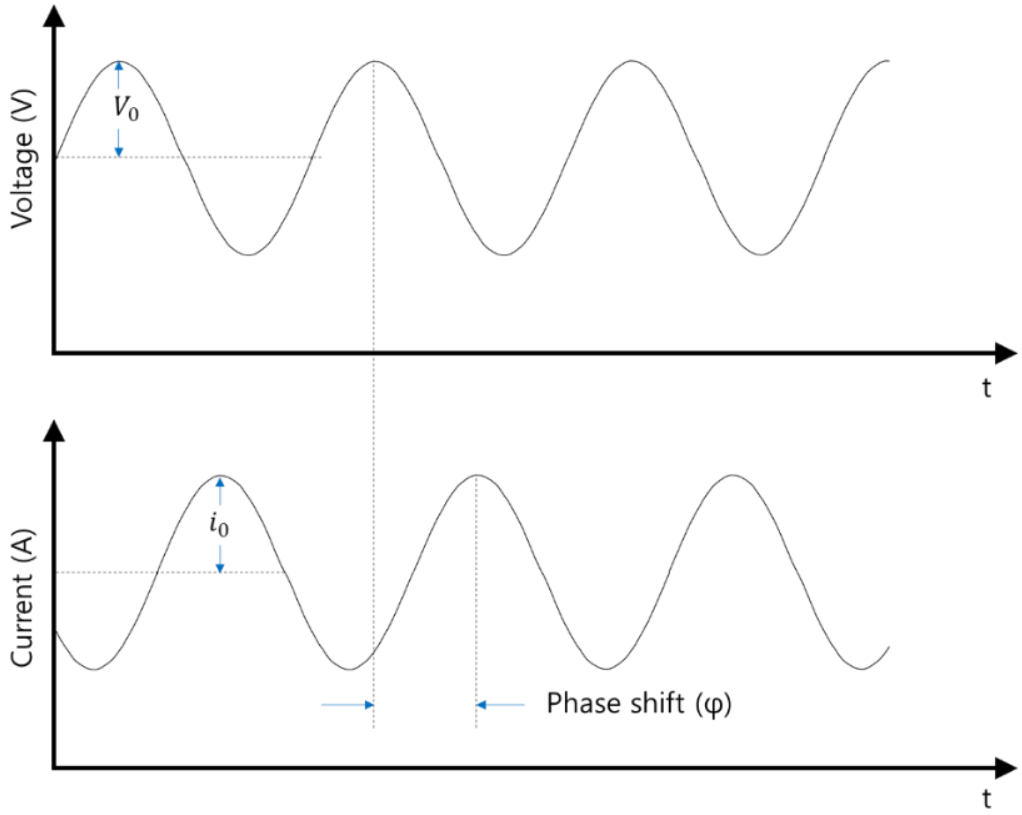

Figure A. 1. 1. Sinusoidal voltage waveform and response current. The current has the same frequency (period), but the phase shifts by φ.

This waveform formula can be converted to phasors form. Equation A.1 – (2) can be re-written as:

$$Z = |Z|(cos\varphi + j\, sin\varphi) \qquad \text{A.1 - (3)}$$

$$Z_0: Amplitude\ of\ Impedance, \varphi: Phase\ shift$$

$$R = |Z| cos\varphi,\ X = |Z| sin\varphi$$

$$Z = R + J\,X = Z' + JZ'' \qquad \text{A.1 – (4)}$$

where R (Z') is the real part and X (Z'') is the imaginary part of impedance, respectively. X is called reactance, and the unit is Ohm.

For accurate impedance measurement, a linear behavior is mandatory. Because some electrochemical reactions are not always linear, the current is not always proportional to the AC voltage. For that reason, AC voltage should be as low as possible, with usual values around 10 to 20 mV.

If a small AC signal (around 10 – 20 mV) is taken in the I-V curve of the device, the response can be assumed linear, as shown in Fig. A.1.2.

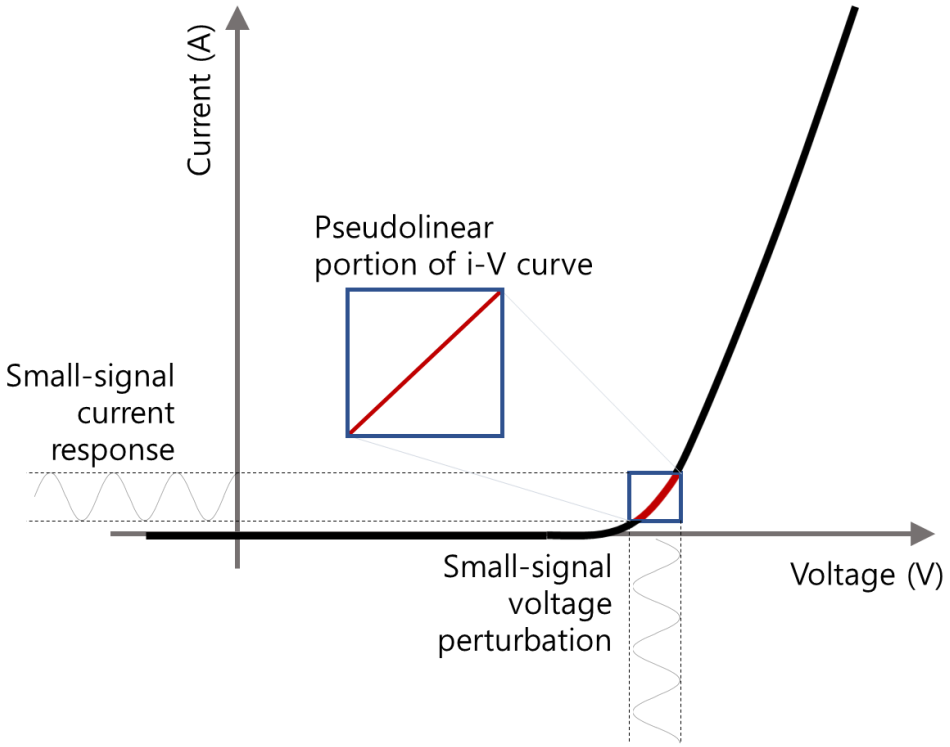

Figure A.1.2. Impedance is measured and analyzed in pseudolinear intervals using a small disturbance input signal.

A.1.1. Nyquist plot

Fig. A.1.3 shows one of the most popular formats for evaluating electrochemical impedance data: the Nyquist plot. The imaginary impedance component (Z'') is plotted against the real impedance component (Z') at each applied frequency. Since capacitance is mainly observed in the Nyquist plot for fuel cells or PSCs, the Y-axis component is shown as (-Z''). Capacitance C indeed gives a negative imaginary value with the module $Z'' = -1/\omega C_{dl}$.

The plot in Fig. A.1.3. illustrates the expected response of a simple electrochemical cell [A1].

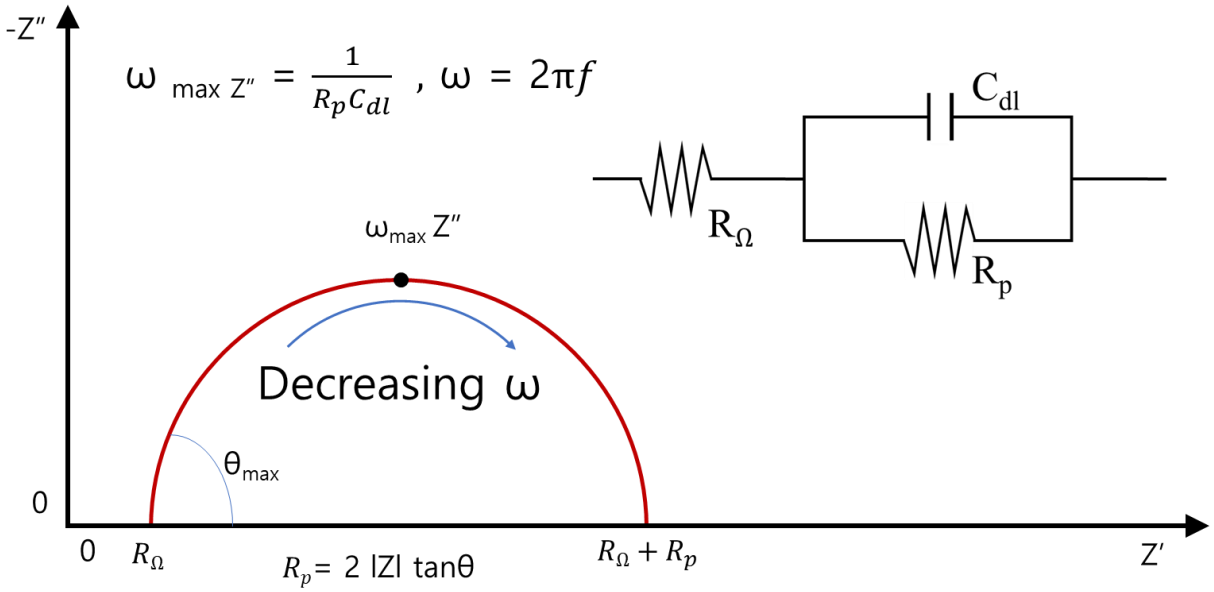

Figure A.1.3. Nyquist plot for a simple electrochemical system [A1]

The frequency reaches its high limit at the leftmost end of the semicircle where it touches the x-axis (R_Ω), while touching it at the rightmost end of the semicircle at its low frequency limit. For the latter, the sample cell also approximates pure resistance, but now the value is ($R_\Omega + R_p$).

The Nyquist plot has several advantages. The primary one is that the plot format makes it easy to see the effects of the ohmic resistance. Taking data at sufficiently high frequencies, it is easy to extrapolate the semicircle toward the left, down to the x-axis, to read the ohmic resistance. The shape of the curve (often a semicircle) does not change when the ohmic resistance changes. Another advantage of this plot format is that it emphasizes circuit components in series, such as R_Ω.

The Nyquist plot format also has some disadvantages. For example, frequency does not appear explicitly. Secondly, although the ohmic resistance and polarization resistance can be easily read directly from the Nyquist plot, the electrode capacitance can be calculated only after the frequency information is known. As shown in Figure A.1.4, the frequency corresponding to the top of the semicircle, ω_{max}, can be used to calculate the capacitance only if R_p is known.

Although the Nyquist format emphasizes series circuit elements, if high and low impedance networks are in series, the low impedance circuit probably will not be seen since the larger impedance controls plot scaling.

A.1.2. Bode plot

Fig. A.1.4 b) shows the Bode plot for the same data as the one used in the Nyquist plot in Fig. A.1.4 a). The Bode plot form is a logarithm function of the frequency versus the absolute value | Z | calculated by eq A.1 - (4):

$$|Z| = \sqrt{Z'^2 + Z''^2} \qquad 2.4 - (4)$$

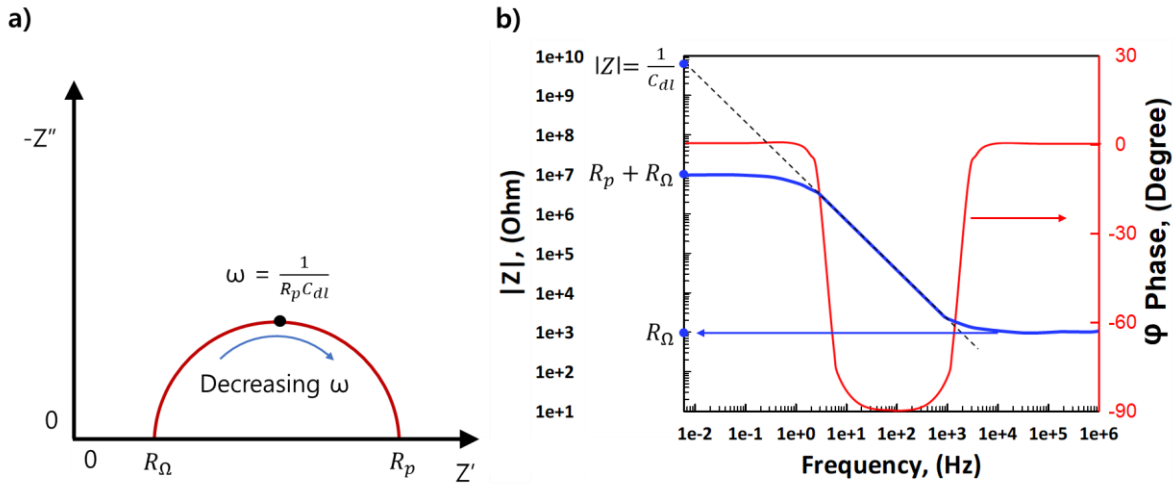

Figure A.1.4. Example of a Bode plot corresponding to the data of Nyquist plot. The image is adapted from Princeton Applied Research, Basics of IS [A1]

This allows the phase shift φ of each impedance to be calculated. Bode plots have several advantages that distinguish them from Nyquist plots. Since the frequency is represented on one axis, it is easy to understand from the graph how the frequency represents the impedance. The Bode plot takes a logarithmic value for frequency and expresses a very wide range of frequencies in one graph. It also shows the impedance value on the logarithmic axis and the impedance range on the same axis easily. This is advantageous to study when the impedance is affected by frequency, such as when the impedance is strongly affected by the capacitor.

The log | Z | vs. log ω curve converts the values of R_p and R_Ω. At the highest frequency in Fig. A.1.4 b), the ohmic resistance (R_Ω) corresponds to the impedance, and "log R_Ω" can be obtained as a part parallel to the frequency axis of the high frequency section. The resistance (R_Ω) is obtained at high frequencies, and log (R_Ω + R_p) can be obtained at the low frequencies of the parallels to the frequency axis. At intermediate frequencies, this curve should be a straight line with a slope of -1.

At intermediate frequencies, the impedance of the capacitor C_{dl} can control the total impedance of the presented Bode plot (Fig. A.1.4 b). The capacitor becomes the controlling component whenever R_Ω and R_p differ by more than a factor of 100 or so.

Extrapolating this line to the log | Z | axis at ω=1 (log ω =0, f=0.16 Hz), yields the value of C_{dl} from the relationship:

$$Z_c = \frac{-j}{\omega C_{dl}}$$

$$\log|Z| = \log\left(\frac{1}{\omega C_{dl}}\right)$$

$$= -\log \omega C_{dl} \quad = -\log \omega - \log C_{dl} \quad = -\log 2\pi f - \log C_{dl}$$

$$= -\log 2\pi - \log f - \log C_{dl}$$

Then, the Bode plot (log | Z | vs. log f, or log | Z | vs. log ω) has a slope of –1 in this region.

At log ω = 0, frequency (f) has this relation: ω=2πf =1, f = 0.16Hz.

Thus, The double-layer capacitance, C_{dl}, can be calculated from equation A.1 - (5):

$$\log|Z| = -\log C_{dl} \qquad (\text{at } f \cong 0.16\text{Hz})$$

or

$$C_{dl} = \frac{1}{|Z|} \qquad \text{A.1 - (5)} \qquad \text{where} \quad \omega = 2\pi f = 1$$

The Bode plot format also shows the phase angle, φ. At the high and low frequency limits, where the behavior of the sample is resistor-like, the phase angle is nearly zero. At intermediate frequencies, φ increases as the imaginary component of the impedance increases. The φ vs. log ω. The Bode plot is a useful alternative to the Nyquist plot. It lets us avoid the longer measurement times associated with low frequency R_p determinations. Furthermore, the log |Z| vs. log ω plot sometimes allows a more effective extrapolation of data from higher frequencies. The Bode format is also desirable when data scatter prevents adequate fitting of the Nyquist semicircle. In general, the Bode plot provides a more precise description of the electrochemical system's frequency-dependent behavior than the Nyquist plot, where frequency values are implicit rather than explicit. On some electrochemical processes, there are more than one rate-determining step. Each step represents a system impedance component and contributes to the overall reaction rate constant. The impedance experiment can often distinguish among these steps and provide information on their respective rates or relaxation times.

A.1.3. Impedance spectroscopy applied to electronic-ionic mixed conductor material

Our Study deals with the transport and ageing properties of ionic, electronic mixed conducting perovskite. As previously seen, the IS method can observe charge transport, recombination, and ionic motion of PSC by various application conditions, IMPS / IMVS being the methods of the IS measurement.

The DC voltage is maintained by the short circuit (IMPS) or open circuit (IMVS) of the PSC while measuring IS, where light intensity is a variable. With these methods, we can observe charge transport, carrier recombination (diffusion coefficient), and ion motion [A2].

From Nyquist spectra of PSCs, the semicircle's diameter represents the resistance and is generally electronic transport and recombination processes. Meanwhile, the low frequency semicircle is due to ion diffusion and / or interfacial charge accumulation between the perovskite and electron-selective layers. Guillén et al. studied charge transport and recombination by analyzing the semicircle at high frequency for titania-based conventional structures [A3]. Besides, there are carrier recombination researches about the planar structured PSC devices similar to our device by the IMPS / IMVS methods. Further, the charge accumulation due to ion migration was found by analyzing the Nyquist plot semicircles and the Bode plot plateau at the low frequency domain[A4-6]. Lastly, an ion migration study can also prove the formation of a redox layer ($Ag^+ + I^- \rightarrow AgI$) of ion and electrode material [A7-9].

For the remainder of this thesis, IS will be an effective tool to study ion migration with GD-OES. In addition, we are preparing the setting for the aforementioned IMPS / IMVS.

A.1.4. IS data fitting from the Nyquist plot

The Nyquist plot is composed of real impedance (Z') and imaginary impedance (-Z''). The starting point on the Z' axis with an arc means one resistor (the point R1 at Fig. A.1.5). A single arc on Nyquist implies a couple of one resistor (R_1) and one capacitor (C_2) in parallel {name as PRC}. According to Fig. A.1.5 a, the result is deduced as an equivalent circuit is R_1+C_2/R_2 because the starting point is not zero. In the case of two arcs (Fig. A.1.5b), two PRCs can theoretically constitute two equivalent circuits (Series model: R1+C2/R2+C3/R3, Parallel model: $\{R_1+C_2/(R_2+C_3/R_3)\}$.

When choosing a circuit model, a Bode plot (Fig.A.1.4) is a reference. At high frequencies (10 kHz-1 MHz), the geometrical capacitance (C_2) of the planar solar cells is observed in both pristine and

polarized conditions. The Series model has a problem in that the order of the result values is reversed when the data fitting system C_2 is superior to C_3. This problem makes it impossible to fit the Nyquist result that follows a large semicircle with a small semicircle, as shown in Figure A.1.5 b. Thus, the Parallel model $\{R_1+C_2/(R_2+C_3/R_3)\}$ is appropriate to reflect the results where the geometric capacitance (C_2) dominates in the high-frequency region. After choosing the reasonable fitting model, we used EC-Lab fitting software from Bilogics©.

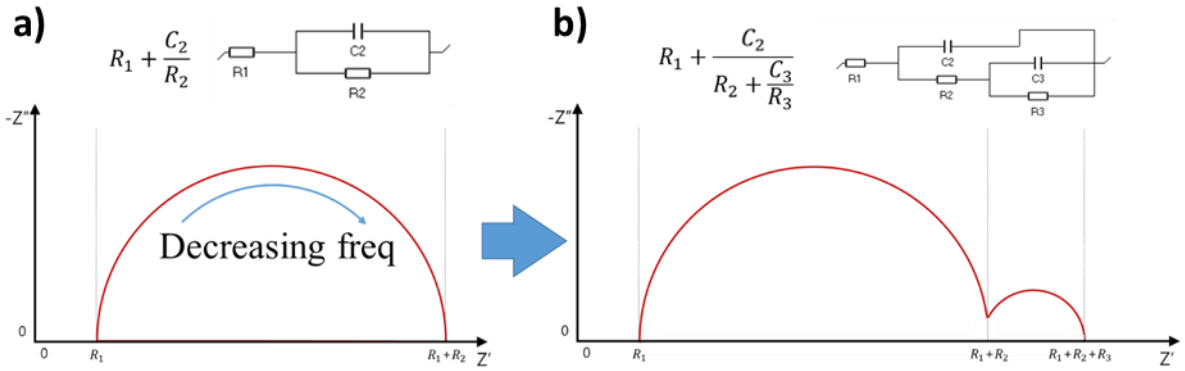

Figure A.1.5. The circuit models used for data fitting according to Nyquist plot a) single arc case and b) double arc case.

A.2. GD-OES plasma condition optimization.

When using GD-OES, the primary aim is to control the sputtering rate and resolution. If the sputtering rate is too fast, the signal from elements composing two different layers might overlap in detected spectra. When we first used GD-OES provided by Institut Lavoisier de Versailles – ILV and Institut Photovoltaïque d'Île-de-France – IPVF, GD-OES sputter run finished in 24 seconds (Figure A.2.1). Even though the measurement conditions were strictly the same (sample structure and plasma parameters: 420Pa, 17W, 3000Hz, and 4% O_2 mixed Ar gas), the measurement rate was too fast compared to measurements by Horiba Scientific (60 s) (Chapter 4, Figure 4.2). For instance, a quick comparison reveals two profile overlap when we analyze the 3CP solar cell (ITO/PEDOT:PSS/3CP/PC60BM/Ag). Ag is detected with 3CP (name as Ag tail). Moreover, PEDOT:PSS (with S) is detected with 3CP (Pb and I). The main reason why the Ag tail is observed is that the crater form is a parabolic shape, and Ag atoms on edge are later detected. However, the overlap with PEDOT:PSS and 3CP is not an expected result.

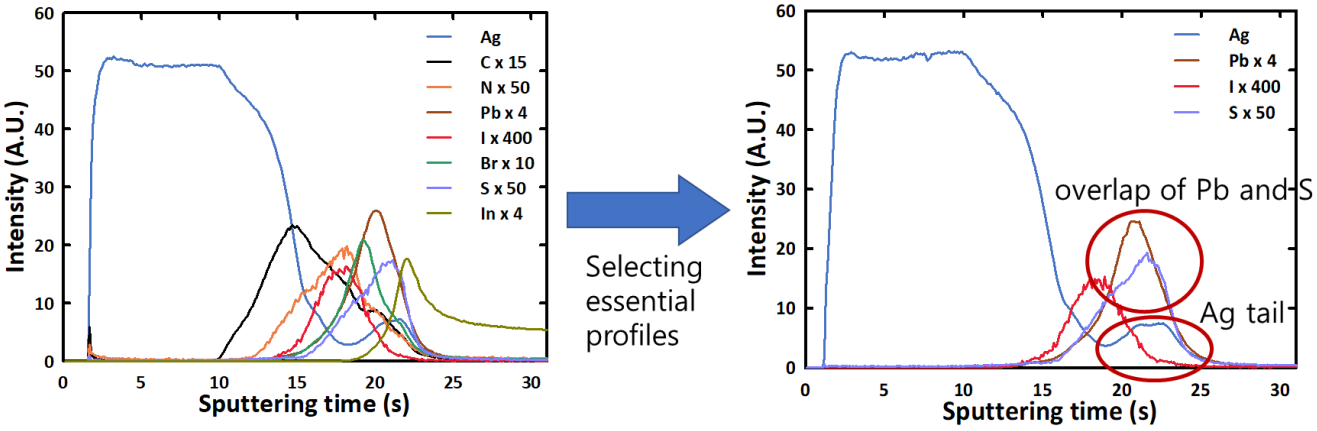

Figure A.2.1. The first GD-OES result with the model provided from ILV-IPVF.

In order to obtain the same sputter rate as in the previous experimental conditions, the sputtering rate should be reduced. The sputtering rate depends on the plasma conditions. Within the safe range of parameters set by the experts, the user can select five. The objective of this section is to introduce:

A.2.1 How sputtering is influenced by each parameter.

A.2.2 The final optimized plasma condition for the model provided from ILV-IPVF.

A.2.1 How sputtering is influenced by each parameter

Figure A.2.2. displays the user-controllable parameters in control software Quantum. Those five parameters are Pressure, Power, Frequency (of RF pulse), Duty cycle, Resulting power: Actual consumed power for sputtering.

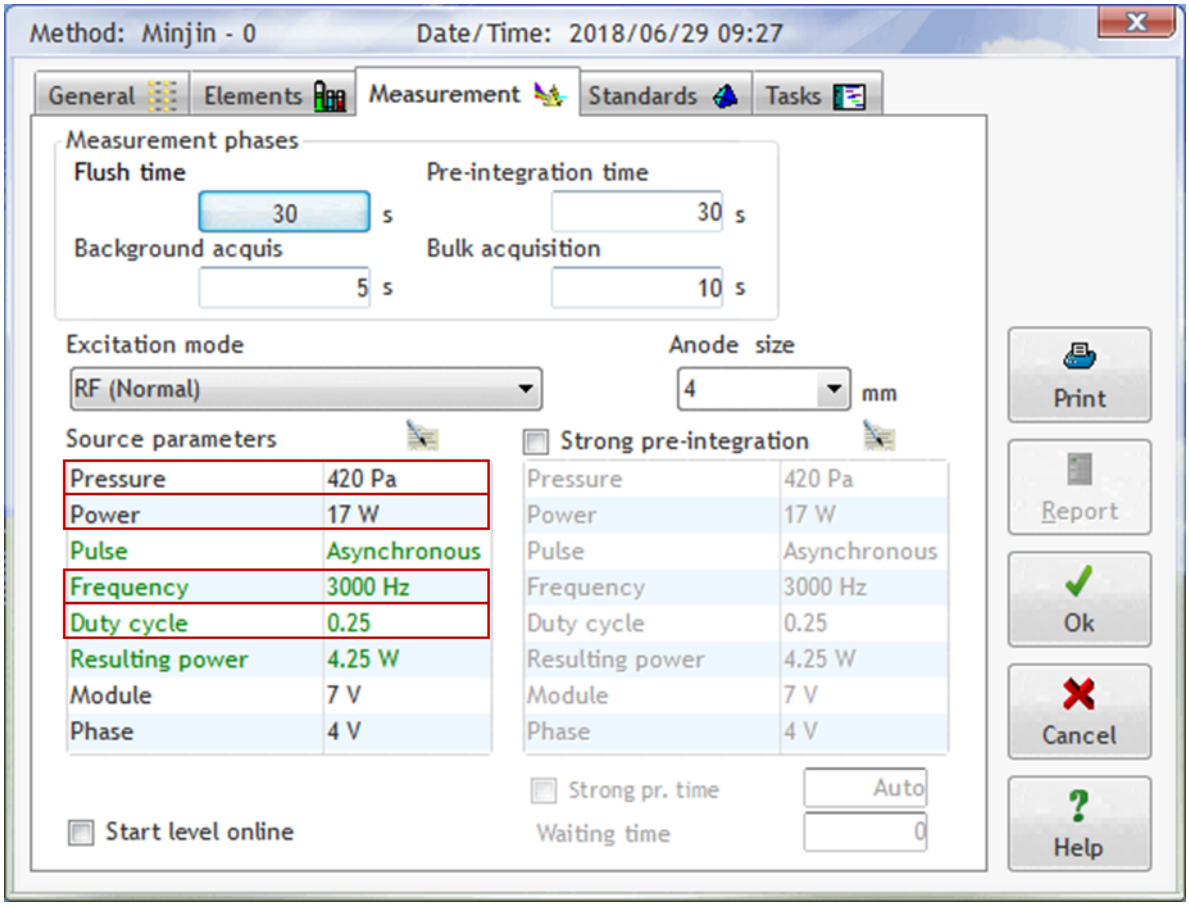

Figure A.2.2. User controllable parameters for GD-OES plasma condition.

Each parameter can be understood more readily by referring to the schematics (Figure A.2.3.). The higher the pressure of plasma gas means the greater the number of collisions in the plasma. High power accelerates the sputtering rate. However, simply converting the power into a sputtering rate is a complex problem because too high power leads to sample deterioration RF frequency always stays the same, 13.56 MHz, and never varies. The frequency of pulsing determines how many times we turn the RF signal on and off. Selecting a low frequency can stress the sample by exposing it to the plasma for a long time continuously. If the selected frequency does not damage the sample, then the frequency is acceptable. Since this value does not affect the net power, it does not affect the sputtering rate. Duty cycle is ratio occupied by RF On between starts of two consecutive RF pulses (Max = 1.0). The product of the power

and duty cycle determines net power. Although a user cannot directly set the net power, it can be controlled indirectly with power and duty cycle settings. In order to transfer the method from one GD-OES system or model to another, we need to adjust the sputtering rate (in our case, to slow it down while transferring from Horiba scientific to ILV-IPVF), Table A.2.1. summarises the effects of each parameter in terms of sputtering rate.

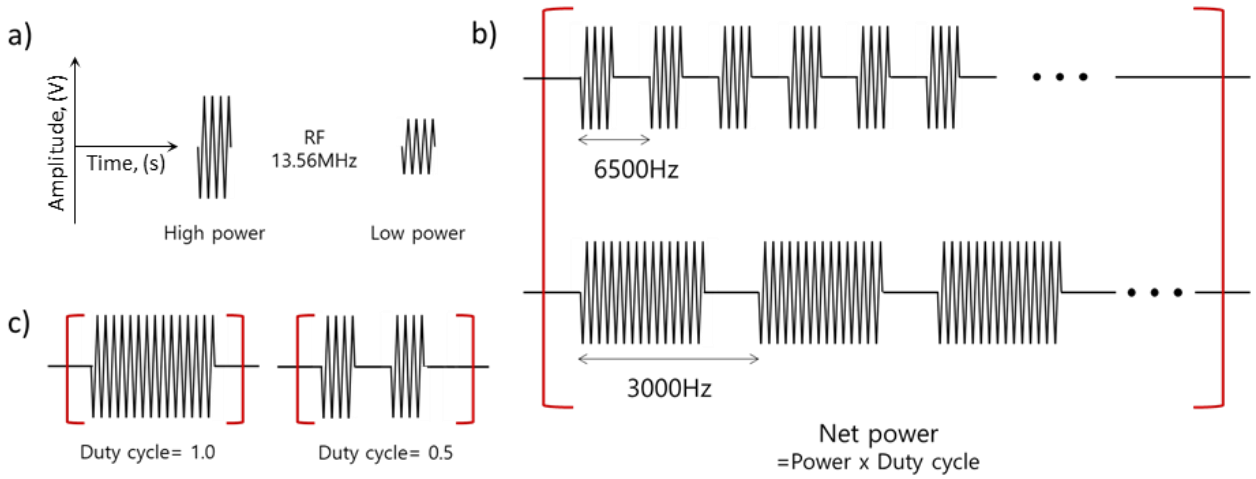

Figure A.2.3. Schematics elucidating the plasma AC power source working principle of GD-OES. a) an example of different power. b) an example frequency, and c) an example of the duty cycle.

Parameter (English)	Value	Sputtering rate
Plasma forming gas pressure	Increase	Increase
Power	Increase	Increase
Frequency	Increase	Same
Duty cycle	Increase ($0<x\leq1$)	Increase
Net power	Power · Duty cycle	-
Plasma gas	Ar 100%	Normal
	Ar 96%: O_2 4%	Faster for C-containing layer

Table A.2.1. Summary of the relation user-controllable parameters and sputtering rate.

A.2.2 The final optimized plasma condition for the GD-OES system provided from ILV-IPVF

The previously optimized GD-OES measurement conditions are 420 Pa pressure, 17 W power, pulsing frequency 3000 Hz, and gas composition 4% O_2 mixed in Ar. As a result of the new GD-OES system, carbon-containing layers (PEDOT:PSS/3CP/$PC_{60}BM$) were etched in 12 seconds. Optimization aims to reduce the measurement rate. The purpose of O_2 is to compensate slow sputtering of the C-containing layer by Ar ions. If we use 100 % of Ar gas, we could slow down the sputtering rate for PEDOT:PSS/Perovskite/PCBM stacks. We first removed O_2 and reduced the pressure to 250 Pa. Figure A.2.4b shows that the Ag tail is clearly separated from the perovskite layer's elements, and the C profile is relatively flat. In a pure argon environment, $PC_{60}BM$ (C-rich layer) plays a role in isolating the Ag results from 3CP.

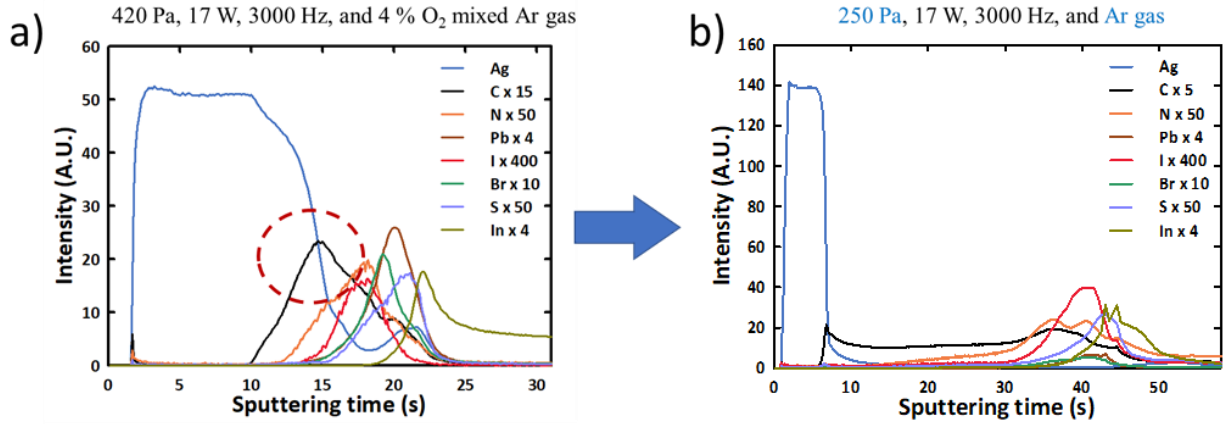

Figure A.2.4. GD-OES profile lines a) with the conditions optimal for Horiba scientific system (Ar+4% O_2) and b) with conditions optimal for ILV-IPVF system (pure Ar as the plasma forming gas).

Further, we saw that the sputtering rate was slowed down by lowering the power (Figure A.2.5). As far as discussed in section A.2.1, the lower power (15 W) resulted in about twice the measurement time. 15 W was adopted for the following experiments because the elements of the perovskite layer showed that detection was terminated at 60 s (Chapter 5. Figure 5.10). We also tested higher frequency (6500 Hz) to see the difference in heat impact on a sample. As a result, both frequencies (3000 Hz and 6500 Hz) show the same etching rate. We stayed with 3000Hz condition to keep the parameters similar to before (420 Pa, 17 W, 3000 Hz, and 4% O_2 mixed in Ar gas) because the results are similar.

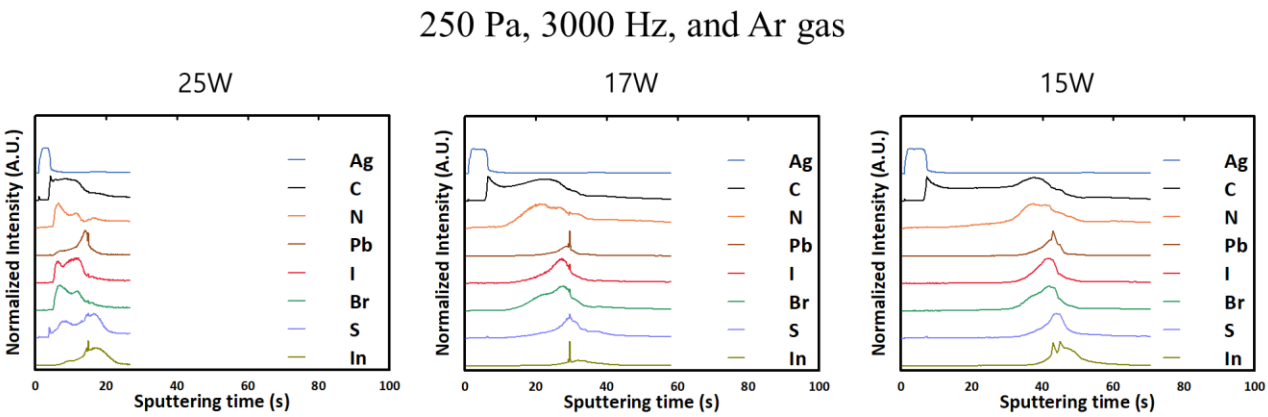

Figure A.2.4. GD-OES profile lines with various power a) 25 W, b) 17W, and c) 15W.

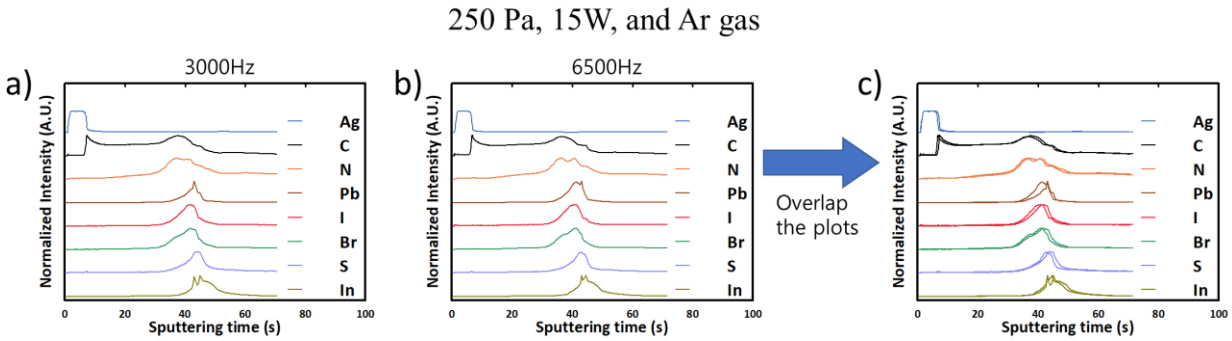

Figure A.2.5. GD-OES profile lines with different frequencies a) 3000 Hz and b) 6500 Hz. c) a superimposed plots demonstrating that varying frequency results are almost the same.

In this section, the user parameters controlling sputtering rate were varied to find an optimum sputtering rate for perovskite solar cells. Since our experiment aimed to observe ion migration, a measurement time of about 60 seconds or more was required. This task was to find the optimal conditions. Experiments with user parameter study allowed us to find plasma conditions successfully. Plasma conditions are:

Pressure 250 Pa, Power 15 W, Pulsing frequency 3000 Hz, Duty cycle = 0.5, and plasma forming gas pure Ar (100 %).

A.3. References

[A1] H, Lee, Under the direction of Yvan Bonnassieux, Thesis: Analysis of Current-Voltage Hysteresis and Ageing Characteristics for $CH_3NH_3PbI_{3-x}Cl_x$ Based Perovskite Thin Film Solar Cells: http://theses.fr/2018SACLX009.

[A2] M. De Bastiani, G. Dell'Erba, M. Gandini, V. D'Innocenzo, S. Neutzner, A. R. S. Kandada, G. Grancini, M. Binda, M. Prato, J. M. Ball, M. Caironi, and A. Petrozza., *Adv. Energy Mater*. **2016**, 6, 1501453.

[A3] J. Li, Q. Dong, N. Li, L. Wang, Direct Evidence of Ion Diffusion for the Silver-Electrode-Induced Thermal Degradation of Inverted Perovskite Solar Cells, *Adv. Energy Mater*. **2017**, 1602922.

[A4] C. Besleaga, L. E. Abramiuc, V. Stancu, A. G. Tomulescu, M. Sima, L. Trinca, N. Plugaru, L. Pintilie, G. A. Nemnes, M. Iliescu, H. G. Svavarsson, A. Manolescu, and I. Pintilie., *J. Phys. Chem. Lett*. **2016**, 7, 5168–5175.

[A5] R. Chen, B. Long, S. Wang, Y. Liu, J. Bai, S. Huang, H. Li, X. Chen, Efficient and Stable Perovskite Solar Cells Using Bathocuproine Bilateral-Modified Perovskite Layers. *ACS Appl. Mater. Interfaces*. **2021**, *13*, 24747−24755

[A6] Y. Wang, S. Dong, Y. Miao, D. Li, W. Qin, H. Cao, L. Yang, L. Li, S. Yin, BCP as Additive for Solution-Processed PCBM Electron Transport Layer in Efficient Planar Heterojunction Perovskite Solar Cells. *IEEE J. Photovolt*. **2017**, *7*, 550-557.

[A7] M. Cai, Y. Wu, H. Chen, X. Yang, Y. Qiang, L. Han, Cost-Performance Analysis of Perovskite Solar Modules. *Adv. Sci.* **2017**, *4*, 1, 1600269.

[A8] J. Carrillo, A. Guerrero, S. Rahimnejad, O. Almora, I. Zarazua, E. Mas-Marza, J. Bisquert, G. Garcia-Belmonte, IonicReactivity at Contacts and Aging of Methylammonium Lead Triiodide Perovskite Solar Cells. Adv. Energy Mater. 2016,6, 1502246.

[A9] Y. Kato, L. K. Ono, M. V. Lee, S. Wang, S. R. Raga, Y. Qi, Silver Iodide Formation in Methylammonium Lead Iodide Perovskite Solar Cells with Silver Top Electrodes. Adv. Mater. Interfaces 2015, 2, 1500195.

A.4. Peer-reviewed publication

FULL PAPER

ADVANCED FUNCTIONAL MATERIALS
www.afm-journal.de

Reversible Photoinduced Phase Segregation and Origin of Long Carrier Lifetime in Mixed-Halide Perovskite Films

Subodh K. Gautam, Minjin Kim, Douglas R. Miquita, Jean-Eric Bourée, Bernard Geffroy, and Olivier Plantevin**

Mixed-halide hybrid perovskite semiconductors have attracted tremendous attention as a promising candidate for efficient photovoltaic and light-emitting devices. However, these perovskite materials may undergo phase segregation under light illumination, thus affecting their optoelectronic properties. Here, photoexcitation induced phase segregation in triple-cation mixed-halide perovskite films that yields to red-shift in the photoluminescence response is reported. It is demonstrated that photoexcitation induced halide migration leads to the formation of smaller bandgap iodide-rich and larger bandgap bromide-rich domains in the perovskite film, where the phase segregation rate is found to follow the excitation power-density as a power law. Results confirm that charge carrier lifetime increases due to the trapping of photoexcited carriers in the segregated smaller bandgap iodide-rich domains. Interestingly, these photoinduced changes are fully reversible and thermally activated when the excitation power is turned off. A significant difference in activation energies for halide ion migration is observed during phase segregation and recovery process. Additionally, the emission linewidth broadening is investigated as a function of temperature which is governed by the exciton–optical phonon coupling. The mechanism of photoinduced phase segregation is interpreted based on exciton–phonon coupling strength in both mixed and demixed (segregated) states of perovskite films.

1. Introduction

Over the past few years, organic–inorganic halide perovskites have attracted tremendous attention as a promising material for low-cost preparation and highly efficient photovoltaic and light-emitting devices. These hybrid perovskite materials show unique optoelectronic properties such as high absorption coefficient, long carrier diffusion length, and small exciton binding energy.[1,2] To date, various combinations and ratios of monovalent inorganic cations (such as formamidinium $(CH(NH_2)_2^+$ = FA), methylammonium $(CH_3NH_3^+$ = MA), Cs, and Rb) and halide anions (I^- and Br^-) have been used for bandgap tuning as well as a means of improving efficiency and stability of perovskite photovoltaic devices.[3] One of the most influential improvement was the incorporation of cesium cations in perovskite structure to fine-tune Goldschmidt tolerance factor toward more structurally stable black phase perovskite with improved performance of photovoltaic devices.[3–5] Therefore, triple-cation based mixed-halide perovskites (Cs, FA, MA) $Pb(I, Br)_3$ have been found more suitable for solar cell application. Unfortunately, even such most advanced perovskite materials still suffer from instabilities of the bandgap when subjected to photoexcitation under continuous light illumination.[6,7] As originally reported by Hoke and coworkers, $MAPb(I_{1-x}Br_x)_3$ undergoes reversible halide phase segregation under light illumination into separate iodide- and bromide-rich domains within the

Dr. S. K. Gautam, D. R. Miquita, Dr. O. Plantevin
Université Paris-Saclay
CNRS
Laboratoire de Physique des Solides
Orsay 91405, France
E-mail: subodh-kumar.gautam@csnsm.in2p3.fr;
olivier.plantevin@u-psud.fr

M. Kim, Dr. J.-E. Bourée, Dr. B. Geffroy
LPICM
CNRS
Ecole Polytechnique
Institut Polytechnique de Paris
route de Saclay, Palaiseau 91128, France

The ORCID identification number(s) for the author(s) of this article can be found under https://doi.org/10.1002/adfm.202002622.

DOI: 10.1002/adfm.202002622

D. R. Miquita
Centro de Microscopia – Universidade Federal de Minas Gerais
Belo Horizonte, MG 31270-901, Brazil

B. Geffroy
Université Paris-Saclay
CEA
CNRS
NIMBE
LICSEN
Gif-sur-Yvette 91191, France

parent phase.[6] In recent years, it is commonly reported that light-induced phase segregation process in mixed halide $MAPb(I_{1-x}Br_x)_3$ and $CsPbBr_xI_{3-x}$ perovskites is initiated by segregation of iodine ions which causes a red-shift in the photoluminescence (PL).[7,8] On the other hand, phase segregation can also induce a PL blue-shift as reported in $CsPbBr_{1.2}I_{1.8}$ nanocrystals subjected to photoexcitation and external electrical biasing.[7] Furthermore, other reports suggest that variation of energy bandgap of mixed halide perovskite could also be due to lattice distortion as light illumination could generate lattice expansion or contraction.[9–11] Therefore, the existing literature on phase segregation is often subject to controversy.

Another puzzling feature under debate in hybrid perovskites is the unusual long carrier lifetime. Several mechanisms have been proposed to explain the long carrier lifetime of perovskite materials, such as large polarons formation, Rashba effect and photon recycling.[12] Moreover, recombination of excited charge carriers through trap-mediated channels also influences the rate of halide segregation and recombination lifetime.[13] The nature of trap states and trapped carrier type (electrons or holes) in segregated domains are not yet entirely understood although it was reported that electrons are more likely to be trapped than holes.[14,15] Such existing reports imply that excited charge carriers trapping in trap-states and corresponding energy levels within the bandgap could alter the phase segregation dynamics. Recently, it was also demonstrated that excited charge carriers could couple with the perovskite lattice to create a polaron,[16–18] which could promote the halide ion segregation. A strong exciton–phonon coupling is expected in such soft and ionic hybrid perovskite materials at room temperature.[19,20] Eventually, the Cs cation-based mixed halide perovskite (partially exchanging FA cation with Cs) unveils lower electron–phonon coupling strength and exhibits high structural stability against photoinduced phase segregation.[18] Therefore, it is interesting to study the role of exciton–phonon coupling in triple-cation mixed halide perovskite (TC-MHP) films during phase segregation process and the role of trapped charge carrier under photoexcitation.

In the present study, we have explored different aspects of photoexcitation induced phase segregation in triple-cation mixed-halide $(MA_{0.17}FA_{0.83})_{0.95}Cs_{0.05}Pb(I_{0.83}Br_{0.17})_3$ perovskites (TC-MHP) films and quantitatively rationalized the spectroscopic processes that occur during phase segregation and recovery processes. We demonstrate the laser power dependent evolution of segregated halide domains and their kinetics with laser exposure time. We performed time-correlated single photon counting (TCSPC) measurements along with low-temperature PL studies to read the nature of photoexcited carriers trapping states in phase segregated domains, revealing their role in long decay lifetime. We discuss the emission linewidth broadening with rising temperature, which is governed by exciton–optical phonon coupling in both segregated and remaining nonsegregated domains of TC-MHP film. Additionally, recovery kinetics of phase-segregated films is studied under dark at different temperatures and activation energies of halide ion migration are derived.

2. Results and Discussion

2.1. Photoexcitation Induced Phase Segregation

The TC-MHP perovskite film shows high optical absorbance and exhibits the direct band gap (E_g) of ≈1.625 eV, calculated using the Tauc's relation as presented in Figure S1 (Supporting Information). The surface morphological properties of TC-MHP film is also presented in Figure S2 (Supporting Information): a SEM image shows the uniformly distributed nanostructure with average grain size of ≈175 ± 50 nm. We have performed laser power dependent PL measurements at room temperature (296 K) to provide insight into the photoexcitation induced spectroscopic variation in TC-MHP film in terms of carrier trap-states and recombination dynamics. **Figure 1**a shows the normalized PL spectra as a function of laser power density (P_{exc}). With increasing excitation power density, a continuous redshift of about ≈58 meV is observed in emission peak: it goes from 1.625 eV (1 mW cm^{-2}) to 1.566 eV (840 mW cm^{-2}), concurrent with the increase in PL emission intensity (I_{em}). In Figure 1b, data clearly shows that PL intensity increases as a power law of excitation power, with an exponent ≈3/2 (i.e., $I_{em} \propto P_{exc}^{b}$, with $b = 1.48$) for power-densities up to 380 mW cm^{-2}. Generally, in the case of free excited carrier recombination, I_{em} grows linearly with P_{exc} (i.e., $I_{em} \propto P_{exc}$).[21] In present case, this possibility is readily exempted at room temperature, because excitonic feature is not observed in the absorption spectrum (Figure S1, Supporting Information). The unusual ≈3/2 power low PL response points the participation of intra-gap states in recombination process that act as traps for electrons or holes. Therefore, superlinear growth of PL intensity suggests that photogenerated carrier trapping at available defects or traps sites competes with bimolecular electron/hole recombination process in TC-MHP film.[21,22] At higher excitation power-density (above 380 mW cm^{-2}), the power law changes from superlinear to sublinear owing to the fact that trap-mediated recombination process is dominated by bimolecular recombination process controlled with Auger losses. Therefore, at higher excitation power-density, the saturation in I_{em} is attributed to the saturation of radiative bimolecular recombination centers, as Auger losses starts playing a key role in recombination process.

Figure 1c shows the red-shift and broadening in PL emission linewidth as a function of excitation power-density which confirms the participation of low energy sub-bandgap states in recombination process. To further confirm the photoexcitation induced red-shift in PL emission, time dependent PL measurements were performed at given excitation power-densities and shown in Figure S3a–f (Supporting Information). At low-excitation power-density (1 mW cm^{-2}), the position of PL spectrum remains unchanged and shows significant increment in PL intensity over exposure time. The increase in PL intensity might be related to the filling of existing nonradiative traps sites in TC-MHP film. At higher excitation power-densities, results show the red-shift and an increase in PL intensity with exposure time, indicating the formation of low-energy sub-bandgap states and filling of existing trap sites.[23] The laser-induced heating possibility is safely ruled out here since temperature dependent PL emission exhibit blue-shift with increasing temperature

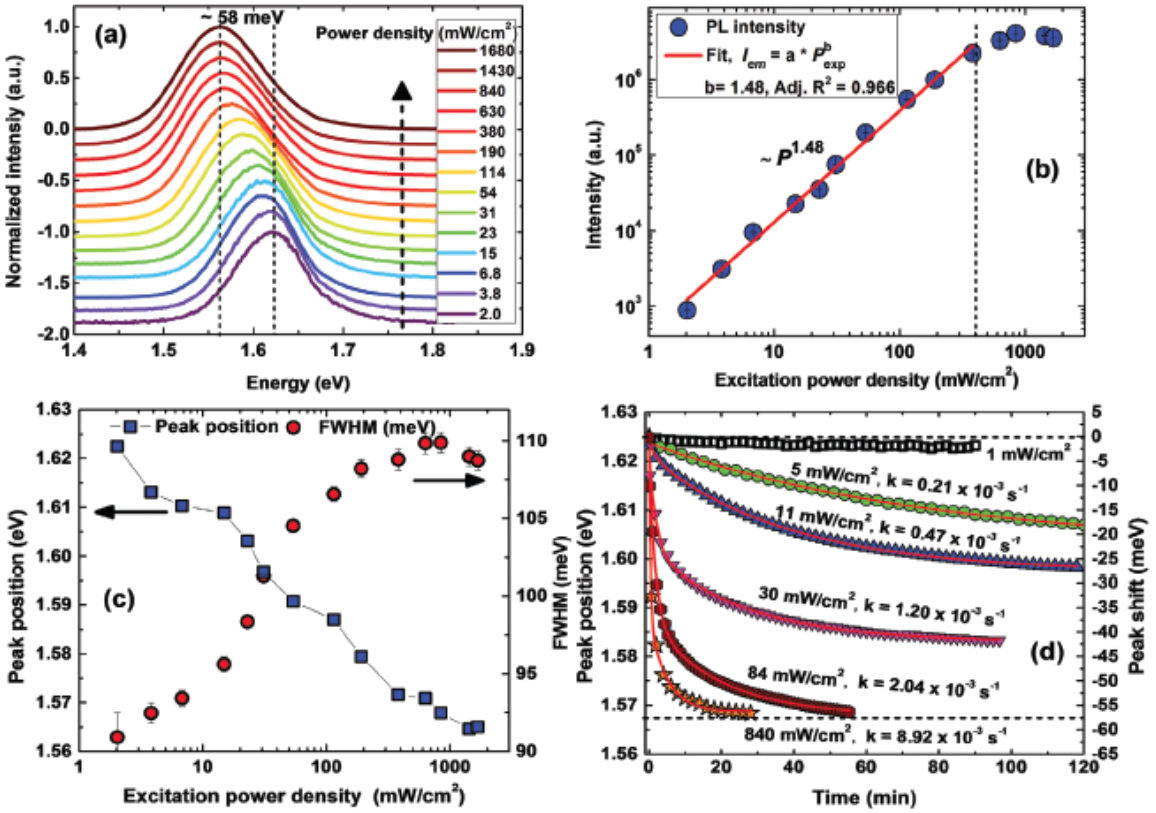

Figure 1. a) Power-dependent photoluminescence spectra of triple-cation mixed-halide $(MA_{0.17}FA_{0.83})_{0.95}Cs_{0.05}Pb(I_{0.83}Br_{0.17})_3$ perovskite film showing red shift in photoluminescence with increasing excitation power-density at 296 K. b) Logarithmic plot, showing increase in integrated PL intensity as a power law of excitation power-density, with an exponent of ≈3/2 (red line). c) Plot of red shift in PL emission peak and line-width broadening as a function of laser power density. d) Time dependent red-shift in PL emission under different excitation power-densities and fitted exponential curves to calculate phase segregation rate constants.

(discussed in later section). It is observed that increasing excitation power leads to faster shifting of PL emission peak (Figure S3, Supporting Information). In particular, it is noted that photoexcited TC-MHP film shows red-shifted PL emission at ≈1.564 eV which corresponds to the standard PL emission from $FAPbI_3$ perovskite. It confirms that the magnitude of redshift is related to the evolution of localized low-bandgap energy states, which might be related to halide ion migration and iodide-rich perovskite phase. Therefore, it establishes the possibility of photoexcitation induced halide ion migration and formation of smaller-bandgap iodide-rich perovskite domains in TC-MHP film that yields red-shift in PL emission.

Figure 1d shows the redshift in peak position as a function of time at given excitation power densities. Peak position values are extracted using PL emission data (Figure S3, Supporting Information) fitted with Gaussian–Lorentzian (Voigt) function. The first order phase segregation rate constant (k_{seg}) is calculated from subsequent fitting of exponential red-shifting curves at different excitation power densities. It is found that at excitation power ≤ 1 mW cm^{-2}, PL emission peak remains stable at a position of ≈1.624 eV and reveals that no phase segregation occurs up to long exposure time. At P_{exc} = 5 mW cm^{-2}, PL peak shifts slowly in exponential manner and shows ≈20 meV redshift after 140 min illumination; the corresponding k_{seg} value is found to be 0.21×10^{-3} s^{-1}. The PL emission peak shifts faster with increasing excitation power-density and exhibits higher k_{seg} value. The maximum redshift in PL emission peak is about ≈56 meV for P_{exc} = 84 mW cm^{-2} and no further shift is observed at higher P_{exc} value. The k_{seg} value increases in a nonlinear fashion with increasing P_{exc}, from 0.21×10^{-3} s^{-1} for P_{exc} = 5 mW cm^{-2} to 8.92×10^{-3} s^{-1} for P_{exc} = 840 mW cm^{-2}. Therefore, high k_{seg} value corresponds to faster exponential growth of iodide-segregated domains. It is interesting to note that k_{seg} in TC-MHP shows lower propensity for halide segregation than the reported MA-based mixed halide perovskite with a similar halide composition range ($0.2 < x < 0.5$).[8,13] Furthermore, a relationship between PL-redshift and halide composition variation is established using nonlinear bandgap variation as a function of halide composition ratio (Br, x = 0–1.0) under Vegard's law expression and presented in Figure S4 (Supporting Information). The PL-emission values of mixed and segregated domains are used to fit the nonlinear bandgap variation curve as a function of

bromide concentration. Result shows that PL-redshift follows the nonlinear decrease in bandgap value with reduction in Br-concentration (enrichment in iodide) in TC-MHP film. It confirms that photoexcitation induces halide composition changes due to halide ion migration and leads to formation of segregated halide domains in TC-MHP film. Moreover, PL emission broadening during phase segregation may also occur due to the change in halide composition (decrease in bromide and enrichment of iodide content) as interpreted from Figure 1c. However, the PL width broadening with varying halide composition may also include other complex phenomenon such as increased lattice disorder (due ion migration and related point defects). Furthermore, threshold excitation density of phase segregation (P_{th}^{Seg}) is also calculated using different laser power densities at two different temperatures and found to be ≈2.0 mW cm^{-2} at 296 K and ≈1.5 mW cm^{-2} at 330 K (Figure S5, Supporting Information). In comparison to 296 K, the observed low P_{th}^{Seg} value at 330 K reveals that lower-excitation density input is required for initiating the phase segregation process at higher temperature (faster segregation rate). The estimated P_{th}^{Seg} value of TC-MHP is about 100 times higher as compare to reported values of ≈30 and ≈40 μW cm^{-2} for $MAPb(I_{0.5}Br_{0.5})_3$ at 300 K,[8,24] which is meaningful as triple cation perovskites were developed for their increased robustness as compared to single cation perovskites.

2.2. Phase Segregation and Carrier Lifetime

To better understand the phase segregation process and gain an insight into the charge-carrier trapping dynamics in photo-excited TC-MHP film, we performed TCSPC measurements. **Figure 2** shows the PL decay curves of red-shifted PL emission on a semi-logarithmic scale measured just after the laser excitation at different power-densities. The exponential fit of PL-decay curves exhibit two decay components as a fast (τ_1) and a slow (τ_2) one, as plotted in inset of Figure 2. At lower power exposure (≤1 mW cm^{-2}), the calculated decay lifetime components are $\tau_1 \approx 752 \pm 18$ ns (94%) and $\tau_2 \approx 1985 \pm 175$ ns (6%),

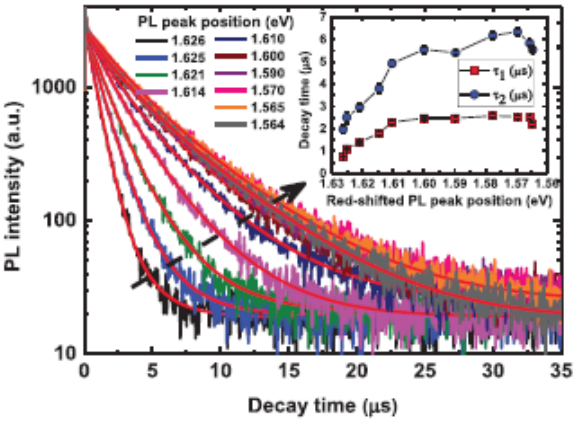

Figure 2. PL decay spectra measured on red-shifted PL emission position after light soaking of different excitation power-densities at room temperature (296 K) with fitted exponential decay curves. Inset: Lifetime components as a function of PL emission position.

which increase nonlinearly to maximum value of $\tau_1 \approx 2580 \pm 78$ ns (63%) and $\tau_2 \approx 6343 \pm 142$ ns (37%) after increasing the excitation power-density. However, lifetime components start decreasing at higher power-densities when no more redshift occurs in PL emission peak. The average lifetime of both components is calculated by considering their weighted fraction and it is found that average lifetime increases from ≈0.82 to ≈3.94 μs as PL emission shift from 1.624 to 1.564 eV as a function of excitation power-density. The relative weighted contribution of τ_1 component decreases from 94% to 63% concurrently with increase in τ_2 component from 6% to 37%. It confirms that during photoinduced population of low energy bandgap states, excited charge carriers start funneling into these low-energy bandgap states where they live longer and release slowly.

To further confirm the photoexcitation induced halide phase segregation in TC-MHP film, we have monitored its emission under continuous laser excitation at high P_{exc} (840 mW cm^{-2}). We were able to record the PL emission arising from segregated bromide–rich domains even for such low initial Br-concentration (17%) in TC-MHP film. **Figure 3**a shows time dependent red-shift in PL emission under continuous excitation and Figure 3b shows the evolution of a weak emission band at ≈2.33 eV, attributed to bromide-rich domains, where PL intensity grows with exposure time and saturates within 28 min of exposure time. The segregation rate constant is calculated from time dependent exponential growth of integral intensities of bromide- and iodide-rich domains. It is found that PL emission from iodide-rich domains shows higher segregation rate (5.58×10^{-2} s^{-1}) than the bromide-rich domains (0.93×10^{-2} s^{-1}). Theoretically and experimentally it is reported that Pb—Br bond is shorter and stronger than the Pb—I bond.[25,26] Therefore, due to higher Pb–Br binding energy, bromide ions may require high activation energy[27] and causing slower segregation rate. Figure 3c shows the TCSPC measurement on both mixed and segregated bromide- and iodide-rich domains. PL emission decays rapidly in bromide-rich domains at 2.33 eV whereas longer PL-decay time is observed in iodide-rich domains (1.564 eV). PL decay curve from bromide-rich domains exhibits amplitude-weighted lifetimes of $\tau_1 \approx 5$ ns (96%) and $\tau_2 \approx 24$ ns (4%), respectively. The shorter carrier lifetime and significantly weaker emission from the bromide-rich domains as compared to iodide-rich region suggest that photogenerated charge carriers may quickly funnel and accumulate in the low-energy bandgap iodide-rich domains. Mao and co-workers report that the low bandgap iodide-rich domains efficiently trap the free-carriers, reveal their dominant role as radiative recombination centers.[28] Similar assumptions of charge transfer between segregated phases (bromide-rich and iodide-rich domains) as well as trap-mediated recombination have been proposed in the recent studies.[6,13] Therefore, it is expected that conduction/valence band of segregated low-bandgap iodide-rich domains would serve as a sink for excited carriers from bromide-rich regions and remaining mixed TC-MHP regions, where they are long lived until recombination as schematically shown in Figure 3d. The nature of trap states or trapping carrier type (electrons or holes) is not yet entirely understood in hybrid perovskite materials,[29,30] although reports have suggested that electrons are more likely to be trapped than holes.[14,15] It is understood

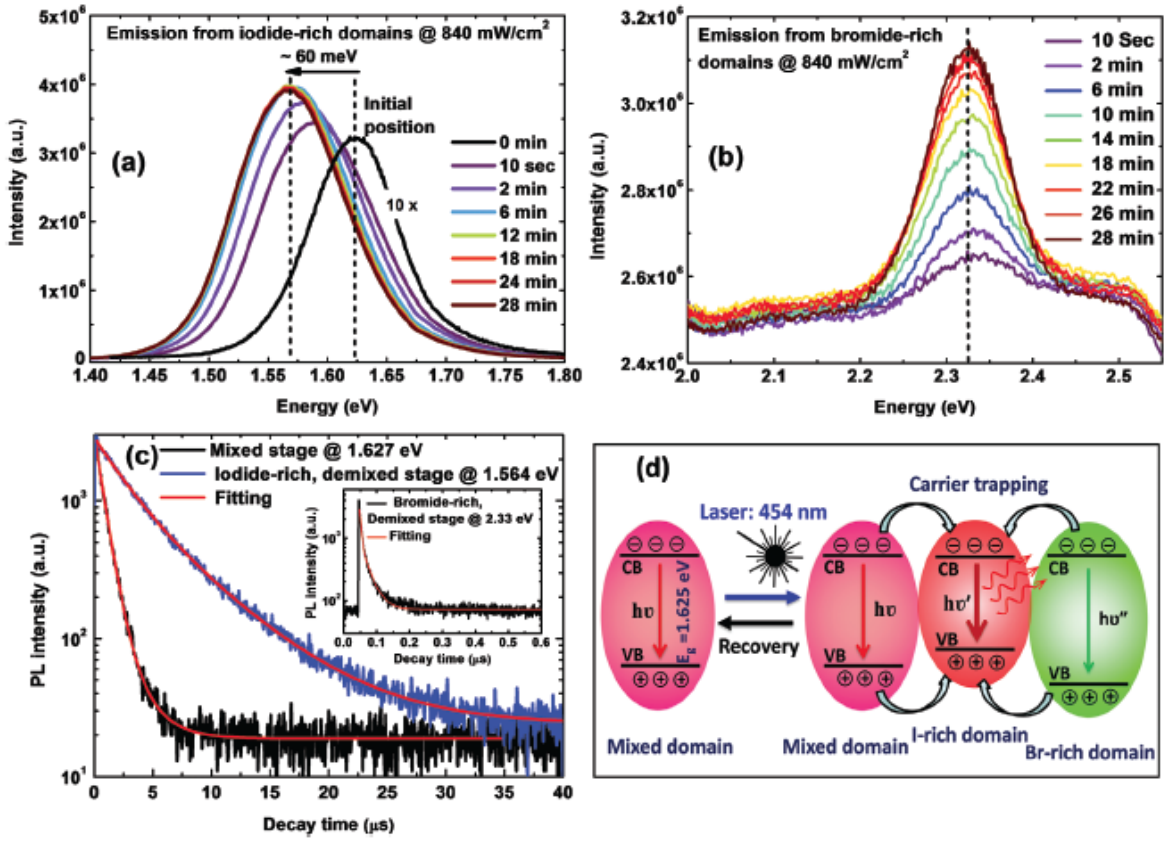

Figure 3. Spectroscopic observation of halide phase segregation in triple-cation mixed-halide $(MA_{0.17}FA_{0.83})_{0.95}Cs_{0.05}Pb(I_{0.83}Br_{0.17})_3$ perovskite film. a) Time dependent red-shift in PL emission and evolution of PL spectra from iodide-rich domains under continuous wave excitation (P_{exc} = 840 mW cm^{-2}). b) Time dependent evolution of PL spectra from bromide-rich domains under continuous wave excitation (P_{exc} = 840 mW cm^{-2}). c) A comparative analysis of PL decay spectra from initial mixed stage and segregated iodide and bromide-rich domains. Inset: PL decay spectrum from bromide-rich domains shows faster decay time. d) Schematic illustrating the reversible phase segregation process where carrier trapping and recombination in segregated smaller bandgap iodide-rich domain generates red-shifted PL emission.

that estimated difference in the conduction band energies for $MAPbI_3$ and $MAPbBr_3$ is significantly low (≈0.09 eV) while, the remaining difference in bandgap energy is mainly due to larger offset in their valence band energies (≈200 meV).[8,27] Therefore, valence band alignment of iodide-rich domains would act as a major energy barrier for holes to move from the iodide-rich phase back to remaining mixed phase and/or bromide-rich domains. Thus, slow release of trapped charge carriers (mainly holes) from smaller-bandgap iodide-rich domains are likely to contribute in slower recombination and responsible for long carrier lifetime in phase segregated TC-MHP film.

2.3. Activation Energies of Halide Ion Migration and Recovery Kinetics under Darkness

The recovery kinetics of phase segregated TC-MHP film is studied under darkness at different temperatures. Initially, TC-MHP film is illuminated at high excitation power-density (840 mW cm^{-2}) to achieve the phase segregated stage; then recovery process in PL emission is monitored at different time intervals using very low excitation power-density (<1 mW cm^{-2}) as shown in Figure S7a–e (Supporting Information). Results reveal that phase segregation is reversible under darkness with nearly complete recovery of original PL emission spectra. In recovery process, PL emission peak recover back to original position as a function of time concurrently with decrease in PL intensity. It confirms the reduction of existing low-bandgap trapping sites of iodide rich domains due to remixing of halide ions under dark. The first-order phase segregation and recovery rate constants are determined from exponential fits of PL peak positions as a function of time and shown in Figures S6 and S7 (Supporting Information). During photo-induced segregation process, the slowest segregation rate constant ($k_{seg} = 0.29 \times 10^{-3}$ s^{-1}) is observed at lower temperature (250 K). By contrast, increasing temperature leads to fastest segregation rate as extracted values are $K_{seg} = 0.81 \times 10^{-3}$, 1.28×10^{-3}, 2.39×10^{-3}, 8.92×10^{-3}, and 20.29×10^{-3} s^{-1} for 260,

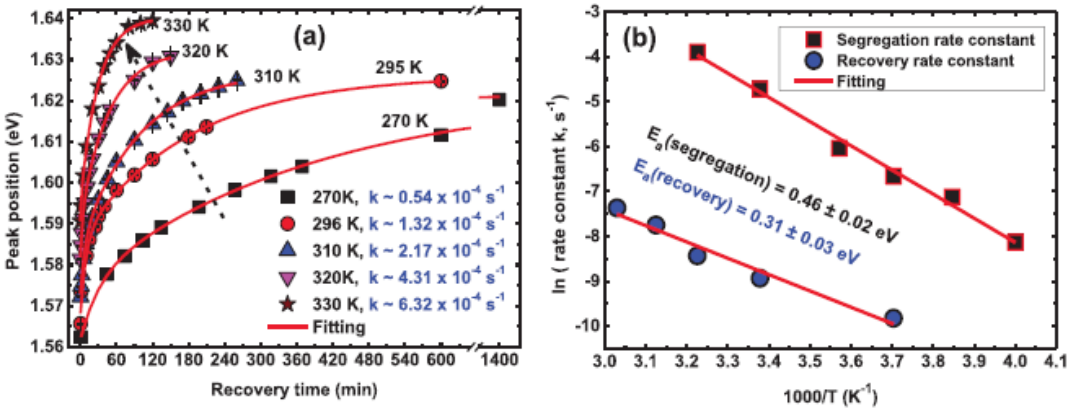

Figure 4. a) Time dependent recovery rate dynamics of phase segregated triple-cation mixed-halide $(MA_{0.17}FA_{0.83})_{0.95}Cs_{0.05}Pb(I_{0.83}Br_{0.17})_3$ perovskite film under dark at different temperatures with exponential fitted curves. b) Arrhenius plots of ln (segregation and recovery rate constants) versus 1000/T for activation energies of halide ion migration during phase segregation and recovery processes.

270, 280, 296, and 310 K, respectively. Similar trends in recovery rate constants are observed at different temperatures under darkness. In **Figure 4**a, results confirm that recovery dynamics is highly temperature sensitive. However, the overall recovery process in dark occurs on a much slower timescale than the photoinduced phase segregation process at a given temperature. At room temperature (296 K), segregated TC-MHP film recovers itself completely in 10 h under dark. Moreover, increase in temperature leads to faster recovery of segregated films as ≈5 h at 310 K, 2.5 h for 320 K and less than 2 h at 330 K, respectively. Similarly, the corresponding recovery rate constant (k_{rec}) is increased from 1.32×10^{-4} to 6.32×10^{-4} s^{-1}, as film temperature raised from 296 to 330 K. However, decreasing temperature below 270 K, the recovery kinetics is almost frozen since the PL emission recovers in ≈24 h at 270 K with an very slow rate ($k_{rec} = 0.54 \times 10^{-4}$ s^{-1}). Thus, decrease in temperature leads to reduction of halide ion mobility in TC-MHP film. Similar results are reported by our co-workers that ionic conduction is frozen below 263 K in $MAPbI_3$ perovskite based solar cells.[31]

The activation energy of halide ion movement is estimated in two different photoexcitation induced phase—segregation ($E_a^{Seg.}$) and dark-recovery ($E_a^{(Rec.)}$ processes. In Figure 4b, an Arrhenius plot is constructed from the natural log of the rate constants (k) obtained at different temperatures versus 1000/T, using the following Arrhenius equation

$$\ln(k) = -\frac{E_a}{RT} + \ln(A) \quad (1)$$

where E_a is the activation energy, R is the universal gas constant, and A is a pre-exponential factor. Activation energies of halide ion movement in two different processes are calculated by least square fitting of linear data points and reveal that activation energy in phase segregation process $E_a^{(Seg.)}$ is 0.46 ± 0.02 eV which is found to be higher than in case of recovery process, $E_a^{Rec.} \approx$ 0.31 ± 0.03 eV. Indeed, these calculated E_a values are consistent with the reported values of forward photosegregation activation energies of order ≈0.27–0.28 eV for $MAPb(I_{0.5}Br_{0.5})_3$.[6,24] Moreover, the calculated E_a values are also consistent with prior studies of halide ion motion, where activation energies of halide vacancy Br^- (I^-) have been reported in between 0.09 and 0.27 eV (0.08 and 0.58 eV), respectively.[6,26,32,33] The differences in reported activation energy may in part be due to different local stoichiometry of perovskite structure (different halide concentration and incorporation of different cations) which influences the halide ion mobility. In present case, two different E_a values confirm the two different halide ion migration mechanisms of both phase segregation and recovery processes. The high $E_a^{Seg.}$ value in phase segregation process indicates that a high activation energy is required to alter the lead—halide bonds for initiating halide ion migration. On the other hand, comparably low $E_a^{Rec.}$ value in recovery process may be due to the fact that back-diffusion of halide ions is driven by halide concentration gradient[33] or entropically driven intermixing[34,35] to return the perovskite into a homogeneous condition. In other possible way, once the trapped charge carriers have recombined, the created local electric field vanishes and then the halide ions start back-diffusion to fill the vacancies left in the original position.

2.4. Low-Temperature Dynamics and Role of Exciton–Phonon Coupling

The temperature dependent PL measurements are performed for in-depth understanding of mixed and demixed stage (segregated phases) in TC-MHP film over a range of temperature (T = 300–10 K). **Figure 5**a shows the temperature-dependent PL spectra of mixed stage (parent phase), on a semilogarithmic scale measured at low excitation power-density (<1 mW cm^{-2}) and exhibits a single emission peak with low energy asymmetry at low-temperature (10 K). The low-energy asymmetry in PL emission is related to presence of bound excitons and shallow energy levels by iodine interstitials defects.[36,37]

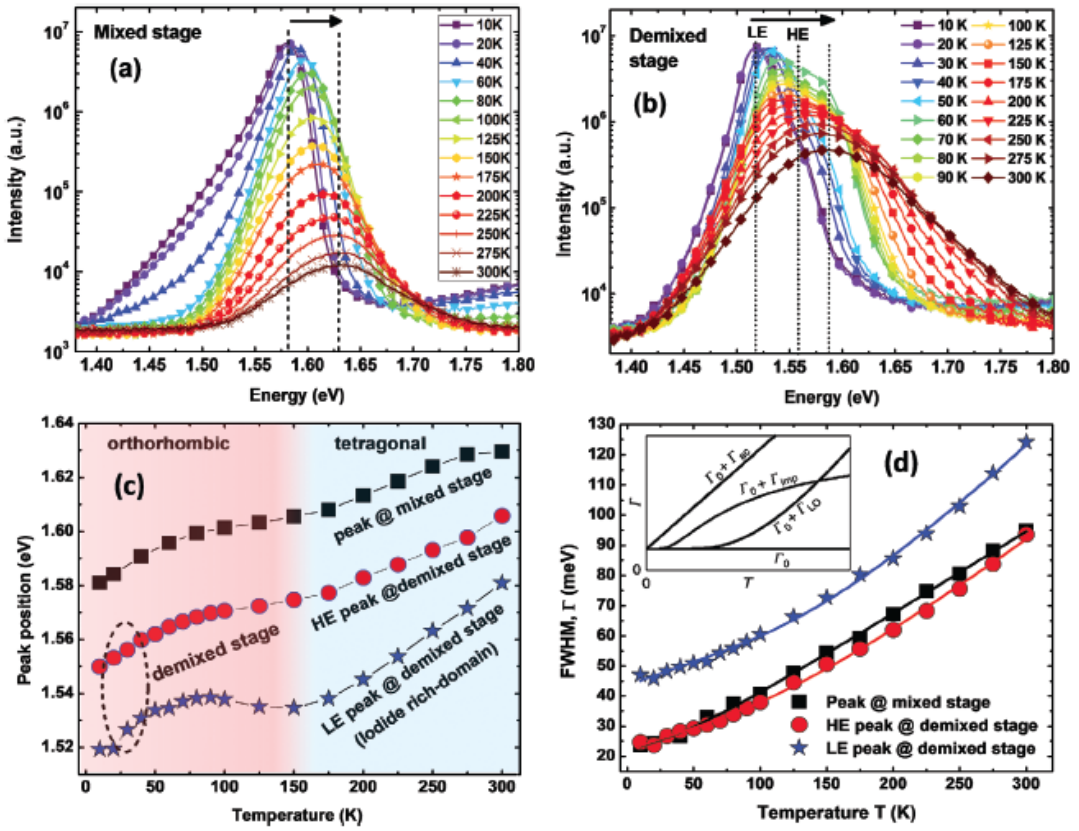

Figure 5. Temperature dependent PL emission characteristics of triple-cation mixed-halide $(MA_{0.17}FA_{0.83})_{0.95}Cs_{0.05}Pb(I_{0.83}Br_{0.17})_3$ perovskite film in both mixed and demixed (segregated phase) stages. a) Temperature-dependent PL spectra at low excitation power-density ($P_{exc} = 1$ mW cm^{-2}) and b) PL spectra of demixed stage under excitation with high power-density ($P_{exc} = 840$ mW cm^{-2}). c) A comparison of blue-shift response of emission peaks in both mixed and demixed stages as a function of temperature. d) The linewidth broadening of PL spectra in both mixed and demixed stages as function of temperature (symbols) along with least square fitting curves (solid lines) to examine the exciton–phonon coupling.

Figure 5b shows the semilog scale temperature dependent PL spectra of demixed stage measured at high power-density (840 mW cm^{-2}). For demixed stage dynamics, first sample was illuminated at high power (840 mW cm^{-2}) at room temperature to create phase segregated domains and then cooled down to 10 K under continuous photoexcitation. In Figure 5b results show the presence of two emission peaks located at 1.574 and 1.534 eV at 10 K, where, low-energy emission peak (LE-peak) is related to iodide-rich phase and high-energy emission peak (HE-peak) corresponds to remaining mixed halide phase. Figure 5c shows the blue-shift response of PL emission in both mixed and demixed stages with increasing temperature. In demixed stage, both peaks are red-shifted as compared to emission peak of mixed stage caused due to local change in halide composition of TC-MHP film after phase segregation. Furthermore, irrespective of perovskite composition, PL emission peaks of both mixed and demixed stages exhibit nonlinear blue-shift when temperature rises from 10 to 300 K. Generally, this behavior of perovskites is related to the thermal expansion of the lattice and stabilization of valence band energy.[38] The response character of blue-shift with temperature changes near $T \approx 150$ K in both stages, reveals the standard phase transition from orthorhombic to tetragonal phase in TC-MHP film. In mixed stage, PL emission peak experiences a blue-shift of 18 meV as rising the temperature from 10 to 80 K, while after phase transition to tetragonal phase, the PL peak exhibits a blue-shift of 24 meV when rising temperature from 150 to 300 K. In demixed stage, HE-peak follows the similar response and exhibits the blue-shift of ≈15 and ≈25 meV in orthorhombic (10–80 K) and tetragonal phase (150–300 K), respectively. However, LE-peak (iodide-rich domain) in demixed stage shows blue-shift of ≈18 meV in orthorhombic phase and large blue-shift of ≈45 meV in tetragonal phase when temperature goes from 150 to 300 K.

Furthermore, we carefully examine the temperature dependent PL linewidth broadening to study the contributions

of charge-carrier interactions with phonons in both mixed and demixed stages using Segall's expression[39]

$$\Gamma = \Gamma_{inh} + \Gamma_{ac} + \Gamma_{LO} + \Gamma_{imp} \quad (2)$$

$$\Gamma = \Gamma_{inh} + \gamma_{ac} T + \frac{\gamma_{LO}}{\exp(\hbar\omega_{LO}/k_B T) - 1} \quad (3)$$

where Γ_{inh} is the inhomogeneous broadening contribution that arises from scattering due to exciton–exciton interactions and crystal disorder, and is temperature independent. In expression (2), Γ_{ac} and Γ_{LO} are the homogeneous broadening terms resulting from acoustic and longitudinal optical (LO)-phonon (Fröhlich) scattering with charge carrier–phonon coupling strength of γ_{ac} and γ_{LO}, respectively. Acoustic phonons, whose energy is much smaller than $k_B T$, mainly relate to the deformation potential interaction which is linearly dependent on temperature. The exciton LO-phonon coupling (Fröhlich coupling) coefficient is associated with Bose–Einstein distribution of the LO-phonons, where $\hbar\omega_{LO}$ is the optical phonon energy of weakly dispersive LO-phonon branch. The FWHM of emission peaks are plotted as a function of temperature along with the least square fitting using Equation (3). The inset of Figure 5d demonstrates the typical PL linewidth broadening pattern with temperature associated with different scattering mechanisms. Result makes it apparent that Fröhlich coupling to LO-phonons is the predominant cause of linewidth broadening with rising temperature. Therefore, the scattering term from ionized impurities (Γ_{imp}) is excluded in Equation (3) for the rest of the analysis. In mixed stage, the calculated exciton LO-phonon coupling strength is ≈14.82 meV with LO-phonon energy of ≈22.8 meV. In demixed stage, HE-peak follows a similar response of linewidth broadening with increasing temperature; the corresponding coupling strength and LO-phonon energy are ≈38.86 and 86 meV, respectively. On the other hand, LE-peak shows large broadening in linewidth with temperature and the corresponding Fröhlich coupling strength and LO-phonon energy are ≈46.70 and ≈168 meV, respectively. Therefore, strong exciton LO-phonon coupling is observed in LE-peak of demixed stage, which may be due to the strong interaction of phonons with long lived charge carriers trapped in low energy iodide-rich domains.

3. Discussion

In the different scenario of photoexcitation induced phase segregation in mixed halide perovskite, excited-charge carriers play a main role either caused by light illumination[40,41] or by electrical injection.[7,42–45] In present case, photoexcited phase segregation would be initiated by charge separation arising from the carrier trapping on surface defects sites and at the grain boundaries (e.g., electrons and leaving behind holes) which attribute to the formation of local electric fields.[33,46,47] Furthermore, ion migration induced segregated domains having a significant offset in valence band and conduction band energies create a degree of charge separation between the randomly distributed segregated domains and remaining mixed halide phase, which thus establishes a local electric field in the film. The high barrier in valence-band energies between both iodide-rich domains and mixed halide perovskite act to draw holes away from the electrons. Thus photoexcitation induced local electric field promotes the degree of halide segregation and charge separation by further trapping of excited carriers into smaller-energy bandgap iodide-rich domains in a feedback loop. The phase segregated halide domains are stabilized under photoexcitation when a steady state is reached. A high Fröhlich coupling is observed in these iodide-rich domains due to strong interaction of soft ionic lattice with long lived excited charge carriers. It is reported that segregated halide clusters are stabilized by the presence of a photogenerated trapped polaron in the hybrid perovskites.[18] Therefore, high exciton LO-phonon coupling in iodide-rich domains induces sufficient polaronic strain which is able to locally change the free energy for halide demixing and leads to stabilize the segregated domains under photoexcitation. Eventually, concentration gradient of halide ions and limited funneling of photoexcited charge carriers into iodide-rich domains are also limits to the further growth of segregated domains under photoexcitation.

4. Conclusions

In summary, our findings provide new insights into the halide ion migration and phase segregation effect in triple-cation mixed-halide perovskite film when subjected to photoexcitation. We demonstrate that laser-excitation induced phase segregation in TC-MHP film leads to formation of smaller-bandgap iodide-rich and larger-bandgap bromide-rich domains where iodide-rich domains efficiently traps the photoexcited-carriers, revealing their dominant role in the origin of unusual long carrier lifetime (larger than 1 µs). Moreover, we found that phase segregation process is fully reversible under darkness and recovery rate increases with rising temperature. It is also shown that activation energy of halide ion migration is higher during photoexcitation induced phase segregation process as compared to recovery process under darkness. In addition, temperature-dependent PL studies have been performed for better understanding of exciton–phonon coupling in both mixed and demixed (segregated) states. A high Fröhlich coupling is observed in the segregated iodide-rich domains as compare to demixed (parent) phase due to strong coupling of phonons with long lived trapped charge carriers. Thus, high coupling strength in segregated iodide-rich domains may be responsible for the limited growth and stabilization of segregated halide domains under photoexcitation. These findings will help to understand the key issues of phase segregation in the mixed halide perovskite materials for the development of efficient solar cells and optoelectronic devices.

5. Experimental Section

The triple-cation mixed halide hybrid perovskite thin films (thickness ≈380 nm) were prepared using spin coating technique on glass substrates. At first, for the materials' synthesis, the $(MA_{0.17}\ FA_{0.83})\ Pb(I_{0.83}\ Br_{0.17})_3$ perovskite precursor solution was prepared by dissolving PbI_2 (1.1 M), FAI (1.0 M), $PbBr_2$ (0.2 M), MABr (0.2 M) in a 44 wt% mixture of anhydrous *N*,*N*-dimethylformamide (DMF) and dimethyl sulfoxide (DMSO). The solution was kept on stirring and then 42 µL

(5 vol%) of CsI (1.5 M in DMSO) was added in the resultant solution at room temperature. The precursors of FAI and PbI_2 were purchased from Sigma Aldrich; MABr from Solaronix; PbI_2 and CsI from Alfa Aesar. Before thin film coating, glass substrates were initially cleaned in deionized water, acetone, 2-propanol sequentially by ultrasonication followed by drying in dry nitrogen gas. In general, a dynamic dispense is preferred in synthesis process as it is a more controlled process that produces less substrate-to-substrate variation. The triple-cation solution was dispensed after the spin revolution stabilized at 6000 rpm. The total spinning time was 30 s and then 200 µL of chlorobenzene was dropped for 5 s to remove residual solvent. Films were annealed at 100 °C in nitrogen ambient for 1 h, allowing solvent evaporation and thin films crystallization.

The surface morphology measurement of prepared TC-MHP films were carried out using field-emission scanning electron microscopy (FE-SEM, JSM-7000 F) at CNRS-CSNSM, Orsay. The UV–visible absorption measurements were performed using Cary 5000 UV-VIS-NIR double beam spectrophotometer. Photoluminescence spectroscopy studies on mixed halide perovskite sample were performed in reflection geometry with a Horiba-JY Quantamaster spectrometer equipped with a R13456 photomultiplier (Hamamatsu) detector. A continuous-wave fiber-coupled laser diode (MDL-III-454 nm/90-800 mW) from CNI was used; it had a wavelength of ≈454 ± 5 nm at different excitation powers and was focused on the sample on a spot size of ≈1.75 mm diameter. The TCSPC measurements were carried out using NanoLED source (Horiba), which had an excitation of 482 nm and was pulsed at 25 kHz. For low-temperature measurements the samples were glued with silver paste in an optical closed-cycle cryostat from ARS Instruments equipped with two quartz windows.

Supporting Information

Supporting Information is available from the Wiley Online Library or from the author.

Acknowledgements

This work was supported by the LabEx PALM (ANR-10-LABX-0039-PALM), and IRS MOMENTOM (Université Paris-Saclay). The authors would like to thank Maria Carolina de Oliveira Aguiar (UFMG, Belo Horizonte, Brazil and LPS, Orsay, France) for careful English reading and corrections.

Conflict of Interest

The authors declare no conflict of interest.

Keywords

exciton–phonon coupling, hybrid perovskites, long carrier lifetime, phase segregation, triple-cation mixed-halide perovskites

Received: March 23, 2020
Revised: April 10, 2020
Published online:

[1] Y. Fu, H. Zhu, J. Chen, M. P. Hautzinger, X. Y. Zhu, S. Jin, *Nat. Rev. Mater.* **2019**, *4*, 169.
[2] J.-P. Correa-Baena, M. Saliba, T. Buonassisi, M. Grätzel, A. Abate, W. Tress, A. Hagfeldt, *Science* **2017**, *358*, 739.
[3] M. Saliba, T. Matsui, J. Y. Seo, K. Domanski, J. P. Correa-Baena, M. K. Nazeeruddin, S. M. Zakeeruddin, W. Tress, A. Abate, A. Hagfeldt, M. Grätzel, *Energy Environ. Sci.* **2016**, *9*, 1989.
[4] M. Abdi-Jalebi, Z. Andaji-Garmaroudi, S. Cacovich, C. Stavrakas, B. Philippe, J. M. Richter, M. Alsari, E. P. Booker, E. M. Hutter, A. J. Pearson, S. Lilliu, T. J. Savenije, H. Rensmo, G. Divitini, C. Ducati, R. H. Friend, S. D. Stranks, *Nature* **2018**, *555*, 497.
[5] Y. Hu, E. M. Hutter, P. Rieder, I. Grill, J. Hanisch, M. F. Aygüler, A. G. Hufnagel, M. Handloser, T. Bein, A. Hartschuh, K. Tvingstedt, V. Dyakonov, A. Baumann, T. J. Savenije, M. L. Petrus, P. Docampo, *Adv. Energy Mater.* **2018**, *8*, 1.
[6] E. T. Hoke, D. J. Slotcavage, E. R. Dohner, A. R. Bowring, H. I. Karunadasa, M. D. McGehee, *Chem. Sci.* **2015**, *6*, 613.
[7] H. Zhang, X. Fu, Y. Tang, H. Wang, C. Zhang, W. W. Yu, X. Wang, Y. Zhang, M. Xiao, *Nat. Commun.* **2019**, *10*, 1.
[8] S. Draguta, O. Sharia, S. J. Yoon, M. C. Brennan, Y. V. Morozov, J. S. Manser, P. V. Kamat, W. F. Schneider, M. Kuno, *Nat. Commun.* **2017**, *8*, 200.
[9] F. Ruf, P. Rietz, M. F. Aygüler, I. Kelz, P. Docampo, H. Kalt, M. Hetterich, *ACS Energy Lett.*. **2018**, *3*, 2995.
[10] D. Kim, J. S. Yun, P. Sharma, D. S. Lee, J. Kim, A. M. Soufiani, S. Huang, M. A. Green, A. W. Y. Ho-Baillie, J. Seidel, *Nat. Commun.* **2019**, *10*, 1.
[11] H. Tsai, R. Asadpour, J. C. Blancon, C. C. Stoumpos, O. Durand, J. W. Strzalka, B. Chen, R. Verduzco, P. M. Ajayan, S. Tretiak, J. Even, M. A. Alam, M. G. Kanatzidis, W. Nie, A. D. Mohite, *Science* **2018**, *360*, 67.
[12] J. Huang, Y. Yuan, Y. Shao, Y. Yan, *Nat. Rev. Mater.* **2017**, *2*, 17042.
[13] A. J. Knight, A. D. Wright, J. B. Patel, D. P. McMeekin, H. J. Snaith, M. B. Johnston, L. M. Herz, *ACS Energy Lett.* **2019**, *4*, 75.
[14] G.-J. A. H. Wetzelaer, M. Scheepers, A. M. Sempere, C. Momblona, J. Ávila, H. J. Bolink, *Adv. Mater.* **2015**, *27*, 1837.
[15] T. Leijtens, G. E. Eperon, A. J. Barker, G. Grancini, W. Zhang, J. M. Ball, A. R. S. Kandada, H. J. Snaith, A. Petrozza, *Energy Environ. Sci.* **2016**, *9*, 3472.
[16] X.-Y. Zhu, V. Podzorov, *J. Phys. Chem. Lett.* **2015**, *6*, 4758.
[17] W. Nie, J. C. Blancon, A. J. Neukirch, K. Appavoo, H. Tsai, M. Chhowalla, M. A. Alam, M. Y. Sfeir, C. Katan, J. Even, S. Tretiak, J. J. Crochet, G. Gupta, A. D. Mohite, *Nat. Commun.* **2016**, *7*, 1.
[18] C. G. Bischak, C. L. Hetherington, H. Wu, S. Aloni, D. F. Ogletree, D. T. Limmer, N. S. Ginsberg, *Nano Lett.*. **2017**, *17*, 1028.
[19] K. Miyata, D. Meggiolaro, M. Tuan Trinh, P. P. Joshi, E. Mosconi, S. C. Jones, F. De Angelis, X. Y. Zhu, *Sci. Adv.* **2017**, *3*, e1701217.
[20] M. Fu, P. Tamarat, J. B. Trebbia, M. I. Bodnarchuk, M. V. Kovalenko, J. Even, B. Lounis, *Nat. Commun.* **2018**, *9*, 1.
[21] F. Vietmeyer, P. A. Frantsuzov, B. Janko, M. Kuno, *Phys. Rev. B* **2011**, *83*, 115319.
[22] M. Baranowski, J. M. Urban, N. Zhang, A. Surrente, D. K. Maude, Z. Andaji-Garmaroudi, S. D. Stranks, P. Plochocka, *J. Phys. Chem. C* **2018**, *122*, 17473.
[23] S. Draguta, S. Thakur, Y. V. Morozov, Y. Wang, J. S. Manser, P. V. Kamat, M. Kuno, *J. Phys. Chem. Lett.* **2016**, *7*, 715.
[24] T. Elmelund, B. Seger, M. Kuno, P. V Kamat, *ACS Energy Lett.* **2020**, *5*, 56.
[25] M. Benavides-Garcia, K. Balasubramanian, *J. Chem. Phys.* **1994**, *100*, 2821.
[26] S. J. Yoon, S. Draguta, J. S. Manser, O. Sharia, W. F. Schneider, M. Kuno, P. V. Kamat, *ACS Energy Lett.* **2016**, *1*, 290.
[27] K. T. Butler, J. M. Frost, A. Walsh, *Mater. Horiz.* **2015**, *2*, 228.
[28] W. Mao, C. R. Hall, A. S. R. Chesman, C. Forsyth, Y. Cheng, N. W. Duffy, T. A. Smith, U. Bach, *Angew. Chem.* **2019**, *131*, 2919.
[29] J. M. Ball, A. Petrozza, *Nat. Energy* **2016**, *1*, 16149.
[30] S. D. Stranks, *ACS Energy Lett.* **2017**, *2*, 1515.
[31] H. Lee, S. Gaiaschi, P. Chapon, D. Tondelier, J. E. Bourée, Y. Bonnassieux, V. Derycke, B. Geffroy, *J. Phys. Chem. C* **2019**, *123*, 17728.

[32] F. Ebadi, M. Aryanpour, R. Mohammadpour, N. Taghavinia, *Sci. Rep.* **2019**, *9*, 11962.
[33] D. W. DeQuilettes, W. Zhang, V. M. Burlakov, D. J. Graham, T. Leijtens, A. Osherov, V. Bulović, H. J. Snaith, D. S. Ginger, S. D. Stranks, *Nat. Commun.* **2016**, *7*, 11683.
[34] X. Tang, M. Van Den Berg, E. Gu, A. Horneber, G. J. Matt, A. Osvet, A. J. Meixner, D. Zhang, C. J. Brabec, *Nano Lett.* **2018**, *18*, 2172.
[35] A. J. Barker, A. Sadhanala, F. Deschler, M. Gandini, S. P. Senanayak, P. M. Pearce, E. Mosconi, A. J. Pearson, Y. Wu, A. R. Srimath Kandada, T. Leijtens, F. De Angelis, S. E. Dutton, A. Petrozza, R. H. Friend, *ACS Energy Lett.* **2017**, *2*, 1416.
[36] O. Plantevin, S. Valère, D. Guerfa, F. Lédée, G. Trippé-Allard, D. Garrot, E. Deleporte, *Phys. Status Solidi B* **2019**, *256*, 1900199.
[37] D. Meggiolaro, S. G. Motti, E. Mosconi, A. J. Barker, J. Ball, C. Andrea Riccardo Perini, F. Deschler, A. Petrozza, F. De Angelis, *Energy Environ. Sci.* **2018**, *11*, 702.
[38] M. I. Dar, G. Jacopin, S. Meloni, A. Mattoni, N. Arora, A. Boziki, S. M. Zakeeruddin, U. Rothlisberger, M. Grätzel, *Sci. Adv.* **2016**, *2*, e1601156.
[39] S. Rudin, T. L. Reinecke, B. Segall, *Phys. Rev. B* **1990**, *42*, 11218.
[40] D. J. Slotcavage, H. I. Karunadasa, M. D. McGehee, *ACS Energy Lett.* **2016**, *1*, 1199.
[41] M. C. Brennan, S. Draguta, P. V. Kamat, M. Kuno, *ACS Energy Lett.* **2018**, *3*, 204.
[42] P. Vashishtha, J. E. Halpert, *Chem. Mater.* **2017**, *29*, 5965.
[43] I. L. Braly, R. J. Stoddard, A. Rajagopal, A. R. Uhl, J. K. Katahara, A. K. Y. Jen, H. W. Hillhouse, *ACS Energy Lett.* **2017**, *2*, 1841.
[44] T. Duong, H. K. Mulmudi, Y. Wu, X. Fu, H. Shen, J. Peng, N. Wu, H. T. Nguyen, D. Macdonald, M. Lockrey, T. P. White, K. Weber, K. Catchpole, *ACS Appl. Mater. Interfaces* **2017**, *9*, 26859.
[45] H. Lee, S. Gaiaschi, P. Chapon, A. Marronnier, H. Lee, J.-C. Vanel, D. Tondelier, J.-E. Bourée, Y. Bonnassieux, B. Geffroy, *ACS Energy Lett.* **2017**, *2*, 943.
[46] J. M. Azpiroz, E. Mosconi, J. Bisquert, F. De Angelis, *Energy Environ. Sci.* **2015**, *8*, 2118.
[47] N. Ahn, K. Kwak, M. S. Jang, H. Yoon, B. Y. Lee, J.-K. Lee, P. V Pikhitsa, J. Byun, M. Choi, *Nat. Commun.* **2016**, *7*, 13422.

ADVANCED FUNCTIONAL MATERIALS

Supporting Information

for *Adv. Funct. Mater.,* DOI: 10.1002/adfm.202002622

Reversible Photoinduced Phase Segregation and Origin of Long Carrier Lifetime in Mixed-Halide Perovskite Films

Subodh K. Gautam, Minjin Kim, Douglas R. Miquita, Jean-Eric Bourée, Bernard Geffroy, and Olivier Plantevin**

Supplementary Information

Reversible Photo-Induced Phase Segregation and Origin of Long Carrier Lifetime in Mixed-Halide Perovskite Films

Subodh K. Gautam[1,a)], Minjin Kim[2], Douglas R. Miquita[1,3], Jean-Eric Bouree[2], Bernard Geffroy[2,4] and Olivier Plantevin[1,b)]

[1] Université Paris-Saclay, CNRS, Laboratoire de Physique des Solides, 91405, Orsay, France.

[2] LPICM, CNRS, Ecole Polytechnique, Institut Polytechnique de Paris, route de Saclay, 91128 Palaiseau, France.

[3] Centro de Microscopia - Universidade Federal de Minas Gerais, Belo Horizonte, MG, 31270-901- Brasil

[4] Université Paris-Saclay, CEA, CNRS, NIMBE, LICSEN, 91191, Gif-sur-Yvette, France

S1: Absorbance and photoluminescence spectra

Fig. S1 shows the optical absorbance and photoluminescence spectra of triple-cation mixed-halide $(MA_{0.17}\,FA_{0.83})_{0.95}Cs_{0.05}\,Pb(I_{0.83}\,Br_{0.17})_3$ perovskite film. The TC-MHP perovskite film exhibits high optical absorbance after 1.60 eV and exhibit the direct band gap (E_g) of ~ 1.625 eV, obtained from absorbance data using Tauc's relation [1].

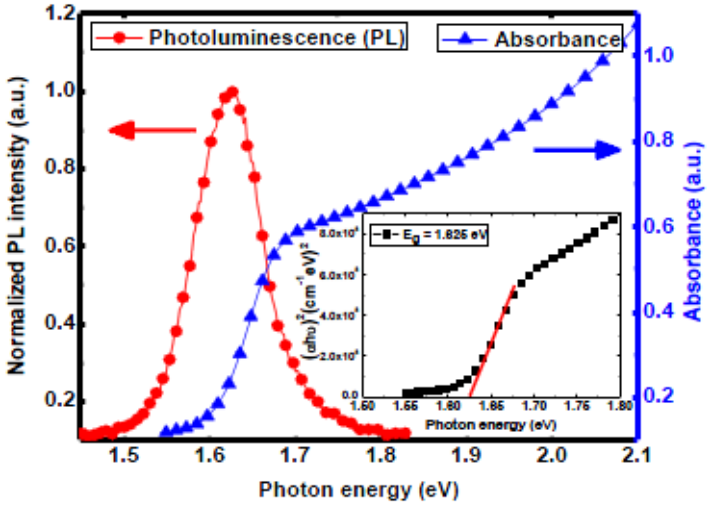

Figure S1: Absorbance and photoluminescence spectra of triple-cation mixed-halide $(MA_{0.17}\,FA_{0.83})_{0.95}Cs_{0.05}\,Pb(I_{0.83}\,Br_{0.17})_3$ perovskite film.

S2. Film morphology and average grain size

The surface morphology of the triple-cation mixed-halide perovskite thin film was studied using field emission-scanning electron microscope (FE-SEM) technique, and the result is shown in the Fig. S2. The image was taken at low dimension scale and reveals that the surface of the perovskite film is formed by a dense nano-structured grains uniformly distributed. The grain sizes were measured from SEM image analysis using ImageJ software and a histogram of grain sizes was plotted, revealing an average morphological grain size of about 175 ± 50 nm. The uniform distribution and grain interconnection in film may play a significant role in the enhanced charge transport and optical properties.

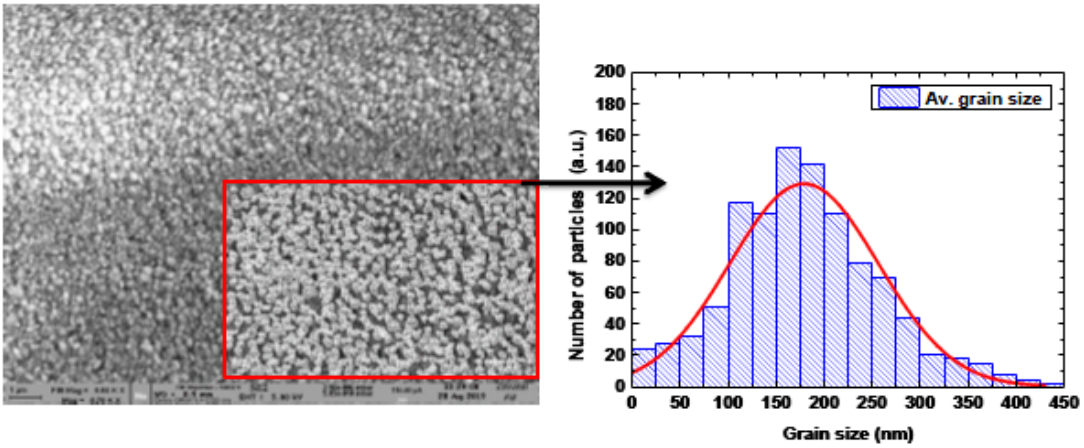

Figure S2: FE-SEM image of the surface of triple-cation mixed-halide $(MA_{0.17}\,FA_{0.83})_{0.95}Cs_{0.05}\,Pb\,(I_{0.83}\,Br_{0.17})_3$ perovskite film along with the histogram of grain sizes extracted from SEM image.

S3. Time dependent PL emission at different given excitation power-densities

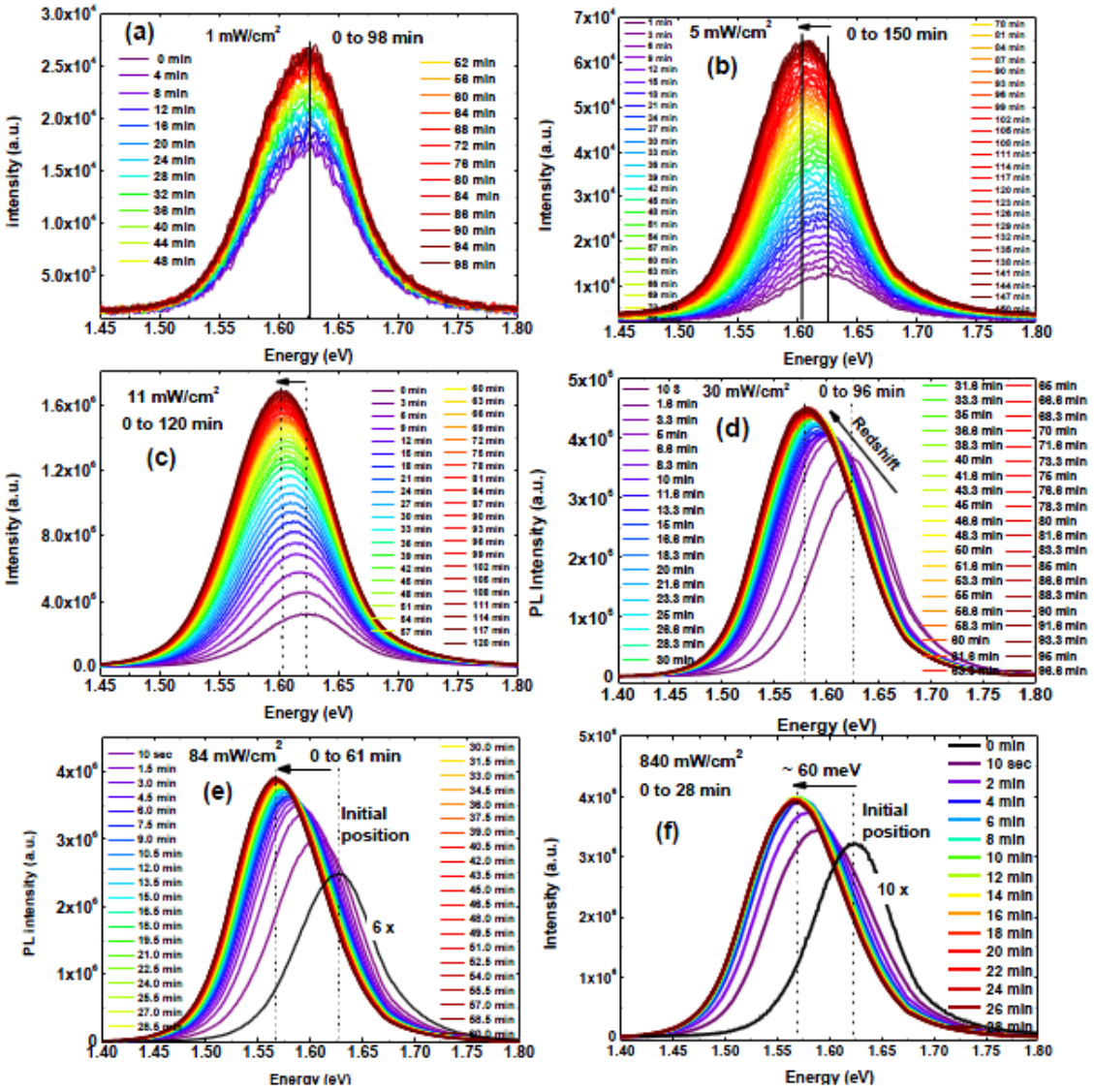

Figure S3: (a-e) Time dependent spectroscopic observation of halide phase segregation in triple-cation mixed-halide $(MA_{0.17}FA_{0.83})_{0.95}Cs_{0.05}Pb(I_{0.83}Br_{0.17})_3$ perovskite film at different excitation power densities.

S4. Relationship between photo-induced PL-shift and halide composition variation

The photo-excitation induced phase segregation induced in mixed halide perovskite was first confirmed by Hoke and colleagues [2] in $MAPb(I_{1-x}Br_x)_3$ thin films via concerted PL and powder X-ray diffraction (pXRD) measurements. McGehee and coworkers have shown that $MAPb(I_{1-x}Br_x)_3$ material undergo phase segregation and that 23% of the material segregates into iodide-rich inclusions [2]. The band gap variation by photo-excitation in mixed halide perovskite materials can also be estimated from their halide composition content. A relationship between PL-redshift and halide composition variation is establish using Vegard's law expression, [$E_{g\text{-}mix} = E_g.I(1-x) + E_g.Brx - bx(1-x)$] where E_g is bandgap and b is a bowing parameter to account for the degree of non-linear deviations. In present case, PL-emission values of mixed and segregated domains are used to fit the non-linear bandgap variation curve as a function of Br-concentration (x = 0 to 1.0) content and shown in Fig S4.

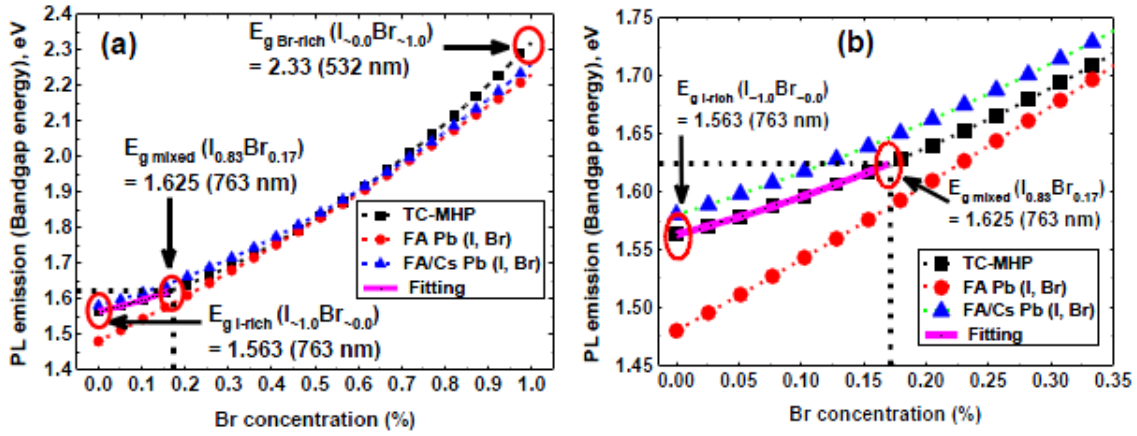

Figure S4: (a) The PL emission shift (solid pink line) is compared with estimated non-linear band gap variation as a function of bromide (Br) composition (x = 0 to 1.0) using Vegard's law expression. PL-emission values of mixed and segregated stages in TC-MHP film are compared with data points acquired from *Rehman, W. et al.* [5] and *Eperon, G.E. et al.* [6]. (b) A zoomed non-linear fitted curve of PL emission shift (solid line) for estimating Br-composition variation.

The PL-emission values of 1.625 eV, for mixed state ($I_{0.83}Br_{0.17}$), 1.564 eV for segregated I-rich ($I_{\sim1.0}Br_{\sim0}$) and 2.33 eV for Br-rich ($I_{\sim0}Br_{\sim1.0}$) domains are used to draw the bandgap variation

curve. Fig. S4 (b) shows zoomed fitted curve for clarity. Result shows that bandgap variation curve is best fitted with bowing parameter b = 0.48 eV for TC-MHP film. For comparison, other mixed halide data points acquired from literature for E_g-values range from 1.48 to 2.23 eV for [b = 0.15 eV, $FAPb(I_{1-x}Br_x)_3$ [5] and 1.58 to 2.26 eV for [b = 0.35 eV $FA_{0.83}Cs_{0.17}Pb(I_{1-x}Br_x)_3$] [6].

A non-linear decrease in bandgap under photo-excitation confirms the decreasing in the Br-concentration in parent phase of TC-MHP film. Results are also in agreement with the structural change absorbed by parent mixed halide reported by Draguta, S. et al. [4] and McGehee's prior XRD-based estimates [2]. Therefore, results confirm that photo-induced PL redshift follow the change in halide composition where bromide concentration decreases (enrichment in iodide) and segregates as separated bromide-rich domains.

Effect of composition variation on PL linewidth broadening

The PL emission broadening in mixed TC-MHP may be due to the change in halide composition (decrease in bromide and enrichment of iodide content) as interpreted from Fig. 1(c). However, the PL width broadening with varying halide composition may include other complex phenomenon such as increased lattice disorder (due ion migration and related point defects). The role of electron-phonon coupling role in linewidth broadening is well discussed in the main article (from temperature dependent studies, Fig. 5 (d)) and found that electron-LO phonon coupling strength is higher in segregated domains as compare to parent TC-MHP phase.

S5. Threshold excitation density of phase segregation

The threshold excitation density of phase segregation (P_{th}^{Seg}) is calculated at 296 K and 330 K. Fig. S5 shows the PL- peak position a function of excitation power-density. Results show that P_{th}^{Seg} value is ~ 2.0 mW/cm^2 at 300 K higher than the P_{th}^{Seg} ~ 1.5 mW/cm^2 at 330 K. In comparison to 296K, the observed low P_{th}^{Seg} value at 330 K reveals that lower-excitation density input is required for initiating the phase segregation process at higher temperature (faster segregation rate). The estimated P_{th}^{Seg} value of TC-MHP is about 100 times higher as compare to reported values of ~30 μW/cm^2 and ~40 μW/cm^2 for MAPb($I_{0.5}Br_{0.5}$)$_3$ at 300 K [4, 7] which is meaningful as triple cation perovskites were developed for their increased robustness as compared to single cation perovskites.

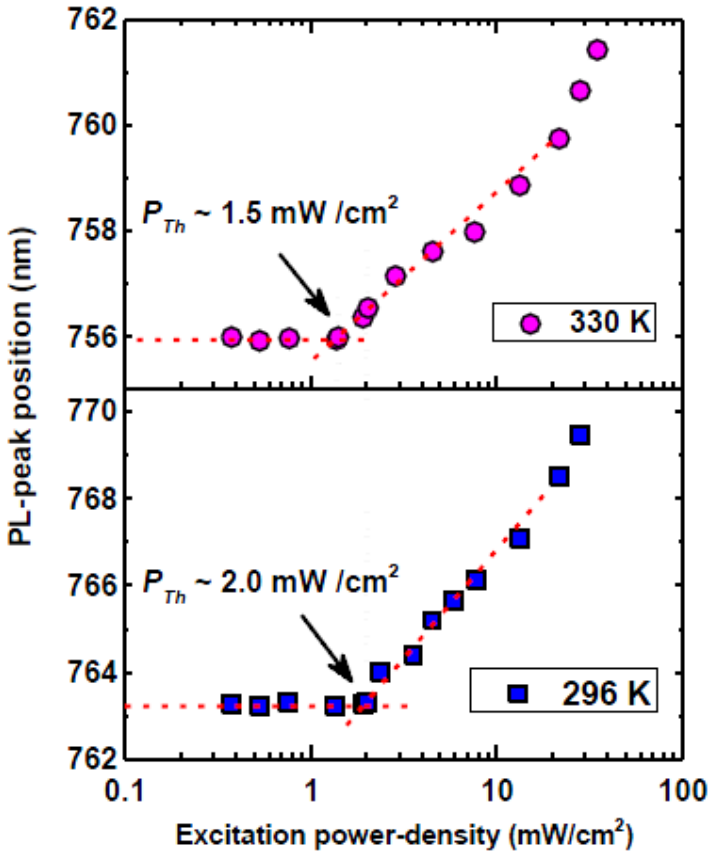

Figure S5: PL-peak position as a function of excitation power density for threshold excitation energy of phase segregation at two different temperatures (300 K and 330 K).

S6. Time dependent phase segregation dynamics of TC-MHP film excited at different temperatures.

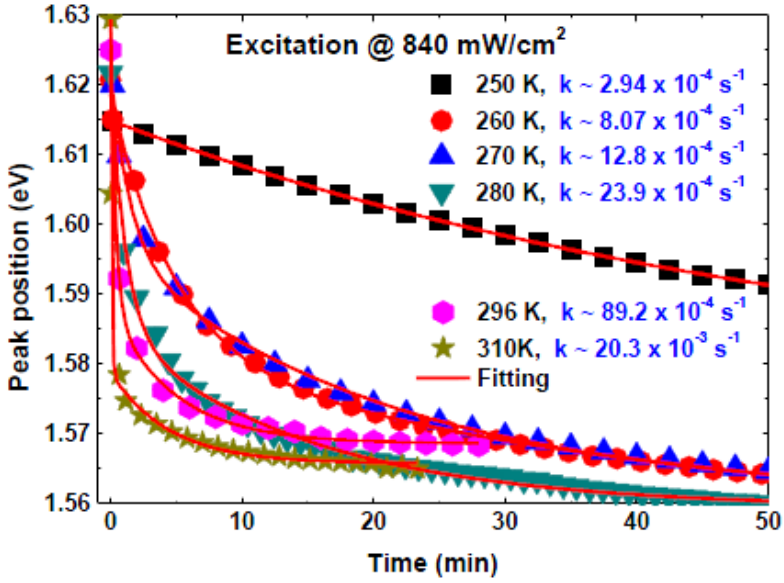

Figure S6: Time dependent red-shift in PL peaks excited with 840 mW/cm^2 excitation power and fitted by exponential curves to calculate the phase segregation rate constants at different temperatures.

S7. Time dependent recovery dynamics of phase-segregated TC-MHP film under dark at different temperatures.

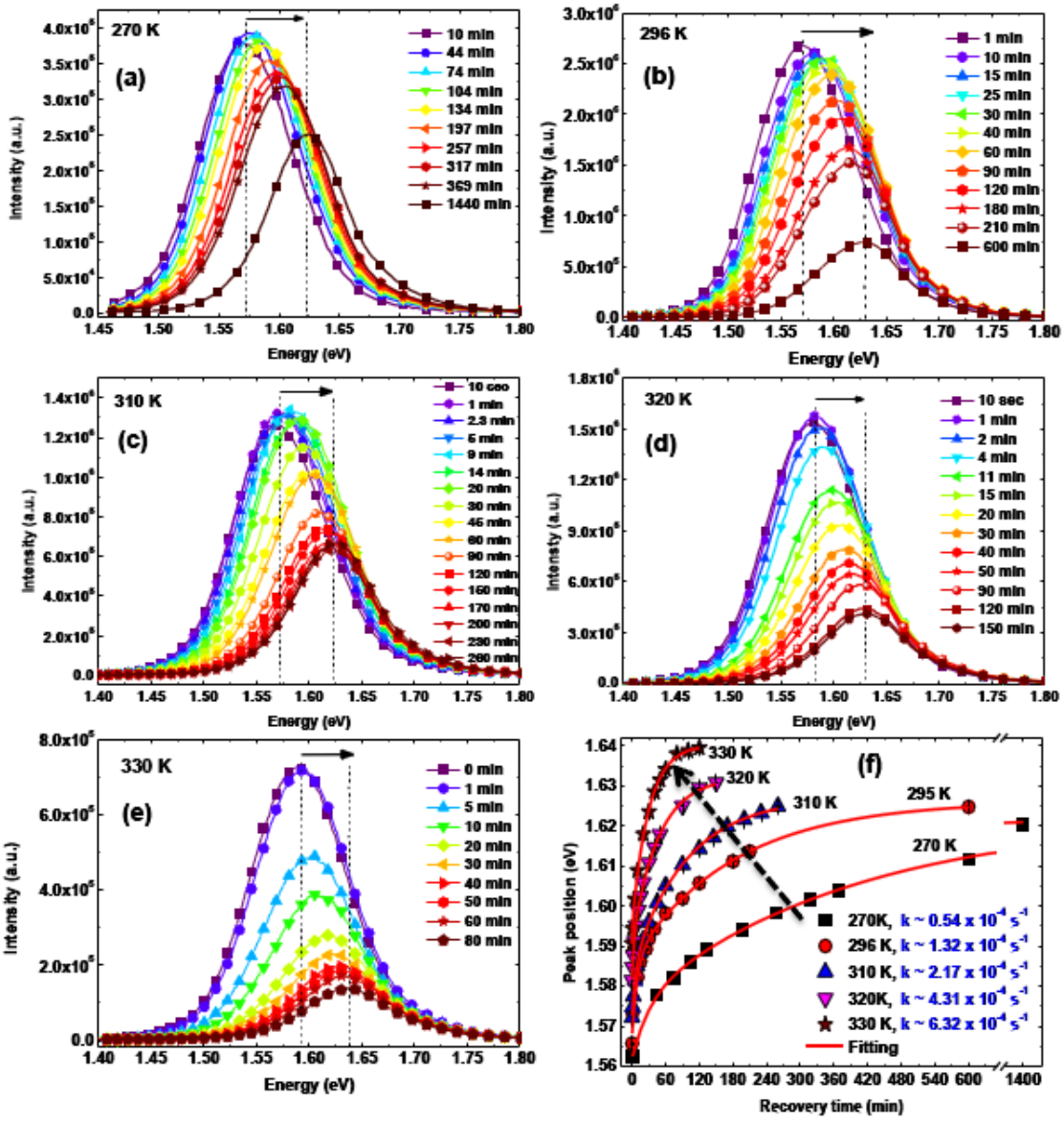

Figure S7: (a-e) Time dependent PL spectra of recovery process of phase segregated triple-cation mixed-halide $(MA_{0.17}FA_{0.83})_{0.95}Cs_{0.05}Pb(I_{0.83}Br_{0.17})_3$ perovskite film at different temperatures. **(f)** Analysis of recovery rate constants of segregated film at different temperatures with exponential fitted curves.

References

[1] J. Tauc R. Grigorovici A. Vancu, *Phys. Status Solidi* **1966**, 15, 627

[2] E. T. Hoke, D. J. Slotcavage, E. R. Dohner, A. R. Bowring, H. I. Karunadasa, M. D. McGehee, *Chem. Sci.* **2015**, *6*, 613.

[3] S. J. Yoon, S. Draguta, J. S. Manser, O. Sharia, W. F. Schneider, M. Kuno, P. V. Kamat, *ACS Energy Lett.* **2016**, *1*, 290.

[4] S. Draguta, O. Sharia, S. J. Yoon, M. C. Brennan, Y. V. Morozov, J. S. Manser, P. V. Kamat, W. F. Schneider, M. Kuno, *Nat. Commun.* **2017**, 8, 200.

[5] W. Rehman, D. P. McMeekin, J. B. Patel, R. L. Milot, M. B. Johnston, H. J. Snaith and L. M. Herza, *Energy Environ.* **2017**, Sci. 10, 361

[6] G. E. Eperon, S. D. Stranks, C. Menelaou, M. B. Johnston, L. M. Herz and H. J. Snaith, *Energy Environ. Sci.* **2014**, 7, 982–988

[7] T. Elmelund, B. Seger, M. Kuno and P. V. Kamat, *ACS Energy Lett.* **2020**, 5, 56-63

ECOLE DOCTORALE

Titre : Analyse de la migration ionique et des caractéristiques de vieillissement pour les cellules solaires pérovskite halogénée en couches minces à base de triple cations et $CH_3NH_3PbI_{3-x}Cl_x$.

Mots clés : Cellules Solaires Pérovskite (PSCs), Pérovskite halogénée à base de triple cations (3CP), Migration ionique, Vieillissement, Spectroscopie d'Emission Optique par Décharge Plasma (GD-OES), Spectroscopie d'Impédance (IS)

Résumé: Les matériaux pérovskites hybrides organiques-inorganiques (HOIPs) ont suscité beaucoup de travaux de recherche en chimie et en science des matériaux de par leurs propriétés photoélectriques attrayantes (rendement de conversion énergétique de plus de 25 %). Cependant, malgré des avancées considérables dans ce domaine de recherche, plusieurs questions concernant la physique des ions dans les matériaux pérovskites restent en suspens. Dans cette thèse, l'analyse de pérovskites hybrides de type CH3NH3PbI3-xClx (MAPI) et de type {3CP: $(MA_{0.17}FA_{0.83})_{0.95}Cs_{0.05}Pb(I_{0.83}Br_{0.17})_3$ (MA: Methylammonium, FA: Formamidinium)} sont présentées à la fois en films minces et en cellules solaires (PSCs).

L'optimisation de la synthèse de la pérovskite hybride halogénée de type 3CP sera présentée. Les cellules solaires à base de pérovskite 3CP seront ensuite fabriquées selon une structure inversée (type p-i-n) et caractérisées optiquement et électroniquement. La spectroscopie d'émission optique par décharge plasma (GD-OES) a permis une mise en évidence expérimentale directe de la migration des ions dans les HOIPs à base de MAPI et de 3CP sous un champ électrique constant appliqué. Les résultats GD-OES in-situ et ex-situ ont montré que le 3CP avait une récupération plus rapide de la migration des ions par rapport au MAPI. Grâce à la Spectroscopie d'Impédance (IS), le phénomène d'accumulation d'ions à l'interface n'a été observé qu'avec un balayage de tension pendant 2 minutes.

Enfin, le mécanisme de vieillissement des PSCs a été étudié avec le vieillissement des performances des cellules solaires, les mesures d'IS et GD-OES. Une augmentation des ions accumulés à l'interface, due au vieillissement, est observée au bout de 10 jours. Les résultats démontrent que les ions halogénures de la couche HOIP diffusent dans l'électrode d'argent supérieure sous forme d'halogénures d'argent (AgI et AgBr) comme cela a déjà été proposé dans la littérature.

Lors du développement d'une pérovskite encore améliorée, cette étude peut suggérer un critère d'évaluation du matériau.

Title : Analysis of Ion Migration and Ageing Characteristics for Triple-cation and $CH_3NH_3PbI_{3-x}Cl_x$ Perovskite Based Thin-Film Solar Cells

Keywords : Perovskite Solar Cells (PSCs), Triple-cation Lead Halide (3CP), Ion migration, Ageing, GD-OES, Impedance Spectroscopy

Abstract: Hybrid organic-inorganic perovskite materials (HOIPs) have emerged as an exciting research topic in chemistry and materials science for their attractive photoelectrical properties (over 25% efficiency). However, despite their processing advantages (low-cost solution process) and outstanding solar to electrical energy conversion properties, HOIPs materials suffer from several drawbacks such as environmental stability impeding their commercialization. In this thesis, analyses of $CH_3NH_3PbI_{3-x}Cl_x$ (MAPI) and Triple-cation Lead Halide {3CP: $(MA_{0.17}FA_{0.83})_{0.95}Cs_{0.05}Pb(I_{0.83}Br_{0.17})_3$ (MA: Methylammonium, FA: Formamidinium)} based perovskite thin films and solar cells are presented.

First, the optimization of the halide perovskite layer (3CP) is introduced. 3CP based Perovskite Solar Cells (PSCs) are then manufactured in the inverted (p-i-n) planar structure and characterized optically and electrically. Direct experimental evidence of ion migration in HOIPs (MAPI and 3CP)under an applied electric field was found by the Glow Discharge Optical Emission Spectroscopy (GD-OES). The results shows that 3CP had faster ion migration recovery compared to MAPI. The Impedance Spectroscopy (IS) observes the ion accumulation phenomenon at the interface with a voltage sweep for 2 min.

Finally, the ageing mechanism of the PSCs was investigated with solar cell performance ageing, IS, and GD-OES. An increase in ageing-related ion accumulation at the interface was observed for ten days. After long-term ageing, halogen ions were observed in the top silver electrode with GD-OES. The results demonstrate that halide ions in the HOIP layer diffuse into silver electrode in the form of silver halide (AgI and AgBr), as already mentioned in the literature.

When developing a more improved perovskite material and evaluating the material properties, this study can suggest one criterion for material evaluation.

Institut Polytechnique de Paris

91120 Palaiseau, France